THEORETICAL STUDIES OF ANISOTROPIC ION TRANSPORT SYSTEMS

A THESIS
SUBMITTED IN PARTIAL FULFILMENT
OF THE REQUIREMENTS FOR THE DEGREE
OF
DOCTOR OF PHILOSOPHY IN CHEMISTRY
IN THE
UNIVERSITY OF CANTERBURY
by

Stephen T. Grice

University of Canterbury
1993

... quidquid agunt homines, nasci,
nuberem, moriri, gaudea, discursus,
nostri farrago libelli est.

To my good friend, David Mann, and my loving mother, Bernadette Frances.

Abstract

Ab initio calculations of potential energy surfaces have been applied to a range of chemical problems. Specifically these methods have been applied to the Diels-Alder reaction between butadiene and acetylene. The structure of the reactants, the C_s transition state, and the products have been calculated. The transition state geometry and energy is analysed in terms of orbital interactions and distortion energy relative to the separated reactants. The increase in energy of the filled π-orbital of acetylene not involved in bonding changes is the major contributor to the activation energy for the Diels-Alder reaction of butadiene with acetylene being greater than that found between butadiene and ethylene. Comparisons with a series of other related Diels-Alder reactions are discussed.

The calculation of interaction potentials of a series of open shell ions with helium has been combined with moment method calculations to determine the ion transport properties of systems that involve anisotropy. First the theory of the moment methods used to calculate the transport properties of ions in dilute gases is reviewed. The theory for spherically symmetric ions in a spherically symmetric gas is briefly discussed, followed by a review of the recent specialisation of the theory for diatomic ions in diatomic gases to atomic ions in a diatomic gas.

The theory of spherically symmetric systems is then applied to open shell ions that have orbital angular momenta greater than zero. Any theoretical treatment of the ion transport properties of such ions must recognise that more than one collision channel is available to the collision partners. Two classical models are developed that involve non-adiabatic transitions between these collision channels during a collision and between collisions. The models are used to study the mobilities of the following ions: C^+ (^2P), C^{+*} (^4P), N^+ (^3P), O^+ (^4S), O^{+*} (^2P), Si^+ (^2P), Si^{+*} (^4P). A summary and discussion is given.

The theory of atomic ions in diatomic gases is then applied to the $Li^+—N_2$ and the $Li^+—CO$ systems. *Ab initio* calculations of the rigid rotor potential energy surfaces for these systems are followed by calculations of the transport cross sections and transport coefficients. Comparisons of the transport coefficients derived from existing potential energy surfaces show that the potential energy surfaces calculated in this work are significantly better, and as good as can be derived from comparison of the theoretical and experimental ion transport results.

Contents

List of Tables

List of Figures

Chapter 1

Introduction

The foundation stone of modern theoretical chemistry is the Schroedinger equation. The solution of the Schroedinger equation has allowed theoretical chemists to examine a wide range of chemical phenomena. This thesis starts with a review of the *ab initio* methods used to solve the Schroedinger equation for the calculation of the interaction potentials of open shell ions with inert gases, the potential energy surface of small ion-molecule systems, and the reactant, product, and transition state energies and geometries of a Diels-Alder reaction studied in this thesis.

The calculations of the Diels-Alder reaction between acetylene and butadiene are presented in chapter 3.

At the time that this work began the theory of ion transport of spherically symmetric ions in spherically symmetric gases was well developed. The interaction potentials of many of the halide anion-inert gas and alkali metal cation-inert gas systems had been used to calculate the ion transport coefficients and *vice versa*. Thus many of the systems to which the theory was applicable had been studied and reported. The main objective of this thesis was to extend the application of ion transport theory to systems that involved some form of anisotropy.

A brief review of the current state of ion transport theory is given in chapter 4.

It was proposed to extend the application for spherically symmetric systems to the study of open shell systems in which one or more interaction potentials correlate with the collision partners. The results of the calculations have been summarised and discussed in chapter 5.

To further investigate the effects of anisotropy on ion transport properties it

was proposed to calculate the potential energy surface of the prototypical (A^+—B_2) atomic ion-diatom system, Li^+—N_2. These calculations have been detailed in chapter 6. The potential energy surface was then combined with trajectory calculations to obtain transport cross sections, and the transport coefficients were calculated from these in the usual way. These calculations are the subject of chapter 7. The calculation of atomic ion-diatom systems was then extended to a system of greater anisotropy (A^+—BC), the Li^+—CO system. The potential energy surface of this system was then calculated and compared to the results for Li^+—N_2. These calculations are presented in chapter 8. The potential energy surface was then used to calculate the transport coefficients of Li^+ ions in CO gas in a similar fashion to that described for the Li^+—N_2 system.

Finally a conclusion and brief discussion of the likely future direction of this work is presented.

Chapter 2

Theory and Computation of Chemical Systems

2.1 Introduction

Since the genesis of quantum mechanics, physicists and chemists have attempted to rationalise the behaviour of chemical systems in a new way. Application of the theory has led to new insights about the nature of chemical systems and has revolutionised understanding in the physical sciences. The advent of the silicon chip enabled theoretical chemists to calculate numerical properties of chemical systems of interest to experimentalists, and on some occasions to challenge and overturn their results [1]. Today, theoretical chemistry has advanced to the point that it is a method that experimentalists with a general background in quantum chemistry routinely use to rationalise their experimental results. Although many of the theories used have become more complicated, the use of high speed digital computers and standard packages such as GAMESS [2] and GAUSSIAN [3, 4] have rendered the application of theory very accessible to all chemists. The trend towards reliance on theory will continue as computing speed increases and costs decrease.

Today there exist two main approximate methods used in calculating the electronic structure of molecules and their chemical interactions, Valence Bond (VB) theory and Molecular Orbital (MO) theory. Valence Bond theory was first used by Heitler and London [5] over 60 years ago to describe the ground state of the hydrogen molecule. It constructs a total electronic wavefunction from the one-electron

atomic orbitals, allowing bonding of the valence electron pairs between the atomic orbitals of the bonding pair in the intuitive chemical way. Molecular orbital theory was also developed in the late 1920's by Hund and Mulliken. It constructed a total electronic molecular wavefunction from molecular orbitals which are themselves a linear combination of basis functions. Although less intuitive this method has dominated theoretical chemistry as it has the advantage that as the molecular orbitals are linear combinations of basis functions, then they can be chosen such that they are orthogonal simplifying the numerical difficulty of the calculation.

2.2 The Schroedinger Equation

The principal aim of all *ab initio* methods is to solve the time-independent Schroedinger equation, see equation 2.1,

$$H\Psi = E\Psi \tag{2.1}$$

where H is the spin free nonrelativistic Hamiltonian operator, which is a function of the positions and momenta of the particles of the system. The Hamiltonian operator represents the total energy of the system which is a sum of the operators for the kinetic T, and potential energy V components.

$$H = T + V \tag{2.2}$$

The kinetic energy operator, T, is the sum over the particles of the system of the differential operator.

$$T = -\frac{h^2}{8\pi^2}\sum_i \frac{1}{m_i}\nabla_i^2, \tag{2.3}$$

The potential energy operator, V, is a sum over the distinct pairs of ith and jth particles with the electronic charge e_i and e_j, that are a distance r_{ij} apart.

$$V = \frac{1}{4\pi\epsilon_0}\sum_i \sum_{j>i} \frac{e_i e_j}{r_{ij}} \tag{2.4}$$

Solution of equation 2.1 for a many electron system will result in eigenfunctions each one a solution of time-independent Schroedinger equation. Only the few eigenstates with the lowest eigenvalues are of interest when studying chemical systems.

2.2.1 Born-Oppenheimer Approximation

Simplification of the Hamiltonian can be achieved by neglect of the kinetic energy of the nuclei, and treating the Coulombic repulsion between the nuclei as a constant. This is justified on the basis that nuclei are much more massive than electrons and therefore to a good approximation we can consider the electrons as moving in a field of fixed nuclei, however it should be noted that this approximation is not rigorously valid and deviations from it are observed for chemical systems. The remaining terms give rise to the Born-Oppenheimer electronic Hamiltonian operator, which is expressed in atomic units in equation 2.5,

$$H_{el} = -\sum_i \frac{1}{2}\nabla_i^2 - \sum_i \sum_\lambda \frac{Z_\lambda}{r_{i\lambda}} + \sum_i \sum_{j>i} \frac{1}{r_{ij}} + \sum_\lambda \sum_{\nu>\lambda} \frac{Z_\lambda Z_\nu}{r_{\lambda\nu}} \tag{2.5}$$

where the Greek subscripts denote summation over the nuclei and the subscripts i and j represent summation over the electrons of the system. This Hamiltonian and its approximated solutions are the basis of modern quantum chemistry.

2.3 Molecular Orbital Theory

Most *ab initio* calculations reported to date have used Molecular Orbital Theory. Its popularity stems from the fact that the method describes multi-electron wavefunctions as products of molecular orbitals that are themselves linear combinations of basis functions. These molecular orbitals can be chosen such that they are orthogonal thereby greatly simplifying the complexity of the calculation. The molecular orbitals are then varied to self consistency by invoking the variation principal. Several authorative reviews [6] and books [7] have been published on Molecular Orbital Theory.

2.3.1 The Hartree-Fock Method

The Hartree-Fock method is the most basic molecular orbital method that complies with the Pauli exclusion principal. The Hartree-Fock wavefunction is constructed from a Slater determinant of one-electron molecular orbitals, ψ_i, which are a product of a spatial function χ_i and a spin function which can be either α or β. The spin functions are orthonormal in spin space.

$$\Psi = \frac{1}{\sqrt{n!}} \begin{vmatrix} \psi_1(1) & \psi_1(2) & \dots & \psi_1(n) \\ \psi_2(1) & \psi_2(2) & \dots & \psi_2(n) \\ \vdots & \vdots & \ddots & \vdots \\ \psi_n(1) & \psi_n(2) & \dots & \psi_n(n) \end{vmatrix} \tag{2.6}$$

The spatial molecular orbitals are linear combinations of basis functions χ_{ij} which approximate the atomic orbitals.

$$\chi_i = \sum_j c_{ij}\phi_j \tag{2.7}$$

The coefficients c_{ij} are then varied to self consistency by minimising the energy of the wavefunction. This process leads to a set of integro-differential equations known as the Hartree-Fock equations which is written in diagonal form for closed shell systems in equation 2.8.

$$F\phi_i = \epsilon_i\phi_i \tag{2.8}$$

These equations are then solved when using a finite basis with the Roothaan-Hall equations which are written in matrix form 2.9,

$$F(c)c = Sc\epsilon \tag{2.9}$$

where the Fock matrix, F, is defined as

$$\begin{aligned} F_{ij} &= H_{ij}^{core} + \sum_\nu \sum_\lambda P_{\nu\lambda} < \phi_i^*(1)\phi_j(1) \mid \frac{1}{r_{12}} \mid \phi_\nu^*(2)\phi_\lambda(2) > \\ &\quad -\frac{1}{2} < \phi_\lambda^*(1)\phi_i(1) \mid \frac{1}{r_{12}} \mid \phi_\nu^*(2)\phi_j(2) > \end{aligned} \tag{2.10}$$

and H_{ij}^{core} is the Hamiltonian for the energy of an electron in the field of the nuclei of the system.

$$H_{ij}^{core} = -\frac{1}{2}\nabla^2 - \sum_\lambda \frac{Z_\lambda}{r_\lambda} \tag{2.11}$$

The density matrix is the matrix product of the coefficient matrix.

$$P_{\lambda\nu} = 2\sum_i c_{\lambda i}^* c_{\nu i} \tag{2.12}$$

The total electronic energy for the molecular wavefunction is given as

$$E_{elec} = \frac{1}{2}\sum_\lambda \sum_\nu P_{\lambda\nu}(F_{\lambda\nu} + H_{\lambda\nu}^{core}). \tag{2.13}$$

The Roothaan-Hall equations are non-linear because the Fock matrix, F, is itself a function of the orbital coefficients that are to be determined. These equations must be solved iteratively.

2.3.2 The Basis Set

To calculate an algebraic HF wavefunction we must first provide a set of functions known as a basis set. When the basis set approximates a set of atomic orbitals for the atoms of the system, the calculation is also known as a Linear Combination of Atomic Orbitals-Self Consistent Field (LCAO-SCF) calculation.

Slater Type Orbitals (STO) were most popular in early *ab initio* work because they were the exact solution of the Schroedinger equation for the hydrogen atom. However calculating integrals over STOs is time consuming. Slater orbitals are represented by equation 2.14.

$$\phi_{nlm}(\bar{r}) = \left(\frac{(2\zeta)^{2n+1}}{(2n)!}\right)^{1/2} r^{n-1}\exp(-\zeta r)Y_{lm}(\theta,\phi) \tag{2.14}$$

where Y_{lm} represent the associated Legendre polynomials. The orbital exponents ζ_i are a set of chosen constants for a calculation. Because of the numerical difficulty of applying these basis sets, Boys [8] suggested a cartesian basis set of Gaussian basis functions which are given by equation 2.15,

$$g_{lmn}(\bar{r}) = Nx^l y^m z^n \exp(-\alpha r^2) \tag{2.15}$$

where N is the normalisation constant, and α is the orbital exponent. The Gaussian Type Orbitals (GTO) functions have the advantage that the product of two Gaussians centred at different points is itself a Gaussian centred somewhere in between, and that an analytic expression exists for this integral, thus enabling a rapid determination of multi-centred integrals. The major disadvantage of GTO's is that they do not have a cusp at the origin of the orbital. This incorrect behaviour has been partly compensated for by the method of representing an orbital as a linear combination of Gaussian functions [9].

$$\phi_{i,lmn}(\bar{r}) = \sum_j d_{ij} g_{j,lmn}(\bar{r}) \tag{2.16}$$

The coefficients d_{ij} are held constant and various methods have been proposed to determine these coefficients.

2.4 Electron Correlation

The energy of the Hartree-Fock wavefunction can be lowered by improving the basis set from which the molecular wavefunction is constructed. This can be achieved by optimisation of the basis set functions or by increasing the size of the basis set. However, increasing the basis set size will not result in an energy lower than the energy known as the Hartree-Fock limit. The difference between the Hartree-Fock limit and the exact non-relativistic energy of the system is known as the correlation energy, and is a result of the instantaneous repulsions between pairs of electrons of the system.

In the Hartree-Fock approximation the motion of each electron is solved in the presence of the averaged field resulting from the other particles of the system. But the motion of the electrons is correlated and it is unlikely that two electrons approach each other very closely as it requires an increase in energy to do so. Thus the Hartree-Fock approximation artificially describes a wavefunction with electrons in closer proximity than is necessary giving rise to the difference between the Hartree-Fock limit and the exact non-relativistic energy for the system. Although the correlation energy is small compared to the total energy, usually less than 1%, it can be chemically important, and is necessary for a complete description of associative and dissociative processes. Various methods have been developed to include electron correlation energy. All Molecular Orbital (MO) methods use the Hartree-Fock wavefunction as a first approximation. In order to assess the merits of a given method Pople [10] has listed the desirable features of a theoretical model that includes electron correlation. These are

- The theoretical model should be well defined, leading to a unique energy for any nuclear configuration and a continuous potential energy surface.
- It should be size consistent, so that when applied to an ensemble of isolated molecules, calculated energies should be additive.
- It should be exact (equivalent to FCI) when applied to a two-electron system.

- It should be efficient, so that application is possible for large basis sets.
- It should be accurate enough to give adequate approximation to the FCI result.
- It should be variational, so that the computed energy is an upper bound to the correct energy.

None of the current methods [10] in use satisfy all the criteria given above. It is useful to evaluate the suitability of a given method with regard to these criteria.

2.4.1 Configuration Interaction

To correct some of the inherent deficiencies of the Hartree-Fock approximation a Configuration Interaction (CI) calculation can be performed. This method constructs the CI wavefunction from a linear combination of configuration functions which are themselves built of determinants based on exciting electrons in the Hartree-Fock orbitals into the virtual orbitals.

$$\Psi_{CI} = c_o \mid \Psi_{HF} > + \sum_{ar} c_a^r \mid \Psi_a^r > + \sum_{a<b} \sum_{r<s} c_{ab}^{rs} \mid \Psi_{ab}^{rs} > + \ldots \tag{2.17}$$

The coefficients c_o, c_a^r, c_{ab}^{rs}, ... of the configuration functions are then variationally determined by solving the secular equation,

$$\begin{vmatrix} H_{11} - ES_{11} & H_{12} - ES_{12} & \ldots & H_{1n} - ES_{1n} \\ H_{21} - ES_{21} & H_{22} - ES_{22} & \ldots & H_{2n} - ES_{2n} \\ \vdots & \vdots & \ddots & \vdots \\ H_{n1} - ES_{n1} & H_{n2} - ES_{n2} & \ldots & H_{nn} - ES_{nn} \end{vmatrix} = 0 \tag{2.18}$$

where there are n configuration functions. Full Configuration Interaction (FCI) will yield the total correlation energy but it is not practical for reasonably sized molecules (greater that 4 atoms) because of the enormous number of configurations N that are possible, $N = \frac{2a!}{(b!(2a-b)!)}$, where a is the number of basis functions and b is the number of electrons in the system. This is purely a computational problem and several methods have proposed truncating the matrix given in equation 2.18. The CID method includes only the first and third terms of equation 2.17, while the CISD method is a popular method for post SCF *ab initio* calculations and includes the first three terms of equation 2.17.

Other methods truncate the orbitals that are included in the CI calculation. Generally a set of orbitals are considered "inactive" while all others are "active" and participate in the CI expansion.

2.4.2 Multi-Configuration SCF

The Multi-Configuration SCF method variationally minimises both the orbital coefficients and the CI expansion coefficients simultaneously. The optimum MC-SCF must be found iteratively since the secular equation is not linear. This method although computationally expensive has been widely used as it has produced good results involving calculations of chemical reactions. A variation of the MC-SCF method is the Complete Active Space SCF method CASSCF. In this method the orbitals of the Hartree-Fock wavefunction are divided into two groups, the active orbitals and the inactive orbitals. All possible configuration functions are formed from the reference function by exciting the active electrons in the active orbitals. Usually the active orbitals are chosen such that they include only the valence orbitals of the system.

2.4.3 Møller-Plesset Perturbation

Another commonly used approach to the correlation problem is many body perturbation theory. The most commonly used method that uses the Hartree-Fock wavefunction of atoms and molecules as the unperturbed wavefunction is called Møller-Plesset perturbation theory. This method assumes that the FCI ground state wavefunction can be expanded from the Hartree-Fock wavefunction as a series of λ, by separation of the Hamiltonian into two parts.

$$H = H_0 + \lambda H' \tag{2.19}$$

In equation 2.19, H_0 is the unperturbed Hamiltonian which is the sum of one electron operators for each electron of the system. The perturbed Hamiltonian H' is the difference between the exact electronic Hamiltonian represented in equation 2.2 and the Hartree-Fock Hamiltonian. The expanded series is written as

$$\Psi_\lambda = \Psi^{(0)} + \lambda\Psi(1) + \lambda^2\Psi^{(2)} + \ldots \tag{2.20}$$

$$E_\lambda = E^{(0)} + \lambda E^{(1)} + \lambda^2 E^{(2)} + \ldots \tag{2.21}$$

The zeroth order energy is just the sum of the orbital energies, while the first order energy corresponds to the Hartree-Fock energy. The series can be truncated depending on the accuracy or expense of the calculation required to achieve second (MP2), third (MP3), fourth (MP4), ... and so on, order perturbation theory, where the perturbations are taken as a summation over excited configurations. For example the notation MP4SDQ is used to represent a Møller-Plesset calculation to fourth order that includes all single, double, and quadruple excitations from the Hartree-Fock wavefunction. Often these calculation are performed with "frozen core" orbitals, meaning that the inner shell orbitals were fully occupied in all excited configurations. The core orbitals contribute significantly to the total Møller Plesset energy, because the core−−core and core−−valence correlations contributions are quite large. However, they do not contribute significantly to molecular properties like dissociation energies, force constants, etc, because these effects cancel out.

The effect of the perturbation theory is to mix other configurations with the ground state configuration, giving the electrons of the system ways of avoiding each other, and thereby correlating their motion. This generally leads to lower and more accurate energy calculations although this is largely dependent on the behaviour of convergence for a given system, and is not guaranteed as it is in the variational approach. Recent calculations have cast some doubt over the ability of this method to consistently calculate the correlation energy as a function of molecular geometry [10]. However this approach is much more computationally efficient than the CI approach at including correlation energy, and it has been shown that it is size consistent when truncated to any order. This property is vital when attempting to calculate potential energy surfaces for systems that involve molecular dissociation, and Møller-Plesset calculations have become routinely used when calculating correlation effects on ground state molecular wavefunctions.

Chapter 3

A Theoretical Study of the Diels-Alder Reaction

3.1 Introduction

The discovery of the Diels-Alder [$_{\pi}4 + _{\pi}2$] cycloaddition reaction [11] over 50 years ago represents a milestone in organic chemistry [12]. This discovery provided organic chemists with reaction pathways to compounds that were previously difficult or impossible to synthesise using traditional methods. The stereo-specificity of the Diels-Alder reaction allowed chemists to tailor a synthetic path to a target molecule with a particular stereo-isomer in mind. Theoreticians have studied this cycloaddition reaction as it represents one of the textbook examples used to illustrate the Woodward-Hoffmann [13, 14] rules. It is of great significance to theoretical, experimental and synthetic chemistry. It is not surprising then that an enormous amount of literature on Diels-Alder reactions exists, and that the number of papers published annually is increasing at a constant rate.

Three mechanisms have been proposed for the Diels-Alder cyclo-addition reaction, namely (i) a synchronous concerted pathway with the two new σ-bonds forming equally along the reaction co-ordinate, (ii) an asynchronous concerted mechanism where the two new σ-bonds form unequally along the reaction co-ordinate and (iii) a two step process involving a diradical pathway with two stable intermediates and three transition states. Theoretical chemists have applied a variety of methods to

the prototype reaction to elucidate its mechanism and although controversy still exists, the synchronous concerted pathway is favoured by the highest levels of theory [15, 16, 17, 18], and supported by experiment [19, 20].

The synchronous mechanism has had its opponents. Ortega *et al.* [21] have argued that inclusion of electron correlation energy contributions increases the tendencies toward asynchronicity, however the validity of this result is limited by the restriction imposed in the calculations such that the sum of the lengths of the two σ-bonds forming is 4.4 Å. Dewar *et al.* [22] have consistently argued on the basis of semi-empirical calculations that both bonds are significantly developed in the transition state but consider that the synchronicity of this concerted mechanism is yet to be established.

An extensive study of the butadiene-ethylene potential energy surface including both minimal and non-minimal basis sets and electron correlation by the Multi-Configuration SCF (MC-SCF) method, has been reported by Bernardi *et al.* [17]. With a minimal STO-3G basis set they found a "diradicaloid" mechanism (involving two intermediates and three transition states) to be thermodynamically favoured over the concerted process. However, using an extended 4-31G basis set the potential energy surface around the "diradicaloid" pathway flattened resulting in a synchronous and an asynchronous concerted pathway; the synchronous process being slightly lower in energy.

More recently, *ab initio* studies by both Bach *et al.* [18] and Houk *et al.* [23] have both reported the existence of a symmetrical transition state for the reaction of ethylene and butadiene at the RHF/6-31G*, and RHF/3-21G and AM1 [24] level of theory. This is the largest basis set used to date in a study of this reaction and the inclusion of correlation energy and polarisation functions give an activation energy (106.3 $kJmol^{-1}$) [18] which is close to the experimental value (115.1 $kJmol^{-1}$) [18]. Frontier Molecular Orbital theory has been used to rationalise the relative rates of several pericyclic reactions and along with the Woodward-Hoffmann [13, 14] orbital symmetry approach has been successful in correlating the initial reactant orbitals to the final product orbitals. Misleading conclusions can arise from the application of Frontier Molecular Orbital theory due to the restriction of consideration of only the HOMO-LUMO interactions. This has been demonstrated in a theoretical study of the trimerization of acetylene to benzene by Bach *et al.* [25] and in cycloaddition

reactions by Epiotis [26]. Indeed such Frontier Molecular Orbital two electron two orbital interactions are assumed to be stabilising and neglecting other interactions would require pericyclic reactions to proceed without a barrier. Bach *et al.* [25] considers the large activation barrier to the D_{3h} transition state in the trimerization of acetylene to benzene results from the destabilising four electron two orbital interactions. In a later study by Bach *et al.* [18] of the Diels-Alder reaction between butadiene and ethylene both four electron and two electron interactions were estimated by Perturbation Molecular Orbital (PMO) analysis to be destabilising. In its simplest form Frontier Molecular Orbital (FMO) theory is limited in its application to the potential energy surface between minima and should be applied with caution.

While considerable theoretical work has been reported in the ethylene-butadiene reaction [15, 16, 17, 18], the analogous reaction between *cisoid*-1,3 butadiene and acetylene has surprisingly been neglected. Numerous synthetic examples exist for which this reaction is the prototype and an industrial process for this reaction has been the subject of a patent [27]. This reaction is also of considerable interest to the organic chemists of Canterbury University [28, 29]. With the amount of debate surrounding the mechanism of the Diels-Alder reaction in mind we have performed a theoretical study of the reaction of butadiene and acetylene.

3.2 Computational Methods

Most previous studies of the $[_{\pi}4 + _{\pi}2]$ reaction have involved small basis sets and not included polarisation functions. The inadequacy of these calculations in establishing comparisons of alternative pathways is well known. Bernardi *et al.* [17] have used a STO-3G minimal basis set for the reaction of butadiene and ethylene and arrived at a reaction mechanism that is not in agreement with experimental observations. The use of larger basis sets is important for calculating thermodynamic parameters, however the inclusion of electron correlation can become prohibitively expensive. By optimising with larger basis sets at the RHF level of theory and then performing a single point Møller-Plesset calculation to include the correlation energy, a best practical estimate of the transition state energy can be calculated. Bach *et al.* [18] applied this method to the reaction of ethylene and butadiene to calculate the activation energy to within 10 $kJmol^{-1}$ of the experimental value.

To enable the calculation of the activation energy for both the forward and the reverse reactions the geometries of acetylene, *cisoid* and *transoid* butadiene, and 1,4-cyclohexadiene were optimised at the HF level of theory. Harmonic vibrational frequencies were calculated at the HF level of theory. The energies were then calculated for these optimised geometries at the HF//MP2 or MP4SDQ levels of theory. Calculations were performed using both 4-31G and 6-31G* basis sets. The optimised geometries are displayed in figure 3.1 and the energies at the different levels of theory are displayed in table 3.1.

A starting geometry for the C_s transition state of the butadiene-acetylene reaction was provided by AM1 [29, 24] calculations. The distance between the carbon centres undergoing bonding was systematically varied while optimising all other variables to reveal an almost flat surface in the region of the col with only a symmetric exit channel to the products. This gives qualitatively a similar potential energy surface as that described by Bernardi *et al.* at the CAS1 4-31G level of theory [17] and thus it is reasonable to expect that the two transition states have similar geometries. Optimisations of a transition state with a C_s symmetry constraint were performed at the RHF level of theory with both the 4-31G and 6-31G* basis sets with respect to all of the eighteen independent geometrical variables. It was necessary to calculate numerically the second derivative matrix for the variables contributing most to the reaction co-ordinate. Calculation of harmonic vibrational frequencies revealed a single imaginary frequency associated with the symmetric reaction co-ordinate, see figure 3.2.

3.3 Results and Discussion

The optimised geometry of the transition state for the acetylene-butadiene reaction at the HF/6-31G* level of theory has an angle of "attack" (the plane between bond making and bond breaking) θ of 124.8°, and the forming σ-bond has a length of 2.198 Å. In the transition state the C_1—C_2/C_3—C_4 and the C_5—C_6 bonds are lengthened by 0.050 Å and 0.039 Å respectively, while the C_2—C_3 bond length is shortened by 0.083 Å when comparing the transition state geometry with the geometries of the *cisoid*-butadiene and acetylene. The optimised geometries of the reactants and the transition state are displayed in figures 3.1 and 3.2, and the total energies are listed

Table 3.1: Total electronic energies and Zero Point Vibrational Energies for the optimised geometries of acetylene, *cisoid*1,3-butadiene, *transoid*1,3-Butadiene, 1,4-cyclohexadiene and the C_s transition state of their Diels-Alder reaction of butadiene and acetylene.

	RHF[a]	MP2[a]	MP4SDQ[a]	ZPVE[b]	ΔE^b
4-31G					
acetylene	−76.71141	−76.89360	−76.90583	78.6	—
*cisoid*1,3-butadiene	−154.69446	−155.04727	−155.08699	241.4	—
*transoid*1,3-butadiene	−154.69996	−155.05207	−155.09170	242.2	—
1,4-cyclohexadiene	−231.49856	−232.02546	−232.07950	—	−227.6[c]
C_s transition state	−231.34109	−231.90711	−231.94721	328.5	119.7[c]
6-31G*					
acetylene	−76.81783	−77.06461	−77.07999	77.3	—
*cisoid*1,3-butadiene	−154.91346	−155.41539	−155.45735	293.6	—
*transoid*1,3-butadiene	−154.91965	−155.42112	−155.46281	240.3	—
1,4-cyclohexadiene	−231.83352	−232.58962	—	—	−287.8[d]
C_s transition state	−231.66350	−232.45682	—	—	60.9[d]

[a] Energies are in *hartrees*.
[b] Energies are in $kJmol^{-1}$.
[c] Calculated at the MP4SDQ/4-31G//HF/4-31G level of theory.
[d] Calculated at the MP2/6-31G*//HF/6-31G* level of theory.

in table 3.1.

The analogous HF/6-31G* results of Bach *et al.* [18] for the ethylene-butadiene reaction showed that the C_1—C_2/C_3—C_4 bonds of butadiene were lengthened by 0.055 Å and the C_2—C_3 bond was shortened by 0.087 Å. This suggests that the transition state for the reaction of acetylene and butadiene occurs slightly earlier in the reaction co-ordinate than for the ethylene case, as expected from the Hammond postulate. The differences between the transition state geometry calculated in this work and those reported by Bach *et al.* [18] are small in absolute terms, however the general trends in the geometric parameters considered indicate a greater reactant character in the transition state for the acetylene-butadiene reaction compared to the ethylene-butadiene reaction.

At the MP4SDQ/4-31G//HF/4-31G level of theory, ΔE for the reaction of acetylene and butadiene is $-227.6\ kJmol^{-1}$, and at the MP2/6-31G*//HF/6-31G* level of theory ΔE is $-287.8\ kJmol^{-1}$. The calculated transition state energy for the butadiene-acetylene reaction was $119.7\ kJmol^{-1}$ at the MP4SDQ/4-31G//HF/4-31G level of theory. Inclusion of zero-point vibrational energy increases the barrier by 8.4 to $128.2\ kJmol^{-1}$, see table 3.1. The electronic energy differences are calculated

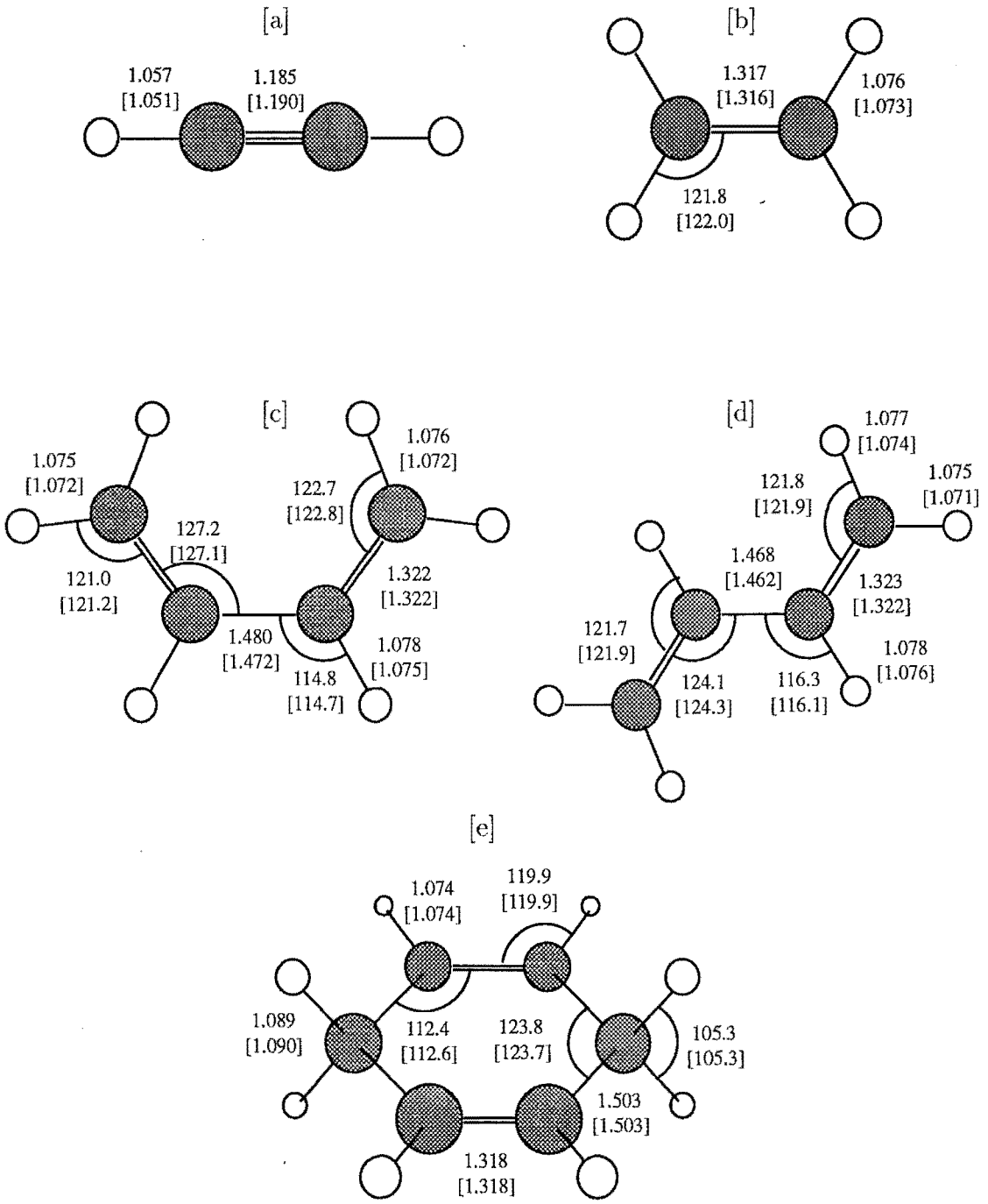

Figure 3.1: HF/4-31G [square brackets] and HF/6-31G* optimised geometries for [a] acetylene; [b] ethylene; [c] *cisoid*-1,3 butadiene; [d] *transoid*-1,3 butadiene and [e] 1,4 cyclohexadiene.

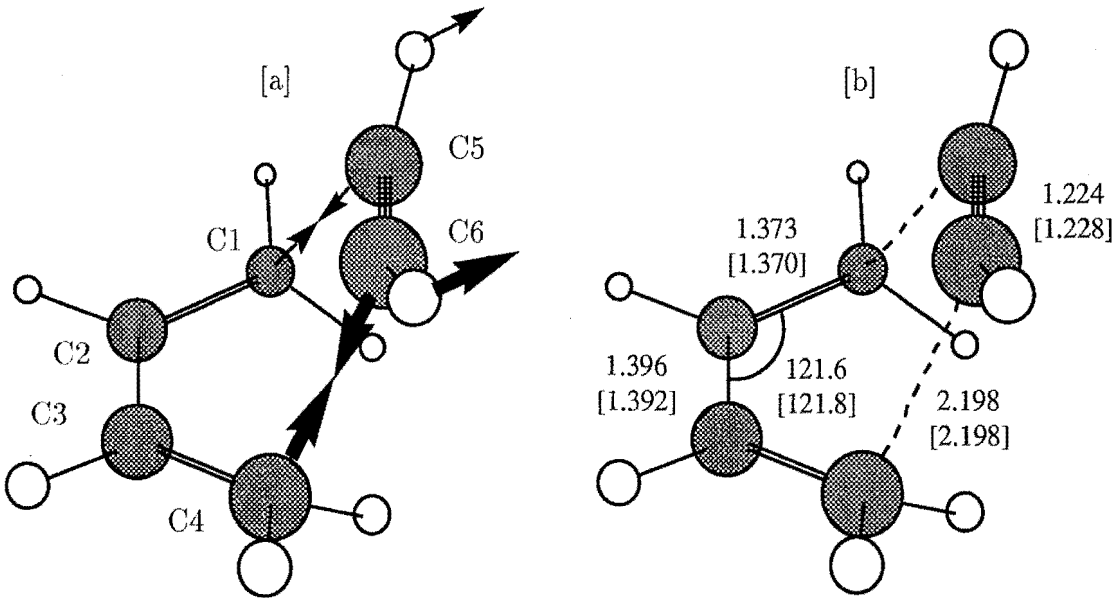

Figure 3.2: [a] C_s transition state dominating vectors of the symmetric vibrational mode of the single imaginary frequency. [b] HF/4-31G [square brackets] transition state and the HF/6-31G* transition state geometry for the reaction of acetylene with 1,3-butadiene.

relative to the energy of *cisoid* 1,3-butadiene and acetylene.

This compares with the energy of the ethylene-butadiene reaction for ΔE of $-219.9\ kJmol^{-1}$and the calculated transition state energy of $77.1\ kJmol^{-1}$at the MP4SDTQ/6-31G*//MP4SDTQ/6-31G* level of theory [18]. The greater exothermicity is consistent with an earlier transition state in the reaction of acetylene and butadiene compared with those for the reaction of ethylene and butadiene, and the increased barrier to reaction is in accord with the observed experimental difficulty of butadiene-acetylene cycloaddition reactions.

The acetylenic hydrogens in the transition state for the reaction of butadiene and acetylene are distorted by 26.5° and 26.9° for the HF/4-31G and the HF/6-31G* calculations, respectively. These values are comparable with those reported by Bach *et al.* [25] for the transition state in the trimerization of acetylene to benzene where a 3-21G SCF calculation gave a transition state of D_{3h} symmetry with the acetylenic hydrogens distorted 28.0° from linearity. Bond lengthening between the acetylenic carbons is also similar with an increase of 0.029 Å in the trimerization transition state and 0.039 Å in the acetylene-butadiene transition state. While the significance of these results are diminished by the level of theory the authors have applied, the

similarities still exist.

The activation barrier in a Diels-Alder reaction is the net effect of distortion energy of the reactants to the transition state geometry, exchange repulsion, and stabilising charge-transfer interactions. Houk *et al.* [30] have noted that the distortion of the reactants in cycloaddition reactions plays a crucial role in decreasing the energy gap between the HOMO and LUMO orbitals, allowing greater "stabilising charge transfer interactions". For the reaction of butadiene and acetylene, the distortion energy of the reactants at the transition state geometry, but at infinite separation was calculated by single point calculation to be 106.2 $kJmol^{-1}$at the MP4SDQ/4-31G level of theory. This value is comparable to the transition state energy of 119.7 $kJmol^{-1}$using the same level of theory, indicating that the magnitudes of the exchange repulsion and charge transfer interactions are similar.

For the trimerization of acetylene reaction Houk *et al.* [30] have reported the distortion energy for the acetylene to the transition state geometry at the STO-3G level of theory as 251 $kJmol^{-1}$. The activation barrier for the forward reaction calculated at the same level of theory was 335 $kJmol^{-1}$, and the 84 $kJmol^{-1}$difference in energy was attributed to the excess of exchange repulsion over charge transfer stabilisation. This contrasts with the acetylene-butadiene reaction where the repulsive and stabilising electronic interactions are approximately balanced at the transition state and the energy required to distort the reactants is approximately equal to the activation barrier for the reaction. The calculations for the Diels-Alder reaction of ethylene and butadiene reported in this study indicate that this is also the case with the repulsive and stabilising interactions approximately balanced.

If one considers only the frontier molecular orbitals, the correlation diagrams for the acetylene-butadiene reaction and the ethylene-butadiene reaction essentially exhibit the same features. In order to rationalise the energetics of these $[_{\pi}4 + _{\pi}2]$ cycloaddition reactions it is therefore necessary to consider the extended frontier molecular orbital arrangements of the separated and distorted fragments relative to the transition state.

In these cycloaddition reactions the distortion of the reactants to the transition state geometry serves to decrease the gap between the HOMO-LUMO orbitals, thereby increasing the stabilising two electron interactions counteracting the destabilising interaction resulting from mixing of filled shells (four electron interactions).

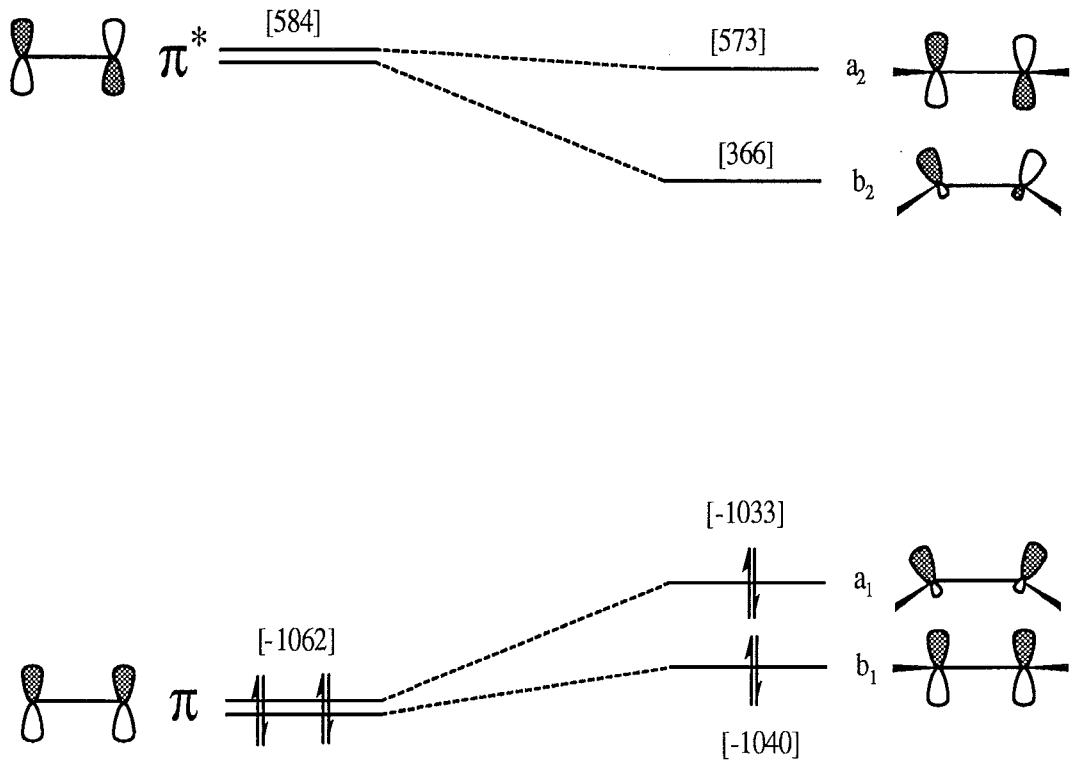

Figure 3.3: Electron correlation diagram for distorted acetylene. One electron energies calculated at the HF/6-31G* level of theory displayed in the square brackets are in $kJmol^{-1}$.

Electron correlation diagrams of the effect of distortion on the reactants are displayed in figure 3.3 and figure 3.4 for acetylene and butadiene respectively at the HF/6-31G* levels of theory.

The electron correlation diagrams for the C_s transition state for the reaction of acetylene with butadiene and ethylene and butadiene including the energies of the calculated fragments at infinite separation are shown in figure 3.5 and figure 3.6 respectively.

For the ethylene Diels-Alder reaction there is 78 $kJmol^{-1}$net destabilisation resulting from distortion of the reactants to the transition state geometry. Interaction of the distorted reactants results in a two electron interaction between the a″ HOMO of butadiene and the a″ LUMO of distorted ethylene, which is for this reaction destabilising. This two electron destabilisation combined with the four-electron three-orbital interaction between the a′ orbitals of distorted butadiene and the a′ orbital of the distorted ethylene gives the net 148 $kJmol^{-1}$destabilisation.

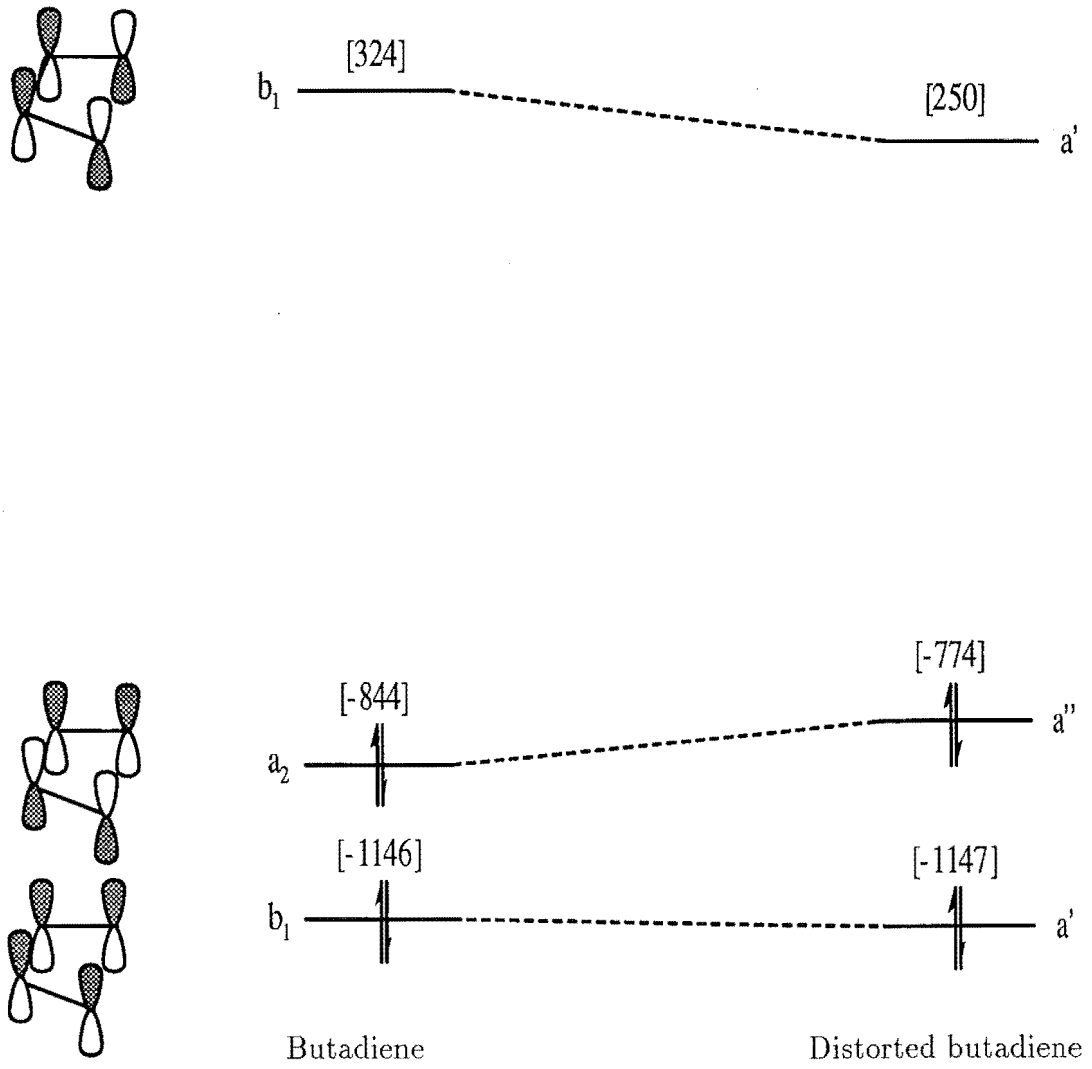

Figure 3.4: Electron correlation diagram for distorted butadiene. One electron energies calculated at the HF/6-31G* level of theory displayed in the square brackets are in $kJmol^{-1}$.

For the acetylene-butadiene there is 120 $kJmol^{-1}$destabilisation resulting from distortion of the reactants to the transition state geometry. Interaction of the distorted reactants leads to a two-electron interaction stabilisation between the distorted butadiene HOMO a'' and the distorted acetylene LUMO b_2. The net destabilisation shown of 222 $kJmol^{-1}$is a result of the four-electron three-orbital interaction between the a' orbitals of the distorted butadiene and the b_1 orbital of distorted acetylene.

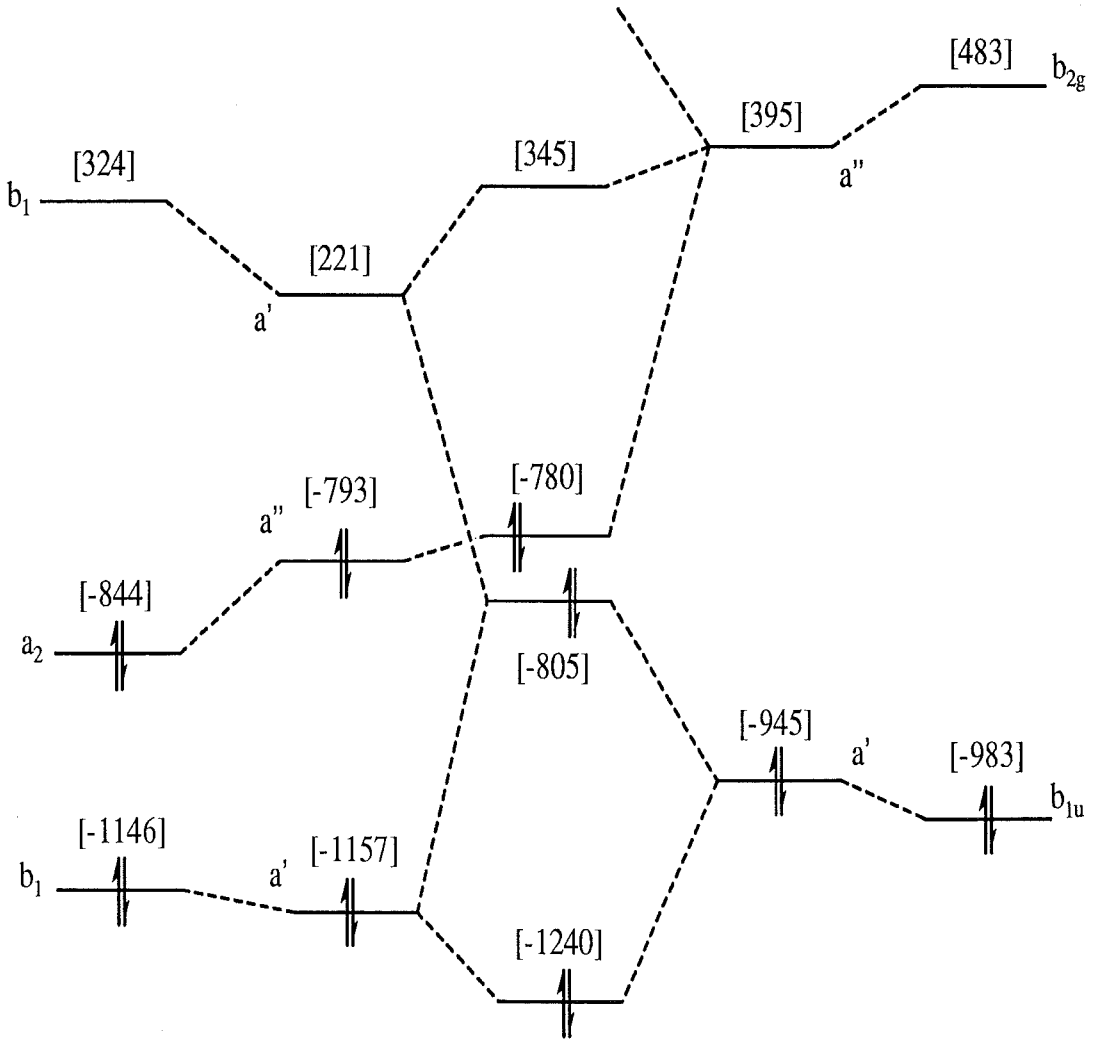

Butadiene Distorted butadiene Transition state Distorted ethylene Ethylene

Figure 3.5: Electron correlation diagram for the C_s transition state for the reaction of ethylene and butadiene. One electron orbital energies are calculated at the HF/6-31G* level of theory displayed in the square brackets in $kJmol^{-1}$.

For the Diels-Alder reaction of acetylene and butadiene there is 42 $kJmol^{-1}$more destabilisation resulting from the distortion of the reactants to the transition geometry and 32 $kJmol^{-1}$more transition state destabilisation from the distorted fragments than for the corresponding reaction with ethylene. These differences contribute to the net electronic energy difference between the reactions of 74 $kJmol^{-1}$, with the reaction of acetylene having the higher transition-state barrier.

A study of the valence orbitals not undergoing bonding changes shows that a

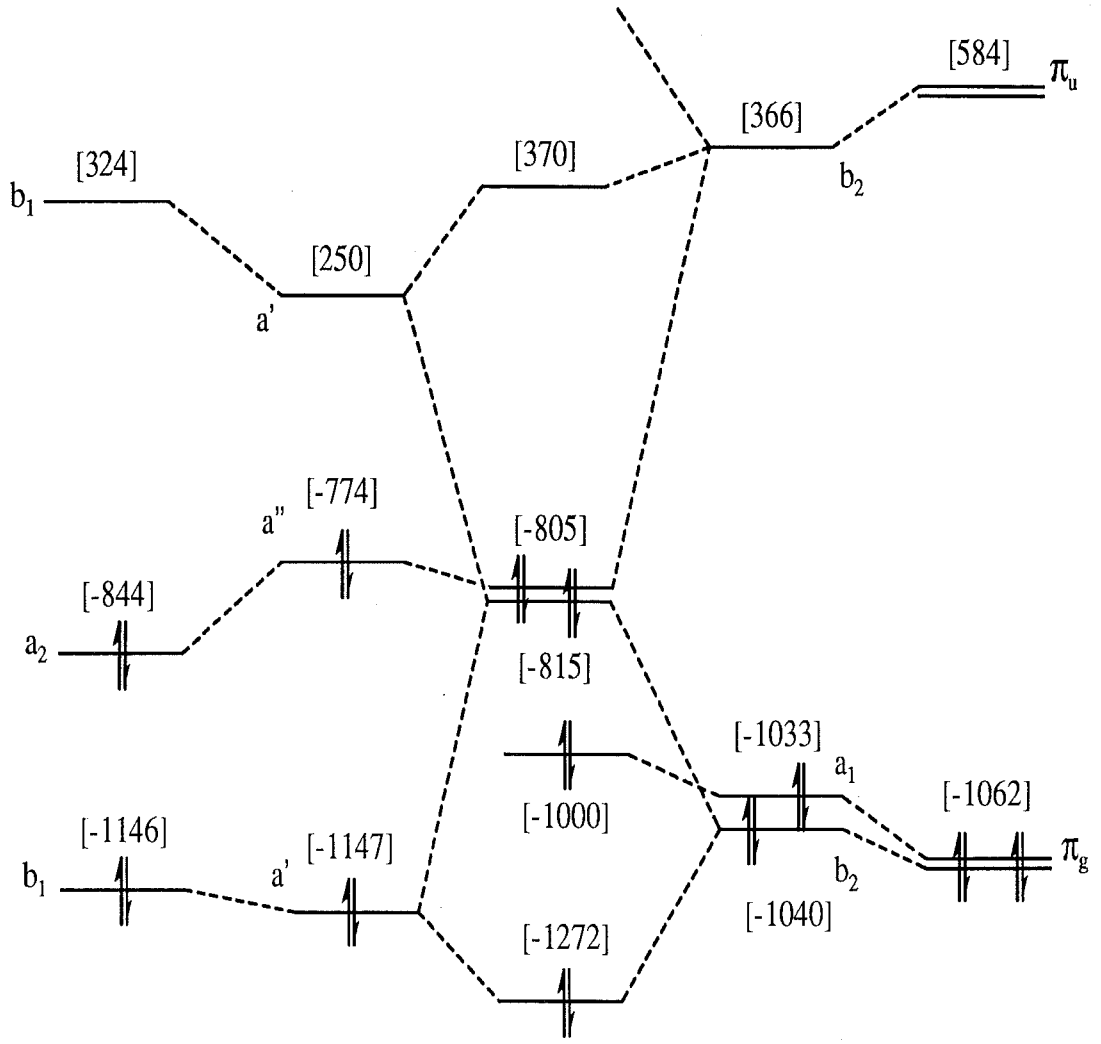

Butadiene Distorted butadiene Transition state Distorted acetylene Acetylene

Figure 3.6: Electron correlation diagram for the C_s transition state for the reaction of acetylene and butadiene. One electron orbital energies calculated at the HF/6-31G* level of theory are displayed in the square brackets in $kJmol^{-1}$.

significant contribution to the greater activation energy for the acetylene-butadiene reaction compared to the ethylene-butadiene reaction is a result of the destabilisation of the a_1 orbital of the distorted acetylene in the transition state. The a_1 orbital is raised in energy as the reactant distorts to the transition geometry. A further increase in energy of this orbital occurs at the transition state, a result of the

geometry constraints that force the a_1 orbital to overlap with the filled orbitals of the butadiene fragment. This increase in energy of 62 $kJmol^{-1}$is a major contributing factor to the difference in the transition barrier of the acetylene and ethylene Diels-Alder reactions.

For the trimerization of acetylene to benzene, a pseudo $[_\pi 4 + {}_\pi 2]$ reaction, the activation barrier is 259 $kJmol^{-1}$calculated [25] at the MP3/3-21G level of theory. The calculated [31] activation barrier for the $[_\pi 2 +_\pi 2]$ cycloaddition of acetylene and ethylene to cyclobutene is in excess of 300 $kJmol^{-1}$. Both reactions have activation barriers significantly greater than the butadiene-acetylene and butadiene-ethylene reactions, largely as a result of filled shell interactions that must be balanced at the transition state.

The orbital interactions and their consequences for a series of related cycloaddition reactions are summarised in table 3.2. The number of filled valency orbitals not undergoing bonding changes is defined as those π orbitals that survive the course of the reaction within the molecule. This number is significant in that it represents the degree of repulsive electron overlap that must be overcome in order to reach the transition state, and is reflected in the Activation energy. The number of HOMO-LUMO interactions is significant in that it represents the amount of two electron-two orbital interactions that are potentially stabilising. This number should be reflected in the exothermicity of of the forward reaction. The increase in the number of filled shell valence orbitals not undergoing bonding changes for the three reactions and the decrease in the number of significantly stabilising HOMO-LUMO interactions result in an increasing activation energy for the reactions as one goes from left to right across the series. The figures in the second row omit interactions involving the LUMO of acetylene as these are high in energy and will not contribute significantly to the stabilisation. The increase in activation energy shown in table 3.2 suggests that there is a trend towards greater reactant character at the transition state. This is indicated by the comparison of the calculated transition state geometries for the acetylene-butadiene and ethylene-butadiene reactions.

The transition-state calculations for the reaction of acetylene with butadiene demonstrate the existence of a synchronous concerted pathway for this reaction at this level of theory. Whether this is the energetically favoured mechanism has yet to be resolved. An STO-3G frequency calculation of the asynchronous geometry

Table 3.2: Calculated activation energies with respect to types of orbital interactions.

Reaction	$[_\pi 4 + _\pi 2]$ [a]	$[_\pi 4 + _\pi 2]$ [b]	$[_\pi 2 + _\pi 2 + _\pi 2]$ [c]
Number of HOMO-LUMO interactions.[d]	2	1	0
Number of filled valency orbitals not undergoing bonding changes.	1	2	3
Calculated Activation Energy ($kJmol^{-1}$).	106.3[e]	170.1[f]	259.4[g]

[a] Butadiene + ethylene.
[b] Butadiene + acetylene.
[c] Acetylene + acetylene + acetylene.
[d] Interaction involving the acetylene LUMO omitted.
[e] MP4SDTQ/6-31G* from Bach *et al.* [18].
[f] RHF/6-31G* (this work).
[g] Estimated MP3/6-31G* from Bach *et al.* [25].

proposed by Bernardi has revealed that the inclusion of Zero-Point Vibrational Energy (ZPVE) favours the asynchronous transition state by 6 $kJmol^{-1}$which exactly cancels the favouring of the synchronous mechanism in the Born-Oppenheimer surface. The region around the synchronous transition state appears to be very flat and it may well turn out that the synchronicity of this mechanism will be determined by vibrational energy. The less constrained asynchronous transition state can be expected to have a lower ZPVE which has largely been overlooked by the theorists. The debate over the Diels-Alder reaction is far from over however our calculations add support to the possibility of a synchronous mechanism existing for Diels-Alder reactions with acetylenic dienophiles.

3.4 Conclusions

For the reaction of butadiene with acetylene, *ab initio* calculations at the HF/6-31G* level of theory have shown the existence of a transition state consistent with a synchronous mechanism for cycloaddition. The higher activation barrier compared

to that calculated for the reaction of ethylene with butadiene is consistent with the presence of an extra filled π shell interaction at the transition state, and this is supported by an increase in the activation barrier for the trimerization of acetylene to benzene. For the reaction of acetylene with butadiene the distortion energy is comparable to the activation barrier requiring that charge transfer and exchange repulsion interactions are of comparable magnitude.

Chapter 4

Ion Transport Theory

It has been over a century since Boltzmann [32] proposed that inter molecular collisions were responsible for physical and chemical properties observed in gases. While Boltzmann's proposal was not enthusiastically endorsed at that time it has since been universally accepted and applied to a wide variety of problems and a vast literature now exists. Despite this interest only a few exact and trivial solutions of Boltzmann's equation are known. Current research aims at finding practical methods that can solve Boltzmann's equation numerically.

The moment equations have been used to calculate non-equilibrium properties of ions in gases without directly requiring a solution of Boltzmann's equation to obtain the one particle distribution function [33, 34, 35]. These methods involve expressing an observable of the system in terms of a single or combination of a set of functions, based on an assumed eigenfunction of the system. If the eigenfunction is reasonably realistic then the observable can then be expressed in terms of a converging kinetic series.

Realistic solutions of actual systems require the use of a reliable potential energy surface. Generally, potential energy surfaces for a given system can be obtained in two ways. Firstly it can be inferred from an observed property of the system, such as rainbow scattering, the virial coefficients, spectroscopy, etc, or it can be calculated using *ab initio* methods. Calculating an observable using a potential energy surface inferred from experiment is solving the inverse problem, and thus no new information is obtained in this process. Note also that this process has mainly been used to infer the interaction potentials of (isotropic) spherically symmetric systems.

Recently [36] many authors have attempted to overcome the difficulties of inferring anisotropy of the potential energy surface of a system from experiments relating to molecular collision phenomena. An extensive database of such ion transport experimental results now exists [37, 38, 39]. Conversely, theoreticians have approached the problem of the internal structure of molecules by calculating an *ab initio* potential energy surface and using it to compare calculated non-equilibrium transport phenomena with experimental results. Unfortunately, the computational requirements for this approach has until relatively recently been prohibitively expensive for all but the smallest anisotropic systems.

The purpose of this chapter is to present the methods and applications of ion transport theory, specifically with the aim of calculating mobilities and diffusion coefficients of ions in dilute gases. No attempt is made at completeness or to exhaustively review the current state of the theory. Rather an overview of the theory relevant to this thesis is given, and the reader is directed to Mason and McDaniels' book [40] *Transport Properties of Ions in Gases*, and several other authoritative works cited therein for original contributions to this field. In the proceeding section the mobility and diffusion coefficients are empirically defined. This is followed by an outline of the Boltzmann equation in section 4.2 and the transport properties using the moment equations in section 4.3. In sections 4.4 and 4.5 the two and three-temperature theories of Viehland [41, 42, 43] are presented. In section 4.6 Viehlands' theory of diatomic ion-diatom systems [44] is presented and then specialised to atomic ion-diatom systems. Finally the application of the theory outlined is reviewed and a conclusion is given.

4.1 Definitions of Ion Transport Properties

4.1.1 The Mobility

When an external electric field, E, is applied to an ensemble of ions in a dilute gas, the ions will accelerate in the direction of the electric field. The ions are subsequently deaccelerated by collisions with the dilute gas, and eventually a steady state drift velocity of the centre of mass of the ensemble, v_d, will be superimposed on the thermal motions of the ions. The mobility of the ions, K, is defined as the ratio of

the drift velocity to the electric field, see equation 4.1

$$K = v_d/E. \tag{4.1}$$

The mobility is a joint property of the ion and the dilute gas. The ion mobility is usually reported as mobility reduced to Standard Temperature and Pressure (STP), K_0, which is defined by equation 4.2,

$$K_0 = K\frac{P}{760}\frac{273.15}{T} \tag{4.2}$$

where P is the pressure in mm Hg, and T is the temperature in units of Kelvin.

4.1.2 The Diffusion Coefficients

A localised ensemble of ions in a dilute gas will also disperse throughout the gas by diffusive flow. The ion flux, Φ, is in the opposite direction to the density gradient, ∇n, and the constant of proportionality is the diffusion coefficient, D, see equation 4.3

$$\Phi = -D\nabla n. \tag{4.3}$$

In the presence of an external electric field the diffusion coefficient becomes a tensor, see equation 4.4, where the diffusion takes place at a different rate parallel and perpendicular to the field.

$$D = \begin{bmatrix} D_\perp & 0 & 0 \\ 0 & D_\perp & 0 \\ 0 & 0 & D_{||} \end{bmatrix} \tag{4.4}$$

4.2 The Boltzmann Equation

Calculation of the ion transport coefficients requires the application of the Boltzmann equation 4.5 to the conditions of the drift tube. Several assumptions and simplifications can be made to the theory. These assumptions are as follows,

- The system involves a trace amount of ions moving in a single dilute neutral gas, in the presence of a uniform homogeneous electrostatic field. This is the "binary gas" assumption.

- The single neutral gas is at equilibrium. This means that the distribution function of the neutral gas can be represented as having a Maxwell-Boltzmann distribution of temperature T.
- The ion density gradients are sufficiently small as to obey Ficks law, and all ion properties other than the ion number density are independent of position.
- The time variation of ion number density is much longer than all other ion properties. This allows the neglect of all time derivatives except $\partial n/\partial t$.
- The effect of chemical reaction on the ion distribution function is negligible. This requirement means that chemically reactive collisions must be orders of magnitude less frequent than non-reactive collisions.

Each assumption in turn will be used in the following derivation. The Boltzmann equation is the central equation to all rigorous kinetic theories of gases. It describes the time progression of the one particle distribution function, f, that in turn describes the position, r, and velocity, v, of the ions in the drift tube,

$$\frac{\partial f}{\partial t} + v \cdot \nabla f + \frac{eE}{m} \nabla_v f = \int \int (f'F' - fF)\, v\sigma \mathrm{d}\Omega \mathrm{d}V, \tag{4.5}$$

where F represents the Maxwell-Boltzmann distribution of the single dilute neutral gas, and σ is the differential scattering cross section for the ion and the neutral.

The ion density function of the ions of mass m, and charge e is given as

$$n(r,t) = \int f(r,v,t)\mathrm{d}v. \tag{4.6}$$

4.3 The Moment Equations

In order to calculate the transport coefficients of the ions in the drift tube requires the solution of the Boltzmann equation to yield f, from which all ion properties can then be acquired. Unfortunately, only trivial solutions to the Boltzmann equation are known, although recent advances in the application of finite difference methods to the field of electron and ion transport [45, 46] suggest that actual ion distribution functions may be obtainable in this way. However the calculation of the transport coefficients for ionic-gas systems with an arbitrary interaction potential currently requires the solution of the moment equations.

The moment equations are constructed by multiplying the Boltzmann equation on the left by an arbitrary function $\phi(v)$ and integrating over the ion velocity, v.

$$\frac{\partial}{\partial t}\int \phi f \mathrm{d}v + \int \phi v \cdot \nabla f \mathrm{d}v + \frac{e}{m}\int \phi E \cdot \nabla_v f \mathrm{d}v = \int\int\int \phi \left(f'F' - fF\right) v\sigma \mathrm{d}\Omega \mathrm{d}V \mathrm{d}v. \tag{4.7}$$

Carrying out the integration over v and neglecting all the time derivatives of functions that are quickly dissipated (the fourth assumption) in the course of a collision event reduces the moment equations to the form given in equation 4.8,

$$\frac{e}{m}E \cdot \langle \nabla_v \phi \rangle - [\langle v\phi \rangle - \langle v \rangle \langle \phi \rangle] \cdot \nabla \ln n = N \langle J\phi \rangle. \tag{4.8}$$

where $J\phi$ is given as,

$$J\phi = N^{-1}\int\int F[\phi(v) - \phi(v')] v\sigma \mathrm{d}\Omega \mathrm{d}V, \tag{4.9}$$

and the moment of A is defined as

$$\langle A \rangle = \int f(v) A(v) \mathrm{d}v. \tag{4.10}$$

The functions ϕ_p are usually chosen such that f forms a complete and orthogonal set in the ion velocity space,

$$f = f^{(0)} \sum_q c_q \phi_q^{\dagger}, \tag{4.11}$$

where $f^{(0)}$, represents some zero-order approximation to the true ion distribution function, such that

$$\int f^{(0)} \phi_q^{\dagger} \phi_p \mathrm{d}v = n N_p \delta_{qp} \tag{4.12}$$

where N_p is the normalisation constant.

The right hand side of equation 4.8 is then transformed and expanded in terms of ϕ_p, using the collision operator J.

$$\langle J\phi_p \rangle = \sum_q \langle \phi_q \rangle f_{pq} \tag{4.13}$$

where f_{pq} is defined as

$$f_{pq} = (nN_q)^{-1} \int f^{(0)} \phi_q^{\dagger} J \phi_p \mathrm{d}v. \tag{4.14}$$

The moment equations then yield an infinite set of linear equations.

$$\left(\frac{e}{m}\right) E \cdot \langle \nabla_v \phi_p \rangle - [\langle v\phi_p \rangle - \langle v \rangle \langle \phi_p \rangle] \cdot \nabla \ln n = (1/N) \sum_q \langle \phi_q \rangle f_{pq} \tag{4.15}$$

If the moments of $v\phi_p$, and $\nabla_v \phi_p$ can be expressed in terms of linear combinations of moments of the ϕ_p's using recurrence relationships, then this leds to a set of linear equations in the moments of the ϕ_p's. This set of linear equations are required to converge such that they can be truncated and solved to an arbitrary accuracy. This procedure is only possible if the function $f^{(0)}$ is chosen such that it is a reasonable approximation to the actual ion distribution function f.

4.4 Two Temperature Theory

Viehland and Mason [41] developed two-temperature theory in order to overcome poor convergence of one-temperature kinetic theory [40, 47]. Two-temperature theory was developed by using an assumed ion distribution function that has a temperature that is different to that of the dilute gas. The convergence properties of the resulting kinetic equations then depends upon the choice of the ion temperature. Convergence of the kinetic equations has been shown to be greatly improved by a choice of T_b that reflects the elevated temperature of the ions in the drift tube. The ion distribution function was expanded in the following way.

$$f = f^{(0)} \sum_{r=0}^{\infty} \sum_{l=0}^{\infty} \sum_{m=-l}^{l} f_{lm}^{(r)} w_b^l L_{(r)}^{(l+1/2)}(w_b^2) Y_l^m(\hat{w}), \tag{4.16}$$

The zeroth order approximation is given as

$$f^{(0)} = n(m/2\pi k T_b)^{3/2} \exp\left(-w_b^2\right), \tag{4.17}$$

where the reduced velocity, w_b, is defined by

$$w_b^2 = mv^2/2kT_b. \tag{4.18}$$

The ion distribution function is a linear combination of products of associated Laguerre, L, associated Legendre, Y, and the moments of the ion velocity.

Substitution of equation 4.16 into equation 4.15 and use of the recurrence relationships of the basis functions, $\phi_{lm}^{(r)}$, results in the following expression.

$$\mathcal{E}\left[\frac{l(l+r+1/2)}{(l+1/2)} \langle \phi_{l-1,0}^{(r)} \rangle^{(0)} - \frac{(l+1)}{(l+1/2)} \langle \phi_{(l+1),0} \rangle^{(r-1)}\right] = \sum_{s=0}^{\infty} \gamma_{rs}(l) \langle \phi_{l,0}^{(s)} \rangle^{(0)}, \tag{4.19}$$

where

$$\mathcal{E} = \left[\left(\frac{m}{2kT_b}\right)^{1/2} \frac{e}{ma_{00}(1)}\right] \frac{E}{N} \tag{4.20}$$

$$\gamma_{rs}(l) = \frac{a_{rs}(l)}{a_{00}(1)}, \tag{4.21}$$

where the matrix elements $a_{rs}(l)$, are defined as

$$a_{rs}(l) = \frac{\int f^{(0)} \phi_{l0}^{(s)} J \phi_{l0}^{(r)} \mathrm{d}v}{\int f^{(0)} \phi_{l0}^{(s)} \phi_{l0}^{(s)} \mathrm{d}v}. \tag{4.22}$$

This analytical expansion leads to the following expression for the mobility, to the second order of approximation,

$$K = \frac{3e}{8N} \left(\frac{\pi}{2\mu k T_{\text{eff}}}\right)^{1/2} \frac{1+\alpha}{\Omega^{(1,1)}(T_{\text{eff}})}, \tag{4.23}$$

where,

$$\frac{3}{2} k T_{\text{eff}} = \frac{3}{2} kT + \frac{1}{2} M v_d^2 (1+\beta), \tag{4.24}$$

and where α and β are given as

$$\begin{aligned} \alpha &\approx \frac{m(m+M)}{5(m^2+M^2)+mMA^*} \\ &\quad \times \left(\frac{10(m+M)}{5m+3MA^*} - \frac{5(m-M)+4MA^*}{m+M}\right) \frac{\mathrm{d}\ln K}{\mathrm{d}\ln(E/N)}, \end{aligned} \tag{4.25}$$

$$\beta \approx \frac{mM(5-2A^*)}{5(m^2+M^2)+4mMA^*} \frac{\mathrm{d}\ln K}{\mathrm{d}\ln(E/N)}, \tag{4.26}$$

and A^* is the dimensionless ratio of collision integrals

$$A^* = \frac{\Omega^{(2,2)}(T_{\text{eff}})}{\Omega^{1,1}(T_{\text{eff}})} \tag{4.27}$$

The logarithmic derivative in equation 4.25 is approximated by

$$\frac{\mathrm{d}\ln K}{\mathrm{d}\ln(E/N)} \approx \frac{(6C^*-5)(T-T_{\text{eff}})}{T_{\text{eff}} - (6C^*-5)(T-T_{\text{eff}})}, \tag{4.28}$$

where C^* is defined in terms of the collision integrals given below,

$$C^* = \frac{\Omega^{(1,2)}(T_{\text{eff}})}{\Omega^{(1,1)}(T_{\text{eff}})}. \tag{4.29}$$

The collision integrals appearing in the equations above depend on the ion-molecule interaction potential via the collision cross sections as defined by Hirschfelder *et al.* [48] that are given below.

$$\Omega^{(l,s)}(T_{\text{eff}}) = \frac{1}{(s+1)!}(kT_{\text{eff}})^{-(s+2)} \int_0^\infty E'^{(s+1)} Q^{(l)}(E') \exp\left(\frac{-E'}{kT_{\text{eff}}}\right) \mathrm{d}E' \tag{4.30}$$

The collision integrals Ω are integrals over the translational energy, E', of the momentum cross section integral, $Q^{(l)}(E')$, which are in turn integrals over the impact parameter, b, of the classical deflection function $\chi(b, E')$,

$$Q^{(l)}(E') = 2\pi \frac{2(l+1)}{(2l+1-(-1)^l)} \int_0^\infty \left[1 - \cos^l \chi(b, E')\right] b\mathrm{d}b. \tag{4.31}$$

The classical deflection function is an integral involving the interaction potential $V(r)$,

$$\chi(b, E') = \pi - 2b \int_{r_0}^\infty \left(1 - \frac{b^2}{r^2} - \frac{V(r)}{E'}\right)^{-1/2} \frac{\mathrm{d}r}{r^2}. \tag{4.32}$$

The lower integration limit r_0 is given as the outermost root of the equation,

$$1 - \frac{b^2}{r_0^2} - \frac{V(r_0)}{E'} = 0, \tag{4.33}$$

and represents the radial separation at the turning point of a trajectory.

4.5 Three Temperature Theory

Although two-temperature theory overcame the convergence problems that resulted from requiring the ion temperature to be identical to that of the dilute gas, some problems remained. For example, the accuracy of the calculated ion diffusion coefficients for systems with high ion-atom mass ratio at high field strengths was poor. Lin *et al.* [43] developed three temperature theory to overcome the deficiencies of the two-temperature theory by using an expansion of the ion distribution function that allowed anisotropy in ion velocity space.

Lin *et al.* expanded the ion distribution function with a small ion density gradient.

$$f = f_0 - \left(f_x \frac{\partial}{\partial x} + f_y \frac{\partial}{\partial y} + f_z \frac{\partial}{\partial z}\right) \ln n \tag{4.34}$$

The ion distribution is then expanded in Cartesian coordinates in terms of the displaced anisotropic distribution.

$$f_{(0,x,y,z)} = f^{(0)} \sum_{p=0}^{\infty} \sum_{q=0}^{\infty} \sum_{r=0}^{\infty} f_{pqr}^{(0,x,y,z)} H_p(w_x) H_q(w_y) H_r(w_z), \tag{4.35}$$

where H_p are the Hermite polynomials, the coefficients $f_{pqr}^{(0,x,y,z)}$ represent the moments of the basis functions over the zero order approximation which is defined as

$$f^{(0)} = n \left(\frac{m}{2\pi k T_\perp}\right) \left(\frac{m}{2\pi k T_{||}}\right)^{1/2} \exp\left(-\left(w_x^2 + w_y^2 + w_z^2\right)\right), \tag{4.36}$$

where the dimensionless velocity components are

$$\begin{aligned} w_{x,y}^2 &= \left(\frac{m v_{x,y}^2}{2kT_\perp}\right)^{1/2} \\ w_z^2 &= \left(\frac{m(v_z - v_{\text{dis}})^2}{2kT_{||}}\right)^{1/2} \end{aligned} \tag{4.37}$$

Note that the parameters v_{dis}, $T_\perp$, and $T_{||}$, can be chosen to optimise the convergence properties of the resulting kinetic equations. Normalisation of the ion distribution function requires that $\langle \phi_{000} \rangle^{(0)} = 1$, and that $\langle \phi_{000} \rangle^{(x,y,z)} = 0$. Cylindrical symmetry of the drift tube implies that $\langle \phi_{pqr} \rangle^{(0,x,y,z)} = \langle \phi_{qpr} \rangle^{(0,x,y,z)}$, and the ion distribution must be symmetrical about the velocity origin requiring that odd functions in velocity must vanish, ie $\langle \phi_{2p+1\,2q+1\,2r+1} \rangle = 0$. Using these conditions and the recurrence relationships of the Hermite polynomials allows one to obtain a linear set of equations in the moments of the basis functions. The equations that determine the mobility, parallel diffusion coefficient, and perpendicular diffusion coefficient respectively are,

$$2r\mathcal{E}\langle \phi_{pq(r-1)} \rangle^{(0)} = \sum_{stu} \gamma(pqr\ stu) \langle \phi_{stu} \rangle^{(0)} \tag{4.38}$$

$$2r\mathcal{E}\langle \phi_{pq(r-1)} \rangle^{(z)} + h_{pqr}^{(z)} = \sum_{stu} \gamma(pqr\ stu) \langle \phi_{stu} \rangle^{(z)} \tag{4.39}$$

$$2r\mathcal{E}\langle \phi_{pq(r-1)} \rangle^{(x)} + h_{pqr}^{(x)} = \sum_{stu} \gamma(pqr\ stu) \langle \phi_{stu} \rangle^{(x)} \tag{4.40}$$

where $\mathcal{E}$ and $\gamma_(pqr\ stu)$, are defined as

$$\mathcal{E} = \left[\frac{m}{2kT_{||}}\right]^{1/2} \frac{e}{ma(001\ 000)} \frac{E}{N}, \tag{4.41}$$

$$\gamma(pqr\ stu) = a(pqr\ stu)/a(001\ 000), \tag{4.42}$$

and

$$h_{pqr}^{(z)} = \left[\frac{kT_{\|}}{2m}\right]^{1/2} \frac{\langle\phi_{pq(r+1)}\rangle^{(0)} + 2r\langle\phi_{pq(r-1)}\rangle^{(0)} - \langle\phi_{001}\rangle^{(0)}\langle\phi_{pqr}\rangle^{(0)}}{Na(001\ 000)}, \quad (4.43)$$

$$h_{pqr}^{(x)} = \left[\frac{kT_{\perp}}{2m}\right]^{1/2} \frac{\langle\phi_{(p+1)qr}\rangle^{(0)} + 2p\langle\phi_{(p-1)qr}\rangle^{(0)}}{Na(001\ 000)}. \quad (4.44)$$

The matrix elements are defined in equation 4.45

$$a(pqr\ stu) = \frac{\int f^{(0)}\phi_{stu}J\phi_{pqr}\mathrm{d}v}{\int f^{(0)}\phi_{stu}\phi_{stu}\mathrm{d}v} \quad (4.45)$$

Equations 4.38, 4.39 and 4.40 can be then truncated and solved with arbitrary accuracy, to yield the drift velocity and hence the mobility, and parallel and perpendicular diffusion coefficients via the following equations

$$v_d = v_{\mathrm{dis}} + \left(\frac{kT_{\|}}{2m}\right)^{1/2} \langle\phi_{001}\rangle^{(0)}, \quad (4.46)$$

$$D_{\|} = \left(\frac{kT_{\|}}{2m}\right)^{1/2} \langle\phi_{001}\rangle^{(z)}, \quad (4.47)$$

$$D_{\perp} = \left(\frac{kT_{\perp}}{2m}\right)^{1/2} \langle\phi_{100}\rangle^{(x)}, \quad (4.48)$$

$$(4.49)$$

respectively. An application of the theory of the previous equations has been implemented by Viehland [43] in a program called `MOBILDIF`.

4.6 Transport Theory of Molecular Systems

Kinetic theory of polyatomic systems is substantially more complex and less advanced due to the presence of anisotropy and the possibility of energy transfer between internal and external modes, ie inelastic collisions. Some authors have attempted to treat polyatomics in terms of parameterised potentials that represent aspects of the ion-molecule interaction [49, 50, 51], however these calculations fail to reproduce the temperature dependence of the transport coefficients. Viehland [52] has used the spherical average of atomic ion-diatom systems and concluded that

> ...the spherical components of the ion-neutral interaction potential fail to reproduce gaseous ion transport data.

Viehland further concluded that

> ...this means that spherical potentials inferred from total cross sections measurements in scattering experiments cannot be used with gaseous ion transport theory for atomic systems to predict or correlate transport data.

The failure of the spherical component of the ion-neutral interaction potential to account for observed ion transport properties results mainly from the neglect of inelastic collisions in the theory.

Viehland [53] has proposed a kinetic theory of polyatomic ion transport based on the Wang Chang-Uhlenbeck-de Boer (WUB) equation. The WUB equation is a semi classical generalisation of the Boltzmann equation which treats internal states of the polyatomic ion quantum mechanically, and the translational states classically. However the implementation of this theory requires the calculation of cross sections that are difficult to compute without compromising approximations [54, 55].

Recently, classical kinetic theory has been developed [44] for diatomics based on the kinetic equation of Curtiss [56]. The Boltzmann equation was derived by neglecting the terms on the left hand side that resulted from considering the momenta and conjugate momenta variables describing the phase space of the internal modes. The collision operator for the diatomic gas was then defined as

$$J(f) = \int [f(r,v',j',t)F(r,V',\mathcal{J}',t) - f(r,v,j,t)F(r,V,\mathcal{J},t)] \times \mid v - V \mid \mathcal{J} b \mathrm{d}b \mathrm{d}\hat{\mathcal{J}} \mathrm{d}\mathcal{J} \mathrm{d}\varphi \mathrm{d}\zeta \mathrm{d}\gamma_r \mathrm{d}V \tag{4.50}$$

where F, represents the distribution function of the neutral gas which is a function of the neutral velocity V, and neutral rotational momenta $\mathcal{J}$. The integral on the right hand side is over the phases of the rotational motions φ, and ζ, of the ion and the diatom respectively. An extra integral over γ_r is required in order to specify the direction of the angular momentum vector of the relative motion.

The ion distribution function was then expanded with the notation given in the following way,

$$f = \left[f^{(0)}(v,j) - f^{(1)}(v,j)\frac{\partial}{\partial r} \right] n(r,t) \tag{4.51}$$

where

$$f^{(0)}(v,j) = \left(\frac{1}{4\pi I k T_{\mathrm{int}}}\right)^{-1} \left(\frac{m}{2kT_{\perp}}\right) \left(\frac{m}{2kT_{\parallel}}\right)^{1/2}$$

$$\times \sum_{kmpqst} f^{(0)}(km\ pqst)B(km\ pqst) \tag{4.52}$$

the zeroth order ion distribution function is

$$f^{(0)}(v,j) = \left(\frac{1}{4\pi IkT_{\text{int}}}\right)^{-1}\left(\frac{m}{2kT_{\perp}}\right)\left(\frac{m}{2kT_{||}}\right)^{1/2}\exp\left(-\epsilon - w^2\right) \tag{4.53}$$

and the internal energy, ϵ, and translational energy, w, are chosen to be

$$w = \tau\cdot(v - v_{\text{dis}}), \tag{4.54}$$

$$\epsilon = \frac{j^2}{2IkT_{\text{int}}}. \tag{4.55}$$

Then the parameters τ, and v_{dis} are constructed to the order of theory required. For an adequate description of diatomic ion diffusion, the analogous spherical polar three-temperature theory must be applied. This requires the construction of the parameters in the following way,

$$\begin{aligned} \tau &= \left(\frac{m}{2kT_{\perp}}\right)^{1/2}(\hat{x}\hat{x}+\hat{y}\hat{y}) + \left(\frac{m}{2kT_{||}}\right)^{1/2}\hat{z}\hat{z}, \\ v_{\text{dis}} &= v_{\text{dis}}\hat{z}. \end{aligned} \tag{4.56}$$

Note that the basis functions $B(km\ pqst)$ are defined as

$$\begin{aligned} B(km\ pqst) = (-1)^{k-m}(4k+2)^{1/2}w^p L_s^{(p+1/2)}(w^2)\epsilon^{q/2}L_t^{(q)}(\epsilon) \\ \times\sum_{\mu\nu}\begin{pmatrix} p & q & k \\ \mu & \nu & -m \end{pmatrix} Y_p^{\mu}(\hat{w})Y_q^{\nu}(\hat{j}). \end{aligned} \tag{4.57}$$

The $3jm$ symbols in brackets are those defined by Edmonds [57]. The coefficients $f(km\ pqst)$ represent the moments of $B(km\ pqst)$ over the ion distribution function. Using the orthogonality properties of the basis functions $B(km\ pqst)$, the normalisation conditions of the ion distribution function, and the recurrence relationships between the basis functions allows the derivation of an infinite set of linear equations that must be solved by a series of approximations with the aim of a rapidly converging result. The drift velocity is obtained from solving the equation

$$\begin{aligned} &\sum_{kpqst} f^{(0)}(k'0\ pqst)\begin{pmatrix} k' & p' & q' & s' & t' \\ k & p & q & s & t \end{pmatrix}^{(m')} \\ &+\frac{eE}{N}\tau_{zz}(-1)^{p'+q'+1}(4k+2)^{1/2}\sum_k(4k+2)^{1/2}\begin{pmatrix} k & k & 1 \\ 0 & 0 & 0 \end{pmatrix} \end{aligned}$$

$$\left[(s')^{1/2}(p'+1)^{1/2}\begin{Bmatrix} q' & k' & p' \\ 1 & p'+1 & k \end{Bmatrix} f^{(0)}(k0\ p'+1q's'-1t')\right.$$
$$\left.+(p')^{1/2}(p'+s'+1/2)^{1/2}\begin{Bmatrix} q' & k & p'-1 \\ 1 & p' & k \end{Bmatrix} f^{(0)}(k0\ p'-1q's't')\right]$$
$$=0 \tag{4.58}$$

The $6jm$ symbols in curly brackets are those defined by Edmonds [57], and the brackets with 10 indices are the collision integrals that are defined by equation 4.59

$$\begin{pmatrix} k' & p' & q' & s' & t' \\ k & p & q & s & t \end{pmatrix}^{(m')} = \frac{M}{N}\int B(k'm'\ p'q's't')^{\dagger}$$
$$\times\left[J\exp(-\epsilon-w^2)B(km'\ pqst)\right]w^2 dw d\hat{w} d\epsilon d\hat{j}. \tag{4.59}$$

Using the coefficient $f^{(0)}(10\ 1000)$, the drift velocity can be obtained using equation 4.60,

$$v_d = v_{\rm dis} + \left(\frac{\pi^{1/2}}{8}\right)^{1/2}\tau_{zz}^{-1} f^{(0)}(10\ 1000). \tag{4.60}$$

In order to calculate the parallel diffusion coefficient, one must then solve equation 4.61 to obtain $f_{||}^{(1)}(10\ 1000)$,

$$\sum_{kpqst} f_{||}^{(1)}(k'0\ pqst)\begin{pmatrix} k' & p' & q' & s' & t' \\ k & p & q & s & t \end{pmatrix}^{(m')}$$
$$+\frac{eE}{N}\tau_{zz}(-1)^{p'+q'+1}(4k+2)^{1/2}\sum_k (4k+2)^{1/2}\begin{pmatrix} k & k & 1 \\ 0 & 0 & 0 \end{pmatrix}$$
$$\times\left[(s')^{1/2}(p'+1)^{1/2}\begin{Bmatrix} q' & k' & p' \\ 1 & p'+1 & k \end{Bmatrix} f_{||}^{(1)}(k0\ p'+1q's'-1t')\right.$$
$$\left.+(p')^{1/2}(p'+s'+1/2)^{1/2}\begin{Bmatrix} q' & k & p'-1 \\ 1 & p' & k \end{Bmatrix} f_{||}^{(1)}(k0\ p'-1q's't')\right]$$

$$=(-1)^{p'+q'+k'}\left(\frac{IkT_{\rm int}}{\tau_{xx}\tau_{yy}\tau_{zz}^2}\right)\left[(k'+1)^{1/2}(p'+1)^{1/2}\begin{Bmatrix} k'+1 & k' & 1 \\ p' & p'+1 & q' \end{Bmatrix}\right.$$
$$\times\left\{(p'+s'+3/2)^{1/2}f^{(0)}(k'+10\ p'+1q's't')\right.$$
$$\left.\left.-(s')^{1/2}f^{(0)}(k'+10\ p'+1q's'-1t')\right\}\right.$$

$$
\begin{aligned}
&-(k'+1)^{1/2}(p')^{1/2}\left\{\begin{array}{ccc} k'+1 & k' & 1 \\ p' & p'-1 & q' \end{array}\right\} \\
&\times\left\{(p'+s'+1/2)^{1/2}f^{(0)}(k'+10\ p'-1q's't')\right. \\
&\left.-(s'+1)^{1/2}f^{(0)}(k'+10\ p'-1q's'+1t')\right\} \\
&+(k')^{1/2}(p')^{1/2}\left\{\begin{array}{ccc} k'-1 & k' & 1 \\ p' & p'-1 & q' \end{array}\right\} \\
&\times\left\{(p'+s'+1/2)^{1/2}f^{(0)}(k'-10\ p'-1q's't')\right. \\
&\left.-(s'+1)^{1/2}f^{(0)}(k'-10\ p'-1q's'+1t')\right\}\Big] \quad (4.61)
\end{aligned}
$$

The parallel diffusion coefficient is then given as

$$
D_{\|}=\left(\frac{\pi^{1/2}}{8}\right)^{1/2}\tau_{zz}^{-1}f_{\|}^{(1)}(10\ 1000). \quad (4.62)
$$

Likewise the perpendicular diffusion coefficient is obtained by solving equation 4.63 for $f_{\perp}^{(1)}(11\ 1000)$,

$$
\begin{aligned}
&\sum_{kpqst} f_{\perp}^{(1)}(k'1\ pqst)\begin{pmatrix} k' & p' & q' & s' & t' \\ k & p & q & s & t \end{pmatrix}^{(m')} \\
&+\frac{qE}{N}\tau_{zz}(-1)^{p'+q'}(4k+2)^{1/2}\sum_{k>0}(4k+2)^{1/2}\begin{pmatrix} k & k & 1 \\ 1 & -1 & 0 \end{pmatrix} \\
&\times\left[(s')^{1/2}(p'+1)^{1/2}\left\{\begin{array}{ccc} q' & k & p' \\ 1 & p'+1 & k \end{array}\right\}f_{\perp}^{(1)}(k1\ p'+1q's'-1t')\right. \\
&=(-1)^{p'+q'+1}\left(\frac{IkT}{2\tau_{xx}^2\tau_{yy}\tau_{zz}}\right)(2k+1)^{1/2} \\
&\sum_{k}(4k+2)^{1/2}(-1)^{k+k'}\begin{pmatrix} k & k' & 1 \\ 0 & 1 & -1 \end{pmatrix} \\
&\times\left\{(p'+1)^{1/2}\left\{\begin{array}{ccc} q' & k & p'+1 \\ 1 & p' & k' \end{array}\right\}\left\{(p'+s'+3/2)^{1/2}f^{(0)}(k0\ p'+1q's't')\right.\right. \\
&\left.-(s')^{1/2}f^{(0)}(k0\ p'+1q's'-1t')\right\}-(p')^{1/2}\left\{\begin{array}{ccc} q' & k & p'-1 \\ 1 & p' & k' \end{array}\right\} \\
&\times\left\{(p'+s'+1/2)^{1/2}f^{(0)}(k0\ p'-1q's't')\right. \\
&\left.\left.-(s'+1)^{1/2}f^{(0)}(k0\ p'-1q's'+1t')\right\}\right], \quad (4.63)
\end{aligned}
$$

and calculating the perpendicular diffusion coefficient using equation 4.64

$$D_\perp = \left(\frac{\pi^{1/4}}{4\tau_{xx}}\right) f_\perp^{(1)}(11;1000). \tag{4.64}$$

4.6.1 Atomic Ions in a Diatomic gas

The theory of diatomic systems based on the classical Boltzmann equation derived by Curtiss *et al.* [56] has been specialised and then reduced to computationally feasible form by Viehland [58] to the case of atomic ions in rigid rotor diatomic gases.

For atomic ions the basis functions defined by equation 4.57 reduces to

$$B(lms) = 2^{1/2} w^l L_s^{(l+1/2)}(w^2) Y_l^m(\hat{w}). \tag{4.65}$$

where the reduced velocity of the atomic ions, w, and the neutral diatoms, W, are defined as follows,

$$\begin{aligned} w_{x,y} &= \left(\frac{m}{2kT_\perp}\right)^{1/2}\left[G_{x,y} + \frac{Mg_{x,y}}{M+m}\right] \\ w_z &= \left(\frac{m}{2kT_\parallel}\right)^{1/2}\left[G_z + \frac{Mg_z}{M+m} - v_{\text{dis}}\right] \qquad (4.66) \\ W &= \left(\frac{M}{2kT}\right)^{1/2}\left[G + \frac{mg}{M+m}\right] \qquad (4.67) \end{aligned}$$

where G is the centre of mass velocity, and g is the relative velocity of the collision partners.

Using these definitions reduces equation 4.58 to

$$\begin{aligned} &\frac{8}{3}\left(\frac{2\mu k(mT+MT_\parallel)}{\pi(m+M)}\right)^{1/2} \sum_{l,s} f_{lms} I^{(m)}(l,s,l',s') + \frac{2qE}{N}\left(\frac{m}{2kT_\parallel}\right)^{1/2} \\ &\times\left[(l'+1)\left(\frac{s'}{(2l'+s)(2l'+1)}\right)^{1/2} f_{l'+1,m,s'-1}\right. \\ &\qquad \left. - l'\left(\frac{l'+s'+1/2}{(2l'+1)(2l'-1)}\right)^{1/2} f_{l'-1,m,s'}\right] = 0, \end{aligned} \tag{4.68}$$

where the collision integrals $I^{(m)}(l,s,l',s')$ are defined as

$$I^{(m)}(l,s,l',s') = \frac{3(m+M)}{64\pi^3 M}\left(\frac{Mm}{2k(mT+MT_\parallel)}\right)^{1/2}$$

$$\times \int \exp(-E_{\rm rot} - W^2 - w^2) B(lms) \left[B(l'm's') - B'(l'm's')\right] \times g b \mathrm{d}b \mathrm{d}\Omega \mathrm{d}E_{\rm rot} \mathrm{d}W \mathrm{d}w \qquad (4.69)$$

where the rotational energy of the diatomic $E_{\rm rot}$, is defined below.

$$E_{\rm rot} = \frac{\mathcal{J}^2}{2IkT} \qquad (4.70)$$

The coefficients f_{lms} are the moments of the basis functions $B(lms)$. The differential variable Ω in equation 4.69 indicates the integral over two spherical polar angles of the angular momentum vector $\mathcal{J}$ of the diatom, the pre-collisional angular phase of the rotational motion of the diatom, and an angle that specifies the pre-collisional direction of the orbital angular momentum, L, of the ion neutral pair.

The drift velocity can be calculated from equation 4.71

$$v_d = v_{\rm dis} + \left(\frac{kT_{\|}}{m}\right)^{1/2} \frac{f_{1,0,0}}{f_{0,0,0}}. \qquad (4.71)$$

Similarly equation 4.61 which is used to calculate the parallel diffusion coefficient reduces to

$$\frac{8}{3}\left(\frac{2\mu k(mT + MT_{\|})}{\pi(m+M)}\right)^{1/2} \sum_{l,s} f^{\|}_{lms} I^{(m)}(l,s,l',s') + \frac{2qE}{N}\left(\frac{m}{2kT_{\|}}\right)^{1/2} \times \left[(l'+1)\left(\frac{s'}{(2l'+s)(2l'+1)}\right)^{1/2} f^{\|}_{l'+1,m,s'-1} - l'\left(\frac{l'+s'+1/2}{(2l'+1)(2l'-1)}\right)^{1/2} f^{\|}_{l'-1,m,s'}\right]$$

$$= \frac{m}{N}\left(\frac{2kT_{\|}}{m}\right)^{1/2} \left[(l'+1)\left(\frac{l'+s'+3/2}{(2l'+3)(2l'+1)}\right)^{1/2} f_{l'+1,m,s'} - (2l'+1)\left(\frac{s'}{(2l'+3)(2l'+1)}\right)^{1/2} f_{l'+1,m,s'-1} + l'\left(\frac{l'+s'+1/2}{(2l'+1)(2l'-1)}\right)^{1/2} f_{l'-1,m,s'} - (2l'-1)\left(\frac{s'}{(2l'+1)(2l'-1)}\right)^{1/2} f_{l'-1,m,s'+1}\right]. \qquad (4.72)$$

The parallel diffusion coefficient is then obtained from $f^{\|}_{1,0,0}$, and equation 4.73,

$$D_{\|} = \left(\frac{kT_{\|}}{2m}\right)^{1/2} \frac{f^{\|}_{1,0,0}}{f_{0,0,0}}. \tag{4.73}$$

Equation 4.63 which is used to calculate the perpendicular diffusion coefficient reduces to

$$\begin{aligned}
&\frac{8}{3}\left(\frac{2\mu k(mT + MT_{\|})}{\pi(m+M)}\right)^{1/2} \sum_{l,s} f^{\perp}_{lms} I^{(m)}(l,s,l',s') + \frac{2qE}{N}\left(\frac{m}{2kT_{\|}}\right)^{1/2} \\
&\times \left[\left(\frac{s'l'(l'+2)}{(2l'+3)(2l'+1)}\right)^{1/2} f^{\perp}_{l'-1,m,s'-1} \right. \\
&\left. - \left(\frac{(l'+s'+1/2)(l'-1)(l'+1)}{(2l'+1)(2l'-1)}\right)^{1/2} f^{\perp}_{l'-1,m,s'}\right] \\
&= \frac{m}{N}\left(\frac{2kT_{\perp}}{m}\right)^{1/2} \left[-\left(\frac{l'(l'+s'+3/2)(l'+1)}{(2l'+3)(2l'+1)}\right)^{1/2} f_{l'+1,m-1,s'} + \right. \\
&\qquad \left(\frac{l's'(l'+1)}{(2l'+3)(2l'+1)}\right)^{1/2} f_{l'+1,m-1,s'-1} + \\
&\qquad \left(\frac{l'(l'+s'+1/2)(l'+1)}{(2l'+1)(2l'-1)}\right)^{1/2} f_{l'-1,m-1,s'-1} + \\
&\qquad \left. \left(\frac{l'(s'+1)(l'+1)}{(2l'+1)(2l'-1)}\right)^{1/2} f_{l'-1,m-1,s'+1}\right].
\end{aligned} \tag{4.74}$$

The perpendicular diffusion coefficient is then obtained from $f^{\perp}_{1,1,0}$, and equation 4.75,

$$D_{\perp} = \left(\frac{kT_{\perp}}{2M}\right)^{1/2} \frac{f^{\perp}_{1,1,0}}{f_{0,0,0}}. \tag{4.75}$$

The rate of convergence of the approximations of the kinetic equations then depends on the choice of the parameters v_{dis}, $T_{\|}$, and $T_{\perp}$. On physical grounds the parameters can be set to meet the following conditions in order to achieve good convergence.

$$\begin{aligned}
\frac{1}{2}kT_{\perp} &= \int f(v)\frac{1}{2}mv^2_{x,y}\mathrm{d}v \\
\frac{1}{2}kT_{\|} &= \int f(v)\frac{1}{2}m(v_z - v_{\text{dis}})^2\mathrm{d}v \\
v_{\text{dis}} &= \int f(v)v_z\mathrm{d}v
\end{aligned} \tag{4.76}$$

4.7 Applications

Viehland has implemented the theory based on the preceding equations in a computer program called `MOBDIF`. The program `MOBDIF` uses as its primary input the reduced form of the collision integrals [58]. The program `MOBDIF` calculates the transport coefficients of spherical systems by using the momentum collision cross sections $Q^{(l)}(E)$ to calculate the required input cross sections via equation 4.77

$$I_8(s,t \mid E) = (s+t)!(t)! \sum_{t'=0}^{t} \frac{1}{(t')!(t-t')!} \sum_{s'=0}^{s+t} \frac{(-1)^{s'+1}}{(s')!(s+t-s')!} Q^{(s'+t')}(E), \quad (4.77)$$

where the usual momentum transfer collision integrals are defined in equation 4.31. Efficient programs to calculate the momentum collision cross sections are available [59]. This application of the theory has been demonstrated to have significant improvements in convergence properties and computational efficiency [58] over the previous Cartesian implementations of the theory.

For atomic ion-diatom systems the collision integrals defined by equation 4.78 are required for input into the program `FINAL`,

$$\sigma^{(s,t)}(E,E') = 2\pi \int_0^\infty \mathrm{d}b \frac{b}{2} \int_{-1}^{+1} \mathrm{d}\cos\chi \frac{1}{\pi^*} \int_0^{\pi^*} \mathrm{d}\phi_L \frac{1}{\pi} \int_0^{\pi} \mathrm{d}\phi_j \times \left[1 - \left(\frac{E'}{E}\right)^{s/2} (\cos\Theta)^s\right] \left(\frac{E'}{E}\right)^t (\sin\Theta)^{2t} \quad (4.78)$$

where π^* is equal to π if the diatomic is homonuclear and equal to 2π if the diatomic is heteronuclear. The program `FINAL` then calculates the integrals defined by equation 4.79.

$$I_8(s,t \mid E) = \frac{1}{kT} \int_0^\infty \mathrm{d}E_{\mathrm{rot}} \exp(-\frac{\epsilon_0}{kT}) \sigma^{(s,t)}(E, E_{\mathrm{rot}}). \quad (4.79)$$

These integrals are the required input to program `MOBDIF`.

The integrals defined by equation 4.78 can be calculated using the classical trajectory program `TRAJECK` written by Dickinson [60, 61], and modified by Viehland and Dickinson [62] to use the action angle variables defined by Smith [63]. The primary input to the program `TRAJECK` is the potential energy surface. The program has been modified to accept a general tabulated potential energy surface, with boundary fitting functions.

4.8 Conclusion

A general outline of moment methods used for obtaining the velocity moments of the one particle distribution function of a trace amount of ions in a dilute gas has been given. A converging kinetic series is obtainable providing that the assumed eigenfunction of the system is realistic. Two-temperature theory is sufficiently accurate to calculate ion mobilities of an arbitrary field strength, however three-temperature theory is required to calculate the ion diffusion coefficients accurately. Viehlands' theory of diatomic ion-diatom transport has been presented and specialised to the atomic ion-diatom case. Implementations of the theory have been outlined and will be used to calculate theoretical transport data for comparison with experiments for a range of spherically symmetric systems and for the atomic ion-diatom systems Li^+—N_2, and Li^+—CO.

It is anticipated that future developments in the study of ion transport will include improved theoretical and experimental methods to study the effects of anisotropy. Viehland [64] has stated his intention of calculating the ion transport properties of the substantially more difficult diatomic ion-atom system using the existing theory. These systems are known to be complicated by the presence of an internal temperature related to ion rotation, and by the possibility of rotational polarisation which has been experimentally observed [65]. Fortunately the internal rotational temperature of the ion must be equal to the ions effective translational temperature. This is a result of the fact that the only mechanism of energy transfer into and out of this internal mode is translational-rotational inelastic collisions with the atomic gas.

In future, actual measurements of the ion distribution function may become routine, and such studies will provide information about anisotropic interactions between molecular species directly. Further progress in the study of ion transport is very likely to strongly overlap with molecular dynamics, and experiments that probe the mechanisms of energy transfer between translational and internal modes of freedom via inelastic collisions for general systems.

Chapter 5

Ion Transport of Atomic Systems

5.1 Introduction

The development of two- and three-temperature theory, as outlined in chapter 4 has led to calculation of the transport coefficients of spherically symmetric systems from interaction potentials. Such calculations are now routine. It is also possible to calculate interaction potentials from accurate data sets of transport coefficients using an inverse procedure [66]. Where possible the results of ion scattering experiments have been compared to ion transport numbers [40] and generally excellent agreement has resulted. Thus interaction potentials of many atomic ion-atom systems have been determined to an accuracy that rivals the best *ab initio* calculations. For example, Viehland [67] has tested some interaction potentials of alkali metal cations and halogen anions with helium and neon gases, and compared the results with ion-beam scattering experiments. Further studies have calculated the interaction potentials directly from a set of ion transport data for a series of alkali metal ion-noble gas systems [51, 67]. Universality and scaling laws for these interaction potentials have been proposed [68] based on these results.

Several interaction potentials for various closed shell ion-inert gas interactions have been proposed. Many of these include explicit expressions of long-range attractive terms and short-range repulsive terms in order to determine the fundamental interaction between the particles involved in its most general sense. Theoretical studies of the transport properties of ions in dilute gases can achieve sufficient accuracy to predict the experimental values [69] and, if there is disagreement, whether

the interaction potential or the experimental data set is at fault. This, fortunately, is not a common occurrence and generally the relationship between theory and experiment has been symbiotic.

5.2 The Transport Calculations of Closed Shell Systems

Because of the relative simplicity of calculating cross sections for closed shell systems, most of the kinetic theory studies of ion transport systems have involved alkali metal cations and halogen anions with the inert gases. The prototypical alkali metal cation-noble gas system is the Li^+—He system. The Li^+—He system is critical in that it represents a standard by which the accuracy of theoretical and experimental methods can be assessed, and the physical limit of dimension which can be adequately described by classical mechanics. Despite the amount of attention this system has received it has only recently been fully characterised. The calculations performed on this system represent a good case study for these type of calculations and measurements. The literature illustrates the relationship between theory and experiment in achieving an accurate picture of ion transport. A review of the Li^+–He system is given in order to examine this relationship.

The first high level *ab initio* study of the Li^+—He ($X,^1\Sigma$) interaction potential was performed by Hariharan and Staemmler [70]. Their Coupled Electron Pair Approximation (CEPA) calculations yielded an interaction potential that was in excellent agreement with the experimental integral scattering cross section measurements of Inouyne and Kita [71], except at short-range where the CEPA results were significantly more repulsive by up to 20%. Gatland *et al.* [72] have reported the results of mobility calculations using electron-gas model interaction potentials for a range of alkali metal cations in inert gases. While the agreement between the theoretical mobilities were generally good, several results, including those of the Li^+—He system were at the boundaries of mutual agreement, while others were beyond the boundaries of mutual agreement. In a further study of the Li^+—He system, Gatland *et al.* [73] made new measurements of the mobility of the Li^+ ions in helium and compared these values to those calculated with two-temperature theory using the interaction potential of Hariharan and Staemmler [70]. The results of these

calculations and the new experimental measurements were in excellent agreement at both low and intermediate E/N, but they departed significantly at high E/N, again questioning the validity of Hariharan and Staemmlers' interaction potential at short separation. Direct inversion of the mobility data to obtain an interaction potential for this system revealed that the theoretical results of Hariharan and Staemmler were too repulsive at short-range. Cassidy and Elford [74] have carefully examined the systematic and random errors in their drift-tube measurements and characterised the low and intermediate E/N mobilities of Li^+ ions in helium at 294K and 80K. Their results were consistently lower than other experimental measurements [73]. These results and conclusions were supported by the experimental results of Løvaas *et al.* [75]. Ahlrichs *et al.* [76] have reported an interaction potential for this system based on a parameterised model interaction potential. Their short-range results are very similar to the results of Hariharan and Staemmler.

In order to resolve the difference in the interaction potentials derived from theoretical calculations and experimental measurements, Larsen *et al.* [77] calculated the mobility of Li^+ in helium using a Kramers-Moyal expansion of the Boltzmann collision integral. This was carried out in order to overcome convergence problems of the two-temperature theory, and they used both the *ab initio* interaction potentials of Hariharan and Staemmler [70], and Senff and Burton [78], with poor and reasonable success respectively. An interaction potential was then developed based on the differences between the two *ab initio* interaction potentials of Sneff and Burton, and Hariharan and Staemmler, and this was used to maximise the agreement between the experimental data set of Løvaas *et al.* and Cassidy and Elford, and the theoretical calculations. This modified interaction potential must be regarded as the most accurate currently available for the Li^+—He system. Such accuracy is only possible after exacting and cooperative application of theory and experiment.

5.3 The Transport Calculations of Open Shell Systems

In contrast to closed shell systems, there are few theoretical studies of open shell atomic ion-atom systems published in the literature [79, 80, 81]. Thus the information contained in the excellent data base of transport properties [37, 38, 39] of open

shell atomic ion-atom systems has largely been neglected, due to the difficulty of calculating cross sections in which two or more collision channels correlate to the non-interacting collision partners. Likewise there are few theoretical studies of electronically excited atomic ion-atom systems [79, 81], although the database of such systems is equally as sparse.

In the following section, a detailed review of the calculations and, where necessary measurements, of ion transport properties will be given for the following open shell atomic ions interacting with helium: C^+ (^2P), C^{+*} (^4P), N^+ (^3P), O^+ (^4S), O^{+*} (^2P), Si^+ (^2P), Si^{+*} (^4P). The mobilities of these open shell systems have been calculated from *ab initio* interaction potentials using two classically limiting cases. The theoretical calculations have been compared with experimental measurements, and the results will be discussed. Finally, the ion transport properties of open shell atomic ion-atom systems are discussed and a conclusion is given.

5.3.1 The Mobility of C^+ (^2P) and C^{+*} (^4P) in Helium

The transport properties of C^+ in helium must be accurately known in order to make experimental determinations of ion-molecule rate constants from drift tube measurements for the reactions of C^+ (^2P). Accurate rate constants are required over a range of temperatures in order to model the chemistry of interstellar clouds. The reaction of $C^+ + H_2$ for example is of particular astrophysical interest [82].

The mobility of C^+ (^2P) ions in helium has been experimentally measured by several groups [83, 84, 85, 86]. Twiddy *et al.* [86] were able to detect the presence of a second species with the same nominal mass as C^+, that had a substantially lower mobility, which they claimed was the metastable ion C^{+*} (^4P). Several other authors have reported observations of an excited metastable C^+ ion which has been assigned to C^{+*} (^4P). If this were confirmed then it would represent one of the first measurements of the mobility of an electronically excited ion.

Several *ab initio* studies of the C^+—He system have been reported. Harrison *et al.* [87], and Cooper and Wilson [88] have reported SCF calculations on the $^2\Pi$ interaction potential. Koch and Frenking [89] have reported calculations at the MP2/6-31G(d,p) and MP4/6-311G(d,p) levels of theory on the optimised structures of $^2\Pi$, $^2\Sigma$, and $^4\Sigma$ of C^+—He. Their results have shown that the $^2\Pi$ surface is weakly bound with a D_e of about 0.025–0.050 eV, and an r_e of about 2.4 Å. Koch

and Frenking have also improved the level of theory of these results in a later paper [90] however these results are qualitatively the same. Young and Coggiola [91] have reported a gas phase ion of nominal mass 16 u generated from a helium discharge between carbon electrodes using high resolution mass spectrometry which they assign to either HeC^+, or $He_2C_2^{2+}$. This ion has not yet been assigned to a specific electronic state.

5.3.1.1 The Interaction Potentials of C^+—He

There are two states of C^+—He that correlate with the the collision partners He $1s^2$ ^1S + C^+ $2s^2p^1$ ^2P. These are the $^2\Pi$ and $^2\Sigma$ molecular ion states. There are two

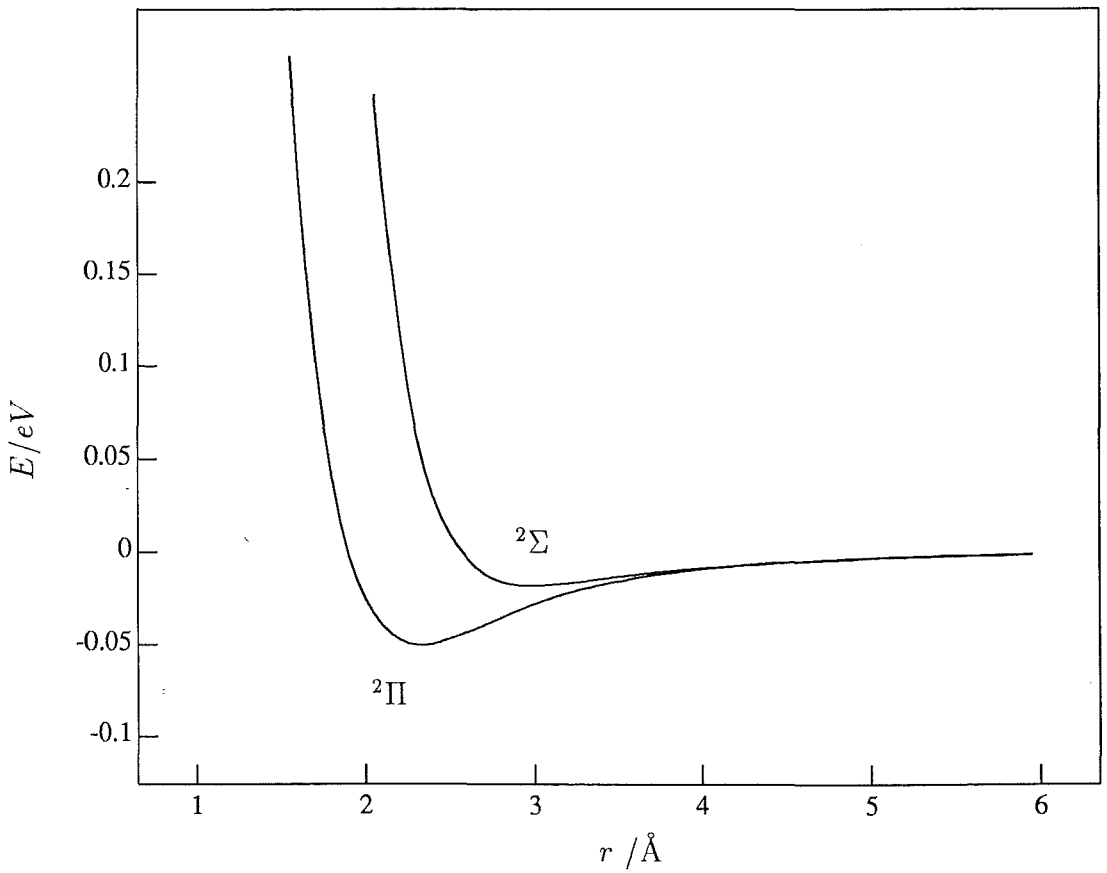

Figure 5.1: The interaction potentials of C^+—He ($^2\Pi$ and $^2\Sigma$) calculated at the MP4SDQ/6-311G+(3df,3pd) level of theory. The interaction potentials are labelled in the figure.

states of C^{+*}—He that correlate with the the collision partners He $1s^2$ ^1S + C^{+*} $2s^1p^2$ ^4P. These are the $^4\Pi$ and $^4\Sigma$ molecular ion states. The interaction potentials

were calculated for the C^+—He ($^2\Pi$, and $^2\Sigma$) and C^{+*}—He ($^4\Sigma$, and $^4\Pi$) states at the MP4SDQ/6-311+G(3df,3pd) level of theory, excluding core contributions to the correlation energy. The results of these calculations are given in tables 5.1 and 5.2 for the C^+—He ($^2\Pi$ and $^2\Sigma$) states arising for the interaction of the C^+ (^2P) ion with He (^1S), and the C^+—He ($^4\Sigma$ and $^4\Pi$) states arising from the interaction of the C^{+*} (^4P) ion with He (^1S). The values for the HF interaction potentials are also given. These interaction potentials have also been plotted in figures 5.1 and 5.2 for the doublet and quartet states respectively. The C^+—He $^2\Pi$ state is attractive with

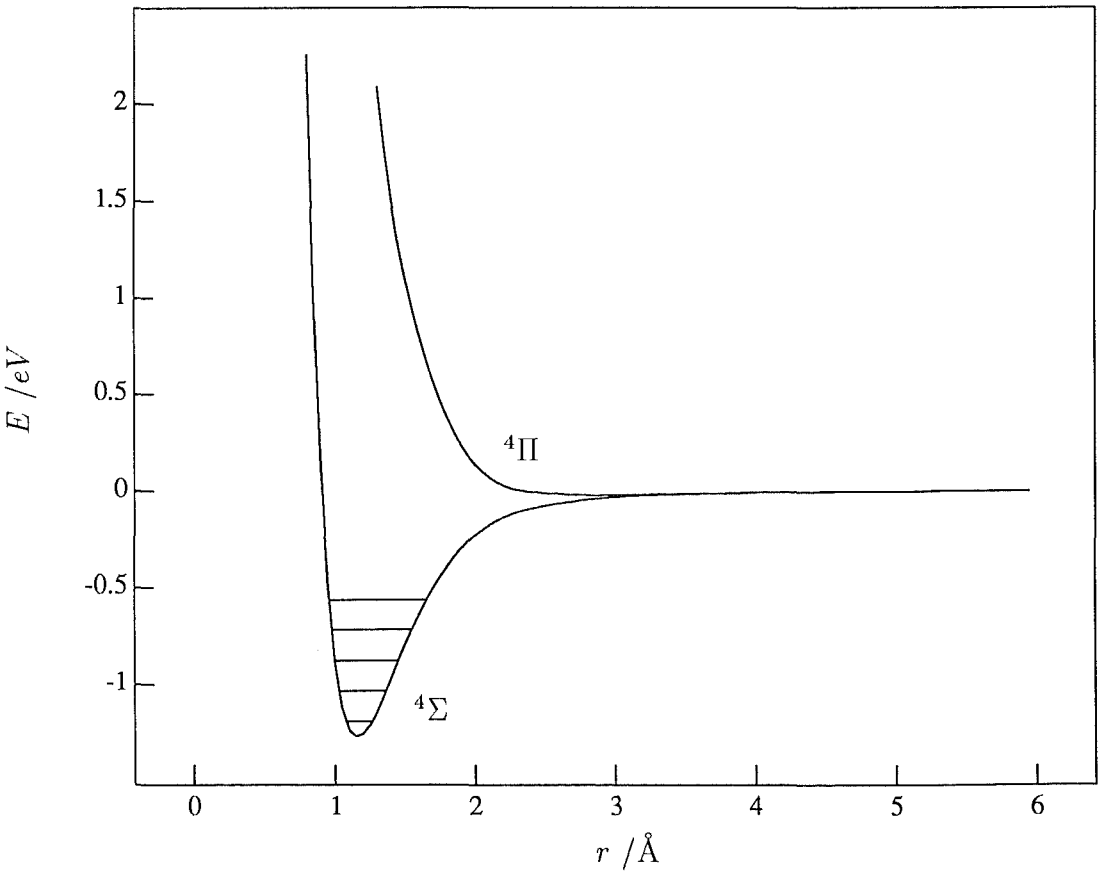

Figure 5.2: The interaction potentials of C^+—He ($^4\Pi$ and $^4\Sigma$) calculated at the MP4SDQ/6-311G+(3df,3pd) level of theory. The interaction potentials are labelled in the figure.

a D_e of 0.050 eV and an r_e of 2.329 Å. The $^2\Sigma$ state has a shallower D_e of 0.018 eV, at a substantially larger r_e of 2.978 Å.

The metastable ion C^{+*}—He $^4\Sigma$ (^4P) interaction potential is very attractive with a D_e of 1.271 eV, and an r_e of 1.158 Å. The $^4\Pi$ state has a D_e of 0.022 eV with an r_e of 2.805 Å. These values should be regarded as improvements on

Table 5.1: HF/6-311+G(3df,3pd) and MP4SDQ/6-311+G(3df,3pd) energies for the HeC$^+$ $^2\Pi$ and $^2\Sigma$ states.

r^a	E^b			
	$^2\Pi$		$^2\Sigma$	
	HF	MP4SDQ	HF	MP4SDQ
1.00	-40.03507	-40.15541	—	—
1.25	-40.10512	-40.22379	—	—
1.50	-40.13415	-40.24956	—	—
1.75	-40.14690	-40.25970	—	—
2.00	-40.15191	-40.26313	-40.13942	-40.25112
2.25	-40.15364	-40.26401	-40.14843	-40.25898
2.50	-40.15402	-40.26392	-40.15186	-40.26185
2.75	-40.15391	-40.26357	-40.15302	-40.26272
3.00	-40.15371	-40.26322	-40.15332	-40.26286
3.25	—	—	-40.15334	-40.26279
3.50	-40.15338	-40.26277	-40.15329	-40.26268
4.00	-40.15319	-40.26253	-40.15316	-40.26251
4.50	-40.15308	-40.26240	-40.15307	-40.26239
5.00	-40.15301	-40.26232	-40.15301	-40.26231
∞	-40.15291	-40.26220	-40.15391	-40.26220

[a] All distances in Angströms
[b] All energies in hartrees

previously published values [87, 88, 89]. The excited metastable state of the C^{+*} (^4P) ion is calculated to be 41666 cm^{-1} above the ^2P state, compared with 43000 cm^{-1} determined spectroscopically [92]. The spectroscopic value is supported by the recent translation energy spectroscopy results of 42984 cm^{-1} reported by Lee *et al.* [93].

5.3.1.2 The Mobility Calculations of C$^+$ (^2P) and C^{+*} (^4P) in Helium

Previous methodologies for the calculation of open shell atomic ion-atom systems have invoked Blanc's law to calculate the combined mobility from the mobilities of the two molecular states in the manner given by equation 5.1.

$$\frac{1}{K_0} = \frac{1}{3K_0(^2\Sigma)} + \frac{2}{3K_0(^2\Pi)} \tag{5.1}$$

Table 5.2: HF/6-311+G(3df,3pd) and MP4SDQ/6-311+G(3df,3pd) energies for the HeC^+ $^4\Sigma$ and $^2\Pi$ states.

r^a	E^b			
	$^4\Sigma$		$^4\Pi$	
	HF	MP4SDQ	HF	MP4SDQ
0.875	-39.97539	-40.05254	—	—
1.00	-40.02952	-40.10586	—	—
1.125	-40.04514	-40.11957	—	—
1.25	-40.04607	-40.11765	—	—
1.375	-40.04221	-40.11050	—	—
1.50	-40.03740	-40.10246	-39.96854	-40.03228
2.00	-40.02478	-40.08180	-40.00117	-40.06819
2.50	-40.02114	-40.07607	-40.01886	-40.07369
2.75	—	—	-40.01946	-40.07405
2.875	—	—	-40.01954	-40.07406
3.00	-40.01996	-40.07444	-40.01955	-40.07402
3.25	—	—	-40.01949	-40.07389
3.50	-40.01950	-40.07386	-40.01940	-40.07376
4.00	-40.01929	-40.07360	-40.01925	-40.07357
4.50	-40.01917	-40.07347	-40.01916	-40.07345
5.00	-40.01910	-40.07338	-40.01909	-40.07338
∞	-40.01899	-40.07326	-40.01899	-40.07326

[a] All distances in Angströms
[b] All energies in hartrees

Blanc's law is only approximate, and the correct classical mechanical procedure for calculating the mobility for an open shell system is to average the transport cross sections for the separate Born-Oppenheimer states over the relative degeneracies. However, Blanc's law is valid for certain limiting cases. For instance, Blanc's law is justified at low field where the mean collision energy is largely thermal and the ratios of mean collision energy of the ions in different gases (or in this case, different states with the same gas) are unity. Blanc's law is also valid when the collision cross sections are independent of the collision energy. This is true when the ratio of collision energy to the well depth of interaction potential tends to infinity, ie at the high field limit. Blanc's law is a valid approximation between these two extremes when the ratios of the mean collision energies for the two Born-Oppenheimer states is close to unity, implying that the application is only justified for intermediate field

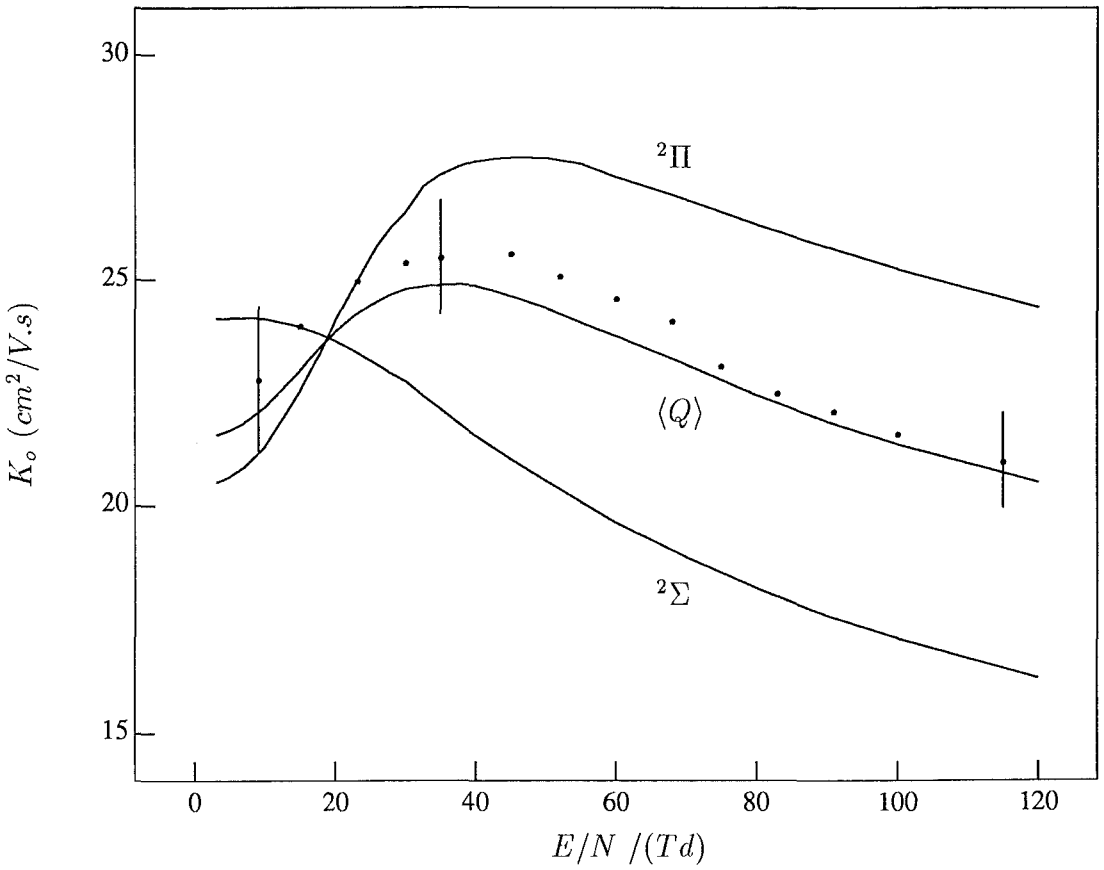

Figure 5.3: The experimental and calculated mobilities of C^+ in helium. The points and the associated error bars are the results of Twiddy *et al.* [86]. The solid curves show the results of the three temperature calculations using the $^2\Pi$ and $^2\Sigma$ interaction potentials, and the "averaged transport cross section" mobility is labelled $\langle Q \rangle$.

strength when the mobilities are similar. This is true of many of the systems studied to date, and it has been suggested that [79] this approximation is valid to within 10%. However, the three temperature calculations for the C^+ ion in helium at $\simeq$ 60 Td have revealed that the effective parallel ion temperature, $T_{||}$, was 2260 K and 4605 K for the $^2\Sigma$ (^2P) and the $^2\Pi$ (^2P) molecular ion states respectively, while the perpendicular temperature, $T_\perp$, was 1421 K and 2268 K for the $^2\Sigma$ (^2P) and the $^2\Pi$ (^2P) molecular ion states respectively. It is clear that Blanc's law is only approximate in such instances.

Thus the published work [79] of the mobility of C^+ in helium has been revised by using the correct classical expression for the open shell atomic ion atom systems and removing the approximations inherent in the application of Blanc's law.

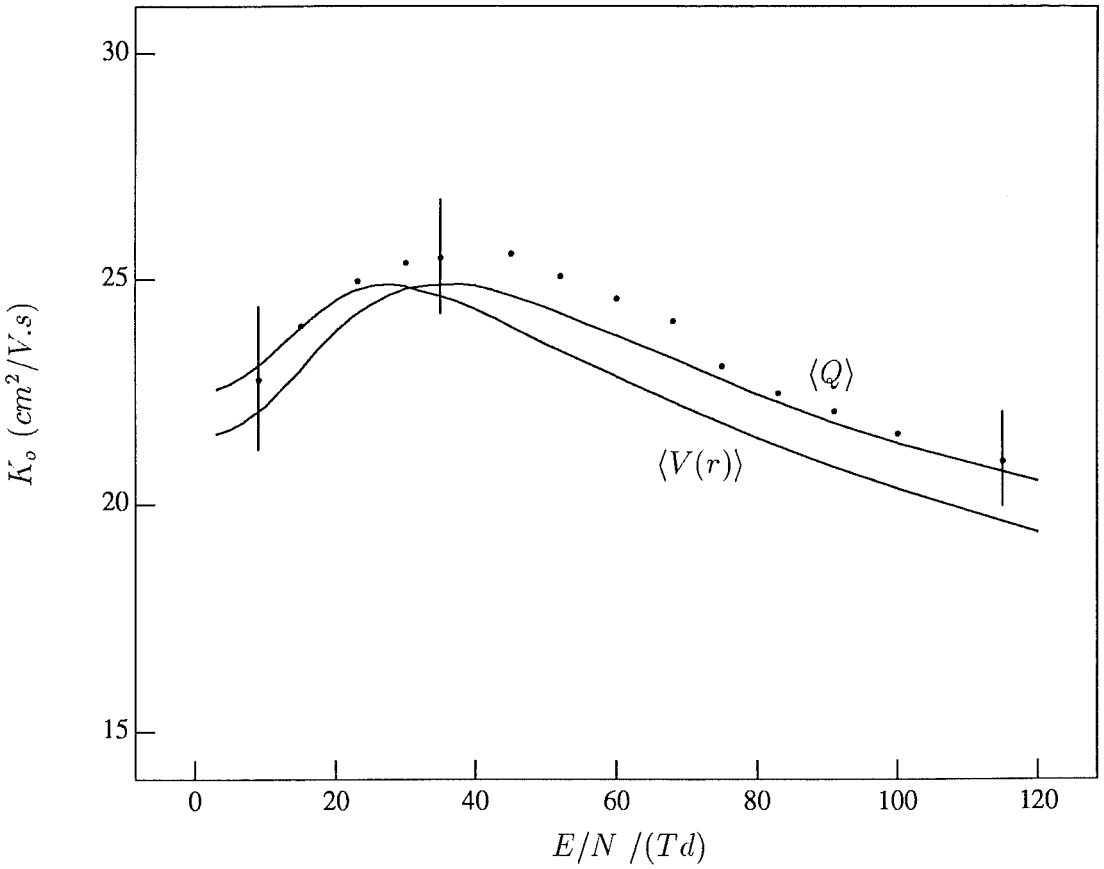

Figure 5.4: The experimental and calculated mobilities of C^+ (^2P) in helium. The points and the associated error bars are the results of Twiddy *et al.* [86]. The solid curves show the results of the three temperature calculations using the "averaged interaction potentials" labelled $\langle V(r) \rangle$, and the "averaged transport cross section" mobility labelled $\langle Q \rangle$.

Figure 5.3 displays the reduced mobility calculated using the interaction potentials of the $^2\Pi$ and $^2\Sigma$ Born-Oppenheimer states. The mobility derived by averaging the "transport cross sections" over the statistical weights according to the degeneracies of the Born-Oppenheimer states is also shown. The experimental points that have been plotted have been reported by Twiddy *et al.* [86]. Figure 5.4 displays the averaged curve displayed in figure 5.3 and compares this with both the experimental results of Twiddy *et al.* [86], and the mobility that results from using an interaction potential that is averaged over the statistical weights according to the degeneracies of the Born-Oppenheimer states. The two curves in figure 5.4 represent two limiting cases. These cases are, the mobility calculated assuming that the transition probability for transitions between the adiabatic Born-Oppenheimer

states is zero, for the "averaged transport cross sections", and unity, for the "averaged interaction potentials". Several points need to be made in relation to these calculations. In calculating the "averaged transport cross section" mobilities it has been assumed that each individual collision takes place on a single random adiabatic Born-Oppenheimer surface. This methodology is significantly more accurate than the previous approach using Blanc's law [79], particularly if the mobility of the different states is substantially different. These calculations have been achieved by averaging the cross sections defined in equation 4.31 over the relative degeneracies of the molecular ion states from which they were derived.

When calculating the "averaged interaction potential" mobility it is assumed that the frequency of transitions between the possible Born-Oppenheimer states is great enough that the ions act according to an effective interaction potential that is obtained by averaging over the adiabatic interaction potentials with the appropriate statistical weights. Thus it is possible to calculate transport coefficients at two extremes. This limitation is a direct result of using quantum mechanics to calculate the interaction potentials and classical mechanics to calculate the transport cross sections. The problem can only be resolved with the application of quantum calculations of the transport cross sections. Unfortunately, such calculations are approximate and complex, and were not attempted because of time restraints.

Returning to consideration of figure 5.3 and 5.4, it is apparent that the mobility curves calculated using the adiabatic interaction potentials don't reproduce the experimental data within the mutual uncertainties. The mobility curve derived from using the average of the transport cross sections does reproduce the experimental results of Twiddy *et al.* [86] within the experimental uncertainty. Thus it seems certain that more than one adiabatic interaction potential is important in determining the gas phase ion mobilities of open shell atomic ions, because a mobility calculated from a single adiabatic interaction potential fails to reproduce the experimental mobility within the mutual uncertainties of theory and experiment. Twiddy *et al.* have quoted experimental errors of 7% below 30 Td, and 5% above 30 Td. However, from figure 5.4, where the results of the "averaged interaction potential" mobility have been combined with some of the results of figure 5.3 it is evident that the two limiting classical cases for the mobility are within the mutual uncertainties of theory and experiment (the accuracy of the three temperature calculations using

program MOBDIF [58] is conservatively 1%). Thus further conclusions regarding the nature of the interactions of the open shell atomic ions-atom collision partners is not possible with this system.

The effect of the spin-orbit interaction on reactivity of C^+ ions in helium has been investigated by Twiddy *et al.* [86], who have found that they could not detect any difference in reactivity from the decay plots of the combined C^+ $^2P_{1/2}$ and $^2P_{3/2}$ signal. The spin-orbit coupling results in two states separated by 8 meV, which is of the same order as thermal energies. Toshima [94] has calculated the rate coefficient for the excitation ($^2P_{1/2} \rightarrow ^2P_{3/2}$) of C^+ ions at low temperature (150 K), to find that this process is rapid and increases with increasing temperature. Thus the observed linear decay of the C^+ (^2P) ions would happen even if the two spin orbit states have significantly different reactivities.

Twiddy *et al.* have also reported the presence of metastable C^+ ions which they assigned to the C^{+*} ^4P ion. The metastable ion had a mobility that was significantly lower than the ground state ion, and they have commented that this implies a substantially different interaction potential is responsible for these observations. This prediction is certainly supported in the calculations reported here, with the exceptionally large well depth of the $^4\Sigma$ molecular state of 1.271 eV. This is most probably the molecular state that Young and Coggiola [91] have observed using their discharge source and high resolution mass spectroscopy. Several vibrational states exist in this species and the first five are displayed in figure 5.2 which were calculated by assuming an harmonic oscillator model ($\omega_e = 1276\ cm^{-1}$) of the diatomic ion.

The same procedure was adopted for the study of the two states that correlate with C^{+*} ^4P + He ^1S, the $^4\Sigma$ and $^4\Pi$ molecular states. The results have been plotted in figure 5.5. While the mobility curves of the $^4\Sigma$ and $^4\Pi$ states bound the experimental results of Twiddy *et al.* [86], both the "averaged interaction potential" and "averaged transport cross section" results for the calculation of the mobility are beyond the mutual uncertainties of the theoretical and experimental results. The much greater mobilities of the "averaged interaction potential" results are anticipated due to the effective interaction potential having a smaller well depth and later a repulsive wall. The difference between the results of Blanc's law [79] and those of the "averaged transport cross sections" illustrate the differences due to the approximations inherent in Blanc's law. Previous results for the calculation of the

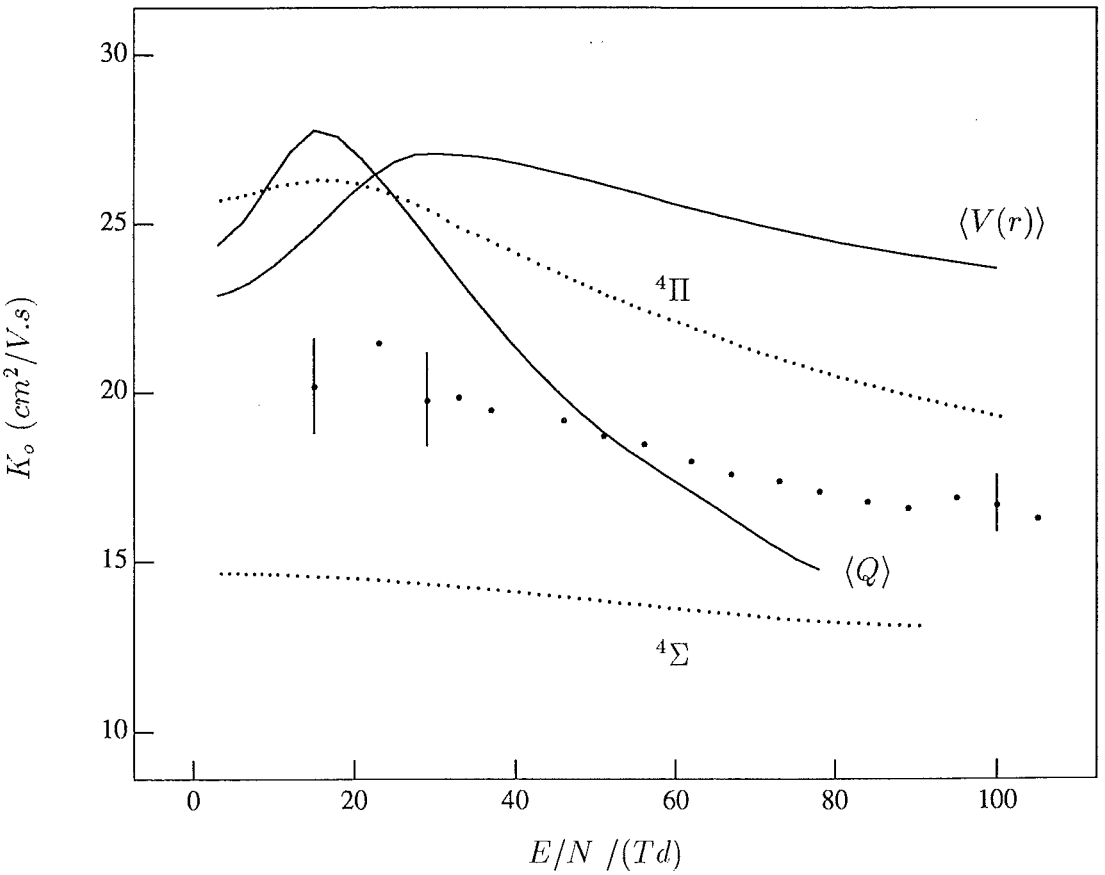

Figure 5.5: The experimental and calculated mobilities of C^{+*} (^4P) in helium. The points and the associated error bars are the results of Twiddy *et al.* [86]. The solid curves show the results of the three temperature calculations using the "averaged interaction potentials" labelled $\langle V(r)\rangle$, and the "averaged transport cross section" mobility labelled $\langle Q\rangle$. The mobilities calculated for the two molecular states are labelled and plotted as dotted lines.

mobility of the metastable C^{+*} ^4P ion using Blanc's law have exhibited excellent correspondence with experiment [79]. This correspondence on reflection appears to be an artifact of these approximations. The two limiting classical approximations fail to give reasonable correspondence with experiment most probably because of the extremely large differences between the interaction potentials of the two molecular states that result with the C^{+*} ^4P ion. Certainly the differences in energy between the two interaction potentials for r less than about 2 Å, far exceeds the possible translation energy of the ions in the range of field strength studied. An accurate theoretical treatment of the C^{+*} ^4P ion requires a quantum calculation of the transport cross sections. However it is likely that the very deep well of the C^+ $^4\Sigma$ ion molecular state is responsible for the significantly lower mobility of the

metastable ion that Twiddy *et al.* [86] have reported. The results reported here do not contradict the assignment of the ^4P state to the metastable ion that Twiddy *et al.* have observed.

The surprising depth of the well of the $^4\Sigma$ C^{+*}—He molecular ion has led to the proposal of a selected ion flow tube investigation to see if the metastable ion can be produced and injected into the flow tube for kinetic studies.

5.3.1.3 Conclusions

MP4SDQ/6-311+G(3df,3pd) interaction potentials have been reported for the $^2\Pi$, $^2\Sigma$, and $^4\Sigma$, $^4\Pi$ states of the molecular ions C^+—He. These interaction potentials have been used to calculate the mobility of the C^+ ^2P and C^{+*} ^4P ions respectively using two classically limiting cases that assume that the transition probability between adiabatic Born-Oppenheimer states is either zero or unity.

The correspondence between experiment and theory for the mobility of the C^+ ^2P ion is excellent. The calculations of the mobilities of either of the two approximations are within the mutual uncertainties of the experimental results. Thus it is not possible to infer which model of the interactions of C^+ ions in the drift tube is most relevant. The calculations for the C^{+*} ^4P ions resulted in mobilities that are not in agreement with experiment for either approximation. It was inferred that neither classical model of ion interactions on which the approximations is based were relevant to the mobility of C^{+*} ^4P ions in helium. The significantly lower mobility of the metastable C^{+*} ion is suggested to have resulted from the very deep well of the C^{+*}—He $^4\Sigma$ interaction potential, supporting the assignment of Twiddy *et al.* [86] of the metastable C^{+*} ^4P ion.

5.3.2 The Mobility of N^+ (^3P) in Helium

The mobility of N^+, like C^+, must be accurately known in order to make experimental determinations of the ion-molecule reaction rate constants of N^+ from flow tube and drift tube measurements. Several reactions of N^+ (^3P) ions are of astrophysical interest. Many authors have reported the mobility of N^+ (^3P) in helium [95, 96, 97, 98, 99]. With the exception of a single set of results by Fhadil *et al.* [99] extending to 145 Td, the literature measurements all terminate around 60 Td.

The values of the reported reduced mobilities at 60 Td range from 16—24 $cm^2/V.s$. Thus the published data sets exhibit wide variation in measurements, preventing a definitive judgement of the actual mobility of the N^+—He system. The mobility of this system has been remeasured to resolve the existing ambiguities and to give an accurate data set for comparison with calculations.

5.3.2.1 Experimental Mobilities and Rate Constants of N^+ (^3P)

The N^+ ions were produced in the drift tube by thermal energy transfer of He^+ to N_2, giving the excited state of N_2^+ ($C,^2\Sigma_u^+$), which can either radiate to the ground state N_2^+ ($X,^2\Sigma_g^+$), or predissociate. These reactions are summarised below.

$$He^+N_2(X,^1\Sigma_g^-) \rightarrow He(^1S) + N_2^+(C,^2\Sigma_u^+) \quad (5.2)$$

$$N_2^+(C,^2\Sigma_u^+) \rightarrow N_2^+(X,^2\Sigma_g^+) \quad (5.3)$$

$$N_2^+(C,^2\Sigma_u^+) \rightarrow N^+(^3P) + N(^4S) \quad (5.4)$$

The dissociative charge transfer reaction took place in 1:99 N_2:He mixture, with a total drift tube pressure of 0.4 *Torr* and a regulated temperature of 298 K. The determination of the drift velocity of N^+ ion for any selected value of E/N involved measurement of the N^+ ion arrival time distribution for seven or eight values of drift distance. The drift velocity and the He^+ ion removal rate via charge transfer to N_2 are variable parameters used to fit the experimental arrival time distribution functions to the model calculations [100]. The mobility of the N^+ ion was calculated from the experimental drift velocities obtained by fitting the ion arrival time distributions modelled on the geometry of the drift tube, the physical conditions selected for the experiment, and the ion/neutral kinetics of the N_2—He system [100, 101]. The depletion rate of N^+ by reaction with N_2 was taken to be $1.8\times10^{-10}cm^2s^{-1}$ [102]. The He^+ ion mobility was measured prior to any experiments undertaken, and it was found to be within 2% of the published values listed in the compilations of Ellis *et al.* [37].

The results of the arrival time modelling for the measurements of the range of E/N 35—140 Td are shown in table 5.3. The mobilities quoted are reduced to standard temperature and pressure. These mobility values are plotted in figure 5.7 along with the results of Fahey *et al.* [95]. The experimental error bars associated with the data set of Fahey *et al.* are those quoted in that study. The results of this

Table 5.3: The mobility measurements of N^+ in helium.

E/N (Td)	35.0	40.0	45.0	50.0	55.0	60.0
K_0 $(cm^2V^{-1}s^{-1})$	21.1	21.2	21.4	21.6	21.3	21.3
E/N (Td)	65.0	70.0	75.0	80.0	85.0	90.0
K_0 $(cm^2V^{-1}s^{-1})$	20.7	20.7	20.0	19.8	19.7	19.6
E/N (Td)	95.5	100.0	105.0	110.0	115.0	120.0
K_0 $(cm^2V^{-1}s^{-1})$	19.1	18.8	18.5	18.4	18.3	18.2
E/N (Td)	125.0	130.0	135.0	140.0	—	—
K_0 $(cm^2V^{-1}s^{-1})$	18.0	17.9	17.9	17.6	—	—

study lie within the respective mutual uncertainties of the two data sets and are almost superimposable for the $E/N \leq 60$ Td. It is evident from the figure that the mobility of the N^+ varies smoothly as a function of E/N.

5.3.2.2 The Interaction Potentials of N^+ in Helium

The adiabatic interaction potentials for the N^+—He ($^3\Sigma$ and $^3\Pi$) molecular ion states correlating with the N^+ (^3P) ion and the He (^1S) atomic ground states were calculated at the MP4SDQ/6-311+G(3df,3pd) levels of theory, excluding core contributions to correlation energy and accounting for basis set superposition error (BSSE) by counterpoise. The results of these calculations are presented in tables 5.4 and 5.5, and compared in figure 5.6. The N^+—He ($^3\Sigma$) molecular ion state exhibits a deep well, $D_e = 0.194$ eV, at $r_e = 1.596$ Å at the MP4SDQ/6-311+G(3df,3pd) level of theory, and $D_e = 0.174$ eV, at $r_e = 1.611$ Å at the MP4SDQ/6-311+G(3df,3pd) + BSSE levels of theory. The depth of this well suggests that collisional stabilisation of the ion may be expected at high pressures and low temperatures, and this appears to be the case. Smith and Adams [103] have observed an m/z 18 signal when N_2 is introduced into the helium buffer flow in the Birmingham selected ion flow drift tube (SIFDT) at 80 K. In contrast the N^+—He ($^3\Pi$) interaction potential exhibits a shallow minimum, $D_e = 0.022$ eV, $r_e = 2.715$ Å, at the MP4SDQ/6-311+G(3df,3pd) + BSSE level of theory.

Previous theoretical investigations of the N^+—He species include SCF calculations by Cooper and Wilson [88] and Liebman and Allen [104]. More recently, Koch *et al.* [105] have reported a thermodynamic study of the N^+—He ($^3\Sigma$) species at

Table 5.4: The MP4SDQ/6-311+G(3df,3pd) energies for N^+ $^3\Sigma$ including the helium basis set, He ($^1\Sigma$) including the N basis set and N^+—He ($^3\Sigma$) as a function of internuclear separation.

r^a	E^b		
	($^3\Sigma$)MP4SDQ N^+ (He basis)	($^1\Sigma$)MP4SDQ He (N basis)	($^3\Sigma$)MP4SDQ N^+—He
0.875	–53.97860	–2.89945	–56.76625
0.9375	–53.97842	–2.89941	–56.80451
1.00	–53.97825	–2.89937	–56.83015
1.125	–53.97796	–2.89930	–56.85966
1.25	–53.97777	–2.89923	–56.87375
1.3125	–53.97770	–2.89920	–56.87763
1.375	–53.97764	–2.89917	–56.88017
1.50	–53.97754	–2.89914	–56.88259
1.625	–53.97744	–2.89911	–56.88296
1.75	–53.97735	–2.89909	–56.88242
2.00	–53.97720	–2.89906	–56.88072
2.125	–53.97714	–2.89905	–56.87992
2.50	–53.97703	–2.89902	–56.87812
3.00	–53.97700	–2.89898	–56.87693
3.50	–53.97700	–2.89896	–56.87644
4.00	–53.97699	–2.89894	–56.87618
5.00	–53.97697	–2.89891	–56.87597
6.00	–53.97697	–2.89890	–56.87591
∞	—	—	–56.87587

[a] All distances are in Angströms
[b] All energies are in hartrees

the MP4SDTQ/6-311G(2df,2pd)//MP2/6-31G(d,p) level of theory. The dissociation energy of the calculation of Koch *et al.* (0.191 eV) is practically identical to that reported here, but this is lowered 10.3% to 0.174 eV when correcting for basis set superposition error by counterpoise. However the equilibrium internuclear distances of Koch *et al.* (1.794 Å) is significantly different to the result reported here (1.611 Å), and this is most probably due to the larger basis set used in the present study, as the levels of theory are very similar.

Table 5.5: The MP4SDQ/6-311+G(3df,3pd) energies for the N^+ $^3\Pi$ including the helium basis set, He ($^1\Sigma$) including the N basis set and N^+—He ($^3\Pi$) as a function of internuclear separation.

r^a	E^b		
	($^3\Pi$)MP4SDQ N^+ (He basis)	($^1\Sigma$)MP4SDQ He (N basis)	($^3\Pi$)MP4SDQ N^+—He
1.25	–53.97799	–2.89923	–56.74190
1.50	–53.97772	–2.89914	–56.82614
1.75	–53.97751	–2.89909	–56.85924
2.00	–53.97732	–2.89906	–56.87152
2.25	–53.97720	–2.89904	–56.87564
2.50	–53.97710	–2.89902	–56.87673
2.75	–53.97705	–2.89900	–56.87683
3.00	–53.97702	–2.89898	–56.87669
3.25	–53.97702	–2.89897	–56.87652
3.50	–53.97701	–2.89896	–56.87638
4.00	–53.97700	–2.89894	–56.87617
5.00	–53.97697	–2.89891	–56.87597
6.00	–53.97697	–2.89890	–56.87591
∞	—	—	–56.87587

[a] All distances are in Angströms.
[b] All energies are in hartrees.

5.3.2.3 The Mobility Calculations of N^+ in Helium

The $^3\Sigma$ and $^3\Pi$ interaction potentials detailed in the previous section were used to calculate the mobility using the program `MOBDIF` [58]. Several points must be made in relation to these calculations. Firstly, the three temperature calculations for the $^3\Sigma$ state did not converge in the E/N range 30—60 Td even though the approximations were calculated to the eightieth order. The poor convergence problems associated with a rapid rise in mobility have been attributed to partial ion runaway [40]. The mobilities derived from using the $^3\Sigma$ and $^3\Pi$ interaction potentials have been plotted in figure 5.7, along with the mobility obtained using the Blanc's law approximation. The $^3\Sigma$ mobility curve has been spline fitted through the region of inconvergence, and although interpolation occurs through the rapid rise in mobility, it is real. Note that in regard to the Blanc's law approximation the rapid rise due to the $^3\Sigma$ mobility curve has resulted in a similar although smaller rise at about 40 Td. This feature is not evident in either of the experimental data sets plotted in the

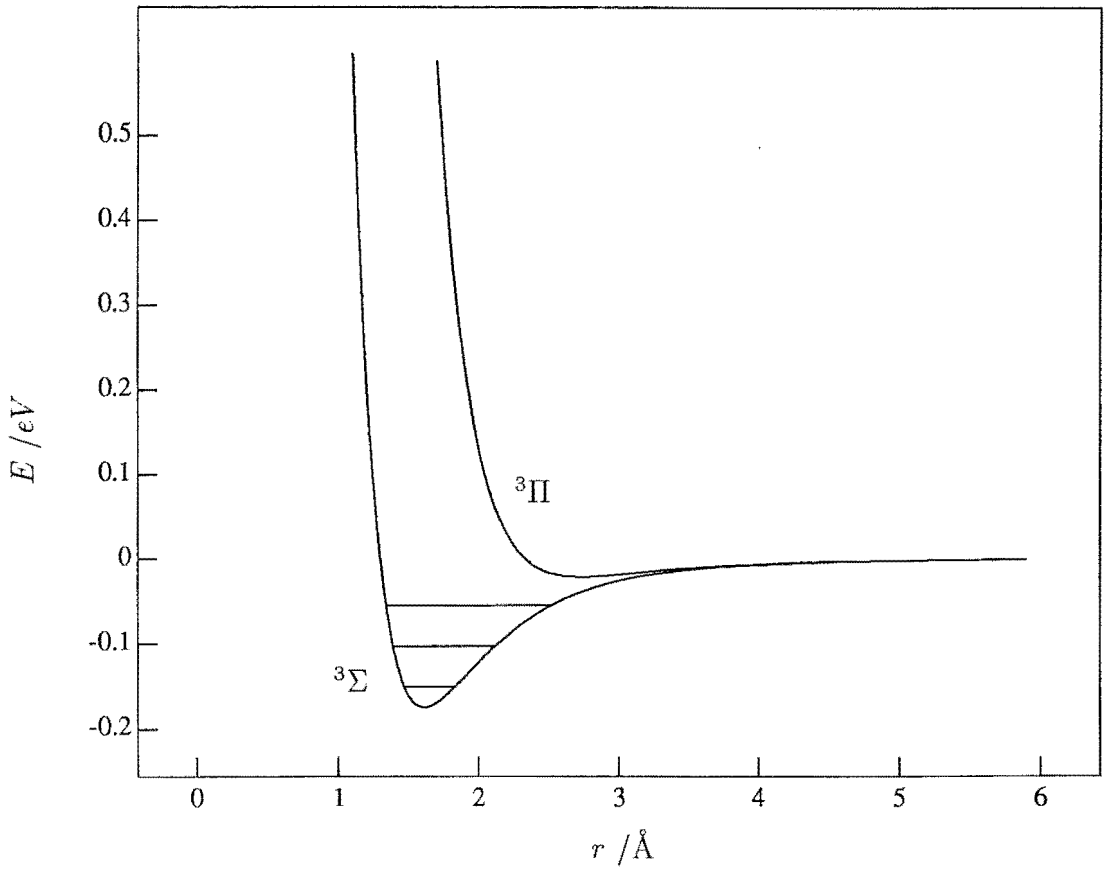

Figure 5.6: The interaction potentials of N^+—He ($^3\Sigma$ and $^3\Pi$) calculated at the MP4SDQ/6-311G+(3df,3pd) + BSSE level of theory. The interaction potentials are labelled in the figure. The three vibrational levels have been calculated assuming an harmonic oscillator ($\omega_e = 383\ cm^{-1}$).

figure. Further comparison of figure 5.7 reveals that neither $^3\Sigma$ or $^3\Pi$ interaction potentials can adequately describe the observed ion mobilities of N^+ in helium.

The two classically limiting cases that were outlined in section 5.3.1.2, namely "averaged interaction potential" and the "averaged transport cross sections", were used to calculate mobility of N^+ in helium. These have been plotted in figure 5.8. At low E/N, the classically limiting case that corresponds best with the experimental values is the "averaged transport cross section" case. This limiting case assumes that the transition probability between adiabatic Born-Oppenheimer states is zero. The results are within the mutual uncertainties of the experimental data set of Fahey *et al.* [95] in this region. This suggests that the "averaged transport cross sections" are a reasonable model of the ion-neutral collision event in this energy range. The results of the "averaged interaction potential" are not within the mutual

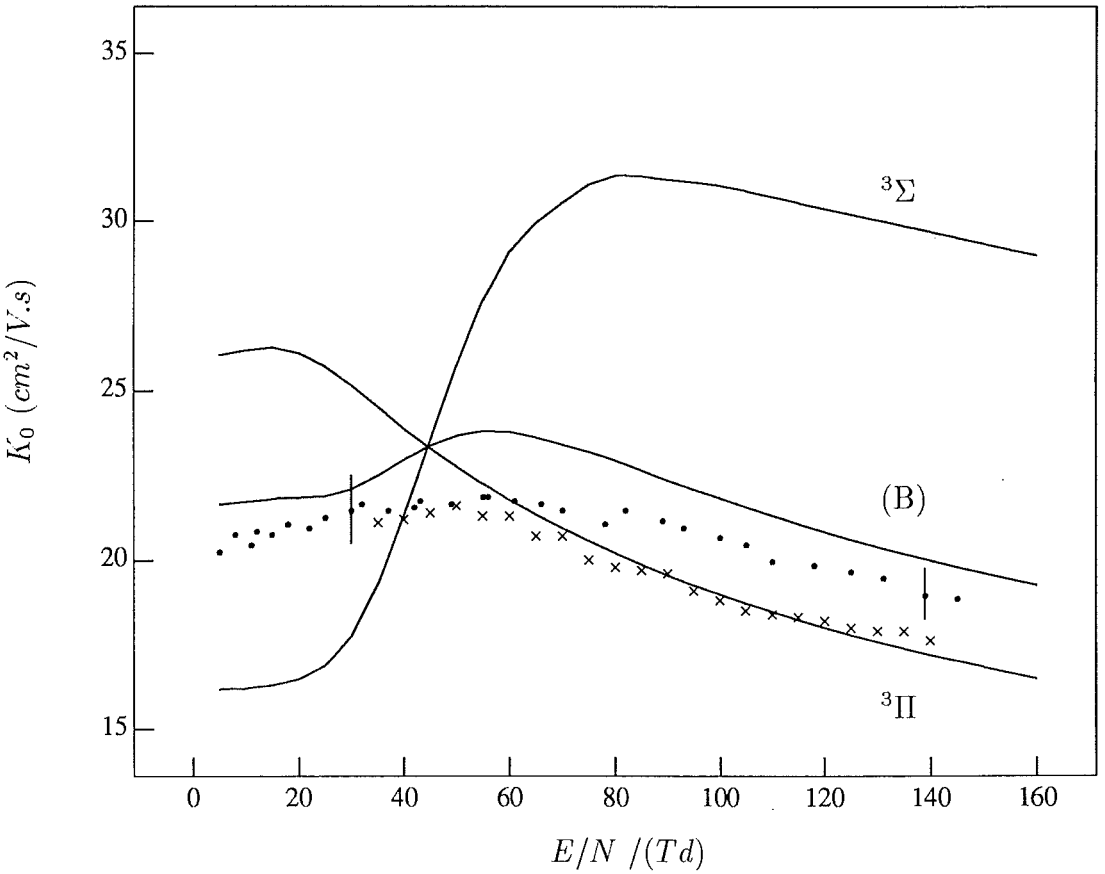

Figure 5.7: The experimental and calculated mobilities of N^+ in helium. The points and the associated error bars are the results of Fahey *et al.* [95]. The crosses are the measured experimental results on the Canterbury drift tube. The solid curves show the results of the three temperature calculations using the $^3\Pi$ and $^3\Sigma$ interaction potentials, and the approximation obtained using Blanc's law (B).

uncertainties of the experimental data set in this region. However, at large E/N, the results of the "averaged interaction potential" mobilities are within the experimental uncertainties of the experimental data sets and are in slightly better agreement with the experimental data set measured on the Canterbury drift tube. This suggests that the averaged interaction potential model is a reasonable interpretation of the ion-neutral collision event. That is, at high collision energies, transitions between the adiabatic Born-Oppenheimer states are frequent, and an effective interaction applies. These conclusions are consistent with the calculations of Toshima [94] for transitions between spin-orbit states of the open shell ions.

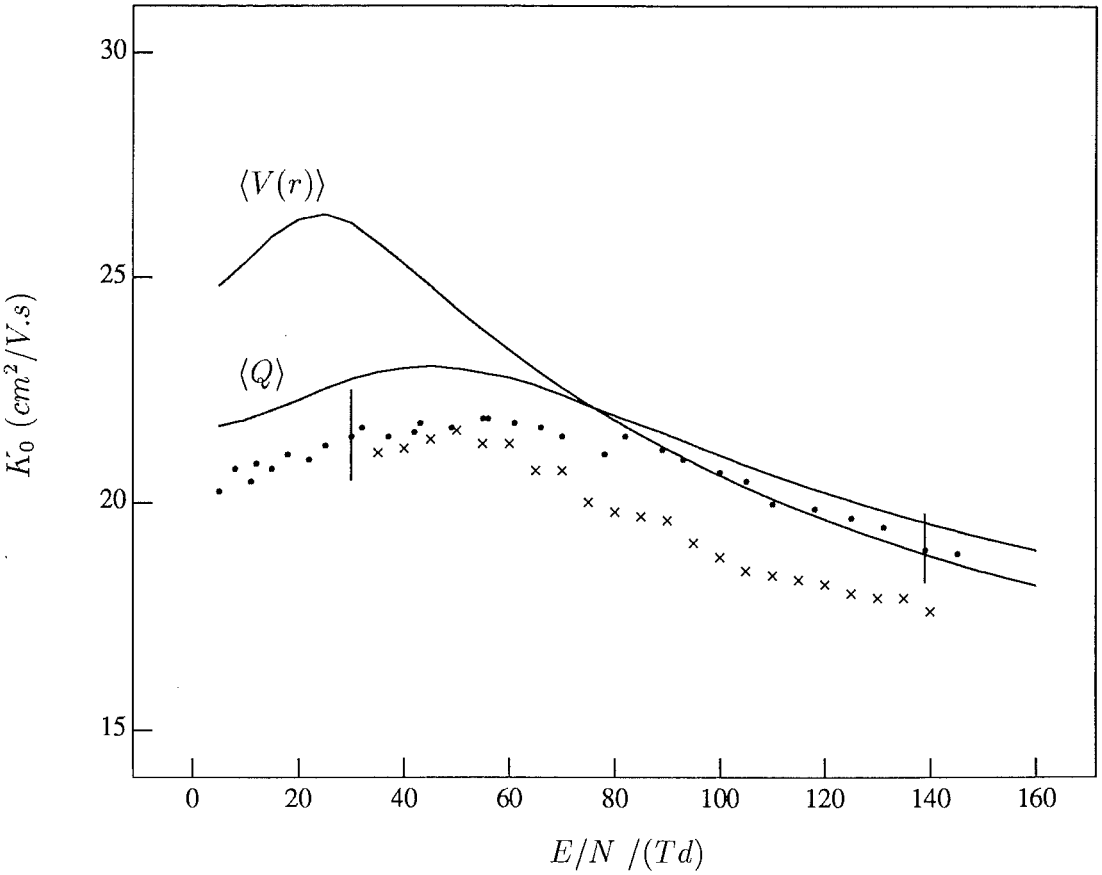

Figure 5.8: The experimental and calculated mobilities of N^+ in helium. The points and the associated error bars are the results of Fahey *et al.* [95]. The crosses are the measured experimental results on the Canterbury drift tube. The solid curves show the results of the three temperature calculations using the "averaged interaction potentials" labelled $\langle V(r)\rangle$, and the "averaged transport cross section" mobility labelled $\langle Q\rangle$.

5.3.2.4 Conclusions

MP4SDQ/6-311+G(3df,3pd) interaction potential have been reported for the molecular ion states of N^+—He $^3\Sigma$ and $^3\Pi$. These interaction potentials were used to calculate the mobility of ^3P ions in helium using three-temperature theory and two classically limiting cases that assume that the transition probability between adiabatic Born-Oppenheimer state is either zero or unity.

The best correspondence between theory and experiment at low E/N occurred when the transition probability between adiabatic states was assumed to be zero. At high E/N both classically limiting cases were within the mutual uncertainties of the theoretical and experimental data sets, however the best agreement was observed

when the transition probability between adiabatic states was assumed to be unity.

5.3.3 The Mobility of O^+ (^4S) and O^{+*} (^2P) in Helium

Simpson *et al.* [81] have published the results of *ab initio* calculations of the mobility of O^+ and O^{+*} in helium using a similar method to that used in this thesis. The results of these calculations were in excellent agreement with reported experimental results. The metastable oxygen cation O^{+*} has been observed both in drift tube studies [106, 107, 108] and in the earth's ionosphere [109, 110] from the analysis of Atmospheric Explorer satellite data. Simpson *et al.* [81] concluded on the basis of their theoretical calculations that the metastable ion was incorrectly assigned to the O^{+*} (^2D) electronic state. Their assignment was made on the basis of comparison of mobility curves calculated from the single interaction potential with lowest relative energy. Given the excellent correspondence between the experimental mobilities of the metastable ion and the theoretical results calculated using the O^{+*}—He $^2\Pi$ (^2P) interaction potential Simpson *et al.* concluded the identity of the metastable ion to be O^{+*} (^2P). This conclusion is supported by the proposal [111] of a curve crossing between the $^2\Pi$ (^2D) and the $^4\Sigma$ (^4S) interaction potential, that could quench the O^{+*} (^2D) to the ground state in experiments that use helium as a bath gas.

For a complete description of this work the reader is directed to the paper published by Simpson *et al.* [81] on the mobility of the O^+ ions in helium or to the thesis of Simpson [112] for a more general treatment. The following section seeks to validate and support the mobility calculations for the metastable ion O^{+*} (^2P) ions in helium of Simpson *et al.* [81] without unnecessary repetition.

5.3.3.1 The Mobility Calculations of O^+ (^4S) and O^{+*} (^2P) in Helium

The results of Simpson *et al.* for the calculation of the ground state O^+ (^4S) ion in helium were in excellent agreement with the observed experimental results [108, 113] over the entire range of field strength studied. Because the orbital angular momenta of the ground state open shell ion is zero there is only one interaction potential to consider between the collision partners, thus simplifying the classical treatment. The excellent correspondence between the experimental results and mobility calculations justifies the theoretical approach for this system.

The mobility calculations for the metastable O^{+*} ions have been repeated using the two classically limiting cases outlined in the previous sections. The Valence Bond (VB) interaction potentials for the $^2\Pi$ (^2P) [81] and $^2\Sigma$ (^2P) [112] molecular ions states were used along with the three temperature program `MOBDIF` [58] to calculate the mobility of O^{+*} (^2P) in helium to an accuracy of at least 1%. The results of these calculations are plotted in figure 5.9 along with the experimental measurements of Rowe *et al.* [107] and Fhadil *et al.* [108]. The experimental uncertainties quoted by Rowe *et al.* [107] (7%) were substantially lower than those quoted by Fhadil *et al.* [108] (4% decreasing to 1% at high field strength).

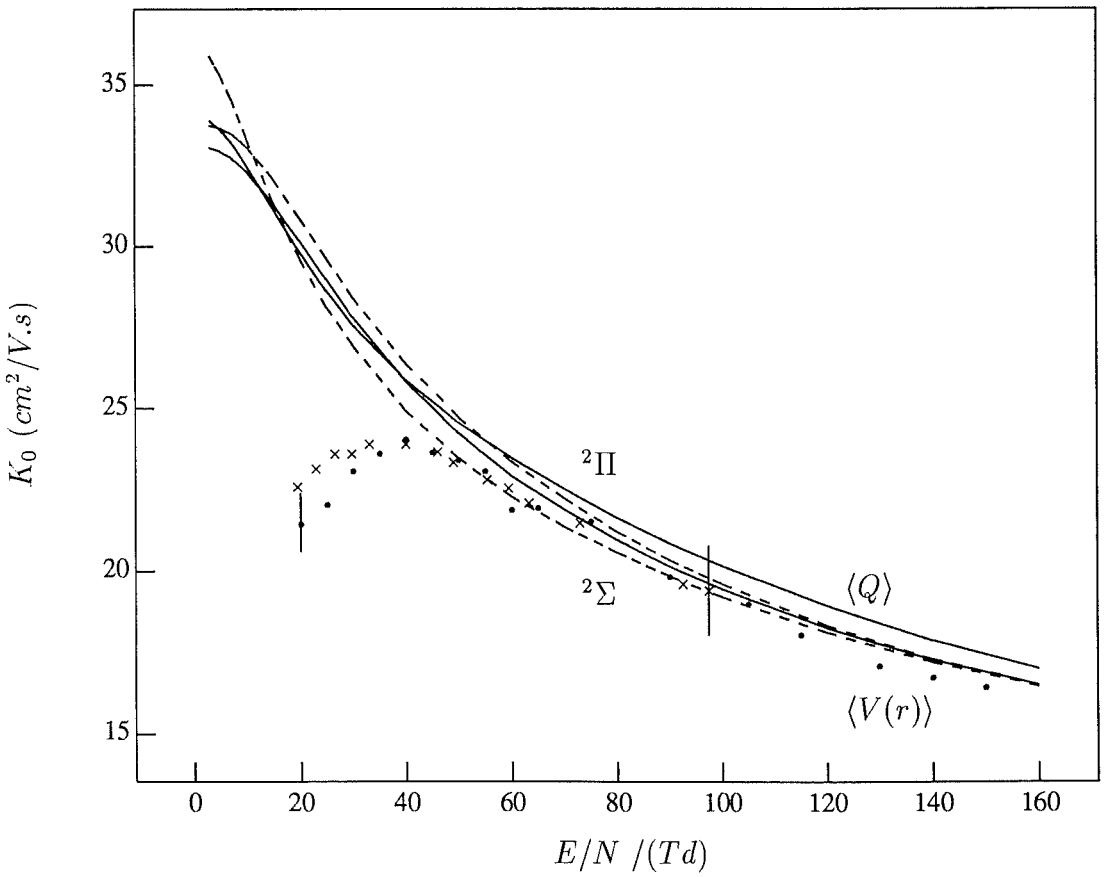

Figure 5.9: The experimental and calculated mobilities of O^+ (^2P) in helium. The bullets and the associated error bars represent the results of Fhadil *et al.* [108]. The crosses and the associated error bars represent the results of Rowe *et al.* [107]. The solid curves show the results of the three temperature calculations using the "averaged interaction potentials" labelled $\langle V(r) \rangle$, and the "averaged transport cross section" mobility labelled $\langle Q \rangle$. The dashed lines show the results of the three temperature calculations using the interaction potential of the given molecular ion state which has been labelled.

Several points need to be made in relation to these calculations. Firstly, the

VB calculations of the O^{+*} $^2\Pi$ (^2P) and O^{+*} $^2\Sigma$ (^2P) molecular ion states resulted in interaction potentials that were much more similar than equivalent interaction potentials that have been studied for other systems. Both interaction potentials exhibited weakly bound ion-induced dipole wells. The VB O^{+*} $^2\Pi$ (^2P) interaction potential reported by Simpson [81] had a $D_e = 0.016\ eV$, at $r_e = 2.512$ Å. The VB O^{+*} $^2\Sigma$ (^2P) interaction potential reported by Simpson [112] had a $D_e = 0.002\ eV$, at $r_e = 3.292$ Å. The mobilities derived from these calculations are also very similar. They are all within the mutual uncertainties of the theoretical calculations over the entire range of field strength plotted. Excellent correspondence exists between all the theoretical calculations and the experimental measurements for $E/N > 60\ Td$. For lower values of field strength the calculated mobilities depart substantially from the calculated values. Simpson *et al.* [81] addressed this discrepancy by increasing the well depth of the O^{+*} $^2\Pi$ (^2P) interaction potential by 0.02 eV. Similar adjustments to any of the interaction potentials considered here would result in equal correspondence. This adjustment to the interaction potential resulted in excellent correspondence between the experimental measurements and the theoretical calculations over the entire range of field strength studied. It is unlikely that such simple changes to the interaction potential could achieve such excellent correspondence for the O^{+*} (^2D) metastable ion [81]. These results support the conclusion that the metastable ion observed in laboratory experiments that use helium as a bath gas should be assigned to the O^{+*} (^2P) state. Thus the interpretation of such experimental data should recognise the possibility of more than one interaction potential contributing to the chemical properties of this ion. Finally, because of the similarity of the calculated mobility data it has not been possible to differentiate which of the two classically limiting cases is the most appropriate model of the ion-neutral interaction in this system.

5.3.4 The Mobility of Si^+ (^2P) and Si^{+*} (^4P) in Helium

Silicon and other metals are produced in the earth ionosphere by the ablation of meteors. These metals (M) can then be ionised by charged transfer with the existing ions to create M^+ ions. The ions have repeatedly been observed by rocket-bourne mass spectrometers [114]. It has also been proposed [115] that ionic species of silicon could be involved in the formation of interstellar SiO, one of the first molecular

species observed in the interstellar medium.

In order to elucidate the observations of the chemistry of ionic silicon in the earth's ionosphere and its possibilities in the interstellar medium, Fahey *et al.* [116] have performed drift tube studies of the reaction of a range of ionic silicon species. In order to analyse the kinetics of these systems, the mobility of Si^+ in helium was measured for what was almost certainly the ground state.

In the next sub-section, a theoretical calculation of the interaction potential of the Si^+—He species is described and then used to calculate the mobility of the Si^+ ion in helium using the two classically limiting cases outlined previously. The experimental and theoretical results are compared and discussed.

5.3.4.1 The Interaction Potentials of Si^+—He

There are two molecular ion states that correlate with the collision partners He $1s^2\ ^1S$ + $Si^+\ ^2P$. These are the $^2\Pi$ and $^2\Sigma$ molecular ion states. As well as the ground electronic states there are two molecular ion states, the $^4\Sigma$ and $^4\Pi$ ion states, that correlate to the metastable collision partners, He ^1S + $Si^+\ ^4P$. The interaction potentials were calculated for the $^2\Pi$, and $^2\Sigma$ and the $^4\Sigma$ and $^4\Pi$ molecular ion states at the MP4SDTQ/6-311+G(3df,3pd) level of theory, excluding core contributions to the correlation energy and including correction for basis set super-position error by counterpoise. The results of these calculations are given in tables 5.6 and 5.7. These interaction potentials have been plotted in figures 5.10 and 5.11, for the doublet and quartet states respectively.

The Si^+—He $^2\Pi$ molecular ion state is attractive with a $D_e = 0.027\ eV$ (r_e = 2.901 Å), which decreases to 0.023 eV ($r_e = 2.921$ Å) when correcting for BSSE by counterpoise. The $^2\Sigma$ molecular ion state has a weak ion-induced dipole minima of $D_e = 0.007\ eV$ at a substantially larger separation of $r_e = 3.862$ Å.

The $^4\Sigma$ molecular ion state of the metastable ion Si^+ (^4P) is much more attractive than either of the doublet interaction potentials relative to the appropriate separated species. The $^4\Sigma$ molecular state has a $D_e = 0.316\ eV$ ($r_e = 1.711$ Å), which decreases to 0.308 eV (r_e = 1.713 Å) when correcting for BSSE by counterpoise. These interaction potentials show relative similarities with the interactions of C^+—He and C^{+*}—He reported here previously. This similarity is noted here and elaborated on further in the section 5.4. The excited metastable ion Si^{+*} (^4P) has been calculated

Table 5.6: MP4SDTQ/6-311+G(3df,3pd) energies for the Si^+—He $^2\Pi$ and $^2\Sigma$ molecular ion states.

r^a	E^b				
	$(^1\Sigma)$MP4SDTQ	$^2\Pi$ MP4SDTQ		$^2\Sigma$ MP4SDTQ	
	He (Si^+)	Si^+ (He)	Si^+—He	Si^+ (He)	Si^+—He
1.50	−2.89921	−288.62838	−291.48044	−288.62869	−291.36992
1.75	−2.89915	−288.62830	−291.50810	—	—
2.00	−2.89911	−288.62825	−291.52017	−288.62836	−291.48543
2.25	−2.89909	−288.62823	−291.52542	−288.62829	—
2.50	−2.89907	−288.62823	−291.52746	−288.62827	−291.51826
2.75	−2.89905	−288.62823	−291.52806	−288.62827	—
3.00	−2.89903	−288.62823	−291.52810	−288.62827	−291.52589
3.25	−2.89902	−288.62822	−291.52794	−288.62825	−291.52689
3.50	−2.89900	−288.62821	−291.52776	−288.62823	−291.52726
3.75	−2.89899	−288.62820	−291.52761	−288.62822	−291.52736
4.00	−2.89898	−288.62819	−291.52749	−288.62820	−291.52736
4.50	−2.89896	−288.62819	−291.52732	−288.62819	—
5.00	−2.89894	−288.62818	−291.52723	−288.62818	−291.52721
5.50	−2.89892	−288.62818	−291.52718	−288.62818	−291.52717
5.75	−2.89892	−288.62818	—	−288.62818	−291.52715
6.00	−2.89891	−288.62818	−291.52714	−288.62818	−291.52714
∞	−2.89899	−288.62818	−291.52708	−288.62818	−291.52708

[a] All distances are in Angströms.
[b] All energies are in hartrees.

to be 40594 cm^{-1} above the ground state Si^+ (^2P). This compares with the value reported by Moore [92] of 44080 cm^{-1}.

5.3.4.2 The Mobility Calculations of Si^+ (^2P) and Si^{+*} (^4P) in Helium

The interaction potentials detailed in the previous section were used to calculate the mobility with the program `MOBDIF` [58] to an accuracy of at least 1%, using the two classically limiting cases outlined previously. The results of these calculations have been compared to the experimental results reported by Fahey *et al.* [116], and plotted in figure 5.12. First, note that both the "averaged transport cross section" mobility, and the "averaged interaction potential mobility" are consistently below the experimental measurements of Fahey *et al.* [116]. The "averaged transport cross section" mobility curve is in best agreement with the results of Fahey *et al.*

Table 5.7: MP4SDTQ/6-311+G(3df,3pd) energies for the $Si^{+\bullet}$—He $^4\Sigma$ and $^4\Pi$ molecular ion states.

r^a	E^b				
	$(^1\Sigma)$MP4SDTQ	$^4\Sigma$ MP4SDTQ		$^4\Pi$ MP4SDTQ	
	He (Si^+)	Si^+ (He)	Si^+—He	Si^+ (He)	Si^+—He
0.75	−2.89957	−288.44358	−290.28786	—	—
1.00	−2.89944	−288.44344	−291.09634	−288.44370	−290.89833
1.125	−2.89936	−288.44339	−291.23438	—	—
1.25	−2.89930	−288.44335	−291.30249	—	—
1.375	−2.88925	−288.44332	−291.33454	—	—
1.50	−2.89921	−288.44330	−291.34828	−288.44348	−291.23109
1.625	−2.89917	−288.44329	−291.35303	—	—
1.75	−2.89915	−288.44327	−291.35363	—	—
1.875	−2.89912	−288.44326	−291.35253	—	—
2.00	−2.89911	−288.44326	−291.35091	−288.44333	−291.31366
2.25	−2.89909	−288.44326	−291.34790	—	—
2.50	−2.89907	−288.44326	−291.34584	−288.44329	−291.33620
2.75	−2.89905	—	—	—	—
3.00	−2.89902	−288.44325	−291.34376	−288.44329	−291.34156
3.25	−2.89902	−288.44325	−291.34326	−288.44328	−291.34222
3.50	−2.89900	—	—	−288.44327	−291.34244
3.75	−2.89899	—	—	—	—
4.00	−2.89898	−288.44324	−291.34257	−288.44325	−291.34244
4.50	−2.89896	−288.44324	−291.34239	−288.44324	−291.34234
5.00	−2.89894	−288.44324	−291.34229	−288.44324	−291.34227
5.50	−2.89892	−288.44323	−291.34224	−288.44323	−291.34222
5.75	−2.89892	−288.44323	−291.34222	—	—
6.00	−2.89891	−288.44323	−291.34220	−288.44323	−291.34219
∞	−2.89899	−288.44323	−291.34213	−288.44323	−291.34213

[a] All distances are in Angströms.
[b] All energies are in hartrees.

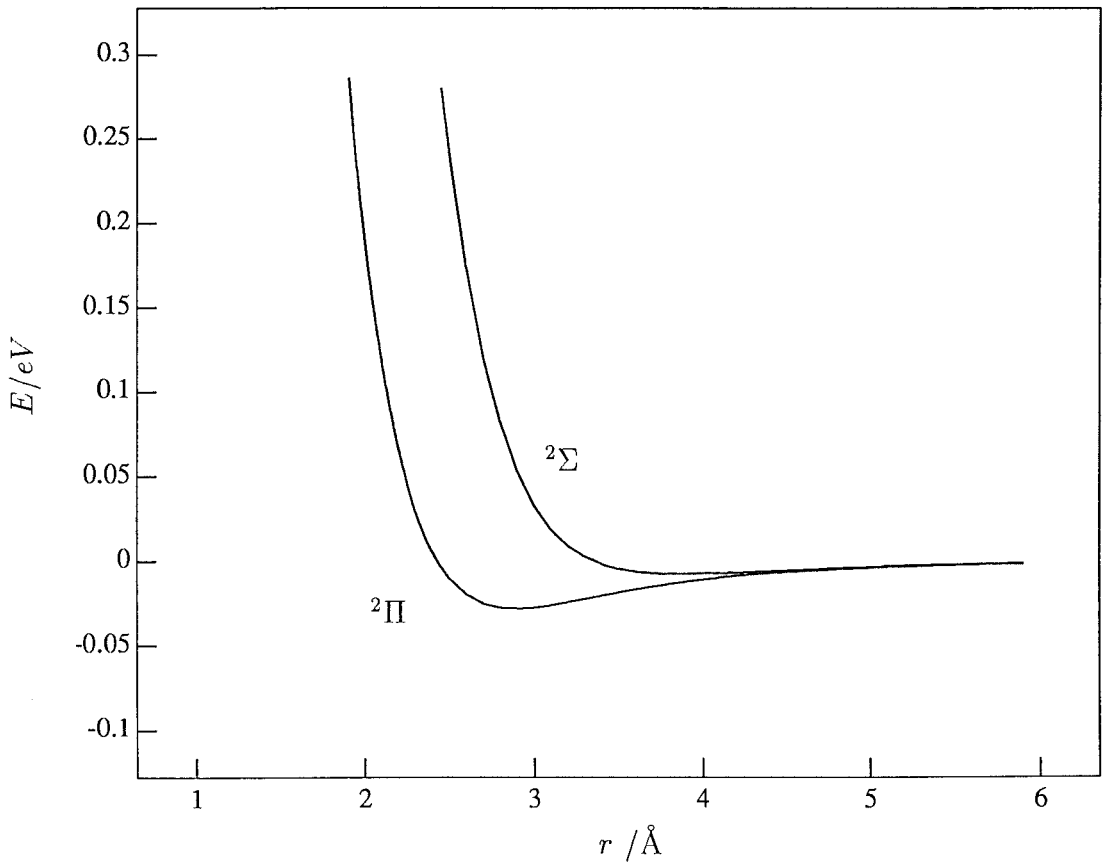

Figure 5.10: The interaction potentials of Si^+—He ($^2\Pi$ and $^2\Sigma$) calculated at the MP4SDTQ/6-311G+(3df,3pd) level of theory. The interaction potentials are labelled in the figure.

[116], although the agreement is only inside the mutual uncertainties of the theoretical (≈1%) and experimental (5%) uncertainties. Agreement between the absolute experimental and theoretical values for the "averaged transport cross sections" has only just been achieved, the two mobility curves behave very similarly over the range of field strength plotted. There is no agreement between the "averaged interaction potential" and the experimental data sets, and it is concluded that the model of rapid transitions between adiabatic Born-Oppenheimer states is not valid for this system. The poor correspondence between the "average interaction potential" limit and experiment means it is doubtful whether this approach could be used in a predictive sense, and suggests that the "averaged transport cross section" approach is more reliable.

A more accurate determination of the experimental mobility for this system would serve two purposes. Firstly it could see if new values would result in better

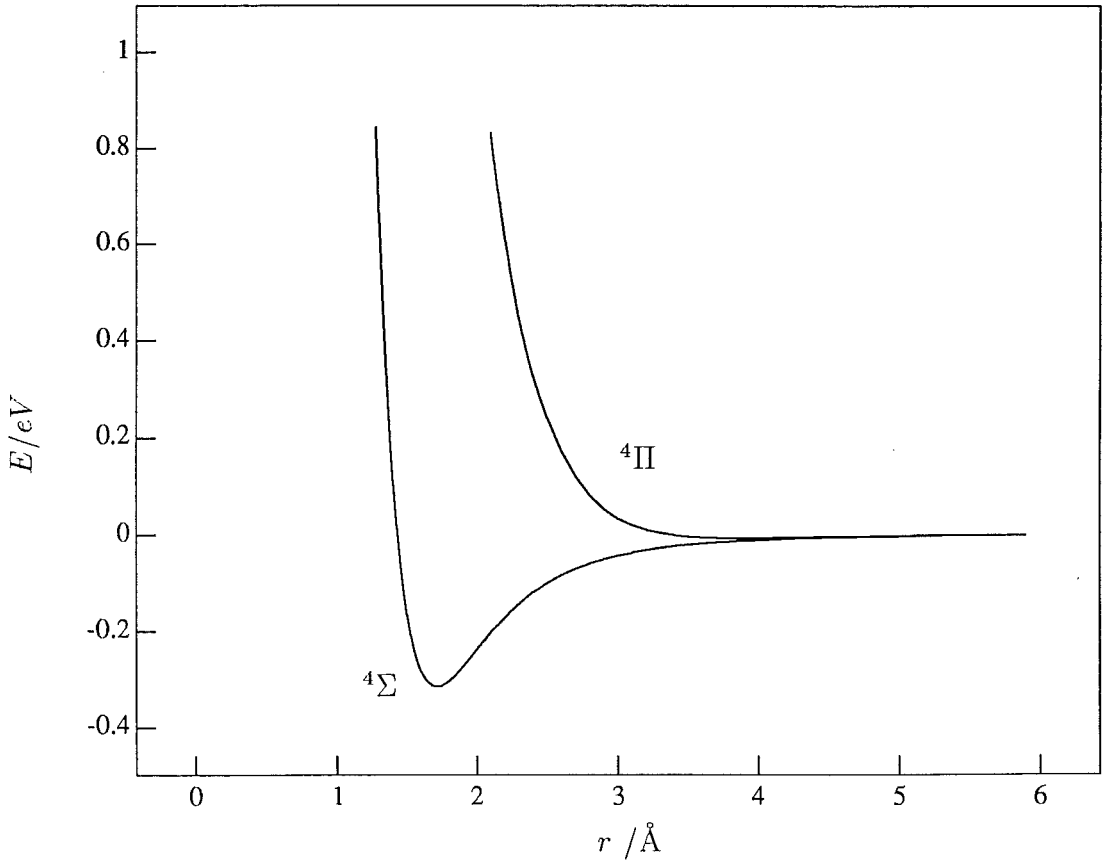

Figure 5.11: The interaction potentials of Si^+—He ($^4\Sigma$ and $^4\Pi$) calculated at the MP4SDTQ/6-311G+(3df,3pd) level of theory. The interaction potentials are labelled in the figure.

agreement with theory, and it could reduce the uncertainty of these measurements leading to a accurate data set with which to test the theory.

Finally, theoretical calculations for the excited state Si^{+*} ^4P have been performed and the results are plotted in figure 5.13. Because the results of the averaged "interaction potential" mobility and the "averaged transport cross section" mobility are substantially different it would be possible to assess which classical model is more appropriate to this system. However, no experiment observation of these ions has been reported.

The chemistry of silicon ions is primarily of importance to those studying reactions related to production of Si^+ ions by ablation of meteors, and it is almost certain that these ions are formed in the Si^+ ^2P ground state.

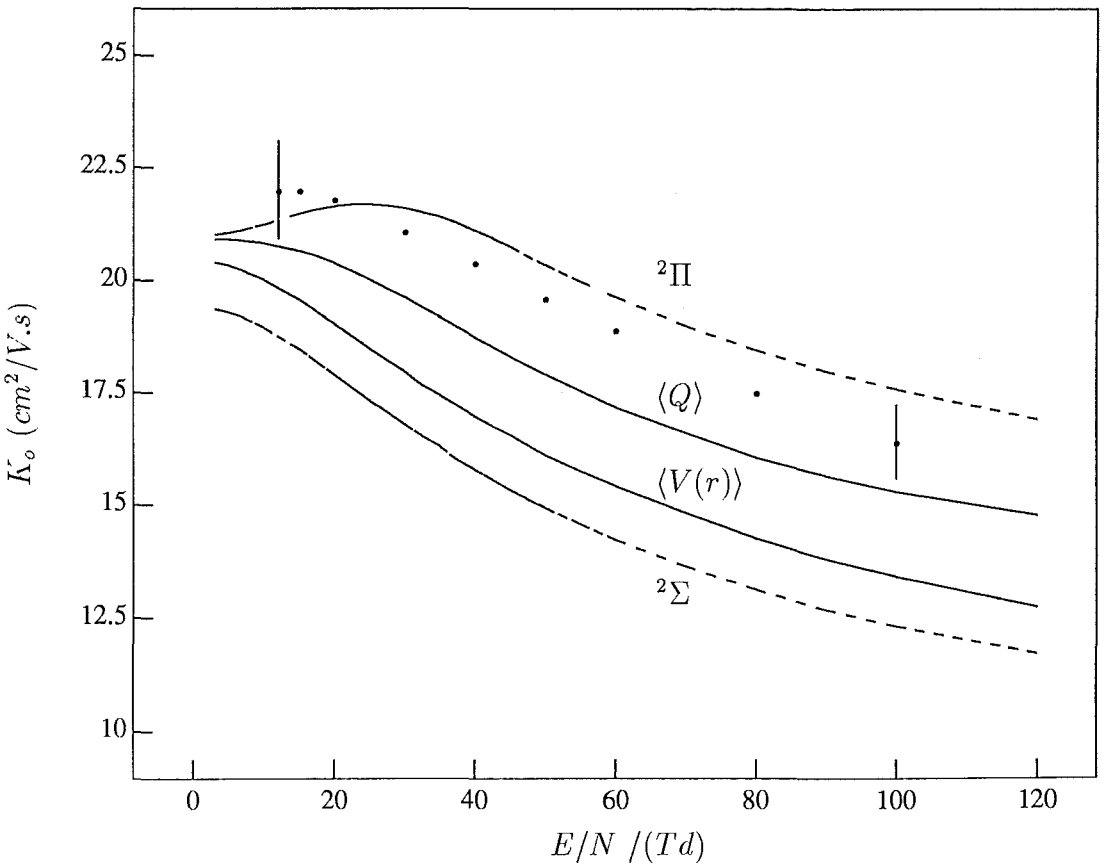

Figure 5.12: The experimental and calculated mobilities of Si^+ (^2P) in helium. The points and the associated error bars are the results of Fahey *et al.* [116]. The solid curves show the results of the three temperature calculations using the $^2\Pi$ and $^2\Sigma$ interaction potentials, and the "averaged transport cross section" mobility is labelled $\langle Q \rangle$.

5.4 Discussion

Interaction potentials and mobilities have been reported for the following ions in helium: C^+ (^2P), C^{+*} (^4P), N^+ (^3P), O^+ (^4S), O^{+*} (^2P), Si^+ (^2P), Si^{+*} (^4P). The equilibrium geometry and well depths of the interaction potentials arising from the Born-Oppenheimer states along with the electron configuration of these systems are given in table 5.8. Many of the features displayed in the table are discussed below.

All of the open shell interaction potentials that have been reported exhibit weakly bound ion-induced dipole wells at equilibrium bond distances greater than 2.0 Å, except the $^3\Sigma$ (^3P) interaction potential of N^+—He, and the $^4\Sigma$ (^4P) interaction potentials of C^{+*}—He and Si^{+*}—He. The $^4\Sigma$ (^4P) interaction potentials of C^{+*}—He and Si^{+*}—He exhibit wells sufficiently deep enough to conclude that substantial

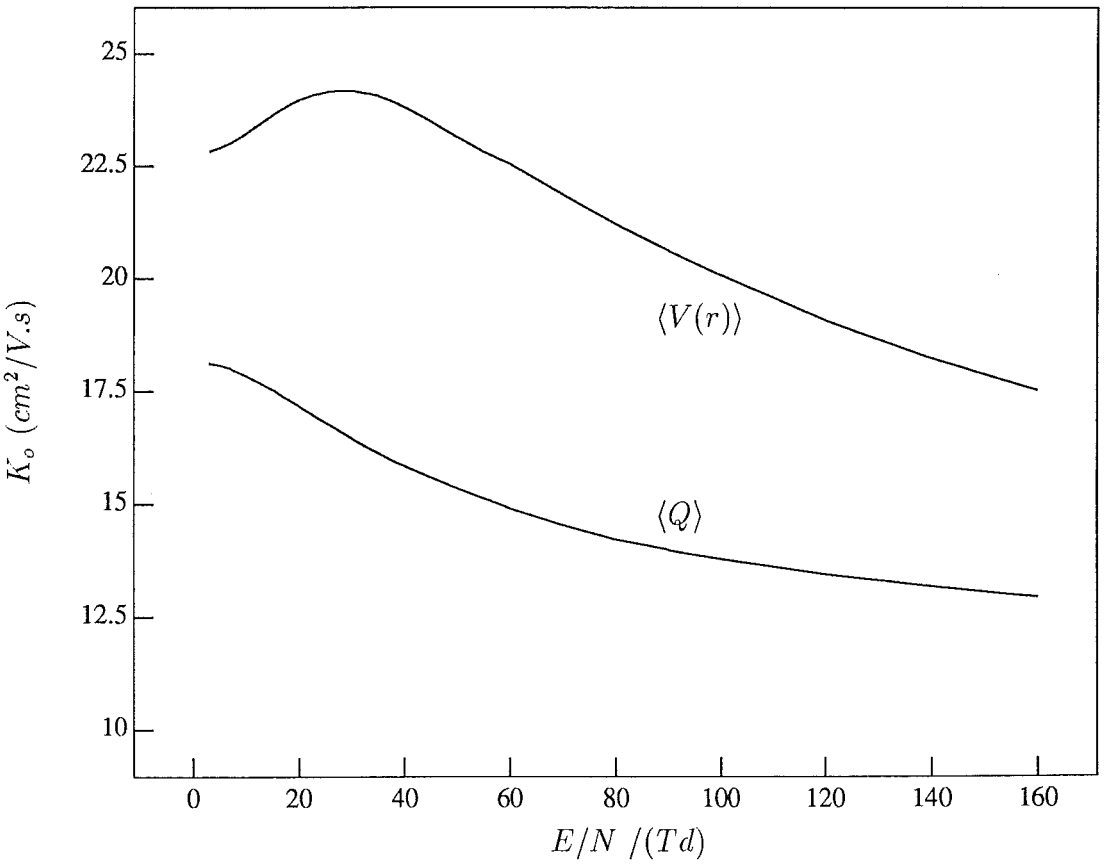

Figure 5.13: The calculated mobilities of Si^{+*} (^4P) in helium. The solid curves show the results of the three temperature calculations using the "averaged interaction potentials" $\langle V(r)\rangle$, and the "averaged transport cross section" mobility is labelled $\langle Q\rangle$.

bonding interactions have occurred. Jemmis *et al.* [117] have reported similar observations in their *ab initio* studies [117, 118, 119, 120] of the helides of carbon and silicon. The well depths and geometries of these structures were analysed in terms of the orbital interactions occurring in these species. For example, the primary interaction for the ground state of C^+—He involves the 2s orbital of the carbon and the 1s orbital of the helium, which produce a bonding 2σ molecular orbital and an antibonding 3σ molecular orbital. The remaining $2p_\sigma$ orbital of carbon mixes to a small degree with the 3σ molecular orbital, and the $2p_\pi$ orbitals of carbon form non-bonding 1π molecular orbitals. Adding 5 e^- to the molecular orbitals of C^+—He leads to a $1\sigma^2 2\sigma^2 3\sigma^2 1\pi^1$ configuration for the $^2\Pi$ (^2P) ground state. Jemmis *et al.* [117] have calculated the equilibrium bond distance and well depth of $^2\Pi$ (^2P) to be 2.509 Å, and $\approx$ 0.10 eV respectively at the QCISD(T)/6-311G(MC)**

Table 5.8: Geometric and thermodynamic properties of molecular ion states.

System	State	r_e [a]	D_e [b]	major e^- configuration
C^+—He	$^2\Pi$ (^2P)	2.329	0.050[c]	$1\sigma^2 2\sigma^2 3\sigma^2 1\pi^1$
C^+—He	$^2\Sigma$ (^2P)	2.978	0.018	$1\sigma^2 2\sigma^2 3\sigma^2 4\sigma^1$
C^{+*}—He	$^4\Sigma$ (^4P)	1.158	1.271	$1\sigma^2 2\sigma^2 3\sigma^1 1\pi^2$
C^{+*}—He	$^4\Pi$ (^4P)	2.805	0.022	$1\sigma^2 2\sigma^2 3\sigma^1 4\sigma^1 1\pi^1$
N^+—He	$^3\Sigma$ (^3P)	1.611[d]	0.194[d]	$1\sigma^2 2\sigma^2 3\sigma^2 1\pi^2$
N^+—He	$^3\Pi$ (^3P)	2.715[d]	0.022[d]	$1\sigma^2 2\sigma^2 3\sigma^2 1\pi^1 4\sigma^1$
O^+—He	$^4\Sigma$ (^4S)	2.42[e]	0.038[e]	$1\sigma^2 2\sigma^2 3\sigma^2 1\pi^2 4\sigma^1$
O^{+*}—He	$^2\Pi$ (^2P)	2.51[e]	0.016[e]	$1\sigma^2 2\sigma^2 3\sigma^2 1\pi^1 4\sigma^2$
O^{+*}—He	$^2\Sigma$ (^2P)	2.42[e]	0.038[e]	$1\sigma^2 2\sigma^2 3\sigma^2 1\pi^2 4\sigma^1$
Si^+—He	$^2\Pi$ (^2P)	2.921[f,d]	0.023[f,d]	$1\sigma^2 2\sigma^2 3\sigma^2 1\pi^4 4\sigma^2 5\sigma^2 2\pi^1$
Si^+—He	$^2\Sigma$ (^2P)	4.039[f,d]	0.004[f,d]	$1\sigma^2 2\sigma^2 3\sigma^2 1\pi^4 4\sigma^2 5\sigma^2 6\sigma^1$
Si^{+*}—He	$^4\Sigma$ (^4P)	1.713[f,d]	0.308[f,d]	$1\sigma^2 2\sigma^2 3\sigma^2 1\pi^4 4\sigma^2 5\sigma^1 2\pi^2$
Si^{+*}—He	$^4\Pi$ (^4P)	3.806[f,d]	0.007[f,d]	$1\sigma^2 2\sigma^2 3\sigma^2 1\pi^4 4\sigma^2 5\sigma^1 2\pi^1 6\sigma^1$

[a] All distances are in Angströms.
[b] All energies are in eV.
[c] All MP4SDQ/6-311+G(3df,3pd) level of theory unless otherwise stated.
[d] Including BSSE.
[e] VB results of Simpson *et al.* [81].
[f] MP4SDTQ/6-311+G(3df,3pd) level of theory.

level of theory. The C^{+*}—He $^4\Sigma$ molecular ion state results from the excitation of an electron from the antibonding 3σ molecular orbital to the 1π molecular orbital leading to a shorter bond and significant net bonding. Jemmis *et al.* [117] calculated that r_e = 1.164 Å for the $^4\Sigma$ (^4P) molecular ion state. We have observed similar values and trends in the values reported here.

An analogous electronic structure occurs for the molecular ions of Si^+—He. The main orbital interaction is between the 3s orbital of the silicon and the 1s orbital of the helium. This interaction leads to the formation of a bonding 4σ molecular orbital and an antibonding 5σ molecular orbital. Excitation of an electron from the antibonding 5σ molecular orbital of the $^2\Pi$ (^2P) ground state to one of the non-bonding 2π molecular orbitals results in the $^4\Sigma$ (^4P) molecular ion state with a substantially shorter and stronger bond. Jemmis *et al.* [117] report a equilibrium bond distance of 1.884 Å for the $^4\Sigma$ (^4P) molecular ion state. Again similar trends and values were observed in this study.

Turning to a discussion of the transport properties of open-shell ion systems, it is evident that, generally, there is agreement between theory and experiment. Agreement is best when the open shell molecular ion has zero orbital angular momentum. In such cases there is only one channel available to the collision partners. The calculation by Simpson *et al.* [81] of the mobility of O^+—He $^4\Sigma$ (^4S) in helium has shown that correspondence between theory and experiment is at least as good as that achieved for other closed shell ion systems [77]. When the open shell ion systems involve non zero orbital angular momentum more than one collision channel correlates to the separated collision partners. Two classically limiting cases have been developed to calculate the mobilities for comparison with experiment. Generally these calculations have resulted in adequate agreement with experiment. The only open shell ion for which the mobility calculated using the two classically limiting cases differed sufficiently (with the exception of C^{+*} and Si^{+*}, which is discussed later) to make a definitive conclusion about which classical model of ion transport was most accurate was the N^+ (^3P) ion. For the N^+ (^3P) ion, the "averaged interaction potential" calculation was substantially different from both the experimental and the "averaged transport cross section results" which were in agreement, at low E/N. However the agreement between the "averaged interaction potential" results and the experimental results was excellent at high E/N, and it was concluded from these observations that non-adiabatic transitions between Born-Oppenheimer states were negligible at low E/N.

Agreement between theory and experiment was best when the interaction potentials for the Σ and Π states of the open shell ion systems with orbital angular momenta greater than zero were most similar. For example, excellent correspondence occurred for all theoretical mobility calculations and experiment for the O^{+*} (^2P), where both interaction potentials exhibited weak ion-induced dipole type minima. The calculations for the mobility of the C^{+*}—He system were not in agreement with experiment. It is likely that the large well depth of the C^{+*}—He $^4\Sigma$ (^4P) interaction potential invalidates both classically limiting cases. Poor correspondence between theory and experiment was observed. It is likely that adequate agreement with experiment can only be achieved with a quantum calculation of the transport cross sections.

The calculations of these first row open shell cations were extended to a calculation of the second row cation Si^+ (^2P) in helium. The measurements and theoretical calculations for the Si^+—He system were at the boundaries of the mutual uncertainties. It is unclear whether the agreement, which is only just adequate, is a result of the large published uncertainties [116] of the experimental data set, or whether the validity of the classically limiting cases is in question. It is concluded that a new measurement of the mobility of Si^+ ions in helium would serve to validate the only set of published values, and to decrease the experimental uncertainty. Again a quantum treatment of the calculation of the transport cross section would serve as a valuable bench mark from which the validity and accuracy of both the classical treatments and the current experimental data set could be assessed.

Clary and Dateo [82, 121] have reported calculations of the experimental rate constants for 34 exothermic reactions of the open shell ions C^+ and N^+ with a series of reactants. They have used analogous classically limiting cases to those used in this chapter (for the calculation of the mobility of open shell ions) and shown that all 34 measured rate constants are within the bounds of the rate constants calculated assuming the transition probability between Born-Oppenheimer states to be zero or unity. They have noted that several different reactions exist where the rate constant agrees with either the upper limit (calculated assuming the transition probability to be unity) or the lower limit (calculated assuming the transition probability to be zero). Their results for the rate constants of open shell systems support our conclusion for the mobilities of these open shell systems in helium. An accurate treatment of open shell ion systems however requires calculation of the matrix elements for non-adiabatic transitions between the different interaction potentials available to the collision partners. This conclusion is equally valid for open shell ion mobility as it is for open shell ion reactivity.

5.5 Conclusion

The interaction potentials and mobilities of the following open shell ions in helium have been calculated: C^+ (^2P), C^{+*} (^4P), N^+ (^3P), O^+ (^4S), O^{+*} (^2P), Si^+ (^2P). Most interaction potentials exhibited weakly bound ion-induced dipole minima at

large separation. The $^4\Sigma$ (^4P) interaction potentials of C^{+*} (^4P) and Si^{+*} (^4P) exhibited deep wells at shorter separation and this was analysed in terms of molecular orbital interactions. The mobilities were calculated using two classically limiting cases. These calculations were generally in agreement with experiment with the exception of the calculation of the mobility of C^{+*} (^4P) ions in helium. This disagreement for the exceptional open shell ion system was rationalised in terms of the large differences between the $^4\Sigma$ and $^4\Pi$ interaction potentials that correlate with the collision partners He (^1S) + C^{+*} (^4P). The results reported here support the calculations of Clary and Dateo [82] for the reactivity of open shell ions. Finally, it is concluded that accurate quantum calculations of the transport cross sections are required in order to assess further the validity of the classically limiting cases used in the approach of this chapter.

Chapter 6

The Potential Energy Surface of Li^+—N_2

6.1 Introduction

The first *ab initio* study of the complete potential energy surface of the species Li^+—N_2 by Staemmler [122] provided valuable input for a number of fitting [123, 124] and scattering [125, 126, 127, 128, 129, 130, 131] studies. The availability of this potential energy surface provided opportunities to compare theory with experiments and to examine the relationship between expectations based on the potential energy surface and the experimental measurements. Most results showed adequate correspondence between experiment and theory for the authors [126, 127, 128, 130] to conclude that the Hartree-Fock (HF) potential energy surface of Staemmler was reasonably accurate in the 1—20 eV energy range. However, other authors [129] have reported contradictory results.

The analytic expression for the rigid rotor potential energy surface of Billing [127] has been tested [62] at energies below 1 eV. Although this potential energy surface was fitted to Staemmler's HF data using 12 parameters, it failed to reproduce the absolute experimental values [132] of the transport properties of Li^+ in N_2 . However, the general form was the same [62]. A number of theoretical investigations [133, 134, 135, 136, 137, 138, 139] of the thermodynamic and structural properties of the Li^+—N_2 system have been reported since Staemmler's paper. These studies have supplied data for the potential energy surface in the regions about stationary

points, but give limited information about the behaviour of the potential energy surface elsewhere.

Hartree-Fock calculations have been shown to be unreliable in reproducing electric multipole moments [7], which are important in long-range interaction effects. Similarly, binding energies in the region of a potential energy minima are not adequately described although the short-range repulsive interaction is described with moderate success [40]. Since there are reservations over the ability of Staemmler's potential energy surface to model accurately measured transport data over a wide energy range, and considering the advances in computer speed in the time since Staemmler reported his results, we have undertaken a detailed examination of the Li^+—N_2 potential energy surface.

In the following section *ab initio* calculations of the Li^+—N_2 potential energy surface are presented. In section 6.2 we describe improvements in the properties of the separate species Li^+ and N_2 with differing basis sets. The potential energy surface is presented and a discussion of the effects of inclusion of electron correlation is presented in section 6.3. Analysis of the potential energy surface and its Legendre expansion, with emphasis on a break down of the angular components of the long-range interaction energy is given in section 6.4.

6.2 Basis Set and Properties

Foremost in our choice of a basis set was the consideration of the properties of the separate Li^+ and N_2 species. Particularly important are the polarisation and electric multipole moments which dominate the long-range interactions between these two subsystems. Staemmler [122] has commented that polarisation functions are critical in reproducing experimental binding energies, quadrupole moments and polarisabilities for the N_2 subsystem. In order to improve on the potential energy surface that Staemmler generated it has been necessary to obtain reasonable properties for N_2 using a more sophisticated basis set and a more elaborate treatment of electron correlation.

The major part of this study involved calculations using the 6–311+G(2df) basis set. This basis set includes an extra f function on the N atomic centres and two extra d's and an extra f function on the Li atomic centre when compared to Staemmler's

best basis set. The addition of extra d polarisation functions to all atomic centres was studied, with the 6–311+G(3df) basis set. This basis set has been shown to be reliable in studies of the interactions between atomic ion/atom systems [140, 141, 69, 79, 80]. An extensive list of the electrical properties obtained with these basis sets is given in table 6.1 along with other experimental and theoretical results.

Table 6.1: Electric properties of N_2.

Basis set	Q^a	H^a	$\alpha_{\parallel}^a$	$\alpha_{\perp}^a$
HF/6–311+G(df)	−1.26	−6.47	14.68	7.01
MP2/6–311+G(df)	−1.22	−6.75	13.81	7.59
MP4SDTQ/6–311+G(df)	—	—	14.39	7.61
HF/6–311+G(2df)	−1.03	−7.35	14.29	8.12
MP2/6–311+G(2df)	−1.27	−6.69	13.67	8.54
MP4SDTQ/6–311+G(2df)	—	—	14.13	8.57
HF/6–311+G(3df)	−0.98	−7.71	14.19	9.32
MP2/6–311+G(3df)	−1.22	−6.74	13.67	9.66
MP4SDTQ/6–311+G(3df)	—	—	14.12	9.73
Staemmler's Results [122]	-0.94^b	-6.78^b	13.46^b	8.20^b
Best Experimental Results	$(-1.093\pm0.05)^c$	—	14.81^d	10.20^d

[a] All electric properties in *a.u.*
[b] Basis set A of that work; see [122].
[c] Hout and Bose; see [142].
[d] Mason and McDaniel; see [40].

The basis set with a HF quadrupole moment, Q, in best agreement with the experimental measurement of Hout and Bose [142], is the 6–311+G(2df) basis set. The HF limit value of the quadrupole moment of N_2 has been calculated numerically by Sundholm [143] to be -0.940 *a.u.* The results for the quadrupole moment quoted here show that there is increasing correspondence with the result of Sundholm with increasing basis set size. The correlated MP2 wavefunctions have similar quadrupole moments ($Q \simeq -1.2$ *a.u.*) for each basis set considered here. The reliability of the quadrupole moment is crucial to the accuracy of the long-range interactions between N_2 and any other ionic system. The hexadecapole moment, H, increases in magnitude with the addition of polarisation functions from −6.47 *a.u.* to −7.71 *a.u.* with basis sets 6–311+G(df) to 6–311+G(3df) respectively, at the HF level of theory, but remains relatively constant for the basis sets considered when including

electron correlation to a MP2 level of theory. Staemmler's own result of −6.78 *a.u.* is consistent with that reported here if you compare the size of the basis sets with respect to the number of polarisation functions included. To our knowledge there is no experimental measurement of the hexadecapole moment of N_2 in the literature.

The dipole polarisability in table 6.1 also shows an increase in magnitude with an increase in the size of the basis set. Greater agreement with experiment is achieved with the inclusion of more polarisation functions in the basis sets. The parallel component of the dipole polarisability, $\alpha_{\|}$, compares favourably with the experimental value, with 2.9%, 4.6%, and 4.6% errors for the 6–311+G(df), 6–311+G(2df), and 6–311+G(3df) basis sets, respectively, at the MP4SDTQ level of theory. The perpendicular component of the dipole polarisability, $\alpha_{\perp}$, approaches the experimental value with 25.4%, 15.0%, and 4.6% errors for the 6–311+G(df), 6–311+G(2df), and 6–311+G(3df) basis sets, respectively, at the MP4SDTQ level of theory.

In addition to the reproduction of the electric multipole moments and the dipole polarisabilities, important to the long-range interaction of N_2 with any ionic species, it is also important to model the structural and thermodynamic properties of N_2. The equilibrium bond distance, the dissociation energy, the force constant, and the total energy of N_2 are presented in table 6.2.

Table 6.2: Structural and thermodynamic properties of N_2.

Basis set	$r_e{}^a$	D_e^a/eV	k_e^a	E^a
HF/6–311+G(df)	2.018	4.87	106.6[b]	−108.97689
MP4SDTQ/6–311+G(df)	2.018	9.40	—	−109.34721
HF/6–311+G(2df)	2.016	5.06	105.9[b]	−108.98391
MP4SDTQ/6–311+G(2df)	2.016	9.48	—	−109.36929
HF/6–311+G(3df)	2.016	5.09	105.9[b]	−108.98486
MP4SDTQ/6–311+G(3df)	2.016	9.54	—	−109.37427
Staemmler's Results	2.081[c]	9.0[c]	110.3[c]	−109.2754[c]
Best Experimental Results	2.074	9.77[d]	99.87[e]	—

[a] All structural and thermodynamic properties in a.u, except D_e.
[b] HF force constants scaled by $(0.89)^2$; see text.
[c] Basis set A of that work; see [122].
[d] Huber and Herzberg; see [144].
[e] Cade and Wahl; see [145].

The equilibrium bond distance calculated for the basis sets used in this study is slightly shorter than the experimental value, by approximately 0.05 *bohr*. Dixon [139] reports an equilibrium bond distance of 2.03 *bohr* using a (11s7p1d)/[5s4p1d] basis set which increased approximately 0.05 *bohr* with inclusion of electron correlation in his configuration interaction (CISD) calculations. We have not optimised the bond distance past the HF level of theory, but it seems reasonable to expect that an inclusion of electron correlation would improve our bond distances in a similar manner.

Electron correlation is also important in the determination of binding energies, as HF calculations cannot adequately describe the dissociation of the closed shell N_2 $(X,^1\Sigma_g^+)$ molecule into two open shell N ^{3}S atoms [7]. HF potentials have been shown to give dissociation energies that are too small and force constants that are too large. The MP4SDTQ bond energies in table 6.2 are nearly double the HF values with the same basis set. Again, the bond energies approach the experimental value, with 3.8%, 3.0%, and 2.4% error using the 6–311+G(df), 6–311+G(2df), and 6–311+G(3df) basis sets, respectively, at the MP4SDTQ level of theory.

The force constants have been calculated at the HF level of theory, and scaled as recommended by DeFrees and McLean [146]. The total energy of the lithium ion in the ground electronic state is -7.23584 *a.u.* and the major requirement of the lithium basis set is that it remains flexible enough to describe any medium-range bonding interactions.

In the following work we have used the 6–311+G(2df) basis set, unless otherwise stated. This represents the best compromise between the accuracy of the molecular properties describing the sub-systems, and expense of characterising the entire rigid rotor potential energy surface. The 6–311+G(2df) basis set has similar MP2 multipole moments to the other basis sets considered and polarisabilities that are comparable with the experiment values. The bond energy and force constants are in good accord with the experimental measurements. It seems likely that the short-range coulombic repulsion interaction is described well by any of the basis sets studied here.

All calculations have been performed using the Gaussian 90 series of programs [4].

6.3 The Potential Energy Surface of Li^+—N_2

The calculations reported here were performed with the bond distance of N_2 fixed to the value optimised at the HF level of theory. The post-HF method used to include electron correlation was Møller-Plesset fourth order perturbation theory, with a frozen core that included $1s$ functions on both N atomic centres. The magnitude of R, the vector connecting the centre of mass of the N_2 molecule and the centre of the Li^+ ion, and θ, the angle between the internuclear vector, r, of N_2, and R, were varied. This coordinate system is displayed in figure 6.1. R was varied to completely characterise the potential energy surface over the energy range 10^{-3}—10^{1} eV for all values of θ. Enough angles were computed to completely characterise the dominant interactions of the Legendre expansion in this energy range. This required calculation of four angles, θ=0°, 22.5°, 45°, 90°. Tables 6.3 and 6.4 contain the total energies for the Li^+—N_2 calculations as a function of R and θ for the HF and the MP4SDTQ levels of theory, respectively.

These potentials have been spline fitted to determine the values of the critical points of the potential energy surface. The spline functions have been determined in a similar fashion to that described by Simpson *et al.* [141]. Each potential function has been tabulated as a series of points (R_i, V_i), where $V_i = V(R_i)$. These points have been fitted by piece-wise cubic splines by developing equations that ensure that (a) the function interpolates the points (R_i, V_i) and (b) that first and second derivatives are continuous. Two additional equations are required for a complete solution of the cubic spline system of equations and these usually involve constraints on the derivatives at the end points. We have set the second derivatives of the short-range end point to equal zero thus achieving a "natural" cubic spline. Then we have extrapolated to shorter R with the potential

$$V(R) = \frac{a}{R^m} + b \qquad \text{for } R < R_1 \tag{6.1}$$

which was fitted using (R_1, V_1), and $(R_1, \partial V_1/\partial R)$ attained after solving the cubic spline system of equations. In this work m was set to equal 6. This extrapolation function was chosen because it closely approximated the behaviour of the short-range *ab initio* points. Enough *ab initio* points were calculated to characterise the repulsive wall of the potential energy surface.

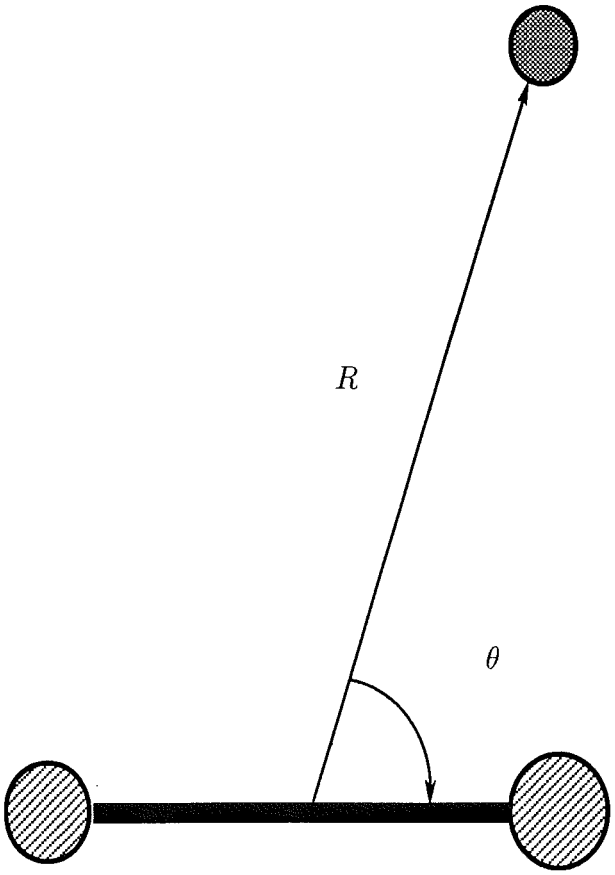

Figure 6.1: The geometry coordinates of a rigid rotor diatom/atom collision.

The long-range potential was determined by fitting the extrapolating function

$$V(R) = \frac{c}{(R-d)^n} \qquad \text{for } R > R_n \tag{6.2}$$

to the points (R_{n-1}, V_{n-1}) and (R_n, V_n). The first derivative of this function at R_n was then used to set the final condition needed to solve the cubic spline system of equations. For the potential energy surface functions n was set to equal 3. The leading long-range interaction terms for the Li^+—N_2 potential energy surface are the ion-quadrupole and the ion-induced dipole interactions. When equation 6.2 is

Table 6.3: HF/6-311+G(2df) total energies of Li^+—N_2.

R [a]	θ=0.0[b]	θ=22.5[b]	θ=45.0[b]	θ=90.0[b]
1.000	—	—	—	−115.65949[c]
1.100	—	—	—	−115.83856
1.200	—	—	−115.51758	—
1.300	—	−115.23747	—	−116.04877
1.350	—	—	—	−116.08099
1.400	−115.28865	−115.54091	−115.88558	−116.10764
1.500	−115.61167	−115.76920	−115.99939	−116.14779
1.625	−115.87413	—	−116.09464	−116.18025
1.700	−115.97860	—	—	—
1.750	−116.03225	−116.07988	−116.15366	−116.19985
2.000	−116.17998	−116.19218	−116.20988	−116.21799
2.250	−116.22686	−116.22785	−116.22731	−116.22319
2.375	−116.23494	—	—	—
2.500	−116.23825	−116.23609	−116.23071	−116.22386
2.750	−116.23812	—	−116.22968	−116.22318
3.000	−116.23499	−116.23263	−116.22769	−116.22228
3.500	−116.22896	−116.22746	−116.22436	−116.22095
4.000	−116.22532	−116.22440	−116.22246	−116.22028
5.000	−116.22218	−116.22176	−116.22086	−116.21978
6.000	−116.22100	−116.22078	−116.22029	−116.21969
6.500	—	—	—	−116.21968
7.000	—	—	—	−116.21968
8.000	−116.22021	−116.22013	−116.21994	−116.21969
10.000	−116.21997	−116.21993	−116.21984	−116.21971
12.000	−116.21987	—	—	−116.21973
∞	−116.21975	−116.21975	−116.21975	−116.21975

[a] bond distances in Angströms.
[b] bond angles in degrees.
[c] Energies in *a.u.*

expanded in inverse powers of R the ion-quadrupole and the ion-induced dipole terms are represented as c/R^3, and $3cd/R^4$, respectively. The values of c and d, which are given in table 6.5, closely correspond to the quadrupole moment and the polarisabilities of the N_2 molecule for the 6-311+G(2df) basis set given in table 6.1. Enough *ab initio* points were calculated at large separation to ensure the extrapolation function exhibited the correct long-range behaviour. The value of c in the

Table 6.4: MP4SDTQ/6–311+G(2df) total energies of Li^+—N_2.

R^a	θ=0.0^b	θ=22.5^b	θ=45.0^b	θ=90.0^b
1.000	—	—	—	−116.05489^c
1.100	—	—	—	−116.23128
1.200	—	—	−115.89033	—
1.300	—	−115.61827	—	−116.43808
1.350	—	—	—	−116.46967
1.400	−115.70788	−115.92658	−116.26847	−116.49576
1.500	−116.00134	−116.15496	−116.38348	−116.53499
1.625	−116.26123	—	−116.47942	−116.56663
1.700	−116.36492	—	—	—
1.750	−116.41823	−116.46519	−116.53882	−116.58575
2.000	−116.56544	−116.57771	−116.59563	−116.60344
2.250	−116.61278	−116.61397	−116.61354	−116.60853
2.375	−116.62117	—	—	—
2.500	−116.62474	−116.62267	−116.61716	−116.60923
2.750	−116.62488	—	−116.61613	−116.60859
3.000	−116.62176	−116.61932	−116.61402	−116.60771
3.500	−116.61538	−116.61377	−116.61035	−116.60634
4.000	−116.61137	−116.61037	−116.60820	−116.60563
5.000	−116.60786	−116.60738	−116.60637	−116.60512
6.000	−116.60654	−116.60629	−116.60573	−116.60503
6.500	—	—	—	−116.60503
7.000	—	—	—	−116.60503
8.000	−116.60565	−116.60556	−116.60534	−116.60505
10.000	−116.60537	−116.60533	−116.60522	−116.60508
12.000	−116.60526	—	—	−116.60509
∞	−116.60513	−116.60513	−116.60513	−116.60513

[a] bond distances in Angströms.
[b] bond angles in degrees.
[c] Energies in *a.u.*

linear arrangement is very similar to the quadrupole moment calculated to the MP2 level of theory. Because the ion-induced dipole interaction is attractive we expect d to have an opposite sign to c. The value of $3cd$ in the linear arrangement is also very close to the value of $\frac{1}{2}\alpha_{\|}$, where $\alpha_{\|}$ is given in table 6.1. In the perpendicular arrangement the value of c is negative because the quadrupole interaction is repulsive. This repulsive interaction leads to a local maxima. Several *ab initio* points

Table 6.5: Fitting parameters for long-range extrapolations of Li^+—N_2.

Fitting parameter	c[a]	d[a]
HF		
θ=0° [b]	−1.164	+1.429
θ=22.5°	−0.889	+1.840
θ=45°	−0.396	+2.330
θ=90°	+0.491	−4.666
MP4SDTQ		
θ=0°	−1.208	+1.947
θ=22.5°	−0.985	+1.966
θ=45°	−0.418	+2.598
θ=90°	+0.899	−7.524

[a] All parameters in *a.u.*
[b] All angles in degrees.

have been calculated beyond the maxima in order to improve the correspondence between the calculated polarisability given in table 6.1 and the values obtained from the fitting function. The value of c is reasonable but the value of d is not in accord with the calculated polarisabilities. Because the leading asymptotic term (the ion-quadrupole term) is reasonable and the extrapolation function is fitted at large R, we have concluded that the error involved in the incorrect fitted polarisability is negligible.

The following general features are exhibited, and listed in table 6.6, for HF, MP2, and MP4SDTQ levels of theory, and plotted for the MP4SDTQ level of theory undertaken in this study. There exists an absolute minimum in the potential energy surface for all the levels of theory at $R \simeq 4.9$ *bohr*, θ=0°. The depth of the minimum is 0.522 eV at the HF level of theory which increases 6.3% to 0.557 eV with the inclusion of electron correlation at the MP4SDTQ level of theory. The MP4SDTQ potential energy surface minimum reported here is very similar to Staemmler's own HF potential energy surface minimum which he quotes at $R \simeq 5.0$ *bohr*, θ= 0° with a depth of 0.56 eV. Between the two minima in the linear arrangement exists a col in the perpendicular arrangement. The col is located at $R \simeq 4.6$ *bohr*, θ= 90° with a relative energy of 0.113 eV at the HF level of theory which decreases slightly (0.9%) to 0.112 eV at the MP4SDTQ level of theory. The col in Staemmler's HF potential

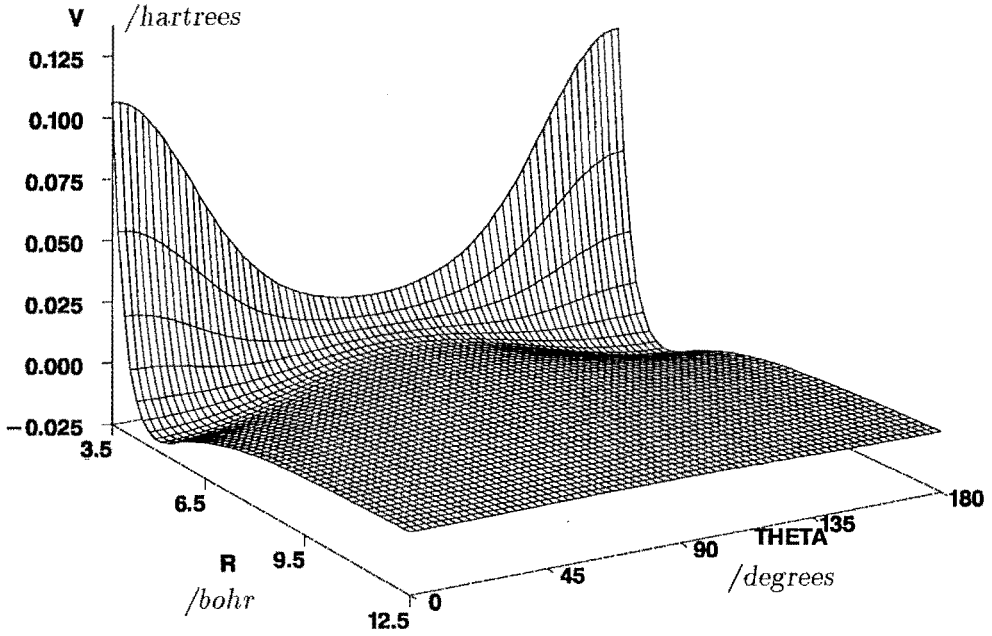

Figure 6.2: The surface plot of the Li^+—N_2 MP4SDQ/6–311+G(2df) potential energy surface as a function of the intermolecular distance and angle.

energy surface was located slightly shorter at $R \simeq 4.5$ *bohr* but much higher at 0.20 eV suggesting that the magnitude of the quadrupole moment is very important in defining the height of the saddle. Staemmler's quadrupole moment for basis set A was 15% smaller in magnitude than the best experimental value available [142]. This leads to over-estimation of the the relative energy of the col in the perpendicular arrangement by almost a factor of 2.

The quadrupole moment is important in determining the character of the long-range interaction which is repulsive at large R in the perpendicular arrangement. The quadrupolar repulsion is then dominated by a charge-induced dipole interaction at smaller R, resulting in a net attraction. Therefore we find a single local maximum exists at $R \simeq 12.4$ *bohr* of 1.89×10^{-3} eV at the HF level of theory, and at $R \simeq 11.8$ *bohr* of 2.74×10^{-3} eV at the MP4SDTQ level of theory. Staemmler reported a local maximum at $R \simeq 15$ *bohr* of 1.3×10^{-3} eV which is again smaller than the energy reported here and at larger R. Features of the potential energy surface in table 6.6 show that the geometries of the critical points are not very dependent on the treatment of electron correlation, except for the region about the local maximum.

Other comparisons of the potential energy surface are best observed graphically.

Table 6.6: Critical points of the potential energy surface of Li^+—N_2.

critical points	HF	MP2	MP4SDTQ
θ=0° [a]			
$R, (V = 0)$	4.129[b]	4.129	4.124
$R, (\partial V/\partial R = 0)$	4.926	4.955	4.948
$V, (\partial V/\partial R = 0)$	−0.01919[c]	−0.2031	−0.02046
$R, (\partial^2 V/\partial^2 R = 0)$	5.626	5.659	5.654
θ=22.5°			
$R, (V = 0)$	4.079	4.079	4.071
$R, (\partial V/\partial R = 0)$	4.912	4.938	4.929
$V, (\partial V/\partial R = 0)$	−0.01677	−0.01478	−0.01808
$R, (\partial^2 V/\partial^2 R = 0)$	5.601	5.580	5.577
θ=45°			
$R, (V = 0)$	3.971	3.968	3.957
$R, (\partial V/\partial R = 0)$	4.758	4.782	4.769
$V, (\partial V/\partial R = 0)$	−0.01097	−0.01182	−0.01205
$R, (\partial^2 V/\partial^2 R = 0)$	5.522	5.559	5.550
θ=90°			
$R, (V = 0)$	3.879	3.902	3.877
$R, (\partial V/\partial R = 0)$	4.615	4.646	4.627
$V, (\partial V/\partial R = 0)$	−0.00415	−0.00382	−0.00413
$R, (\partial^2 V/\partial^2 R = 0)$	5.375	5.446	5.432
$R, (V = 0)$	12.387	11.564	11.815
$R, (\partial V/\partial R = 0)$	9.794	9.128	9.413
$V, (\partial V/\partial R = 0)$	−0.00007	−0.00012	−0.00010
$R, (\partial^2/\partial^2 R = 0)$	16.079	14.777	15.087

[a] All angles in degrees.
[b] All bond distances in *bohr*.
[c] All energies in *a.u.* and relative to $R = \infty$.

Figure 6.3 displays the potential energy surface for θ= 0°, 45°, and 90° at the MP4SDTQ level of theory. The θ= 22.5° potential energy surface was omitted for clarity. Staemmler's HF potential points are also plotted in figure 6.3. Staemmler's θ= 0° potential closely matches the MP4SDTQ potential reported here, however his θ= 90° potential differs significantly from both the HF and MP4SDTQ potentials,

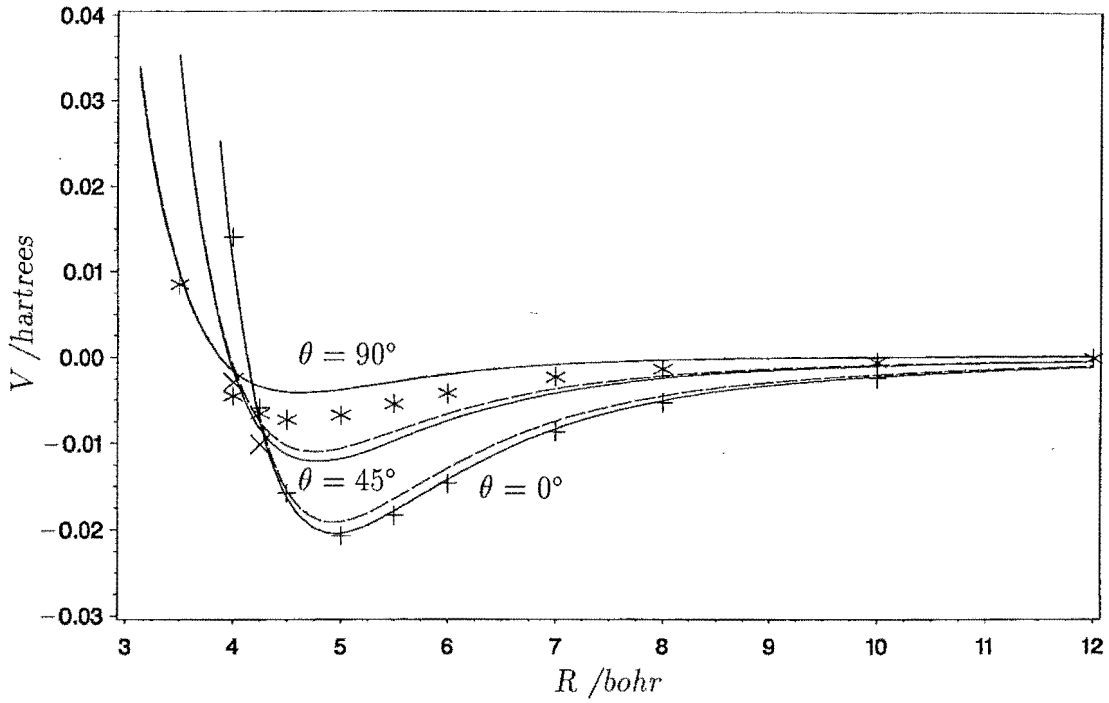

Figure 6.3: The potential energy surface of Li^+—N_2 for θ= 0°, 45°, and 90°. The dashed curves represent the calculations at the HF level of theory. The solid lines represent the calculations at the MP4SDTQ level of theory. Staemmler's points are represented as +, ×, and ∗ for θ= 0°, 45° and 90° respectively.

which are very close together. It seems inter-molecular correlation (dispersion energy) is negligible in the perpendicular approach. Staemmler's points for θ= 45° also suggest values substantially different to the potentials reported here although not enough points were published to draw further conclusions. Comparisons of short-range repulsion are made in figure 6.4. Again the θ= 22.5° potential energy surface was omitted for clarity. From figure 6.4 it can be seen that the exponential repulsion behaviour begins for $R < 3$ *bohr*.

6.4 The Legendre Expansion

The potential energy surface of Li^+—N_2 results from a number of interactions that are best analysed by decomposing the angular variation of these interactions in a truncated Legendre expansion. This is achieved by equation 6.3

$$V(R, \theta_m) = \sum_{n=0}^{k} P_{m,n} V_n(R) \tag{6.3}$$

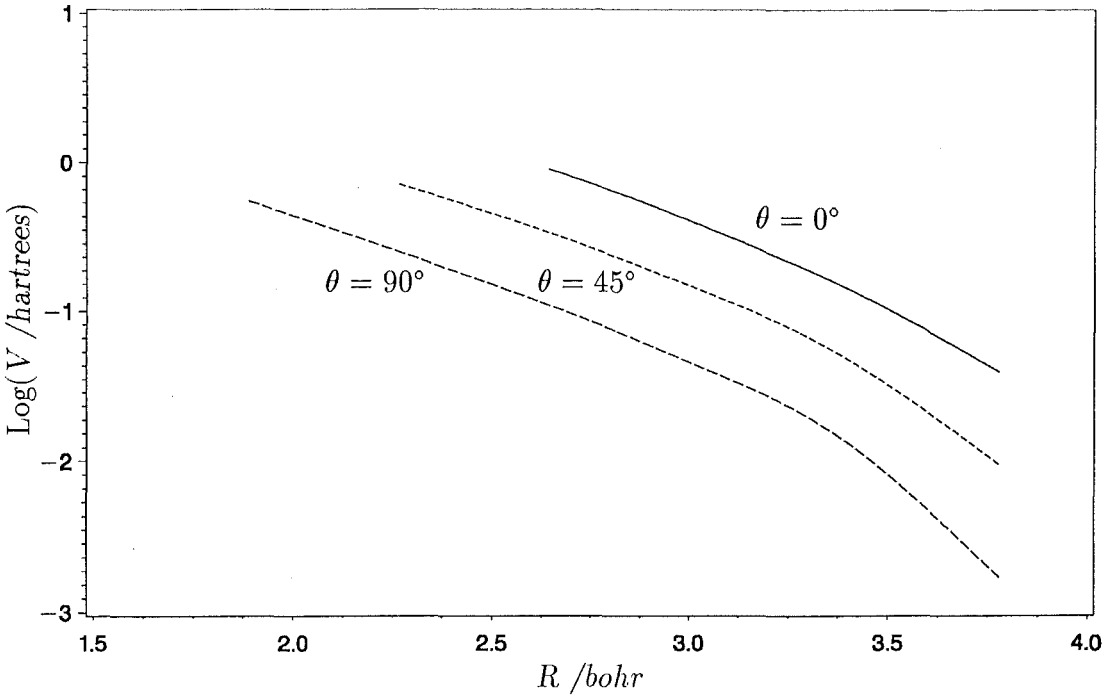

Figure 6.4: The short-range potential energy surface of Li^+—N_2 . The three curves represent the potential energy surface with θ= 0°, 45°, and 90° for the solid line, the short dashed line and the long dashed line respectively, at the MP4SDTQ level of theory.

where $P_{m,n}$ is the n^{th} degree Legendre polynomial of $\cos\theta_m$, and θ_m are the angles for which *ab initio* calculations have been performed, namely

$$\theta_m \in \{0°, 22.5°, 45°, 90°\}. \tag{6.4}$$

The Legendre expansion was performed for the series up to $k = 6$. The odd terms of n vanish in the series as N_2 is a member of the $D_{\infty h}$ point group. The radial functions are obtained using the inverted matrix elements $P^{-1}_{2n,m}$ as radial coefficients as shown in equation 6.5.

$$V_{2n}(R) = \sum_{m=0}^{k/2} P^{-1}_{2n,m} V(R, \theta_m) \tag{6.5}$$

The points for which all θ were calculated for a given R have been inverted directly and shown in table 6.7, and table 6.8 for the HF and MP4SDTQ levels of theory, respectively. These data are plotted in figure 6.5, and some general features are outlined here. The radial function have also been spline fitted in a similar manner to that described for the potential energy surface. The long-range exponent n of equation 6.2 was set to 4, 3, and 5 for V_0, V_2, and V_4 respectively. These exponents

Table 6.7: HF/6–311+G(2df) Legendre expansions of Li^+—N_2.

R [a]	V_0 [b]	V_2	V_4	V_6
1.400	293204[c]	432995	144150	60496
1.500	190728	291156	95869	30070
1.750	56374	92801	31368	6705
2.000	8623	19913	9127	1850
2.250	−6053	−3737	1819	608
2.500	−8950	−9596	−398	190
3.000	−6524	−8088	−845	−36
3.500	−3813	−5076	−523	−48
4.000	−2285	−3219	−302	−22
5.000	−1022	−1539	−106	−17
6.000	−600	−854	−47	−5.3
8.000	−362	−343	−11	−0.7
10.000	−300	−169	−3.0	−0.1

[a] All bond distances are in Angströms.
[b] Zeroth order Legendre expansion; see text.
[c] All bond energies are in 1×10^6 *a.u.*

are consistent with the ion-induced dipole, ion-quadrupole, and ion-hexadecapole interactions which are the leading terms for each radial function respectively. For the V_6 radial function n was set to equal 7.

As expected the potential energy surface exhibits a large anisotropic radial function V_2. It is evident from a comparison between figure 6.5 of this work and figure 6.6 of Staemmler's work that the potential energy surfaces reported here are substantially more anisotropic. At long-range this is mainly due to the larger quadrupole moment of our basis set compared to Staemmler's, again emphasizing the importance of electrical behaviour of the isolated sub-units. In the region of the radial functions' minima the anisotropic radial function V_2, is in fact deeper than the isotropic radial function V_0 in contrast with Staemmler's result. The magnitude of the anisotropic radial function V_2 is also greater than that of the isotropic radial function V_0 at short-range, in agreement with Staemmler's result, although this behaviour is not unexpected, considering the N_2 bond distance is of the order of the inter-nuclear distance between the two sub-units. We can also see the Legendre expansion converges rapidly as a series in n, justifying truncating the series at $n = 6$.

Table 6.8: MP4SDTQ/6-311+G(2df) Legendre expansion of Li^+—N_2.

R [a]	V_0 [b]	V_2	V_4	V_6
1.400	287420[c]	440228	138274	31322
1.500	190356	292648	92878	27901
1.750	56443	93323	30842	6294
2.000	8629	19867	9443	1748
2.250	−6280	−4323	2375	574
2.500	−9341	−10533	84	180
3.000	−6891	−9067	−636	−38
3.500	−3962	−5802	−443	−49
4.000	−2257	−3700	−266	−23
5.000	−847	−1762	−98	−22
6.000	−379	−986	−46	−7.1
8.000	−116	−399	−11	−0.9
10.000	−47	−197	−2.9	−0.1

[a] All bond distances are in Angströms.
[b] Zeroth order Legendre expansion; see text.
[c] All bond energies are in 1×10^6 *a.u.*

The improvements in the long-range potential energy surface reported here are supported by the total cross-section measurements of Gislason *et al.* [131]. Gislason *et al.* have fitted their scattering data to an analytic expression for the deflection function, from which they have inferred an isotropic radial function, which they claim is valid over the range $2.9 \leq R \leq 10.2$ *bohr*. Their isotropic radial function is compared to the one we have derived in table 6.9 and figures 6.6 and 6.7. Excellent agreement at long-range between our isotropic radial function and the isotropic radial function derived by Gislason *et al.* for $R \geq 7$ *bohr* justifies our choice of basis set and method in this region. Gislason *et al.* have suggested that Staemmler's HF method "incorrectly obtains some covalent interaction between the two particles in this region", however our HF surface seems reasonable in this region and we have concluded that the improvement in the basis set was responsible for the agreement between experiment and theory. Waldman *et al.* [133] have used polarised electron-gas theory to calculate the Li^+—N_2 potential energy surface. Their results have been included in table 6.9 for comparison.

The well depth of the isotropic radial function is 0.237 *eV* at the HF level of

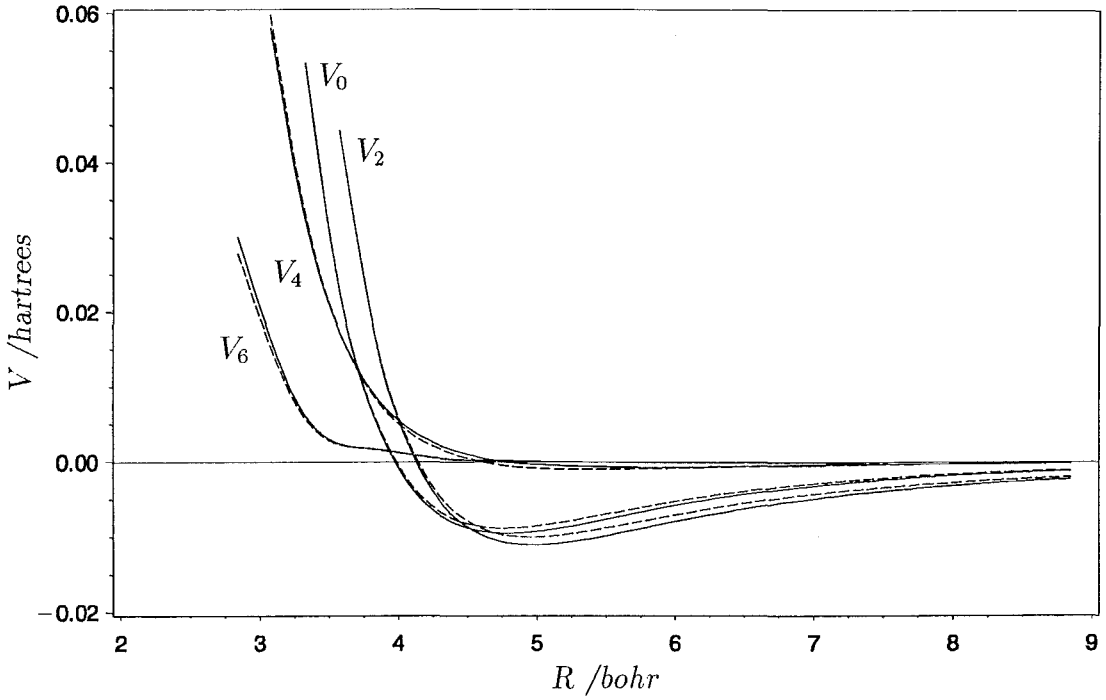

Figure 6.5: The radial functions of Li^+—N_2. The dashed lines represent calculations at the HF level of theory, and the solid lines represent calculations at the MP4SDTQ level of theory for the radial functions of the Legendre expansion. At short-range the curves represent in order of increasing repulsion, V_6, V_4, V_0, and V_2.

theory. This increases to 0.255 eV with the inclusion of electron correlation at the MP4SDTQ level of theory. In the region about the well Gislason's isotropic radial function is approximately 20% deeper than the result reported here. This represents an absolute error of about 0.05 eV and is probably at the upper limit of the accuracy of our calculations. In order to estimate the error in treating the N_2 sub-unit as a rigid rotor, we have optimised the bond distance of the N_2 sub-unit with the value of R set at the well minima. This resulted in a lowering of energy of the minimum by 0.006 eV but is still in error by 18% when compared to Gislason's derived potential. We estimate that the well depth for this basis set is 0.261 eV when correcting for nuclear polarisation [147]. The effect of increasing the basis set size was also investigated by estimating the well depth with a 6–311+G(3df) basis set, and we found the difference between the two potential energy surfaces to be less than the margin of error for these calculations. Simpson [112] has experienced similar discrepancies between *ab initio* potentials and the reported experimental values for spherically symmetric ions in inert gases. These discrepancies were treated by scaling

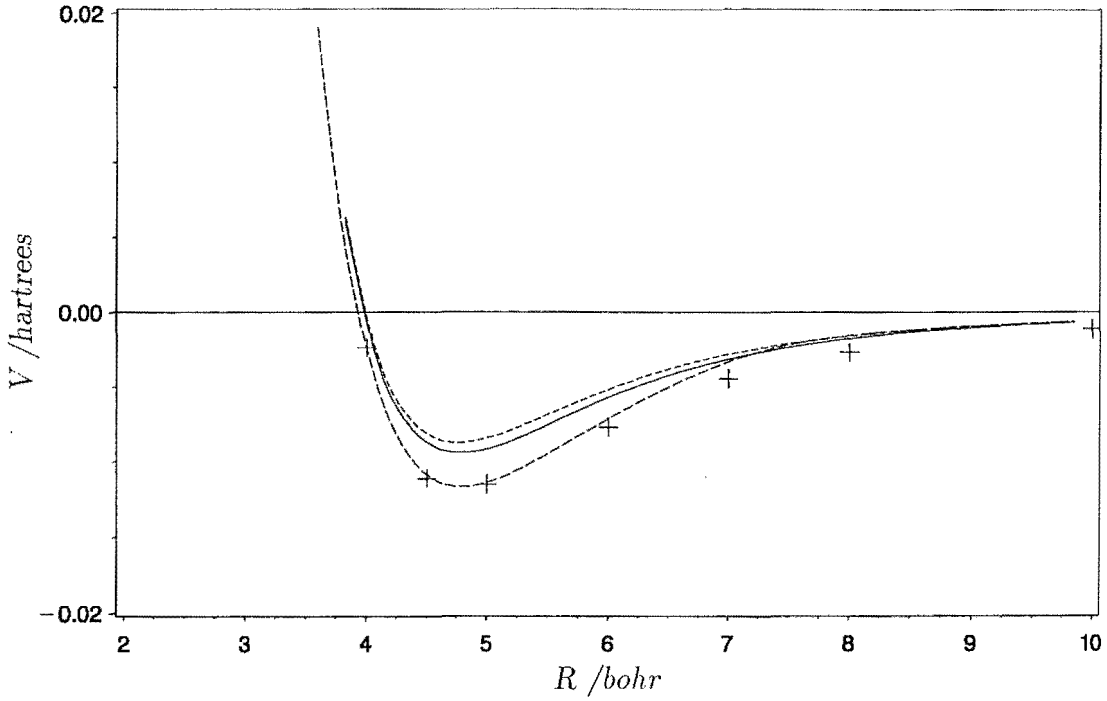

Figure 6.6: The isotropic radial function of the Legendre expansion of Li^+—N_2 . The + represent Staemmler's isotropic radial function. The short dashed line represents calculations at the HF level of theory and the solid line represents the calculations at the MP4SDTQ level of theory. The long dashed line represents the isotropic radial function derived from Gislason's work.

the attractive part of the spherically symmetric potential to the experimentally reported well depths, resulting in improved agreement between theoretically derived mobility curves and experimental mobility measurements. Staemmler's isotropic radial function closely matches Gislason's isotropic radial function in the region of the well, but our previous attempts to match this accuracy with atomic ion/atom systems with the HF method have shown that this agreement is fortuitous.

At short-range we have compared the isotropic radial functions for $R \leq 3.75$ *bohr* in figure 6.7. Kita *et al.* [125] have made total scattering cross-section measurements of the Li^+—N_2 system in this energy range and fitted their scattering results to a function of the form $V(R) = A\exp(-\alpha R)$. This potential is plotted in figure 6.7, along with Staemmler's *ab initio* points and Gislason's scattering results (which are extrapolated slightly beyond the range of reported validity). Gislason *et al.* have commented that the results of Kita *et al.* [125] "agree very well" with their own in this energy range. However Kita *et al.* appears to have over-estimated the range of R for which his functional potential is valid and both Gislason's isotropic radial

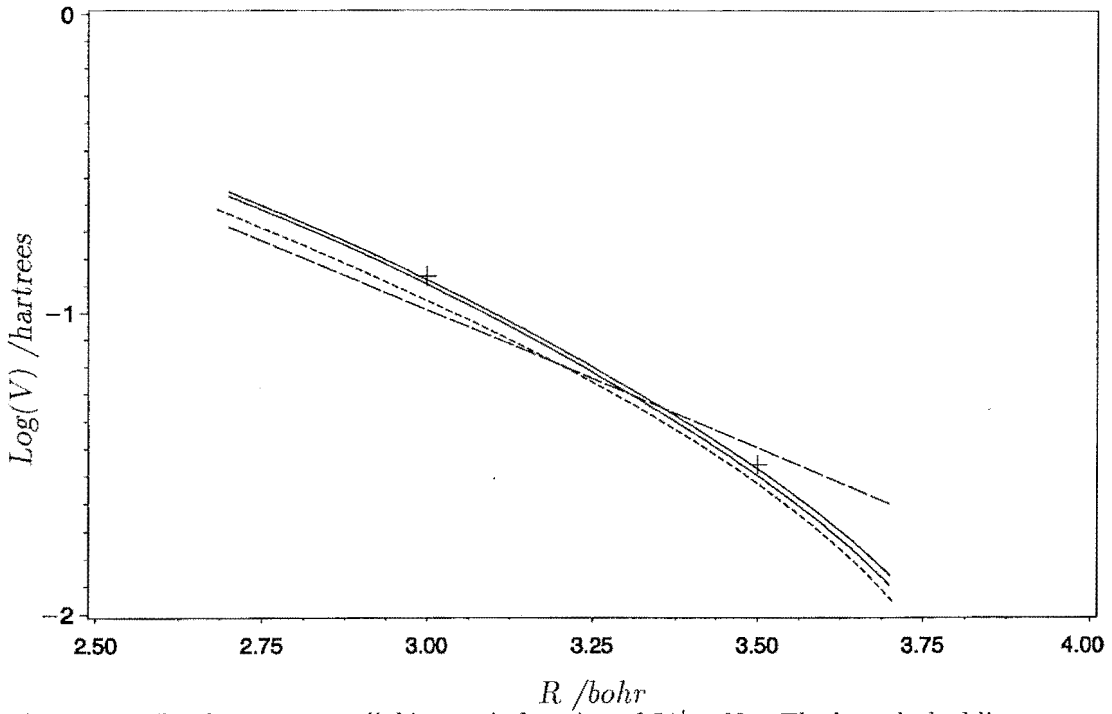

Figure 6.7: The short-range radial isotropic function of Li^+—N_2 . The long dashed line represents the potential fitted by Kita *et al.* to $V = \exp(-\alpha R)$. The short dashed line represents the isotropic radial function of Gislason *et al.* derived from scattering data. Both the HF and the MP4SDTQ levels of theory are represented by the upper solid line. These two levels of theory are sufficiently close to be represented as one line in this region of the potential energy surface. The lower solid line represents $V_{\text{eff},0}$ representing the correction for nuclear polarisation at short-range, and the +'s represent the *ab initio* points of Staemmler.

function and the isotropic radial functions reported here start to depart substantially from the function fitted by Kita *et al.* in the lower energy region of this energy range. The derivatives of the logarithms of the isotropic radial functions of our results and those of Gislason *et al.* are in excellent agreement. However the absolute values differed by an amount that is reasonably constant, suggesting that similar exponents would result when attempting to fit a potential of the form used by Kita *et al.*

We have used Billing's fitting procedure [123] and analytic expression [127], to fit our HF/6–311+G(2df) potential energy surface. Using 35 chosen points and minimising the error using Powell's method [148] in an identical manner to Billing, and using his parameters as starting values we have managed to reduce the fitting error to 4.5%. Further improvement resulted when using the values of the long-range multipole moments reported here as starting parameters. Replacing the quadrupole and hexadecapole moments with the values listed in table 6.1, and then minimising

Table 6.9: Critical points of the Legendre radial functions of Li^+—N_2.

critical points	HF	MP4SDTQ	Staemmler's	Gislason's	Waldman's
V_0					
R ,$(V_0 = 0)$	3.990[a]	3.979	3.932	3.928	3.836
$R, (\partial V_0/\partial R = 0)$	4.759	4.773	4.764	4.793	4.535
$V, (\partial V_0/\partial R = 0)$	−0.00870[b]	−0.00936	−0.01187	−0.01166	−0.00802
$R, (\partial^2 V_0/\partial^2 R = 0)$	5.450	5.481	5.738	5.644	—
V_2					
$R, (V_2 = 0)$	4.120	4.109	4,209	—	—
$R, (\partial V_2/\partial R = 0)$	4.990	5.002	5.024	—	—
$V, (\partial V_2/\partial R = 0)$	−0.01018	−0.01120	−0.00939	—	—
$R, (\partial^2 V_2/\partial^2 R = 0)$	5.620	5.640	5.858	—	—
V_4					
$R, (V_4 = 0)$	4.581	4.759	—	—	—
$R, (\partial V_4/\partial R = 0)$	5.294	5.457	—	—	—
$V, (\partial V_4/\partial R = 0)$	−0.00095	−0.00066	—	—	—
$R, (\partial^2 V_4/\partial^2 R = 0)$	5.651	6.411	—	—	—
V_6					
$R, (V_6 = 0)$	5.348	5.534	—	—	—
$R, (\partial V_6/\partial R = 0)$	6.211	6.189	—	—	—
$V, (\partial V_6/\partial R = 0)$	−0.00005	−0.00006	—	—	—
$R, (\partial^2 V_6/\partial^2 R = 0)$	6.996	6.942	—	—	—

[a] All bond distances in *bohr*.
[b] All energies in *a.u.* and relative to $R = \infty$.

again resulted in an error of only 2.1%. This is an improvement on Billing's attempt to fit Staemmler's HF surface when an error of 6.7% resulted. The optimised parameters are listed in table 6.10.

6.4.1 Nuclear Polarisation of Li^+—N_2

We have optimised the N_2 bond distance at short Li^+—N_2 distances to check if nuclear polarisation is important. Gislason [147] has commented that the nuclear

Table 6.10: Fitted parameters for Billing's potential.

$\bar{\alpha}^{ab}$	2.0626	B_{00}	−0.1322
β_{00}	0.7197	B_{20}	−86.7854
β_{02}	2.0082	α	9.9682
A_{00}	100.88	Q	−0.8110
A_{20}	250.37	H	−7.5793
A_4	48.046	$\frac{1}{3}(\alpha_{\parallel} - \alpha_{\perp})$	4.7821

[a] All parameters in *a.u.*
[b] Billing's formula

$$
\begin{aligned}
V(R,\theta) &= \sum_{k=0,2,4} V_k(R) P_k(\cos\theta) \\
V_0(R) &= A_{00}\exp(-\bar{\alpha}R) + B_{00}\exp(-\beta_{00}R) - \frac{1}{2}\alpha R^{-4} \\
V_2(R) &= A_{20}\exp(-\bar{\alpha}R) + B_{20}\exp(-\beta_{02}R) + QR^{-3} \\
&\quad -\frac{1}{3}(\alpha_{\parallel} - \alpha_{\perp})R^{-4} \\
V_4(R) &= A_4\exp(-\bar{\alpha}R) + HR^{-5}
\end{aligned}
$$

contribution to long-range polarisation effects is negligible, or nearly so, for small molecules such as N_2 and CO. However, with the approach of the Li^+ ion at short-range we should expect to see significant perturbation of the N_2 internuclear distance away from its equilibrium position and corresponding changes to the potential energy surface. Reoptimising the bond length of the N_2 species with the Li^+ ion species at $R = 2.75$ *bohr* with angles $\theta = 0°$, 45°, 90°, has resulted in absolute bond distance changes to r of −0.221, −0.062, and +0.005 *bohr*, respectively, at the HF level of theory. Associated with these changes in bond distances are decreases in energy when comparing the optimised bond distance values with the corresponding value obtained when the bond distance of the N_2 molecule was fixed to its equilibrium distance. The energy is lowered by 2.603, 0.119, and 0.001 eV at the HF level of theory and 1.609, 0.034 and 0.021 eV at the MP4SDTQ level of theory for the angles $\theta = 0°$, 45°, and 90° respectively. A pronounced decrease in the bond length (10%) occurs in the linear arrangement and a slight increase occurs in the perpendicular arrangement for $R = 2.75$ *bohr*. These results are in accord with those described by Staemmler. The decrease in the absolute energy from optimising the N_2 internuclear

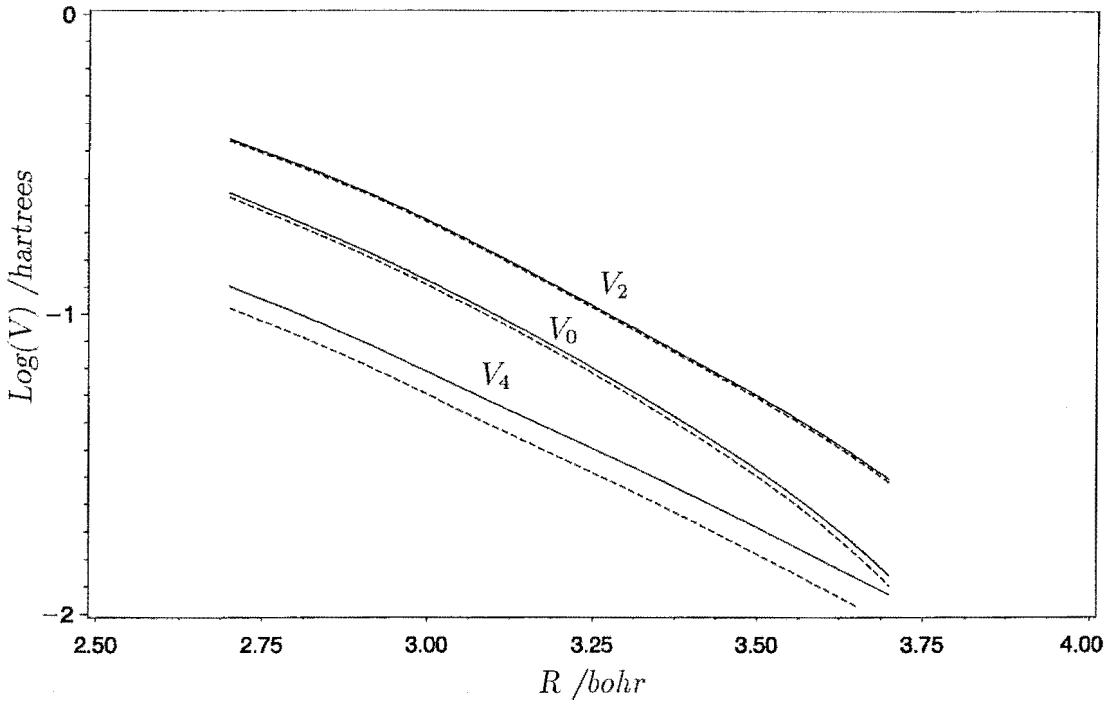

Figure 6.8: The short-range radial functions V_4, V_0, and V_2 of $Li^+ + N_2$ in order of increasing repulsion. The solid lines represent the rigid rotor radial functions. The short dashed lines represent the corrections for nuclear polarisation. Note that the gradients of the radial functions are similar at $R = 2.75$ *bohr*.

distance for the Li^+ ion at short-range appears to be over-estimated at the HF level of theory. A large part of this over-estimation is probably related to the failure of the HF approximation to provide accurate force-constants. We have examined the likely changes to the Legendre expansion functions due to nuclear polarisation. Using equation 6.5 to transform these changes to the potential energy surface at $R = 2.75$ *bohr* has resulted in a lowering of energy to the radial functions. The energy is lowered by 0.374, 0.448, and 0.579 eV at the HF level of theory and by 0.195, 0.050, and 0.448 eV at the MP4SDTQ level of theory for the radial functions V_0, V_2, and V_4, respectively. To account for the effect of nuclear polarisation on the Legendre radial functions we have fitted an analytic function of the form of equation 6.7 to correct the rigid rotor surface.

$$V_{\text{eff},n} = V_n - V_{np,n} \tag{6.6}$$

$$V_{np,n} = (V_n - V_{opt,n}) \exp\left[-\alpha(R - r_{np})\right] \tag{6.7}$$

We have calculated the correction for nuclear polarisation at $r_{np} = 2.75$ *bohr*,

and we have approximated α with that reported by Kita *et al.* [125] (2.127 $bohr^{-1}$) for the radial functions V_0, V_2, and V_4 because log-linear plots of the potential as a function of R reveal similar slopes (see figure 6.8). We have not attempted to theoretically justify this analytic form. However this function is in accord with Staemmlers description of nuclear polarisation at short-range, is physically reasonable, and is exact at $R = 2.75$ $bohr$. With this expression we have avoided expensive calculations optimising r as a function of R, and θ. The values of $(V_n - V_{opt,n})$ are given in table 6.11, and $V_{\text{eff},0}$ is plotted in figure 6.7. Comparing the isotropic

Table 6.11: Parameters to correct for nuclear polarisation of Li^+—N_2.

	HF	MP4SDQ	MP4SDTQ
$(V_0 - V_{opt,0})$	0.01375[a]	0.00751	0.00716
$(V_2 - V_{opt,2})$	0.01646	0.00512	0.00183
$(V_4 - V_{opt,4})$	0.02128	0.01745	0.01648

[a]All parameters in $a.u.$

radial function which has been corrected for nuclear polarisation with the experimentally derived isotropic radial function of Gislason shows improved agreement at short-range. Our corrections for nuclear polarisation have only slightly perturbed the values of the critical points listed in tables 6.6 and 6.9. The relative features have all remained similar to the uncorrected potential energy surface and the most significant differences appear at short-range.

Estimation of the Basis Set Superposition Error (BSSE) by counterpoise correction has been examined for a few points on the potential energy surface. Previous experience with atomic ion-atom systems has shown these effects on the potential energy surface to be comparatively small in the area about the well, and even less significant elsewhere. To fully calculate the BSSE by counterpoise correction for the entire potential energy surface is prohibitively expensive and we estimate that the correction would decrease the well depth of the isotropic radial function by less than 10%. Similar absolute corrections would result for V_2, and V_4.

6.5 Conclusion

Ab initio calculations for the potential energy surface for the the Li^+—N_2 interaction at the HF and MP4SDTQ levels of theory with a 6–311+G(2df) basis set have been performed. We have selected our basis set and method in optimised agreement between the calculated and experimental electrical properties of the isolated sub-units. The calculated quadrupole moment, perpendicular and parallel polarisabilities for the N_2 sub-unit differ from the experimentally reported values by 5.8%, 15.9%, and 4.6%, respectively. The long-range interaction of the Li^+—N_2 system agrees well with the isotropic radial function derived from total scattering cross-sections reported by Gislason *et al.* [131]. The isotropic radial function has a well depth of 0.256 eV at 4.805 *bohr* at the MP4SDTQ level of theory. This is 19.4% less deep than Gislason's result. The short-range isotropic radial function corresponds well with Gislason's derived isotropic radial function although our values are more repulsive. This is explained to some extent by re-optimising the N_2 bond length on approach of the Li^+ ion.

Chapter 7

Cross Sections and Transport Numbers of Li^+—N_2

7.1 Introduction

The study of ion/neutral molecular interactions is important in a wide variety of fields of research including atomic and molecular physics, aeronomy, atmospheric chemistry, gaseous electronics and laser physics. The interaction of atomic ions with diatomic neutrals is particularly important in the f region of the ionosphere [106]. Laboratory measurements of the reaction kinetics of these systems requires reliable values of ion mobilities and diffusion coefficients, and this is why there is considerable interest in the transport properties [107, 149] of these systems. Calculation of the interaction potential of spherically symmetric ions with inert gas atoms, and the transport properties of these ions in these gases to an accuracy comparable to the best experimental values is now routine. Although a large amount of experimental transport numbers involving more complex molecular ion/molecular neutral systems exists, the theoretical understanding of these systems is less advanced. Recent theoretical advances [44, 58] in the kinetic theory of the transport properties of atomic ion/diatomic neutral systems should help exploit some of the information contained in the experimental data.

The fundamental quantity describing transport properties of atomic ions in diatomic neutrals is the potential energy surface. Accurate information about such interactions is limited mainly because of the difficulty of inferring surfaces from

measurements of scattering and transport data, and in the difficulty of calculating with sufficient precision the entire potential energy surface using *ab initio* methods. While *ab initio* methods are the most likely source of reliable information on the potential energy surface of atomic ion/diatomic neutrals, these methods until relatively recently have been prohibitively expensive to use.

In chapters 6 and 8 the rigid rotor potential energy surface of two spherically symmetric ion/diatomic neutral systems have been characterised. These two potential energy surfaces contribute to only a handful of high level *ab initio* calculations available for systems where the diatomic neutral is not hydrogen, or a hydride.

Kinetic theory capable of describing transport properties of molecular systems was first proposed by Viehland *et al.* [53], and based on the Wang Chang-Uhlenbeck-de Boer (WCUB) equation. The WCUB equation, in which the internal states of the species were treated quantum-mechanically and the translational states are treated classically, proved impossible to implement due to the difficulty of calculating reliable cross section without compromising approximations [55, 150]. The difficulties experienced using the semi-classical approach of the WCUB equation may be unnecessary, because it seems likely in certain systems that classical mechanics should perform with reasonable accuracy provided that

- the only electronic and vibrational energy levels accessible to the swarm experiments are the lowest energy ones;
- the rotational levels of the diatomic molecule are so closely spaced that they are well approximated by classical mechanical rigid rotors;
- the translational energy levels are sufficiently close that they appear to be continuous as in the classical limit.

Several authors [49, 50] have attempted to simplify the theory and implementation of transport calculations by using effective spherical interaction potentials. These spherical interaction potentials represent averages of the potential energy surface over orientation. While this approach can directly reproduce neutral atom/diatom transport properties, the spherical interaction potential bears no direct information about the true potential energy surface . Viehland [52] has attempted to use a spherical interaction potential to determine transport properties of atomic ion/diatom systems and concluded,

> "The spherical components of the ion-neutral interaction potentials fail to reproduce gaseous ion transport data."

This is not surprising as spherical interaction potentials inferred from transport properties of neutrals cannot reproduce the temperature variation observed in these systems. In ion/neutral systems the effective temperature of the ion can be varied over a wide range by altering the strength of E/N, and therefore it is unlikely that spherical interaction approximation of the potential energy surface will provide any relevant information.

Having accepted classical mechanics in deriving the kinetic theory of atomic ion/diatom systems it remains to adopt a regime for the calculation of the transport cross sections. Again it seems highly likely that classical mechanics will be sufficiently accurate to describe the ion transport cross sections provided that the systems studied do not include molecular hydrogen or any of its ionic or isotopic forms, and are not at low temperature. Pack [151] has compared cross sections calculated by classical trajectory methods with full quantal and approximate cross sections for the Ar—N_2 systems, and concluded that,

> "... the popular belief that the rotational motion of non-hydride diatomic molecules is essentially classical at room temperature is justified."

These results have been supported by Dickinson and Lee [60], and a further study of the transport properties of the He–N_2 system [61]. The neutral He–N_2 is analogous and isoelectronic to the ion/neutral system Li^+—N_2 . Note also that because ion transport properties are determined by integrals over both elastic and inelastic collision, the errors in the smaller inelastic cross section, where classical mechanics performs poorly, will probably be masked in the averaging process.

The aim of the chapter is test the accuracy of the interaction potentials in chapter 6 by comparing the experimental values of the ion transport coefficients with those derived from the potential energy surface for the Li^+—N_2 system. This is to be achieved by using classical trajectory methods to calculate the transport cross sections and to use these in conjunction with recent classical kinetic theory [44] to calculate the transport coefficients. This kinetic theory was based on the diatom/diatom kinetic theory of Curtiss [56] and restricted to atomic ions in non-vibrating diatomic gases, or non-vibrating diatomic ions in atomic or diatomic gases.

Providing that the calculations of ion transport properties exclude systems including molecular hydrogen and its ionic and isotopic analogues, and that the calculations are not at low temperature it should be possible to attain an accuracy of $> 1\%$ for the transport coefficients [62], rivalling the experimental accuracy [132].

In section 7.2 the details of the trajectory calculations are outlined followed by the calculations of the transport cross sections. In the following section the transport calculation is described which in turn is followed by a discussion of the results. Finally a conclusion is given in section 7.4.

7.2 Classical Trajectory Calculation of Li^+—N_2

Classical Trajectory methods have been widely used in physical problems concerning scattering theory. Ernest Rutherford, perhaps New Zealands' foremost scientist, used one of its earliest applications and proposed the "nuclear atom" model of matter based on its results. Classical trajectory methods are widely used in the areas of nuclear, atomic and molecular scattering, and several reviews exist [152, 153, 154]. Classical trajectory methods work adequately provided that quantum effects, such as tunnelling and interference are not important. Pattengill [152] has published a table concerning atom/diatom scattering results in which classical and quantal scattering results were compared. The correspondence between the scattering methods was sufficient for Pattengill to conclude,

> "... the results indicate that, used with caution, the classical trajectory method can provide a useful approximation at collision energies somewhat above the threshold for rotational excitation."

This is in agreement with Miller [155], who argued that interference and tunnelling effects are rapidly quenched in averaged collision properties such as cross sections. It must be noted that the worst correspondence for the classical and quantal cross sections occurred for systems in which H_2 or a hydride was the diatom, and good correspondence resulted for systems where N_2 or CO was the diatom.

Classical trajectory methods are required to calculate the transport cross sections defined in equations 7.1 and 7.2, for input into the kinetic theory implementations `BIMAX` and `MOBDIF` respectively.

$$Q^{(\lambda,\nu)}(\epsilon) = \frac{1}{kT}\int_0^\infty \mathrm{d}\epsilon_0 \exp\left(-\frac{\epsilon_0}{kT}\right) q^{(\lambda,\nu)}(\epsilon,\epsilon_0), \tag{7.1}$$

$$\Sigma^{(\lambda,\nu)}(\epsilon) = \frac{1}{kT}\int_0^\infty \mathrm{d}\epsilon_0 \exp(-\frac{\epsilon_0}{kT})\sigma^{(\lambda,\nu)}(\epsilon,\epsilon_0). \tag{7.2}$$

These cross sections represent integrations over rotational energy of the integrand which are defined in equations 7.3 and 7.4.

$$q^{(\lambda,\nu)}(\epsilon,\epsilon_0) = 2\pi\int_0^\infty \mathrm{d}b\frac{b}{2}\int_{-1}^{+1}\mathrm{d}\cos\chi\frac{1}{2\pi}\int_0^{2\pi}\mathrm{d}\phi_L\frac{1}{\pi}\int_0^\pi \mathrm{d}\phi_j \times\left[1-\left(\frac{\epsilon'}{\epsilon}\right)^{\nu+\lambda/2}P_\lambda(\cos\Theta)\right] \tag{7.3}$$

$$\sigma^{(\lambda,\nu)}(\epsilon,\epsilon_0) = 2\pi\int_0^\infty \mathrm{d}b\frac{b}{2}\int_{-1}^{+1}\mathrm{d}\cos\chi\frac{1}{2\pi}\int_0^{2\pi}\mathrm{d}\phi_L\frac{1}{\pi}\int_0^\pi \mathrm{d}\phi_j \times\left[1-\left(\frac{\epsilon'}{\epsilon}\right)^{\lambda/2}(\cos\Theta)^\lambda\right]\left(\frac{\epsilon'}{\epsilon}\right)^{\nu}(\sin\Theta)^{2\nu} \tag{7.4}$$

In these integrals, Θ the scattering angles of the collision and ϵ', the post-collisional kinetic energy depend upon the pre-collisional kinetic ϵ and the pre-collisional rotational energy ϵ_0, the impact parameter b, the angle χ between the rotational angular momentum of the diatom, j, and the angular momentum of the relative motion of the collision, L, and the angles conjugate to j and L, namely ϕ_j and ϕ_L respectively. The values of Θ and the post-collisional kinetic energy ϵ' for a given set of starting conditions are obtained with a trajectory calculation. Dickinson and Viehland [62] have modified the Newcastle Trajectory program [156] so that it could treat atomic ion/diatom systems in order to calculate the cross sections defined above. This is achieved by integrating Hamiltons equations using the action-angle variables defined by Smith [63]. Smith defined the classical Hamiltonian for rotationally inelastic atom/diatom scattering as

$$H = \frac{P_R^2}{2\mu} + \frac{L^2}{2\mu R^2} + \frac{j^2}{2I} + V(R,\theta), \tag{7.5}$$

where H represents the classical Hamiltonian, R and P_R represent the conjugate radial coordinate of the collision and its momenta, L represents the orbital angular momentum of the collision pair, j represents the rotational angular momentum of the diatom, and μ and I represents the reduced mass of the atom/diatom collision

and the moment of inertia of the diatom respectively. The potential energy surface is represented as $V(R,\theta)$, which is a function of R, and θ, the angle between R and the inter nuclear vector of the diatom. The action-angle variables were defined and their first derivatives, which are required for numerically solving Hamiltons many bodied equations of motion, are listed in Appendix A of Smiths' paper [63]. The use of action-angle variables allows the reduction of the physical problem to a system of least dynamical variables, and greater economy. Other modifications to the Newcastle trajectory program allowed the initial and final separations of the particles to be much greater. Because the long-range charge-multipole interactions of the ion-molecule systems decrease much more slowly as a function of radial distance the trajectories must be started at larger separation, R_s, and followed until they are again separated by this distance. Also because the well depths of ion-molecule systems are substantially larger compared to neutral systems, and the differences in the long-range interaction region, the trajectories become more convoluted and longer in duration requiring greater precision of the integrating procedure. The code was also modified to calculate the cross sections defined above with a general potential energy surface for any atom/diatom scattering problem.

Numerical evaluation of the integrals defined in equation 7.3 and 7.4 require trajectory calculations for given values of ϵ and ϵ_0. The problem of attaining reasonable cross sections then becomes a trade off between the accuracy required for the application and the number of trajectories needed and therefore of computer time available. In order to minimise the numerical effort required involved a study of a particular potential energy surface of a given system. Initially the study of the Li^+—N_2 system was performed with the use of Billings' potential energy surface. The cross sections were calculated in the following way. The integration over the impact parameter b, was divided at b_s into two separate regions. The smaller impact parameter region was integrated using N1 Gauss-Legendre quadrature points over b^2. In the larger impact parameter region N2 trajectories of b were calculated and the integrals from 0 to ∞ were evaluated by Gauss-Legendre quadrature over the variable y defined by equation 7.6,

$$b = b_s\left(1 - c + \frac{c}{\sqrt{y}}\right) \tag{7.6}$$

where c is a chosen constant. The trajectories are evaluated using N3 values of χ, N4 values of ϕ_L, and N5 values of ϕ_j. The number of the angle values were chosen to minimise the error when evaluated by Gauss-Legendre quadrature. The trajectories are then calculated using the parameters b_s, R_s, c, N1, N2, N3, N4, N5, and ACC, the accuracy parameter of the NAG[1] routine D02CAF which was used to integrate Hamilton's first order equations by a variable order variable step Adams method. These parameters were then systematically varied in order to achieve accurate cross sections, as detailed in the following sub-section.

7.2.1 Calculations of Accurate Cross Sections

Table 7.1 displays the numerical effect of varying the ACC parameter on the values of a few cross sections selected from the 84 calculated. These cross sections were calculated for a total energy of 0.95085 *a.u.* and a kinetic energy of 0.95001 *a.u.*, with R_s= 40 *a.u.*, b_s = 6.0 *a.u.*, c = 0.3, N1=N2=3, and N3=N4=N5=2. Thus it required a total of (N1+N2)×N3×N4×N5=48 trajectories to calculate a set of cross sections. This is a relatively trivial numerical task, requiring a few CPU seconds on an IBM RISC/6000. From surveying the 84 cross sections calculated with program TRAJECK it was concluded that the variable of ACC= 1×10^{-8} was of sufficient accuracy to converge the cross sections to within a fraction of a percent.

Table 7.1: Effect upon transport cross sections of varying the accuracy parameter.

ACC	1×10^{-7}	1×10^{-8}	1×10^{-9}
$q^{(1,0)}$ (a.u.)	14.3681	14.3633	14.3628
$q^{(3,1)}$ (a.u.)	29.4776	29.4352	29.4305
$q^{(12,6)}$ (a.u.)	36.1702	36.0398	36.0254

Table 7.2 summarises the effect of increasing the number of impact parameters, N1 and N2. The ACC parameter was chosen to be 1 $\times10^{-8}$ while all other parameters had the same values as that chosen for table 7.1. From the values of the cross sections it was concluded that at least 12 smaller impact parameters and 3 higher impact parameter values were required to achieve convergence of a few fractions of a percent.

[1] Numerical Algorithms Group

Table 7.2: Effect upon transport cross sections of varying the number of impact parameters sampled.

Lower values	3	4	5	6
Higher values	3	3	3	3
$q^{(1,0)}$ $(a.u.)$	14.3633	15.8362	15.6511	15.6511
$q^{(3,1)}$ $(a.u.)$	29.4352	24.5157	22.9022	23.4102
$q^{(12,6)}$ $(a.u.)$	36.0398	43.9737	48.5140	36.4527
Lower values	8	10	12	12
Higher values	3	3	3	4
$q^{(1,0)}$ $(a.u.)$	15.7084	15.7134	15.7133	15.7133
$q^{(3,1)}$ $(a.u.)$	23.1240	23.0806	23.0888	23.0902
$q^{(12,6)}$ $(a.u.)$	45.3013	41.2331	44.4879	44.4743

Table 7.3 summarises the effect of changing c with N1=12, N2=3. The other parameters were the same as the those used in obtaining the cross section in table 7.2. It was concluded that the choice of c was not important in obtaining reliable cross sections.

Table 7.3: Effect upon transport cross sections of varying the parameter c.

c	0.3	0.4	1.0
$q^{(1,0)}$ $(a.u.)$	15.7133	15.7127	15.7136
$q^{(3,1)}$ $(a.u.)$	23.0888	23.0859	23.0923
$q^{(12,6)}$ $(a.u.)$	44.4879	44.4583	44.4874

Table 7.4 summarises the effect of increasing the number of angles sampled, when c=1.0. The other parameters were the same as those used in obtaining the results in table 7.2. It was concluded that adequate accuracy of the cross sections is achieved by sampling 6 angles at each of the three angular quadratures, χ, ϕ_L, and ϕ_j.

Table 7.5 summarises the effect of changing R_s. The values of N3=N4=N5=6, while all other parameters were set to the values used in obtaining the cross sections as given in table 7.4. It was concluded that the cross section values had converged to within a few tenths of a percent provided that the starting separation was at least 80 $a.u.$

Table 7.6 summarises the effect of changing b_s. The value of R_s used to calculate these cross sections was 80 $a.u.$ while all other parameters were equal to the values

Table 7.4: Effect upon transport cross sections of varying the number of angles sampled for each of the angular quadratures.

Angles	2×2×2	4×4×4	6×6×6	8×6×6	6×8×6	6×6×8
$q^{(1,0)}$ (a.u.)	15.7103	16.0476	16.0427	16.0428	16.0431	16.0429
$q^{(3,1)}$ (a.u.)	23.0657	23.0064	23.0074	23.0067	23.0092	23.0111
$q^{(12,6)}$ (a.u.)	44.4042	43.9595	43.7619	43.7651	43.7410	43.7226

Table 7.5: Effect upon transport cross sections of varying the initial (and final) separations of the trajectories.

$R_s(a.u.)$	40.0	50.0	60.0	70.0	80.0	90.0	100.0
$q^{(1,0)}$ (a.u.)	16.0427	16.0465	16.0442	16.0452	16.0498	16.0487	16.0562
$q^{(3,1)}$ (a.u.)	23.0074	23.0511	23.0414	23.0509	23.0855	23.0771	23.1386
$q^{(12,6)}$ (a.u.)	43.7619	43.8662	43.7296	43.8307	44.0154	43.9541	44.0226

used in obtaining the cross sections in table 7.5. It was concluded that splitting the cross sections at $b_s = 7.0$ *a.u.*allowed adequate accuracy in each impact parameter region.

Table 7.6: Effect upon transport cross sections of varying the impact parameter separating the low- and high- impact parameter regions.

$b_s(a.u.)$	5.0	6.0	7.0	8.0
$q^{(1,0)}$ (a.u.)	16.0466	16.0498	16.0463	16.0243
$q^{(3,1)}$ (a.u.)	23.0600	23.0855	23.0926	23.1805
$q^{(12,6)}$ (a.u.)	43.8751	44.0154	44.0628	43.6725

Table 7.7 extends the survey results of table 7.2. The value of b_s used to calculate these cross sections was 7.0 *a.u.*, and all other parameters used, except N1 and N2, were equal to the values used to obtain the cross sections of table 7.6. It was concluded from table 7.7 and from a similar analysis of the results obtained when $b_s = 80$ *a.u.*, that 20 low- and 4 high-impact parameters must be retained.

The results of tables 7.1 through 7.7 have determined the parameters that allow the accurate calculation of the cross sections defined in equations 7.3 and 7.4. The kinetic theory calculation of the transport coefficients require the rotationally averaged transport cross sections defined in equations 7.1 and 7.2 respectively.

Table 7.7: Effect upon transport cross sections of varying the number of impact parameters sampled.

Low values	10	12	14	16	20
High values	4	4	4	4	4
$q^{(1,0)}$ $(a.u.)$	16.0463	16.0491	16.0499	16.0497	16.0499
$q^{(3,1)}$ $(a.u.)$	23.0926	23.0997	23.0864	23.0834	23.0770
$q^{(12,6)}$ $(a.u.)$	44.0628	41.4012	43.8982	42.7500	42.7981

These have been evaluated by replacing ϵ and ϵ_0 by the quantities

$$y = \frac{\epsilon}{k_b T} \tag{7.7}$$

$$w = \frac{\epsilon_0 - \epsilon}{\epsilon_0 + \epsilon}. \tag{7.8}$$

The integrals were split at the value

$$w_s = \frac{1-y}{1+y} \tag{7.9}$$

and evaluated by N6-point Gauss-Legendre integration in the low w region and by N7-point Gauss-Laguerre integration at high w. The Gauss-Laguerre integration was over the new variable

$$x = y\frac{1+w}{1-w}. \tag{7.10}$$

Table 7.8 summarises the results obtained. Since the transport coefficients are dominated by the rotationally averaged momentum-transfer cross section, and since the rotationally averaged cross sections with higher indices occur only in the higher order approximations of the transport coefficients, it was concluded that the choice of parameters in the last column of table 7.8 represents the least number of trajectories required to calculate the transport coefficients with an accuracy of a few tenths of a percent for Billings' potential energy surface.

Extensive tests have been performed for the accuracy of the cross sections similar to those demonstrated in table 7.1 through 7.8 at several other values of ϵ. Table 7.9 summarises these results for the different orders of ϵ for Billings' potential energy surface.

The results for Billings' potential outlined in table 7.9 were used as a basis from which to calculate the cross sections for the MP4SDTQ/6–311+G(2df) potential

Table 7.8: Effect upon rotationally-averaged transport cross sections of varying the parameters listed.

ACC	1×10^{-7}	1×10^{-8}	1×10^{-8}
R_s $(a.u.)$	60.0	80.0	80.0
b_s $(a.u.)$	8.0	8.0	8.0
b values	10+3	16+3	20+4
Angular quadratures	8×7×7	10×8×8	6×6×6
w values	3+3	3+3	4+4
$\Sigma^{(0,1)}$ $(a.u.)$	14.0822	13.9893	13.9877
$\Sigma^{(1,0)}$ $(a.u.)$	16.0538	16.0456	16.0361
$\Sigma^{(11,0)}$ $(a.u.)$	745.6147	890.5279	925.7402
$\Sigma^{(11,7)}$ $(a.u.)$	13.6138	10.4640	9.2985

Table 7.9: Summary of Li^+—N_2 trajectory parameters used for Billings' potential energy surface.

Range of ϵ (10^{-3})	< 3	3-9.5	9.5-95	> 95
Number of ϵ values	2	5	8	8
Number of ϵ_0 values	16	12	10	8
R_s $(a.u.)$	150	120	100	80
b_s $(a.u.)$	6.0	5.0	4.0	3.0
c	1.0	1.0	1.0	1.0
N1 and N2	20+6	20+6	20+5	20+4
N3=N4=N5	12	10	8	6
Number of trajectories	1437696	1560000	1024000	331776

energy surface presented in chapter 6, because of the similarities of the two surfaces. The actual parameters used to calculate the transport cross sections for the MP4SDTQ/6–311+G(2df) potential energy surface are given in table 7.10.

Note that for the MP4SDTQ/6–311+G(2df) potential energy surface calculations of the cross section the values of b_s are larger than those used for Billings' potential energy surface. These values were chosen after careful examination of table 7.7 at smaller energies. Figure 7.1 displays some selected rotationally averaged transport cross sections for Li^+ ions in N_2 gas at 300°K, as a function of the relative kinetic energy. These cross sections have been defined by equation 7.1, and are qualitatively the same as for atomic ion/atom systems, except at low energies where super-elastic collisions, ie collisions which result in transfer of rotation energy of the

Table 7.10: Summary of Li^+—N_2 trajectory parameters used for the MP4SDTQ/6–311+G(2df) potential energy surface.

Range of ϵ (10^{-3})	< 9.5	9.5-95	> 95
Number of ϵ values	6	8	15
Number of ϵ_0 values	12	10	8
R_s $(a.u.)$	120	100	80
b_s $(a.u.)$	10.0	9.0	8.0
c	1.0	1.0	1.0
N1 and N2	20+6	20+5	20+4
N3=N4=N5	10	8	6
Number of trajectories	1872000	1024000	622080

diatom into kinetic energy of the ion results, become important (see figure 7.1).

Transport cross section calculations of two different potential energy surfaces were performed, namely Billings' potential energy surface , and the MP4SDTQ/6–311+G(2df) potential energy surface. The MP4SDTQ/6–311+G(2df) potential energy surface was modified to account for nuclear polarisation at short separations. Because most of the numerical effort in calculating a set of transport cross sections involved the lower energy cross sections, and because the modified potentials only differ significantly at separations which are probed only by very energetic ion-neutral collisions, it is possible to combine the cross sections at high energy calculated with a modified potential energy surface with cross sections at low energy calculated from the unmodified MP4SDTQ/6–311+G(2df) potential energy surface with negligible error. All low energy calculations of the cross sections were derived from the unmodified MP4SDTQ/6–311+G(2df) potential energy surface , and combined with three separate calculations of the high energy cross sections. They were derived firstly from the unmodified potential energy surface, and secondly from taking nuclear polarisation into account for the HF corrections, and finally from taking nuclear polarisation into account for the MP4SDQ corrections as outlined in section 6.4.1 of chapter 6. These potential energy surfaces will be referred to as GHM, GHM1, and GHM2 respectively. The final cross sections for the GHM1 surface are plotted in figure 7.1 as a function of relative kinetic energy.

The maximum error estimate for the calculation of the cross section detailed is less than half of 1 percent. The parameters listed in table 7.10 represent the

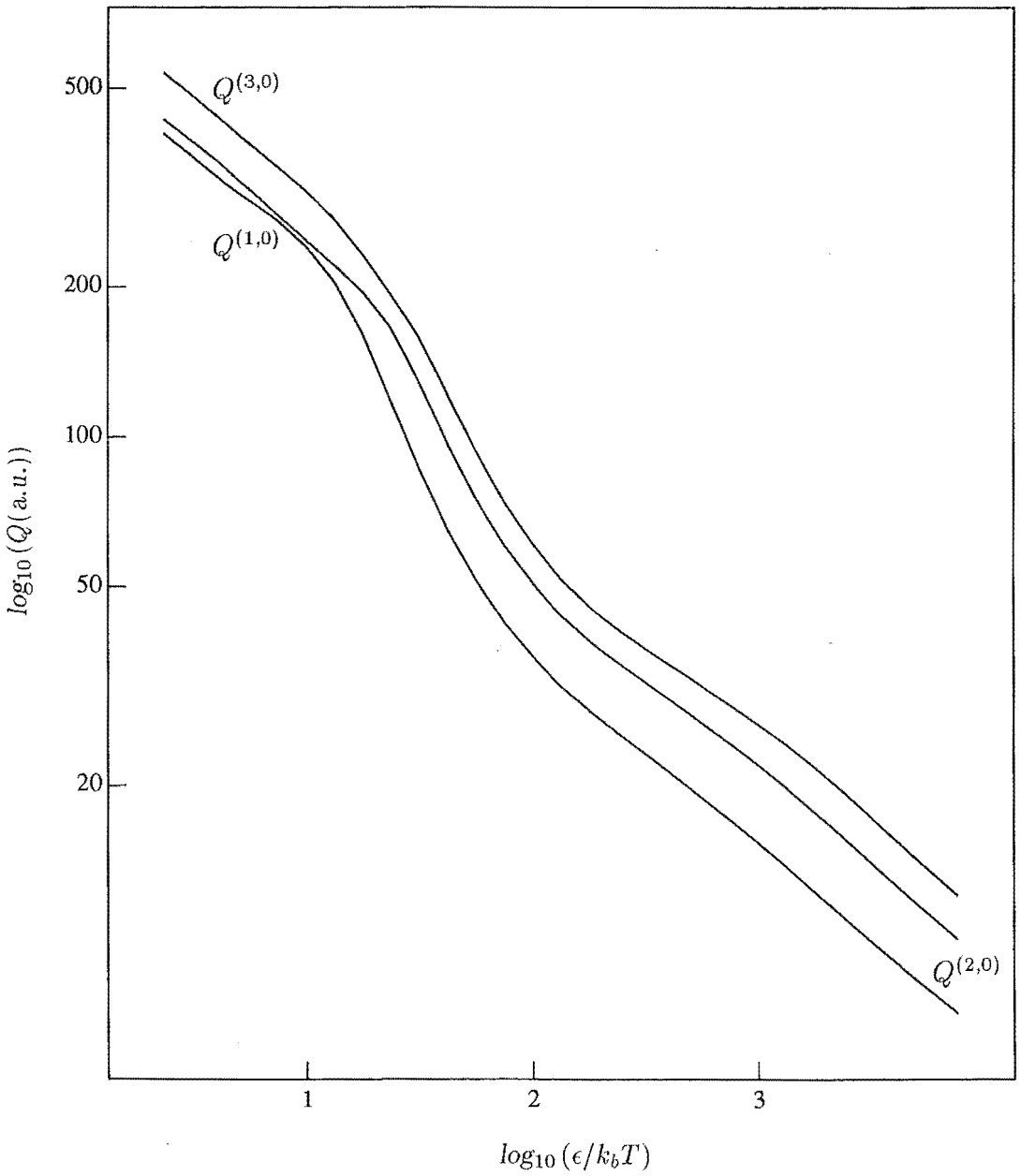

Figure 7.1: The rotationally averaged transport cross sections of Li^+ ions in N_2 gas, as a function of the dimension-less relative kinetic energy. The transport cross sections are plotted as $\log_{10}$ and in *a.u.*The transport cross section curves for the cross sections $Q^{(1,0)}, Q^{(2,0)}$, and $Q^{(3,0)}$ are labelled in the figure. These cross sections have been calculated with the GHM1 potential energy surface (see section 7.3 for an explanation).

minimum number of trajectories required to achieve this numerical accuracy. This number of trajectories in themselves represent a formidable numerical task for a single processor. For example these trajectories can require up to 2 months CPU time on a RISC/6000. Cochrane and Truhlar [157] have examined the viability of using vector pipeline supercomputers (CRAY-1) for solving the problem of classical atom/diatom collisions. They have concluded that re-organisation of code can double the rate of calculation of the trajectory calculations. Viehland [64] intends to use this strategy to improve the efficiency of calculating these cross sections. Efficiency gains of this order are required to make these calculations practical, however such calculations are limited to sites that have access to supercomputers.

7.3 Transport Coefficients of Li^+—N_2

The transport coefficients of Li^+ ions in N_2 gas have been experimentally measured by several groups in the mid seventies [158, 159, 160]. The measurements of the mobility and diffusion coefficients were not in agreement due to the influence that fast clustering reactions had on arrival time distributions. It was not until relatively recently that consistent and accurate values have been available [161, 132].

The trajectories summarised in table 7.9 and 7.10 were used to calculate the rotationally averaged cross sections defined in equations 7.1 and 7.2 for Billings' [123] and the MP4SDTQ/6-311+G(2df) potential energy surface outlined in chapter 6 respectively. The rotationally averaged cross sections defined by equations 7.1 and 7.2 were then used as input into the programs `BIMAX` [162] and `MOBDIF` [58] respectively in in order to calculate the transport coefficients of Li^+ ions in N_2 gas at $T = 300°K$, as a function of E/N.

7.3.1 Transport Coefficients Calculated from Billings' Potential Energy Surface

The initial study of the transport properties Li^+ ions in N_2 gas used Billings' potential energy surface. The mobility calculated from Billings potential energy surface using the trajectory calculations reported by Viehland [62] is plotted in figure 7.2, and the diffusion coefficients are plotted in figure 7.3. The reduced

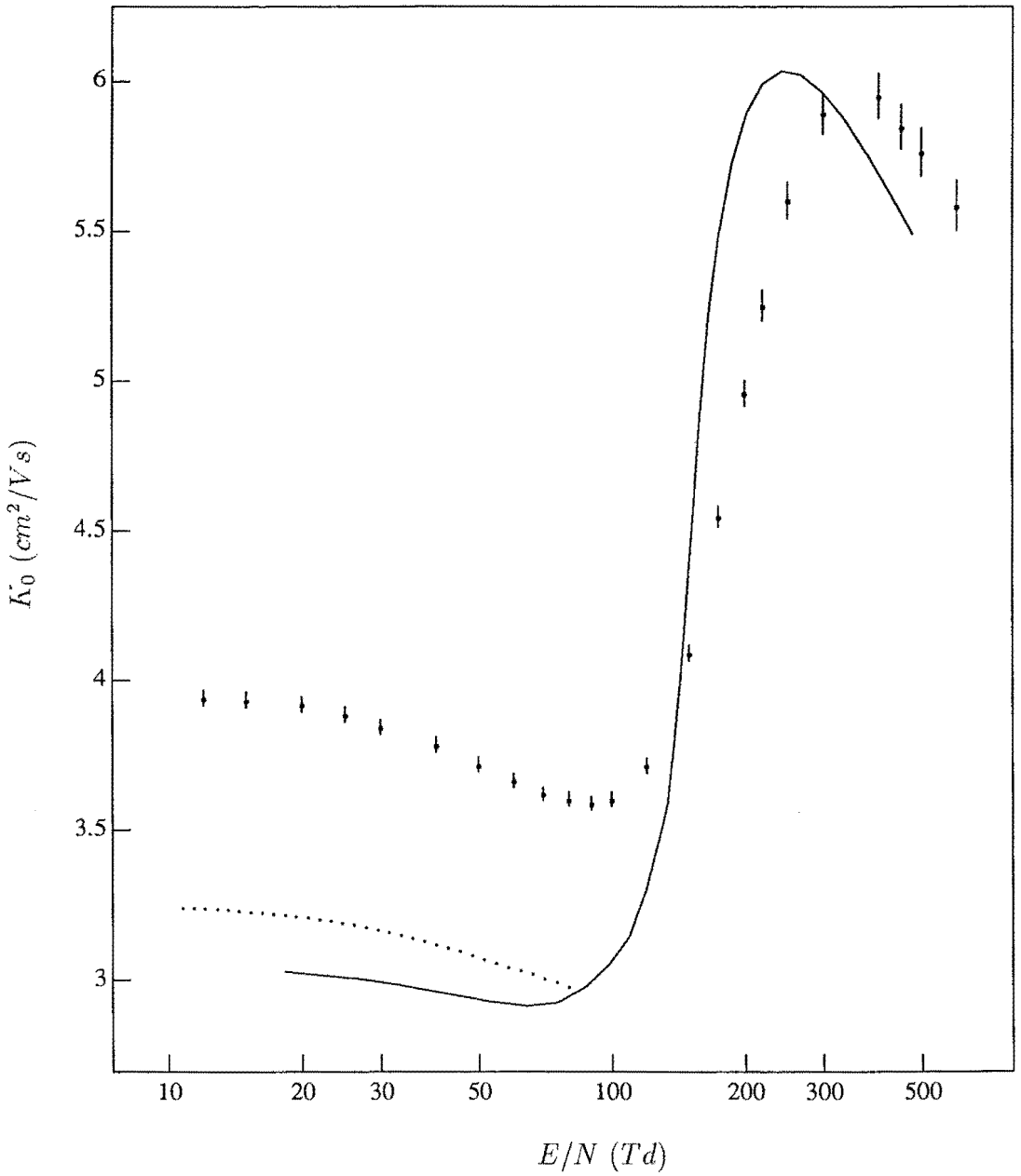

Figure 7.2: The mobility of Li^+ ions in N_2 gas calculated using Billings potential energy surface, at T=300°K, as a function of E/N in units of Td. The points with error bars are the experimental data of Selnæs *et al.* [132]. The solid curve was calculated with the program `BIMAX` , using the cross sections calculated using the parameters as outlined in table 7.9. The dotted curve was calculated using the program `MOBDIF` with the same parameters as for the `BIMAX` calculation using the cross sections defined in equation 7.2.

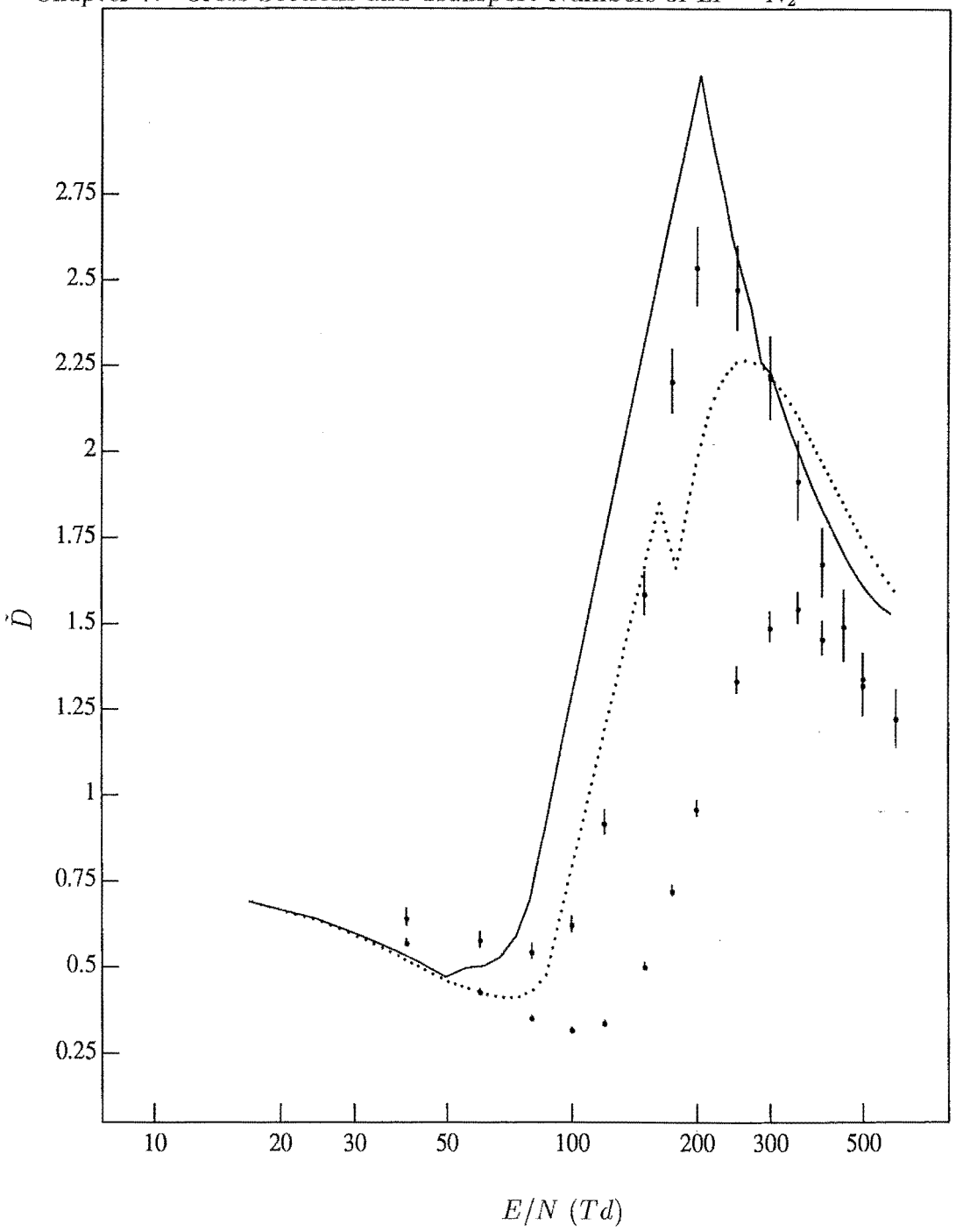

Figure 7.3: The reduced diffusion coefficients of Li^+ ions in N_2 gas calculated using Billings' potential energy surface, at T=300°K, as a function of E/N in units of Td. The points with error bars are the experimental data of Selnæs *et al.* [132]. The solid curve, representing the reduced parallel diffusion coefficient, was calculated with the program `BIMAX`, using the cross sections calculated using the parameters as outlined in table 7.9. The dotted curve, representing the reduced perpendicular diffusion coefficient, was calculated in the same way. Note that the curves were not smoothed in the region of inconvergence that the error associated with the reduced perpendicular diffusion coefficient is similar to the experimental error, while the error for the reduced parallel diffusion coefficient is substantially larger. The reduced diffusion coefficients are dimensionless and defined by equation 7.11.

diffusion coefficients are dimension-less and are defined by Viehland and Mason [67] as

$$\tilde{D} = qD_{\|,\perp}/K_{\rm pol}k_BT_{\rm pol}, \tag{7.11}$$

where $T_{\rm pol}$ is defined as

$$k_BT_{\rm pol} = kT + \frac{1}{3}M(K_{\rm pol}E)^2, \tag{7.12}$$

where k_B is Boltzmann constant, q is the ionic charge, $K_{\rm pol}$ is the limiting mobility at T= 0°K, and $E/N = 0\ Td$ where the interaction potential is dominated by the long-range polarisation interactions, and $T_{\rm pol}$ is the corresponding effective ion temperature at the actual values of T and E/N. Equation 7.11 removes the quadratic dependence of the diffusion coefficients on E/N, and allows a better comparison of the effect of the fundamental quantity of this study, the potential energy surface.

To assess the degree of agreement between the theoretically and experimentally derived results, and hence the validity of the potential energy surface, an estimate of the error of the calculations are required. In these calculations errors can come from several sources. The two main sources are discussed below. Firstly, the main source of this error results from the finite number of trajectories used to calculate the transport cross sections. These errors have been extensively discussed in section 7.2.1. Secondly, Viehland has estimated the error due to the stability of the kinetic theory series in calculation of the transport coefficients, and these values have been altered and refined with further calculations and the results are given in table 7.11. Finally, the estimated accuracy of this theoretical calculation is 1% conservatively, assuming complete convergence and that the system behaves classically. Note also that the two theoretically derived mobility curves do not agree at low E/N because the `BIMAX` calculations only used cross sections above 0.003 *a.u.*, while the `MOBDIF` calculations used cross sections as low as 0.00017 *a.u.* Viehland [62] has estimated that the error from including and excluding the lowest energy cross sections using the `MOBDIF` program to be increased to 6% at the lowest values of E/N, and to be not more than 2% above 80 Td.

Reconsidering figures 7.2 and 7.3 with the given estimates of error it is apparent that the differences between the experimental and theoretical data sets are due to the inaccuracy of Billings' rigid rotor potential energy surface. Further, it can be concluded that the inaccuracies are greatest at large and small internuclear

Table 7.11: Stabilities of calculated transport coefficients.

E/N Range (Td)	Stability K_0 %	$D_\perp$ %	$D_\parallel$ %
0-80	0.1%	0.25%	0.25%
80-100	0.2%	0.5%	0.75%
100-150	inconvergence		
150-300	$\simeq$ 3.0%	$\simeq$ 15%	$\simeq$ 15%
300-500	$<$ 0.6%	$<$ 4%	10-2%
$>$ 500	$<$ 0.1%	$<$ 1%	$<$ 2%

separations. At intermediate internuclear separations there is temporary agreement between the experimental and theoretical transport data, suggesting that the potential energy surface in the region about the potential energy minimum is reasonably accurate.

Thus the need for an accurate potential energy surface in order to calculate accurate transport coefficients for the Li^+—N_2 system is evident. This study was undertaken and presented in chapter 6, and it focussed on correcting the inadequacies of Billings' potential energy surface, particularly with respect to the long-range multipole moments and the treatment of nuclear polarisation.

7.3.2 Transport Coefficients Calculated from the MP4SDTQ-/6–311+G(2df) Potential Energy Surface

The trajectories summarised in table 7.10 have been used to calculate the the three sets of cross sections, GHM, GHM1, and GHM2 detailed in section 7.2.1, and derived from the MP4SDTQ/6–311+G(2df) potential energy surface which was detailed in chapter 6. These cross sections were then used as input into the program `MOBDIF` [58] to calculate the transport coefficients of Li^+ ions in N_2 gas at T =300° K, as a function of E/N. The numerical results of the calculation of the transport properties at low field strength using the program `MOBDIF` [58] are displayed in table 7.12. Note that the mobility K_0, and the parallel $ND_\parallel$, and perpendicular diffusion coefficients $ND_\perp$, have converged to an accuracy of $\pm$ 0.1%, $\pm$ 0.25 % and $\pm$ 0.25 % respectively. Also displayed is the effective ion temperature T_{ions}, the

kinetic energy in the laboratory reference frame $E_{\rm lab}$, and the drift velocity v_d.

Calculations of the transport properties of the Li^+ ions in N_2 gas at high field strength have been performed for the three sets of cross sections defined above. Shown in table 7.13 are the numerical results for high field strength for the GHM1 potential energy surface.

Based on a comparison of the 7th- and 8th-order approximation results from the program `MOBDIF` , the mobility converged to within ±3% near 290 Td, within ±0.6 % near 330 Td, and within ±0.1 % above 530 Td. The convergence of the perpendicular diffusion coefficients was within ±15 % near 250 Td, within ±12 % near 290 Td, within ± 4 % near 330 Td, and within ±1 % above 530 Td. Finally the parallel diffusion coefficients have converged more slowly compared with the perpendicular diffusion coefficients, and were accurate to within ±15 % near 350 Td, within ±10% near 450 Td, and within ±2 % above 530 Td.

The calculated mobilities and diffusion coefficients (made dimension-less equation 7.11) are compared with the results of Selnæs in figures 7.4 and 7.5. In order to assess the importance of the comparisons shown in figures 7.4 and 7.5 it is necessary to discuss separately the precision and accuracy of the calculated values at low, intermediate and high E/N. Based on a detailed analysis in section 7.2, a conservative estimate is that the transport cross sections have an accuracy of ±1 %, assuming that the potential energy surface is accurate. This accuracy exceeds the errors in the calculated values of the transport coefficients due to incomplete convergence at E/N values below about 70 Td. A further source of uncertainty at low E/N is whether the cross sections have been calculated to low enough energy, given that such calculations are time consuming and expensive. The two sets of mobilities calculated for Billings' potential agree very well for E/N values above 80 Td, but at lower values (corresponding to lower energies) the difference grows to as much as 6 %. Using the program `MOBDIF` both with and without cross sections below 0.0022 *a.u.*, it can be shown that computing cross sections at even lower energies would change calculated transport coefficients by a negligible amount over 70 Td, and by no more than 2% at lower values of E/N. Consequently the excellent agreement shown in figures 7.4 and 7.5 confirms the accuracy of the GHM potential energy surface. The small deviations in the theoretical mobility curve from the experimental points near 70 Td probably indicates that slight improvements in the potential

Table 7.12: Transport properties of Li^+ ions in N_2 gas at $T = 300°K$, as calculated from the GHM1 potential energy surface, at low field strength.

E/N (Td)	T_{ion} (K)	E_{lab} (eV)	v_d (km/s)	K_0 (cm^2/Vs)	$ND_{\parallel}$ $10^{18}/cms$	$ND_{\perp}$	ACC
10.24712	303.32	.03921	.10958	3.98011	2.567	2.543	.100
10.86810	303.73	.03926	.11613	3.97724	2.577	2.550	.100
11.52530	304.19	.03932	.12306	3.97407	2.588	2.557	.100
12.22758	304.70	.03939	.13044	3.97049	2.600	2.565	.100
12.96941	305.28	.03946	.13822	3.96658	2.613	2.575	.100
13.76191	305.94	.03955	.14650	3.96219	2.628	2.585	.100
14.59993	306.67	.03964	.15523	3.95738	2.645	2.597	.100
15.49506	307.50	.03975	.16453	3.95202	2.664	2.610	.100
16.44288	308.42	.03987	.17433	3.94615	2.685	2.624	.100
17.45297	309.46	.04000	.18474	3.93967	2.708	2.640	.100
18.52827	310.63	.04015	.19577	3.93253	2.735	2.658	.100
19.67313	311.95	.04032	.20745	3.92471	2.764	2.678	.100
20.89252	313.42	.04051	.21982	3.91614	2.797	2.701	.100
22.19188	315.08	.04073	.23294	3.90677	2.834	2.726	.100
23.57710	316.95	.04097	.24683	3.89656	2.874	2.754	.100
25.05461	319.04	.04124	.26155	3.88546	2.920	2.784	.100
26.63140	321.40	.04154	.27715	3.87341	2.971	2.819	.100
28.31521	324.04	.04189	.29368	3.86034	3.028	2.857	.100
30.11127	327.01	.04227	.31117	3.84625	3.091	2.899	.100
32.03319	330.35	.04270	.32972	3.83108	3.162	2.946	.100
34.08883	334.10	.04319	.34939	3.81481	3.241	2.997	.100
36.28880	338.32	.04373	.37025	3.79743	3.331	3.055	.100
38.64448	343.05	.04434	.39236	3.77895	3.431	3.118	.100
41.16809	348.37	.04503	.41589	3.76006	3.533	3.185	.100
43.87247	354.35	.04580	.44077	3.73934	3.659	3.263	.100
46.77113	361.07	.04667	.46718	3.71774	3.803	3.350	.100
49.87798	368.62	.04765	.49523	3.69544	3.967	3.447	.100
53.20709	377.10	.04874	.52503	3.67270	4.152	3.552	.100
56.77220	386.63	.04998	.55672	3.64986	4.371	3.672	.100
60.58631	397.34	.05136	.59046	3.62735	4.629	3.806	.100
64.66247	409.37	.05292	.62641	3.60560	4.935	3.958	.100
69.01324	422.89	.05466	.66475	3.58509	5.301	4.129	.100
73.64886	438.08	.05663	.70531	3.56441	5.585	4.321	.100
78.56554	455.14	.05883	.74867	3.54673	5.952	4.540	.100
83.78389	474.32	.06131	.79493	3.53136	6.177	4.790	.100

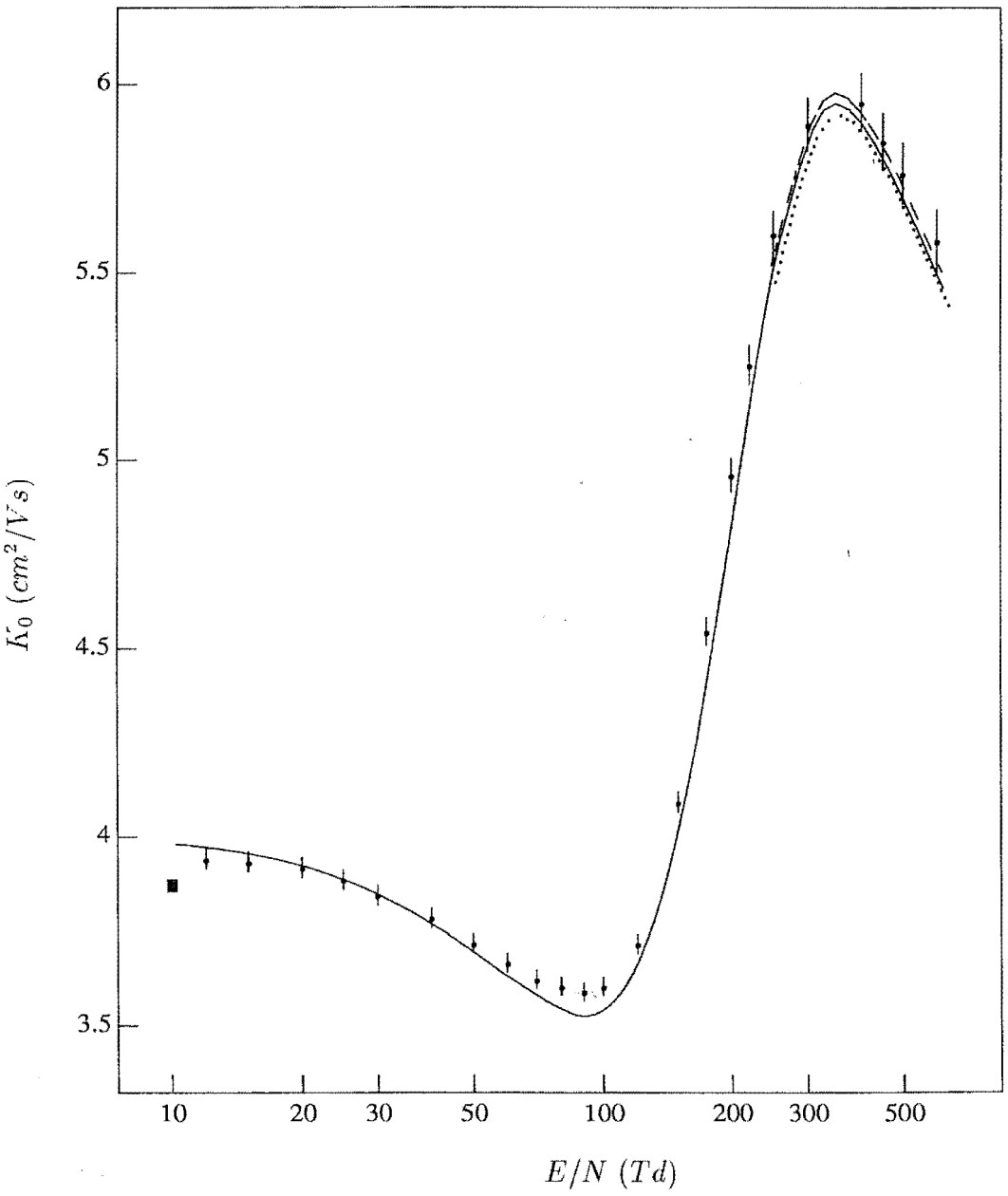

Figure 7.4: The mobility of Li^+ ions in N_2 gas calculated using MP4SDTQ/6–311+G(2df) potential energy surface, at T=300°K, as a function of E/N in units of Td. The points with error bars are the experimental data of Selnæs *et al.* [132]. The solid curve was calculated using the program `MOBDIF` and the GHM1 potential energy surface (which used the MP4SDQ parameters for the correction for nuclear polarisation). The dotted curve at high E/N was calculated using the GHM potential energy surface (which used no corrections for nuclear polarisation), while the dashed curve was calculated from the GHM2 potential energy surface (which corrected for nuclear polarisation using the HF parameters). The mobilities from 85 Td to 250 Td did not converge well and were determined by a spline fit between low- and high-E/N mobilities and dimension-less diffusion coefficients.

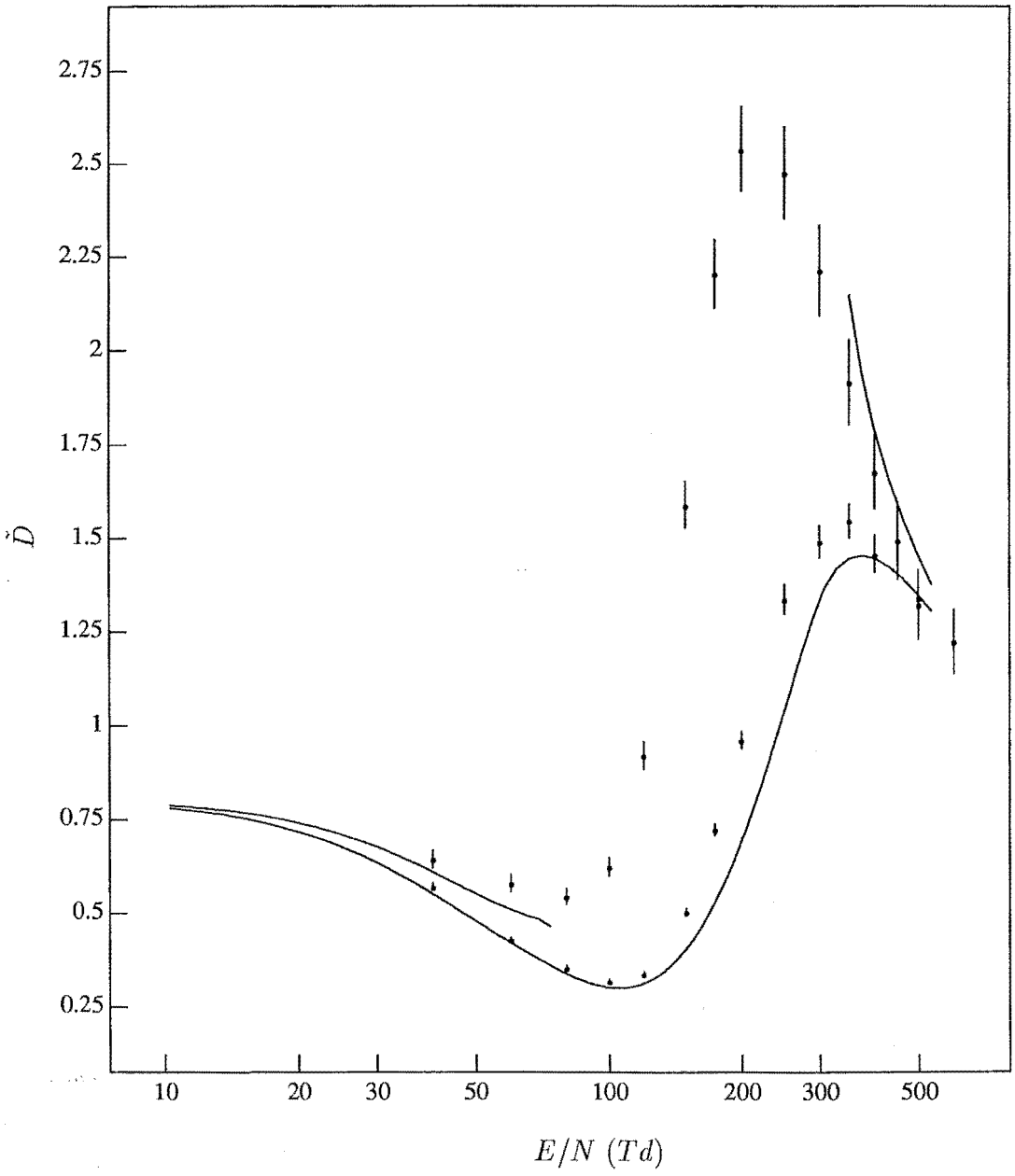

Figure 7.5: The dimension-less diffusion coefficients of Li^+ ions in N_2 gas at T= 300° K as a function of E/N, calculated using the MP4SDTQ/6–311+G(2df) potential energy surface. The points and error bars are the results of Selnæs *et al.* [132]. The solid curves were calculated from the program `MOBDIF` and the GHM2 potential energy surface (which corrected for nuclear polarisation with the MP4SDQ parameters). The diffusion coefficients from 85 to 290 Td did not converge well and were determined for the perpendicular case simply from a spline fit between the low- and high-E/N values.

Table 7.13: Transport properties of Li^+ ions in N_2 gas at $T = 300°K$, as calculated from the GHM1 potential energy surface, at high field strength.

E/N	T_{ion}	E_{lab}	v_d	K_0	$ND_{\|\|}$	$ND_\perp$
(Td)	(K)	(eV)	(km/s)	(cm^2/Vs)	$10^{18}/cms$	
249.06188	4854.84	.62754	3.67600	5.49339	547.879	94.411
260.92014	5417.82	.70031	3.92226	5.59501	554.088	122.283
274.59940	6050.38	.78208	4.19864	5.69091	515.551	150.816
290.25793	6761.13	.87395	4.51600	5.79084	474.641	181.984
307.82624	7559.72	.97718	4.86003	5.87632	446.300	216.535
327.43848	8457.03	1.09316	5.21744	5.93061	435.314	253.783
349.49897	9465.23	1.22348	5.58572	5.94847	437.922	294.312
374.24063	10598.06	1.36991	5.96528	5.93269	452.344	338.681
401.46659	11870.90	1.53444	6.35711	5.89362	476.905	386.614
431.02071	13301.06	1.71931	6.76387	5.84076	509.736	437.966
463.14738	14907.99	1.92702	7.18859	5.77693	550.063	493.371
498.19763	16713.54	2.16040	7.63378	5.70309	597.986	553.716
536.32659	18742.25	2.42264	8.10201	5.62258	653.502	619.682
577.53239	21021.71	2.71728	8.59592	5.53973	716.301	691.888
621.87323	23582.92	3.04835	9.11785	5.45711	786.276	771.101

are possible at separations just beyond the potential energy minimum (R = 6–7 *a.u.*). This conclusion is consistent with the properties of Møller-Plesset calculation methods [10].

Turning to a discussion of the errors for the calculation of transport numbers at high-E/N, it is evident that problems of incomplete convergence have compromised the accuracy of the calculations at intermediate field strength. In addition to the errors from incomplete convergence there is a maximum error of ±0.5 % from the calculations of the transport cross sections. Consequently, the theoretically calculated and experimentally measured transport coefficients agree within the mutual errors. The three curves shown in figure 7.4 show that improved agreement with experiment can be obtained by a more careful treatment of nuclear polarisation at separation below 3.0 a.u. Given the larger error associated with both the measured and calculated diffusion coefficients at high E/N, no additional information is provided by comparisons in figure 7.5.

The calculations of the transport coefficients at intermediate E/N did not converge despite the calculation to the 8th-approximation of kinetic theory using the

program MOBDIF. In retrospect this is not surprising. The trajectory program was not designed to calculate some of the transport cross sections with higher indices required to calculate the higher order approximations, based on previous experience with atomic ion-atom systems. Figure 7.4 shows that the experimental mobility changes by almost a factor of 2 between 100 and 350 Td, a greater and more rapid change than that found in most atomic ion-atom systems. Since the program MOBDIF is known to converge slowly when the mobility is increasing rapidly with E/N, incomplete convergence is not surprising when studying the Li^+—N_2 system.

7.4 Conclusion

A full report of the first calculations of a non spherically symmetric ion-molecule system has been given. The calculation of the transport cross sections required to calculate the transport coefficients were time consuming and expensive compared to neutral systems, because of the greater well depths of ionic systems and the stronger long-range charge-multipole interactions, and also because ionic transport coefficients are required over a wider energy range. Calculations of the transport coefficients using Billings' fit of Staemmlers SCF potential energy surface resulted in mobilities and diffusion coefficients that were beyond the mutual uncertainties of the experimental and theoretical data sets. The differences between the experimental and theoretical data sets were explained in terms of the inaccuracies of Billings' potential energy surface.

Accurate results required the calculation of a new *ab initio* potential energy surface. The MP4SDTQ/6–311+G(2df) potential energy surface was employed in similar calculations to obtain theoretical transport coefficients. While these transport coefficients did not converge at intermediate electric field strengths, at lower and higher field strengths the agreement between the experimental and theoretical data was within the mutual uncertainties. This improved agreement between the theoretical and experimental data sets was interpreted in terms of the better quality of the MP4SDTQ/6–311+G(2df) potential energy surface. Improvements to the computed transport coefficients were achieved by considering some of the physical aspects of the ion molecule collisions, such as nuclear polarisation. Two semi-empirical corrections to the MP4SDTQ/6–311+G(2df) potential energy surface resulted in

improved agreement of the mobilities of Li^+ ions in N_2 gas at high E/N. The comparisons do indicate that the MP4SDTQ/6–311+G(2df) potential energy surface can be improved with a more rigorous treatment of nuclear polarisation.

Further comparisons indicate that slight improvements to the *ab initio* potential energy surface are possible, particularly at separations between 6 and 7 *a.u.* This conclusion is consistent with the known properties of Møller-Plesset calculations at non-equilibrium geometries [10].

Chapter 8

The Potential Energy Surface of Li^+—CO

8.1 Introduction

It has been nearly twenty years since Toennies and co-workers [163] completed inelastic scattering studies on the ion-molecule systems Li^+—CO and Li^+—N_2. These two systems were expected to behave similarly because they were isoelectronic, and had almost identical reduced masses and rotational/vibrational energy spacings. However, significant differences between the "time of flight" (TOF) mass spectra for the two systems were observed and they speculated that the greater probability for vibrational excitation in the Li^+—CO system was due to differences in the "potential hyper-surface". Kita *et al.* [125] have measured integral scattering cross sections at very high energy (500—4000 eV) and have shown that the parameters describing the potential energy surfaces that were derived for the cross sections were very similar for both systems. Support for the integral cross section measurements of Kita *et al.* have been reported by Gislason and coworkers [131].

In order to rationalise the inelastic scattering results of Toennies and to explain the contrasting results of these two experiments, Staemmler [164] performed an *ab initio* study of the Li^+—CO system. Again Staemmlers' study was limited by the processing power of the computers available at that time and this led his study to the "classic" compromise between the quality of the calculation with respect to the inclusion of electron correlation and the quality of the basis set. To complicate

matters further the CO molecule has long been a challenge to quantum chemists because its dipole moment, μ, has the incorrect sign in the HF limit [7]. In fact the CO molecule is often used to test the merit of new post-SCF methods of calculation. Scuseria *et al.* [165] have shown that in order to achieve a dipole moment for the CO molecule that converges on its experimental value both high levels of theory and very large basis sets are required. Staemmler conceded that the theoretical difficulty of calculating the potential energy surface for Li^+—CO led to incorrect long-range behaviour but concluded that the HF results should be reasonably accurate at small intermolecular distances. Despite these short comings Staemmlers' potential energy surface has been used to fit an analytic potential hyper-surface [124].

Thomas [126] has used a reasonably sized basis set to calculate a CISD potential energy surface for the Li^+—CO system. This potential energy surface was then fitted and used to calculate classical rotationally inelastic differential scattering cross sections. The calculated differential scattering cross sections were then compared to experimental measurements [166] with little success which persisted even after vibrational excitation [167], and quantum effects [168] were taken into account. In a further study of low angle scattering [169] Thomas *et al.* suggested that the "unresolved discrepancy" at high scattering angle was due to inaccuracies in the potential energy surface, and that the lack of structure in the classically calculated TOF spectrum for low angle scattering was due to the neglect of quantum effects. However, a later study by Gierz *et al.* [130] reported new differential inelastic scattering cross section data and rationalised the "rotational rainbow" structure observed in the TOF spectrum using a simple classical model.

Several other authors [134, 170, 135, 138, 139, 170] have reported *ab initio* studies of the structural and thermodynamic properties of the Li^+—CO system. These studies provide some information on the location and depth of the stationary points of the potential energy surface.

Hartree-Fock calculations have been shown to be inadequate when calculating the interaction energy at large intermolecular separation for the Li^+—CO system because of the large basis sets and sophisticated treatments of electron correlation which are required to reproduce the electric properties of the CO molecule. The HF results of Staemmler are also of questionable accuracy in the region of the well. Because the only post-SCF potential energy surface available [167] for the Li^+—CO

system was of questionable accuracy at short-range, we have undertaken a detailed examination of the potential energy surface for this system.

In section 8.2 the advancements made to the quality of the theory and the basis set applied are summarised. In section 8.3 the potential energy surface is presented and the requirements for a reliable potential energy surface and comparisons with existing potential energy surfaces are discussed. In section 8.4 the analysis of the potential energy surface and its Legendre expansion, and comparisons to existing Legendre expansions, and the Li^+—N_2 Legendre expansions are made. Finally, a comparison between the potential energy surfaces of the Li^+—N_2 system outlined in chapter 6 and the Li^+—CO system is presented.

8.2 Basis set and Properties

Particular attention must be paid to basis set choice and method when considering a theoretical study of the Li^+—CO system. The correct choice of basis set and method depends on the requirements that the potential energy surface must meet. For example, high energy inelastic/elastic scattering experiments probe only the repulsive parts of the intermolecular potential and do not require accurate values for the multipole moments and polarisabilities which dominate the medium and long-range interaction potential. In order to calculate transport data for comparison with experiment the potential energy surface is required to be accurate over a wide energy range (thermal to a few eV). Because of these constraints the calculated potential energy surfaces currently available [164, 168] are not suitable. To calculate reliable polarisabilities for small molecules requires the addition of diffuse polarisation functions, while the electric multipole moments require the addition of extra polarisation functions with larger exponents. The addition of diffuse s and p functions is necessary for a complete description of medium-range bonding interactions.

The MP4SDTQ/6-311+G(2df) method used in the study of the Li^+—N_2 potential energy surface proved to be of sufficient accuracy to reproduce experimental transport data, see chapter 7. It is reasonable to expect that the same approach for Li^+—CO would result in equal success in light of the similarities between the two systems. However, the difficulty in describing the electric multipole moments of CO has presented new challenges for theory. An extensive list of the electric properties

of the CO molecule for the various basis sets and methods examined in this study are given in table 8.1.

Table 8.1: The electric properties of CO.

Basis set	μ^a	Q^{ab}	$\Theta^{a,b}$	$\alpha^a_{\parallel}$	$\alpha^a_{\perp}$
HF/6–311+G(df)	+0.076	–1.75	4.20	14.04	9.10
MP2/6–311+G(df)	–0.141	–1.71	3.33	15.07	9.74
MP4SDQ/6–311+G(df)	–0.078	—	—	14.81	9.58
HF/6–311+G(2df)	+0.061	–1.58	4.23	13.87	10.03
MP2/6–311+G(2df)	–0.138	–1.57	3.35	14.88	10.63
MP4SDQ/6–311+G(2df)	–0.080	—	—	14.65	10.45
HF/6–311+G(3df)	+0.058	–1.63	4.41	14.05	10.88
MP2/6–311+G(3df)	–0.135	–1.59	3.49	15.07	11.53
MP4SDQ/6–311+G(3df)	–0.084	—	—	14.89	9.95
Staemmlers' HF results	+0.100[c]	–1.56[c]	—	14.13[c]	11.10[c]
Scuserias' [165] results	–0.049[d]	—	—	—	—
Best Experimental results	–0.044[e,f]	–1.86[e]	—	17.55[e]	10.97[e]

[a] All electric properties in a.u.
[b] Quadrupole and octapole moments calculated in centre of mass coordinates.
[c] Basis set C of that work; see [164].
[d] CCSD(T) results of that work; see [165].
[e] Mason and McDaniel; see [40].
[f] Note that a negative dipole moment implies C^-—O^+ bond polarity.

The dipole moment for CO, μ, has been calculated analytically for the HF and MP2 levels of theory and by central difference ($E = \pm 1 \times 10^{-3}$ a.u.) [165] for the MP4SDQ level of theory. These results are a subset of the extensive study of the CO dipole moment by Scuseria *et al.* [165]. In that study Scuseria *et al.* have demonstrated the difficulty of attaining a converged dipole moment using Møller-Plesset methods as a function of the order of the theory. They also concluded that coupled cluster methods which successfully converged to the experimental value of the dipole moment of CO, did so only after using very large basis sets that included *d*, *f*, and *g* polarisation functions. Such basis sets are currently impractical to use in the study of a potential energy surface. As well as the results listed in table 8.1, figure 8.1 displays the dipole moment of CO as a function of the internuclear separation. The results that are plotted have been calculated using the 6–311+G(2df) basis set. The solid vertical line represents the equilibrium bond distance optimised at the HF

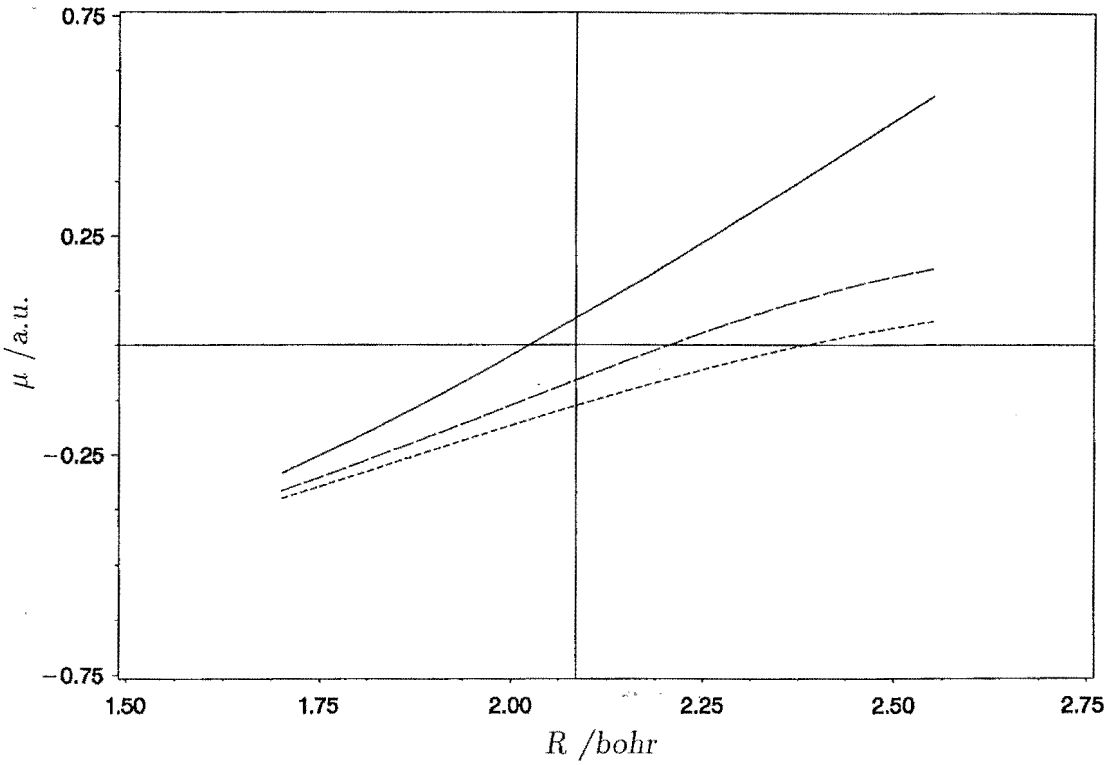

Figure 8.1: The dipole moment of CO as a function of the internuclear distance r, for various level of theory. The HF dipole moment is represented as the solid curve, the dipole moment at the MP2 level of theory is represented as the short-dashed curve and the dipole moment at the MP4SDQ level of the theory is represented at the long-dashed curve. The solid vertical is drawn through the HF/6–311+G(2df) equilibrium bond distance r_e.

level of theory. At this value of r_e the HF dipole moment is +0.076 *a.u.* (a negative sign implies the bond polarity, C^-—O^+). The wrong sign of the dipole moment in the HF approximation is over corrected if electron correlation at the MP2 level of theory is included. This is corrected for again when calculating the dipole moment using the MP4SDQ level of theory, where the dipole moment has a relative error of up to $\simeq$ 80% compared with experiment [40], although the absolute error is small.

The quadrupole moment of CO, Q, is in good agreement with the experimentally measured result [40], and it appears to be more stable with regard to the level of theory used. The 6–311+G(2df) basis set value is in least agreement with experiment, but only differs by $\sim$ 15%. The octapole moment of CO, Θ, is also listed in table 8.1 although no experimental value is available for comparison.

The parallel component of the dipole polarisability, $\alpha_{||}$, is in error of the experimental value by 20%, 14%, and 15% at the HF, MP2, MP4SDQ levels of theory,

respectively. The perpendicular component of the dipole polarisability, $\alpha_\perp$, approaches the experimental value at the HF and MP2 levels of theory, but is in error by 12.7%, 8.6%, and 9.3% at the MP4SDQ level of theory, for the 6-311+G(df), 6-311+G(2df), and 6–311+G(3df) basis sets, respectively. The dipole polarisability in table 8.1 is relatively constant with the inclusion of further d polarisation functions. This suggests that inclusion of very diffuse s and p functions may be required in order to converge to experimental values. This has been investigated by the inclusion of extra diffuse s functions with Gaussian exponents of 0.03963 and 0.07667 for the carbon and oxygen centres, respectively, and extra diffuse p functions with gaussian exponents of 0.02617 and 0.05156 for the carbon and oxygen centres, respectively. This only marginally improved the error in components of the dipole polarisability, $\alpha_\parallel$ and $\alpha_\perp$, when compared with experiment to 2.5% and 14.9% with absolute values of 10.70 *a.u.* and 14.94 *a.u.*, respectively, at the MP2 level of theory.

The structural and thermodynamic properties of CO are listed in table 8.2. It is

Table 8.2: The structural and thermodynamic properties of CO.

Basis set	$r_e{}^a$	D_e^a /eV	k_e^a	E^a
HF/6–311+G(df)	2.086	7.57	81.3[b]	–112.77611
MP2/6–311+G(df)	—	11.45	—	–113.10920
MP4SDQ/6–311+G(df)	—	10.78	—	–113.11707
HF/6–311+G(2df)	2.085	7.60	—	–112.77877
MP2/6–311+G(2df)	—	11.48	—	–113.12748
MP4SDQ/6–311+G(2df)	—	10.70	—	–113.13396
HF/6–311+G(3df)	2.084	7.66	—	–112.78126
MP2/6–311+G(3df)	—	11.57	—	–113.13427
MP4SDQ/6–311+G(3df)	—	10.79	—	–113.14026
Staemmlers' results	2.095[c]	7.62[c]	86.2[c]	–112.73304[c]
Best Experimental results	2.132[d]	11.09[d]	82.9[d]	—

[a] All structural and thermodynamic properties in *a.u.* except D_e.
[b] HF force constants scaled by $(0.89)^2$; see text.
[c] Basis set C of that work; see [164].
[d] Huber and Herzberg; see [144].

also important to closely reproduce the experimental values of the thermodynamic and structural properties to have confidence in the Li^+—CO potential energy surface. The equilibrium bond distance r_e has been calculated only at the HF level of

theory for the basis sets listed in table 8.2. The HF approximation underestimates r_e by a small but significant amount. Inclusion of electron correlation in a study of the N_2 molecule increased r_e by a small amount [139]. An increase in the internuclear separation will impact on the electrical properties of the CO molecule and in particular should improve the agreement between theory and experiment for the dipole moment, see figure 8.1. This effect was examined with the smaller 6-31G* basis set. The HF/6-31G* equilibrium internuclear separation was calculated to be 2.105 *a.u.*, which increased to 2.153 *a.u.* at the MP2/6-31G* level of theory. A similar increase in r_e for the basis sets listed in table 8.2 would result in improved agreement with experiment for r_e and for the dipole moment, which has an estimated value of -0.049 *a.u.* at the experimental separation using MP4SDQ level of theory. This fortuitously agrees with the best results of Scuseria *et al.* [165].

Electron correlation is important in obtaining accurate values for the dissociation energy, D_0. The HF approximation is essentially useless, as it can not adequately describe dissociation of the CO ($^1\Sigma^+$) into the C (^{3}P) and the O (^{3}P) atoms. The MP4SDQ results approach the experimental dissociation energy value with an error of 2.7% for the 6–311+G(3df) basis set.

The force constants have been calculated at the HF level of theory and scaled as recommended by De Frees and McLean [146]. The total energy for CO compares favourably with that quoted for Staemmler in the HF approximation for all the basis sets.

8.3 The Potential Energy Surface of Li^+—CO

In the following work, the 6–311+G(2df) basis set was used unless otherwise stated. This basis set was chosen for its improved properties in the region of the well. Test calculations using the 6–311+G(df) basis set showed that the potential energy surface was underestimated in the region about the well by about 20%. Because of the increased anisotropy of the Li^+—CO potential energy surface compared with the Li^+—N_2 potential energy surface due mainly to the dipole moment of CO, additional point calculations are required to characterise the full rigid rotor potential energy surface. The MP4SDQ method was chosen because of the similarities of this surface and the MP4SDTQ surface in the Li^+—N_2 study, see chapter 6, and the

considerable time savings this method allowed. Both 1*s* orbitals on the carbon and oxygen atoms were frozen.

The calculations were performed with the bond distance of the CO fixed to the value optimised at the HF level of theory. The magnitude of R', the vector connecting the "centre of distance" of the CO molecule and the lithium ion, and θ' the angles between the internuclear vector, r_e, and R' was systematically varied to completely characterise the entire rigid rotor potential energy surface. The data for the potential energy surface is listed in tables 8.3 and 8.4 for the HF and the MP4SDQ levels of theory, respectively. A sufficient number of angles were calculated to fully characterise the angular dependence of the Li^+—CO potential energy surface.

The MP4SDQ potential has been transformed to "centre of mass" coordinates such that the vector R connects the centre of mass of the CO molecule with the Li^+ ion, where θ is the angle between R and the internuclear vector. The transformed potential energy surface was then spline fitted in a similar manner to that described in section 6.4. The short-range extrapolation used was

$$V(R) = a\exp(-bR), \tag{8.1}$$

which was fitted using points (R_1, V_1), and $(R_1, \partial V_1/\partial R_1)$ obtained from solving the equation for a partial natural cubic spline. Enough *ab initio* points were calculated to characterise the repulsive wall of the potential energy surface. The same long-range interaction extrapolation function as that in the Li^+—N_2 potential energy surface was used to fit the Li^+—CO potential energy surface, however n was set to 2 for all angles except $\theta = 90°$, where the ion-dipole interaction vanishes. In the perpendicular approach n was set to 3, where the ion-quadrupole is the leading asymptotic term. When equation 6.2 is expanded in inverse powers of R for $n = 2$, the leading ion-dipole and ion-quadrupole are represented by c/R^2, and $2cd/R^3$, respectively. The values of c and $2cd$ which are given in table 8.5, correspond reasonably well with the known values of the dipole moment and quadrupole moments of CO, see table 8.1. The parameters listed display the correct parity with respect to the angular variation of the leading asymptotic electrostatic terms. Again, enough *ab initio* points were calculated at large separation to ensure the correct behaviour of the fitted asymptotic terms. This required calculations for R beyond 45 *bohr*, resulting in very small relative energies. The fitting parameters were very sensitive

Table 8.3: The HF/6–311+G(2df) rigid-rotor potential energy surface of Li^+—CO.

R^a	$\theta = 0^b$	$\theta = 22.5^b$	$\theta = 45^b$	$\theta = 67.5^b$	$\theta = 90^b$	$\theta = 112.5^b$	$\theta = 135^b$	$\theta = 157.5^b$	$\theta = 180^b$
1.150	—	—	—	−119.59895[c]	−119.72258	−119.61234	—	—	—
1.200	—	—	—	—	—	−119.68767	—	—	—
1.250	−118.26629	—	−119.39865	−119.71403	−119.81578	−119.75010	−119.43544	—	−118.27456
1.275	—	—	—	−119.73815	—	—	—	—	—
1.300	—	—	−119.48145	−119.76060	−119.85124	−119.80168	−119.54726	—	−118.61704
1.313	—	—	−119.50097	−119.77122	—	−119.81310	—	—	—
1.375	—	−119.18275	−119.59135	−119.81876	−119.89366	−119.86252	−119.68033	−119.29578	—
1.500	−119.25830	−119.45760	−119.73670	−119.89022	−119.94279	−119.93116	−119.83099	−119.61623	−119.46922
1.750	−119.73646	−119.80373	—	—	—	−119.99642	−119.97309	−119.91368	−119.87336
2.000	−119.93288	−119.95313	−119.98466	−120.00155	−120.01041	−120.01752	−120.01827	−120.00746	−119.99856
2.250	−120.00716	−120.01052	—	−120.01366	−120.01613	−120.02268	−120.02945	−120.03231	−120.03227
2.500	−120.03158	−120.02931	−120.02301	−120.01731	−120.01729	−120.02260	−120.02979	−120.03541	−120.03739
2.750	−120.03658	−120.03287	—	−120.01774	—	−120.02114	—	−120.03267	−120.03476
3.000	−120.03472	−120.03110	−120.02319	−120.01718	−120.01631	−120.01960	−120.02464	−120.02907	−120.03085
3.125	—	—	−120.02230	—	—	—	−120.02346	—	—
3.250	—	—	—	—	—	−120.01834	—	−120.02596	—
3.500	−120.02757	−120.02507	−120.01975	−120.01582	−120.01526	−120.01740	−120.02069	−120.02355	−120.02471
4.000	−120.02241	−120.02081	−120.01746	−120.01499	−120.01472	−120.01623	−120.01845	−120.02038	−120.02118
5.000	−120.01769	−120.01702	−120.01558	−120.01447	−120.01439	−120.01520	−120.01639	−120.01742	−120.01783
6.000	−120.01606	−120.01572	−120.01497	−120.01441	−120.01440	−120.01488	−120.01560	−120.01621	−120.01645
8.000	−120.01505	−120.01493	−120.01466	−120.01447	−120.01448	−120.01471	−120.01503	−120.01531	−120.01542
10.000	−120.01477	−120.01472	−120.01460	−120.01452	−120.01454	−120.01466	−120.01484	−120.01499	−120.01505
12.000	—	—	—	−120.01455	−120.01456	−120.01464	−120.01475	−120.01485	−120.01488
14.000	−120.01464	—	−120.01459	−120.01456	−120.01458	−120.01463	−120.01471	−120.01477	−120.01479
16.000	—	—	—	—	—	−120.01463	−120.01468	−120.01472	−120.01474
18.000	−120.01461	—	−120.01459	−120.01458	−120.01460	−120.01463	−120.01466	−120.01470	−120.01471
20.000	−120.01461	—	−120.01459	−120.01459	−120.01460	−120.01462	−120.01465	−120.01468	−120.01469
22.000	−120.01460	—	—	—	—	—	—	—	—
24.000	—	—	—	—	—	—	—	—	−120.01466
26.000	—	—	—	—	—	—	—	—	−120.01465
∞	−120.01461	−120.01461	−120.01461	−120.01461	−120.01461	−120.01461	−120.01461	−120.01461	−120.01461

[a] Bond distances in Angströms.

[b] Bond angles in degrees.

[c] Energies in *a.u.*

Table 8.4: The MP4SDQ/6–311+G(2df) rigid-rotor potential energy surface of Li^+—CO.

R^a	$\theta = 0^b$	$\theta = 22.5^b$	$\theta = 45^b$	$\theta = 67.5^b$	$\theta = 90^b$	$\theta = 112.5^b$	$\theta = 135^b$	$\theta = 157.5^b$	$\theta = 180^b$
1.150	—	—	—	−119.95175[c]	−120.07617	−119.96349	—	—	—
1.200	—	—	—	—	—	−120.03877	—	—	—
1.250	−118.70802	—	−119.75680	−120.07002	−120.17078	−120.10121	−119.77964	—	−118.60481
1.275	—	—	—	−120.09471	—	—	—	—	—
1.300	—	—	−119.84149	−120.11765	−120.20665	−120.15285	−119.89136	—	−118.94753
1.3125	—	—	−119.86139	−120.12849	—	−120.16427	—	—	—
1.375	—	−119.55672	−119.95322	−120.17694	−120.24947	−120.21376	−120.02472	−119.63300	—
1.500	−119.64861	−119.83178	−120.09981	−120.24945	−120.29890	−120.28253	−120.17633	−119.95485	−119.80378
1.750	−120.10850	−120.17151	—	—	—	−120.34822	−120.32041	−120.25686	−120.21452
2.000	−120.29766	−120.31671	−120.34650	−120.36128	−120.36670	−120.36990	−120.36729	−120.35389	−120.34387
2.250	−120.36873	−120.37193	—	−120.37304	−120.37239	−120.37560	−120.37983	−120.38105	−120.38032
2.500	−120.39179	−120.38965	−120.38327	−120.37620	−120.37346	−120.37596	−120.38118	−120.38570	−120.38727
2.750	−120.39614	−120.39259	—	−120.37610	—	−120.37483	—	−120.38395	−120.38578
3.000	—	−120.39031	−120.38221	−120.37503	−120.37219	−120.37353	−120.37723	−120.38099	−120.38258
3.125	—	—	−120.38104	—	—	—	−120.37623	—	
3.250	—	—	—	—	—	−120.37244	—	−120.37833	
3.500	−120.38592	−120.38338	−120.37773	−120.37284	−120.37086	−120.37161	−120.37390	−120.37625	−120.37727
4.000	−120.38004	−120.37836	−120.37468	−120.37147	−120.37015	−120.37062	−120.37205	−120.37356	−120.37424
5.000	−120.37438	−120.37365	−120.37196	−120.37039	−120.36967	−120.36984	−120.37052	−120.37126	−120.37158
6.000	−120.37229	−120.37189	−120.37097	−120.37008	−120.36963	−120.36968	−120.37004	−120.37043	−120.37060
8.000	−120.37083	−120.37067	−120.37029	−120.36991	−120.36969	−120.36967	−120.36979	−120.36994	−120.37000
10.000	−120.37034	−120.37026	−120.37006	−120.36986	−120.36973	−120.36970	−120.36975	−120.36982	−120.36985
12.000	—	—	—	−120.36984	−120.36975	−120.36973	−120.36975	−120.36978	−120.36979
14.000	−120.37001	—	−120.36991	−120.36983	−120.36977	−120.36974	−120.36975	−120.36977	−120.36977
16.000	—	—	—	—	—	−120.36975	−120.36976	−120.36976	−120.36977
18.000	−120.36991	—	−120.36986	−120.36981	−120.36978	−120.36976	−120.36976	−120.36977	−120.36977
20.000	−120.36989	—	−120.36985	−120.36981	−120.36978	−120.36977	−120.36977	−120.36977	−120.36977
22.000	−120.36987	—	—	—	—	—	—	—	—
24.000	—	—	—	—	—	—	—	—	−120.36977
26.000	—	—	—	—	—	—	—	—	−120.36978
∞	−120.36980	−120.36980	−120.36980	−120.36980	−120.36980	−120.36980	−120.36980	−120.36980	−120.36980

[a]Bond distances in Angströms.

[b]Bond angles in degrees.

[c]Energies in a.u.

Table 8.5: Fitting parameters for long-range extrapolations of the Li^+—CO potential energy surface.

Fitting parameter	c^a	$2cd^a$
MP4SDQ		
θ =0° [b]	-0.0883	-1.12
θ =45°	-0.0552	-0.481
θ =67.5°	-0.0286	+0.292
θ =112.5°	+0.0318	+0.170
θ =135°	+0.0601	-0.958
θ =180°	+0.0867	-3.22
Fitting parameter	c	$3cd$
θ =90° [c]	-0.0083	-1.12

[a] All parameters in *a.u.*
[b] All bond angles in degrees.
[c] θ = 90° is a special case; see text.

to the last few significant figures of the energy values, although these digits have been truncated in tables 8.3 and 8.4.

The fitted centre of mass potential energy surface for the MP4SDQ/6-311+G(2df) level of theory exhibited the following properties, which are also listed in table 8.6. There exists an absolute minimum at the geometry R=5.330 *bohr*, θ=0°. The depth of the minimum is 0.716 *eV*. There exists a local minimum in the other co-linear approach, at θ= 180°, R=5.344 *bohr*. The depth of this local minimum is 0.475 *eV*. Nearly 70% of the difference between these two well depths can be accounted for by the ion-dipole interaction. Between these two minima there exists a col. The geometry at the col is θ= 87.2°, R = 4.709 *bohr*, with a relative energy of 0.100 *eV*. There also exists an absolute maximum at large separation in the geometry R= 10.684 *bohr*, θ= 96.8°, and with a relative energy of 0.006 *eV*. The maximum is a result of the slightly repulsive ion-dipole and repulsive ion-quadrupole interaction in this geometry at large separation. These repulsive interactions are then dominated largely by ion-induced dipole interactions resulting in a net attraction.

Figure 8.2 displays the MP4SDQ/6-311+G(2df) potential energy surface for Li^+—CO. The angles θ = 22.5°, 67.5°, 112.5°, and 157.5° have been omitted for clarity. Selected values of Staemmler's [164] HF data are also plotted. From a comparison of Staemmlers' data to those reported here it is evident that the inaccuracies

Table 8.6: Critical points of the Li^+—CO potential energy surface.

critical points	MP4SDQ	critical points	MP4SDQ
θ =0°[a]		θ =112.5° [a]	
R[b], $(V=0)$	4.413	$R, (V=0)$	3.711
$R, (\partial V/\partial R=0)$	5.330	$R, (\partial V/\partial R=0)$	4.462
V[c], $(\partial V/\partial R=0)$	–0.02632	$V, (\partial V/\partial R=0)$	–0.00666
$R, (\partial^2 V/\partial R^2=0)$	6.313	$R, (\partial^2 V/\partial R^2=0)$	5.225
		$R, (V=0)$	9.740
		$R, (\partial V/\partial R=0)$	13.270
θ =45°[a]		$V, (\partial V/\partial R=0)$	+0.00013
$R, (V=0)$	4.201	$R, (\partial^2 V/\partial R^2=0)$	15.181
$R, (\partial V/\partial R=0)$	5.153		
$V, (\partial V/\partial R=0)$	–0.01397	θ =135°[a]	
$R, (\partial^2 V/\partial R^2=0)$	5.894	$R, (V=0)$	3.736
		$R, (\partial V/\partial R=0)$	4.503
θ =67.5°[a]		$V, (\partial V/\partial R=0)$	–0.01180
$R, (V=0)$	4.123	$R, (\partial^2 V/\partial R^2=0)$	5.354
$R, (\partial V/\partial R=0)$	4.972	$R, (V=0)$	14.980
$V, (\partial V/\partial R=0)$	–0.00617	$R, (\partial V/\partial R=0)$	21.653
$R, (\partial^2 V/\partial R^2=0)$	5.706	$V, (\partial V/\partial R=0)$	+0.00005
		$R, (\partial^2 V/\partial R^2=0)$	29.133
θ =90°[a]		θ =180°[a]	
$R, (V=0)$	3.964	$R, (V=0)$	3.880
$R, (\partial V/\partial R=0)$	4.632	$R, (\partial V/\partial R=0)$	4.659
$V, (\partial V/\partial R=0)$	–0.00373	$V, (\partial V/\partial R=0)$	–0.01746
$R, (\partial^2 V/\partial R^2=0)$	5.527	$R, (\partial^2 V/\partial R^2=0)$	5.344
$R, (V=0)$	8.545	$R, (V=0)$	22.133
$R, (\partial V/\partial R=0)$	10.663	$R, (\partial V/\partial R=0)$	33.992
$V, (\partial V/\partial R=0)$	+0.00017	$V, (\partial V/\partial R=0)$	+0.00003
$R, (\partial^2 V/\partial R^2=0)$	13.497	$R, (\partial^2 V/\partial R^2=0)$	44.687

[a] All bond angles in degrees
[b] All bond distances in a.u.
[c] All bond energies in a.u.

in the description of the electrical properties of the CO molecule have impacted on the Li^+—CO potential energy surface. The HF approximation which predicts the incorrect sign for the dipole moment of CO also incorrectly favours the Li^+—O–C minimum over the Li^+—C–O minimum. An accurate method for calculating the potential energy surface for Li^+—CO must account for electron correlation. The

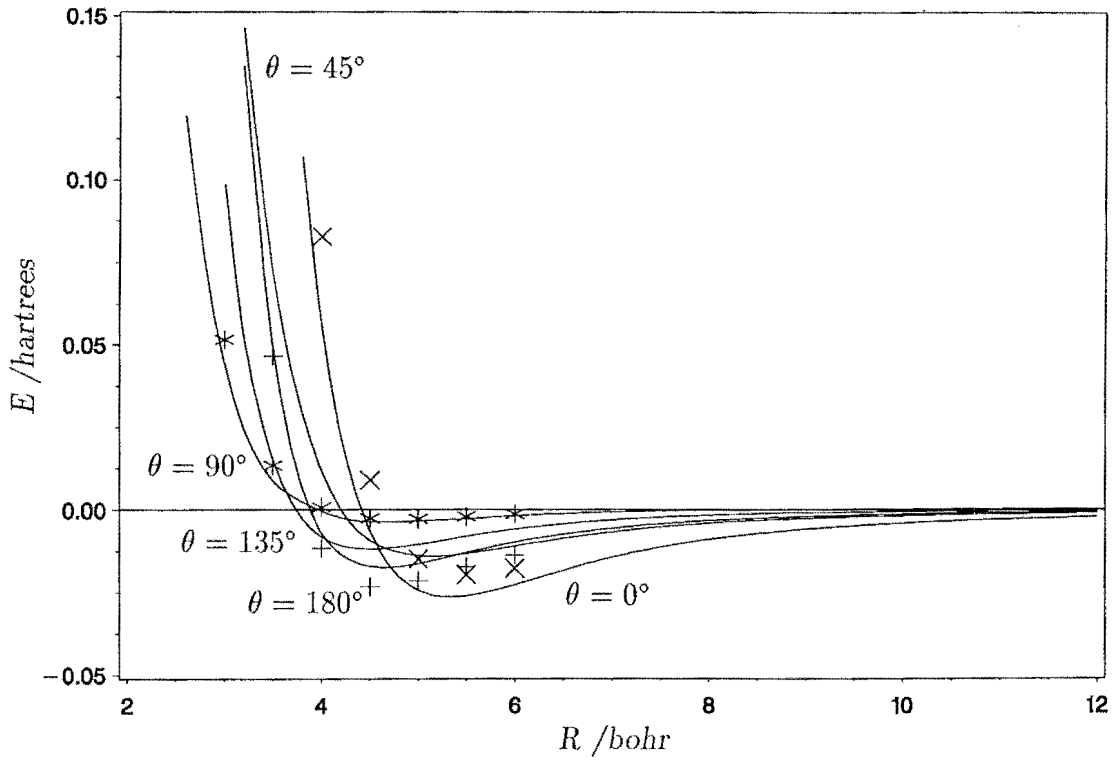

Figure 8.2: The MP4SDQ/6–311+G(2df) potential energy surface for Li^+—CO as a function of R. The angles of θ have been graphed and marked in the figure. Staemmler's HF points are represented as +, $*$ and $\times$ for the angles $\theta = 0°$, 90°and 180°, respectively.

general features of the MP4SDQ/6–311+G(2df) calculations on Li^+—CO are evident in the surface plot graphed in figure 8.3. This figure graphs the potential energy surface as a function of the internuclear separation R, and angle θ. Other comparisons of the potential energy surface are best observed graphically.

The short-range potential energy surface of Li^+—CO is plotted in figure 8.4. It is evident that exponential repulsion begins for $R < 3$ *bohr*. Comparing the short-range repulsive region of the potential energy surface of Li^+—CO with the results of Staemmler shows the discrepancies between the two calculations, particularly in the two co-linear approaches. There is a substantial degree of anisotropy in the potential energy surface reported here, particularly at small intermolecular separation. The medium and long-range potential energy surface is largely dominated by electrostatic and polarisation interactions. This is investigated in the next section.

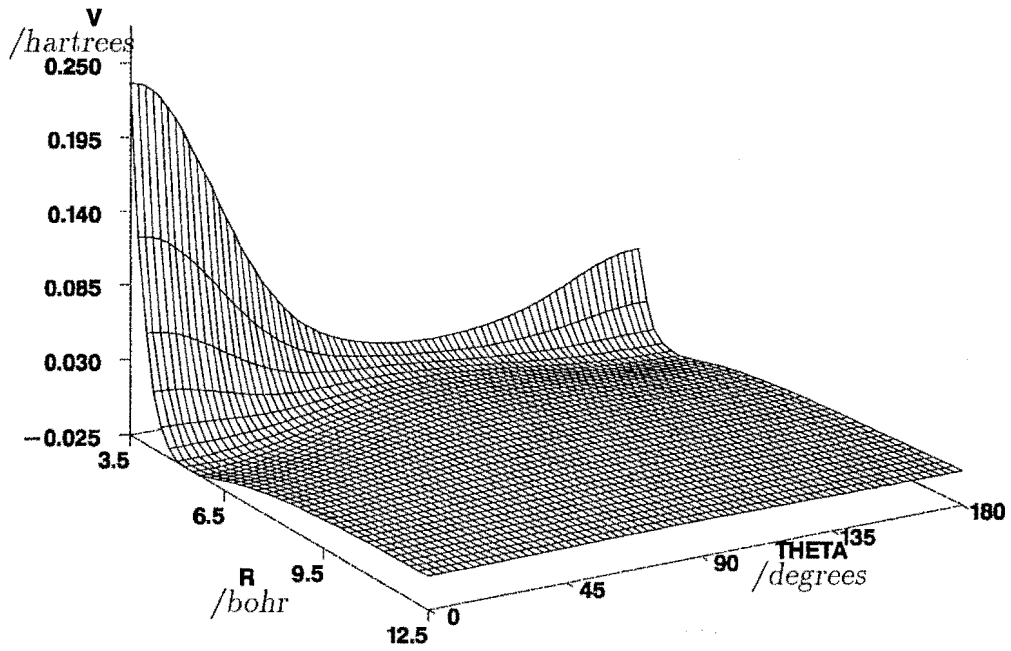

Figure 8.3: The surface plot of the MP4SDQ/6-311+G(2df) potential energy surface as a function of the intermolecular distance and angle.

8.4 The Legendre Expansion

The potential energy surface of Li^+—CO can be analysed in terms of a number of interactions based on the decomposition of the angular variation in a truncated Legendre expansion, as given by equation 6.3. We have calculated the potential energy surface for the angles

$$\theta_m = \{0°, 22.5°, 45°, 67.5°, 90°, 112.5°, 135°, 157.5°, 180°\}. \tag{8.2}$$

Because the CO molecule belongs to the $C_{\infty v}$ point group, all terms are non-vanishing, unlike the Li^+—N_2 system. The radial functions are obtained from inverting equation 6.3 in the manner shown in equation 8.3,

$$V_n(R) = \sum_{m=0}^{k} P^{-1}_{n,m} V(R, \theta_m) \tag{8.3}$$

where $P^{-1}_{n,m}$ are the inverted matrix elements of the matrix $P_{n,m} = P_n(\cos\theta_m)$. The points for which all θ were calculated for a given R have been inverted directly and are listed in table 8.7.

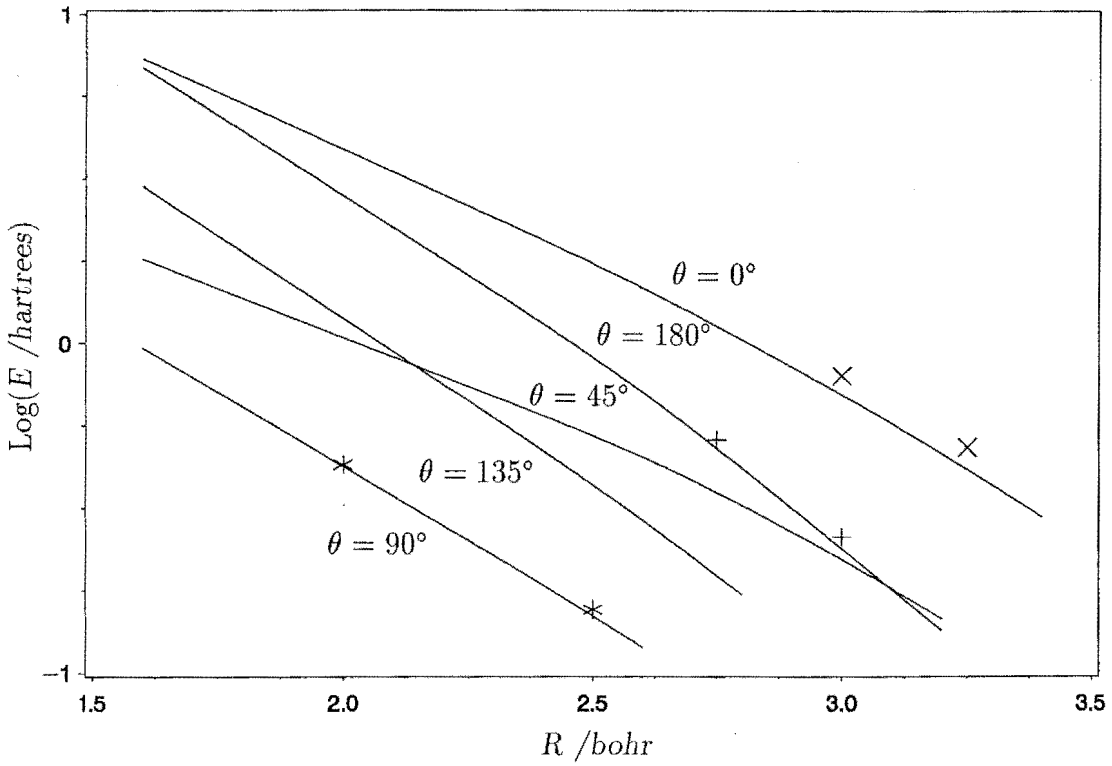

Figure 8.4: The short-range MP4SDQ/6-311+G(2df) potential energy surface of Li^+—CO, as a function of R. The angles of θ have been graphed and labelled in the figure. Staemmler's HF points are represented as $\times$, $*$, and $+$ for the angles $\theta = 0°$, 90°and 180°, respectively.

The expansion was tested for convergence in the expansion for k up to 8. Firstly, there is a noticeably slow convergence in the series V_n, as a function of n, especially for $R \sim 3$ *bohr*. Inclusion of the terms V_n $(0 \leq n \leq 4)$ calculated from the inversion of the data for $\theta = 0°, 45°, 90°, 135°, 180°$, resulted in a potential energy surface that is in error by 20% at short-range R and intermediate angle θ. Inclusion of the V_5 and V_6 terms by including angles $\theta = 67.5°$ and 112.5° improved the correspondence with the calculated potential energy surface to within an average error of less than 1%. Further inclusion of V_7 and V_8 terms did not significantly improve the fit, and indeed these terms are comparatively small compared to other expansions in table 8.7, at all internuclear separations. It was concluded that sufficient accuracy can be obtained by restricting $k = 6$.

The radial functions have also been spline fitted in a similar manner to that described for the potential energy surface. The long-range exponent of equation 6.2 was set to 4, 2, 3, 4, and 5 for V_0, V_1, V_2, V_3, and V_4, respectively. The exponent n was

Table 8.7: The radial Legendre expansion functions directly inverted from the Li^+—CO MP4SDQ/6–311+G(2df) potential energy surface.

R^a	$V_0{}^b$	V_1	V_2	V_3	V_4	V_5	V_6	V_7	V_8
1.5	196125[c]	58175	316391	14161	102823	2066	22732	3186	5531
2.0	11556	16586	24427	5383	11239	1044	1640	93	171
2.5	–9393	–1579	–11121	–939	583	256	172	3	23
3.0	–7476	–3944	–10521	–1734	–459	30	36	17	5
3.5	–4422	–3042	–6996	–1281	–372	–18	–5	15	–1
4.0	–2537	–2066	–4540	–839	–247	–2	–17	5	–2
5.0	–933	–1093	–2173	–321	–78	9	0	1	–1
6.0	–421	–695	–1195	–153	–34	0	0	0	0
8.0	–128	–364	–482	–49	–8	0	0	0	0
10.0	–52	–226	–241	–20	–3	0	0	0	0

[a] All bond energies are in Angströms.
[b] Zeroth order Legendre expansion; see text.
[c] All bond energies are in 1×10^6 a.u.

set to 6 and 7 for V_5 and V_6, respectively. For all the expansions d was small compared with R_n, suggesting that the leading terms of the expansion in inverse powers of R were dominant. The MP4SDQ/6–311+G(2df) expansions $V_n(0 \leq n \leq 6)$ are plotted in figure 8.5 and at short-range in figure 8.6 with the expansions of Thomas *et al.* [167] $V_n(0 \leq n \leq 4)$ plotted as dashed lines.

The potential energy surface reported here is very anisotropic, especially in the region $R \sim 3$ *bohr*. In this region of the potential energy surface a radial Legendre expansion including V_n only up to $n = 4$ gives qualitatively the incorrect potential energy surface. This is in agreement with the findings of Thomas *et al.* who in a later paper [169] conceded that in the perpendicular approach his 5 angled Legendre expansion gave "the wrong sign for the slope meaning the force was in the wrong direction". The anisotropy of the Li^+—CO system decreases at large intermolecular separations where the potential energy surface is dominated by electrostatic and polarisation interactions. For this reason we can expect that *ab initio* derived potential energy surfaces should converge providing they have similar values for the multipole moments and polarisabilities. This results in improved agreement between the expansion of Thomas *et al.* and those reported here, at long-range.

For $R < 3$ *bohr* the anisotropy of the potential energy surface also decreases as the radial functions V_2, V_0, and V_4 become increasingly more dominant. Experiments

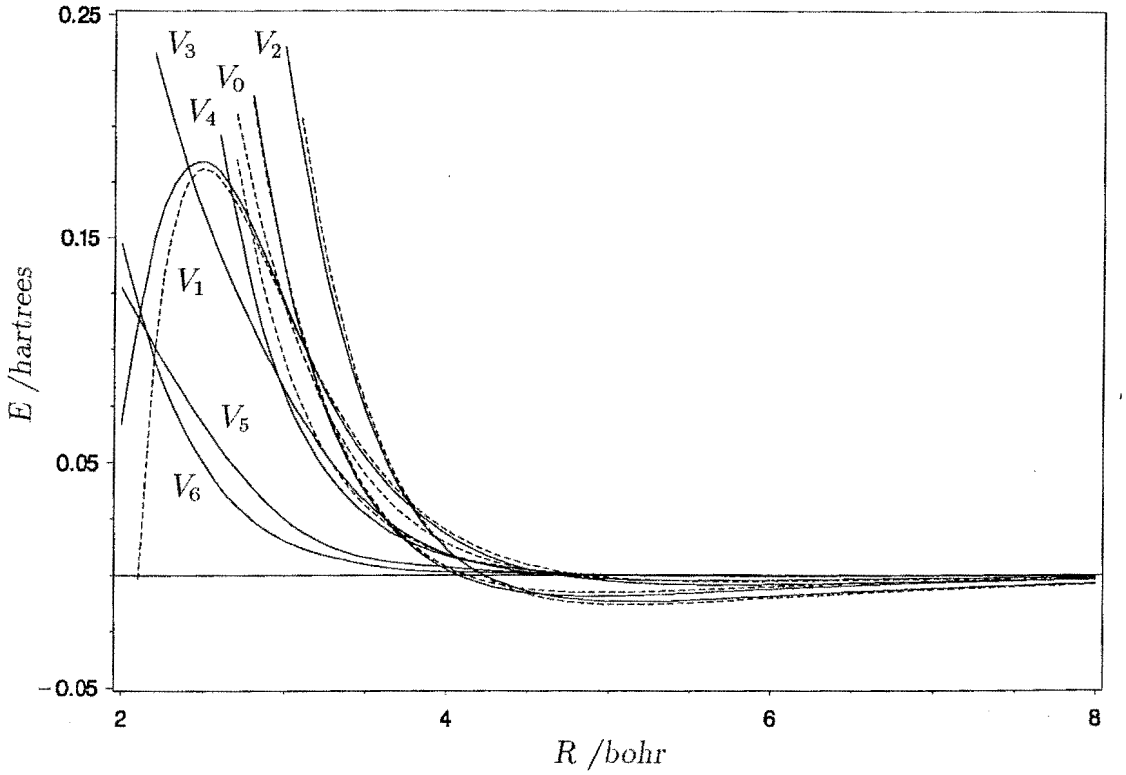

Figure 8.5: The Legendre radial functions of the MP4SDQ/6–311+G(2df) potential energy surface for Li^+—CO. The radial functions V_n are labelled in the figure. The solid lines represent the MP4SDQ/6–311+G(2df) potential energy surface, while the dashed lines represent the CISD+Q data of Thomas *et al.*

that probe the potential energy surface about $R \sim 3$ *bohr* are therefore very difficult to describe theoretically, and it is not surprising that attempts to do so have met with mixed success [126, 130, 167, 169].

Now examining each expansion in turn, we can see that the correspondence between the MP4SDQ/6–311+G(2df) isotropic radial function and the CISD+Q isotropic radial function of Thomas *et al.* is very good. This is supported by Figure 8.7 where these two expansions are plotted along with the experimentally derived radial isotropic function of Gislason *et al.* [131]. The same data set are plotted at short-range in figure 8.8. Note that while the correspondence between the two *ab initio* derived expansions is reasonably good for $R > 2.5$ *bohr*, the divergence at shorter intermolecular separation is only an artifact of the fitting function Thomas *et al.* used which is not valid in this region. Note the poor agreement between the two V_3 expansions. The disagreement in this region is most probably responsible for a large part of the error of the Thomas *et al.* expansion at

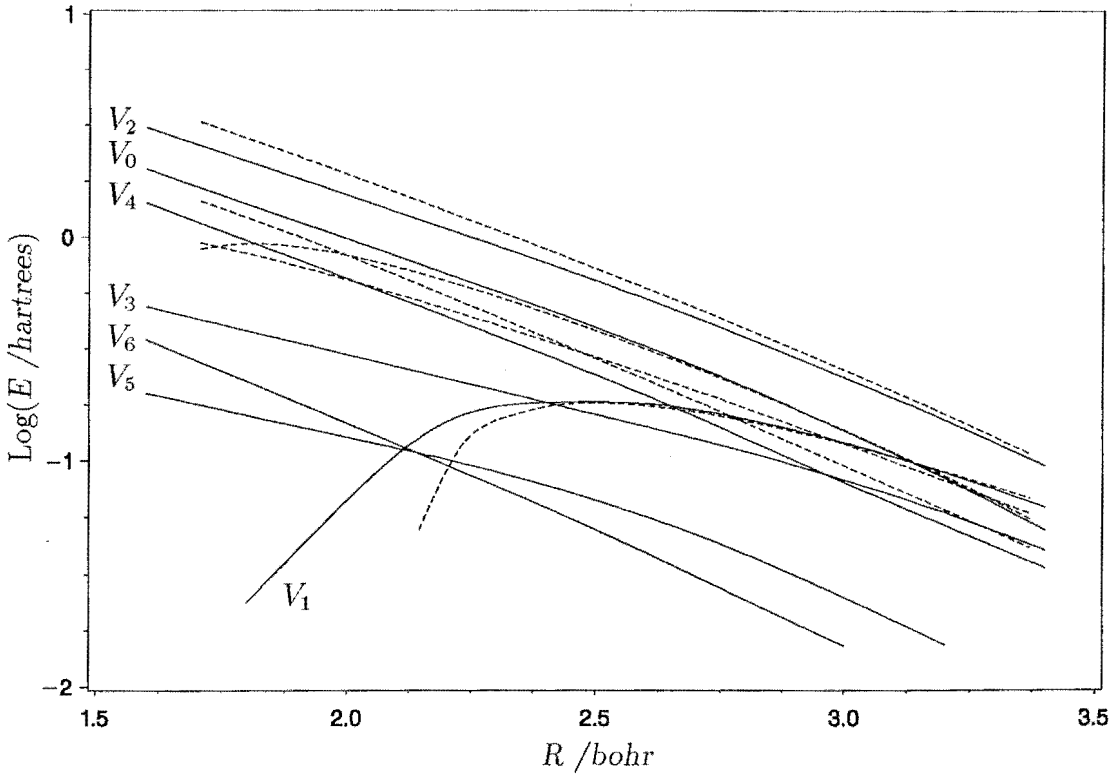

Figure 8.6: The short-range Legendre radial functions of Li^+—CO. The radial functions V_n are labelled in the figure. The solid lines represent the MP4SDQ/6–311+G(2df) potential energy surface, while the dashed lines represent the CISD+Q data of Thomas *et al.*

short-range. Correspondence between the MP4SDQ/6–311+G(2df) expansion V_0 and the experimentally derived results of Gislason *et al.* are also good, even though Gislason *et al.* results have also been reported beyond the range of reported validity ($2.8 \leq R \leq 10.8$ *bohr*). These two expansions differ by a relatively small amount at small intermolecular separation, (see the log-linear plot in figure 8.8). The effect of nuclear polarisation on V_0 is examined later in this section.

Returning to the radial function V_1 of the Legendre expansion, it can be seen in figure 8.5 that correspondence between the MP4SDQ/6–311+G(2df) function and Thomas *et al.* results are good for $R > 3$ *bohr*, but they diverge at smaller intermolecular separations. This is most probably due to the nature of the fitting function Thomas *et al.* have employed. Another noticeable feature of the V_1 radial function is its maximum at $R \sim 2.8$ *bohr*. This results partly from the definition of the co-ordinate system which places the C atom of the CO molecule closer to the Li^+ ion for a given R, which favours the Li^+—O–C configuration at short-range. At

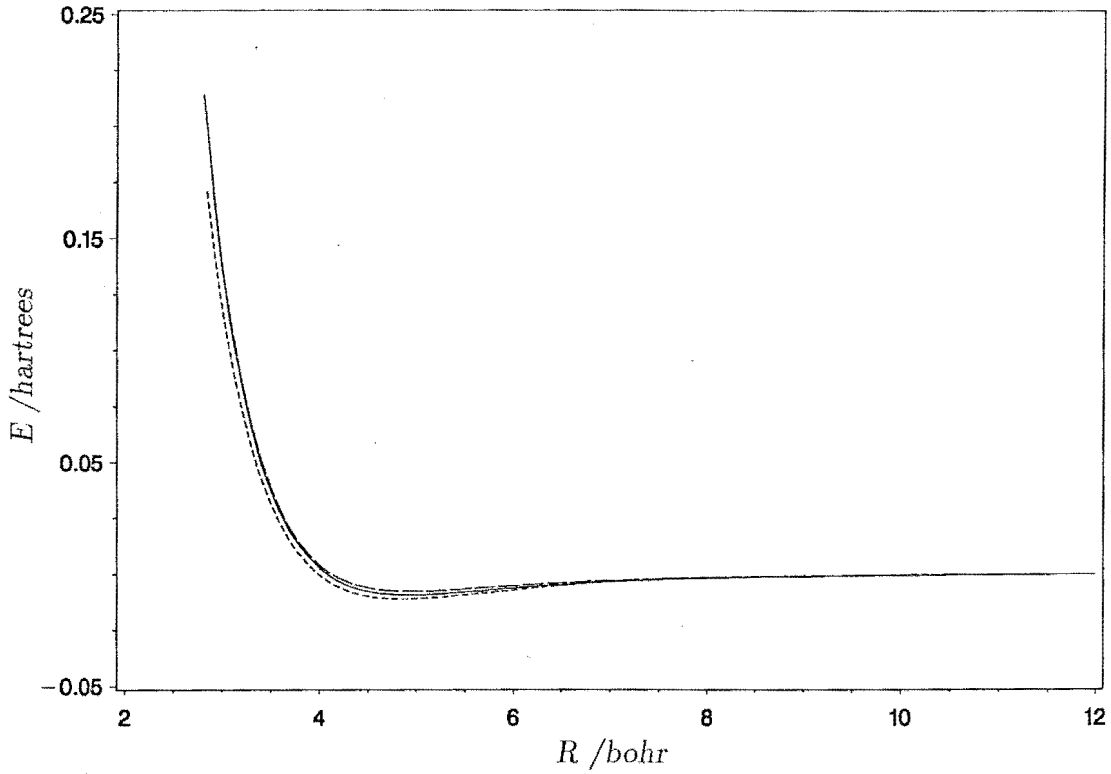

Figure 8.7: The isotropic radial function of Li^+—CO. The solid curve represents the isotropic radial function calculated to the MP4SDQ/6-311+G(2df) level of theory. The dashed line represents the results of Gislason *et al.* [131]. The long dashed line represents the fitted expansion of V_0 of Thomas *et al.* [167].

very large intermolecular separation the V_1 term dominates, and the fitted dipole moment, $\mu = -0.073$ *a.u.*, is in reasonable agreement with the experimental result [40].

The radial function V_2 also corresponds well with Thomas' own expansion, but diverges at short-range, see figure 8.6. The radial function V_2 is dominant in determining the potential energy surface from short to relatively large intermolecular separations. Note that the Thomas *et al.* CISD+Q expansion for V_2 doesn't diverge from the V_2 reported here until much smaller R than is plotted in figure 8.8 because of the extra fitting functions used to ensure accuracy in this region.

The long-range fitted quadrupole moment, $Q \simeq 1.4$ *a.u.* is also in reasonably good agreement with experiment [40], and the polarisation term $3cd$ displays the correct parity.

For the other radial function V_3 and V_4 the MP4SDQ/6-311+G(2df) expansion

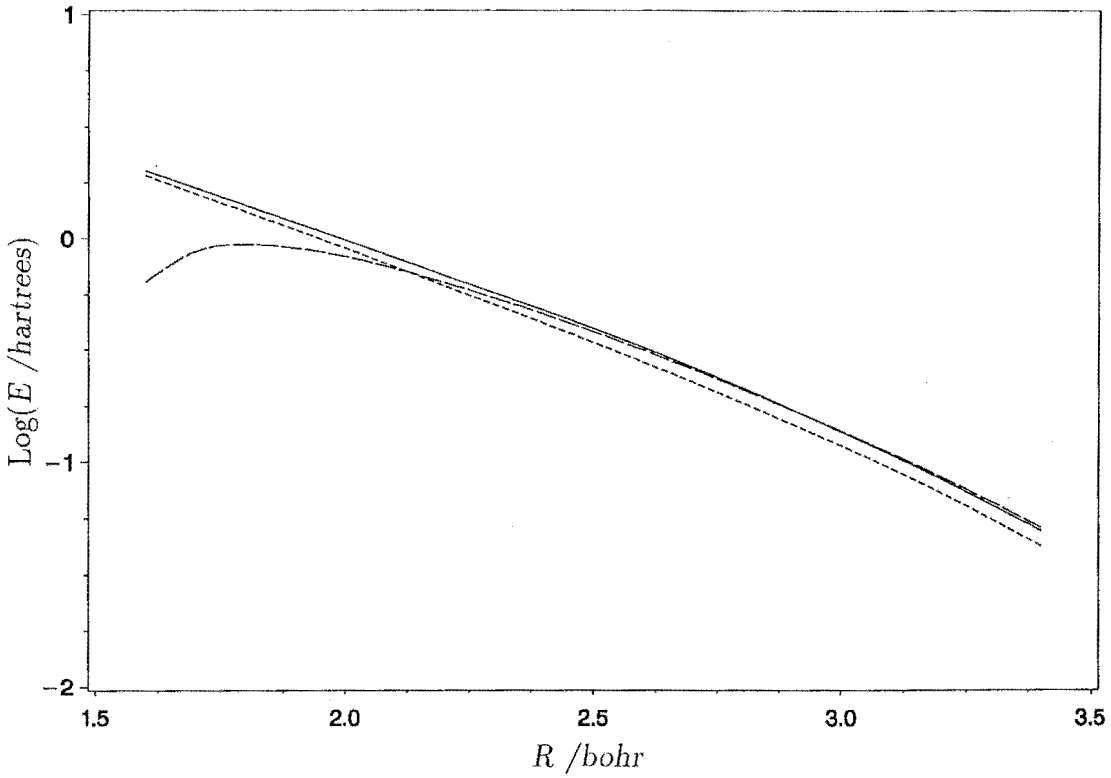

Figure 8.8: The short-range isotropic radial function of Li^+—CO. The solid curve represents the isotropic radial function calculated to the MP4SDQ/6–311+G(2df) level of theory. The short dashed line represents the results of Gislason *et al.* [131]. Note that Gislasons' results have been extrapolated beyond the range of reported validity. The long dashed line represents the fitted expansion of V_0 of Thomas *et al.* [167].

and the Thomas *et al.* expansion are not in agreement. Thomas *et al.* have stated that the convergence of their expansions is incomplete especially at short-range. Thus the MP4SDQ/6–311+G(2df) results represent a significant improvement over the only other post-HF potential energy surface currently available.

8.4.1 Nuclear Polarisation of Li^+—CO

The TOF measurements of Toennies *et al.* [166] for the inelastic differential scattering of Li^+ from N_2 and CO investigated the rotational/vibrational inelastic cross-sections for collision energies < 10 eV. They observed similar rotational excitation cross sections but very different vibrational excitation cross sections between the two systems. The TOF spectra showed an increased likelihood of vibrational inelastic scattering when Li^+ ions collided off CO, when compared to the TOF data for

Table 8.8: Critical points of the Legendre radial functions of Li^+—CO.

critical points	MP4SDQ	Thomas's	Gislason's	Staemmler's
V_0				
R ,$(V_0 = 0)$	4.074[a]	4.185	3.987	4.176
$R, (\partial V_0/\partial R = 0)$	4.934	4.868	4.857	5.027
$V_0, (\partial V_0/\partial R = 0)$	−0.00920[b]	−0.00811	−0.01121	−0.00797
$R, (\partial^2 V_0/\partial R^2 = 0)$	5.639	5.746	—	—
V_1				
$R, (\partial V_1/\partial R)$	2.487	2.377	—	—
$V_1, (\partial V_1/\partial R)$	+0.18461	+0.19324	—	—
$R, (\partial^2 V_1/\partial R^2)$	2.954	2.497	—	—
$R, (V_1 = 0)$	4.695	4.889	—	—
$R, (\partial V_1/\partial R = 0)$	5.713	5.731	—	—
$V_1, (\partial V_1/\partial R = 0)$	−0.000437	−0.00287	—	—
$R, (\partial^2 V_1/\partial R^2 = 0)$	6.501	6.700	—	—
V_2				
$R, (V_2 = 0)$	4.236	4.193	—	—
$R, (\partial V_2/\partial R = 0)$	5.163	5.174	—	—
$V_2, (\partial V_2/\partial R = 0)$	−0.01164	−0.01304	—	—
$R, (\partial^2 V_2/\partial R^2 = 0)$	6.087	5.841	—	—
V_3				
$R, (V_3 = 0)$	4.657	4.742	—	—
$R, (\partial V_3/\partial R = 0)$	5.613	5.667	—	—
$V_3, (\partial V_3/\partial R = 0)$	−0.00234	−0.00246	—	—
$R, (\partial^2 V_3/\partial R^2 = 0)$	6.465	6.516	—	—
V_4				
$R, (V_4 = 0)$	5.062	5.106	—	—
$R, (\partial V_4/\partial R = 0)$	5.963	5.917	—	—
$V_4, (\partial V_4/\partial R = 0)$	−0.00061	−0.00063	—	—
$R, (\partial^2 V_4/\partial R^2 = 0)$	6.496	7.103	—	—

[a] All bond distances in *bohr*.

[b] All energies in *a.u.* and relative to $R = \infty$.

the Li^+—N_2 system. However, Kita *et al.* [125] measured integral elastic scattering cross sections for both Li^+—N_2 and Li^+—CO systems and showed that these cross sections and the potential energy surfaces derived from them were very similar. Staemmler [164] attempted to rationalise the increased likelihood of vibrational excitation of CO, despite the similarities of the short-range potential energy surface, by a study of the equilibrium bond distance of the diatomic (r_e) as a function of its geometry. This study showed "pronounced" differences between the Li^+—CO and Li^+—N_2 systems at short-range.

The effects of nuclear polarisation on the Li^+—CO system have been examined in a similar fashion to that described in section 6.4.1. Gislason *et al.* [147] have commented that long-range polarisation effects are negligible, or nearly so for small molecules, however they quoted [171] values that suggested that nuclear polarisability, α_{np}, was significantly larger for the CO molecule (0.27 a.*u.*) than for the N_2 molecule (> 0.03 a.*u.*). The greater polarisability of CO should be even more exaggerated at short-range where it is anticipated that significant perturbation of the CO bond distance away from its equilibrium position should led to corresponding changes to the potential energy surface.

Reoptimising the bond length of the CO species with the Li^+ species fixed at $R' = 1.5$ Å (in the "centre of distance" coordinate system) at various angles θ', led to the following results. The bond length changes Δr for $\theta' = 0°$, 45°, 67.5°, 90°, 112.5°, 135°, and 180° were –0.262, –0.087, –0.017, +0.012, +0.017, –0.038 and –0.208 *bohr*, respectively, at the HF level of theory. The bond length changes were associated with decreases in energy for these configurations of 3.152, 0.193, 0.006, 0.003, 0.006, 0.032 and 1.817 *eV* for the angles $\theta' = 0°$, 45°, 67.5°, 90°, 112.5°, 135°, and 180°, respectively, at the HF level of theory. At the MP4SDQ//HF level of theory changes were 2.251, 0.005, 0.030, 0.027, 0.037, 0.026, and 1.601 *eV* for angles $\theta' = 0°$, 45°, 67.5°, 90°, 112.5°, 135°, and 180°, respectively. These results are summarised in table 8.9.

As with the Li^+—N_2 system, a pronounced decrease in the bond length (> 10%) occurs in both linear arrangements, with the greatest decrease (–0.262 *bohr*) occurring as the Li^+ ion approaches the C centre of the CO molecule. Small increases in r are observed in the region, $90° \leq \theta' \leq 112.5°$, about the perpendicular approach. Similar features are also observed in the Li^+—N_2 system. These results are in

Table 8.9: Bond distance differences (Δr_e) and Energy differences (ΔV) for nuclear polarisation of Li^+—CO.

θ'^a	Δr^b		ΔV^b	
	HF	MP4SDQ	HF	MP4SDQ
0°	–0.262	—	-0.11582	-0.08270
45°	–0.087	—	-0.00708	-0.00019
67.5°	–0.017	—	-0.00021	-0.00110
90°	+0.012	—	-0.00010	-0.00098
112.5°	+0.017	—	-0.00022	-0.00136
135°	–0.038	—	-0.00119	-0.00096
180°	–0.208	—	-0.06676	-0.05882

[a] All angles in degrees.
[b] All parameter in a.u.

accord with the observations of Staemmler [164]. However, Staemmler correctly points out that the dipole moment of CO may play a crucial role in the behaviour of nuclear polarisation of Li^+—CO especially at short-range, thus complicating the numerical complexity of calculating its effect. These optimisations have been performed at the HF level of the theory, where the dipole moment has the incorrect sign. Optimisation of Li^+—CO in the Li^+—C–O geometry at the HF level of theory has resulted in a large bond length decrease because such a decrease changes the sign of the dipole moment (see figure 8.1) and allows a relatively stabilising interaction. Optimisation of the Li^+—CO system in the Li^+—O–C geometry has also resulted in a decrease in the CO bond length, although it is smaller than that for the Li^+—C–O geometry. It is expected that geometry optimisations of the Li^+—CO system that included a treatment of electron correlation would result in qualitatively *vice versa* changes for the two linear geometries. Inclusion of electron correlation during the optimisation is prohibitively expensive.

It is most likely that bond length dependence of the dipole moment of CO is the cause of the greater vibrational inelastic cross sections of Li^+—CO compared to Li^+—N_2. It is unfortunate that this interesting problem must await advances in computer speed and storage before an adequate treatment of electron correlation of the potential energy surface, particularly with respect to r and θ, will allow accurate calculations of vibrationally inelastic properties of these systems. If the *ab*

initio method used could have provided the correct qualitative picture of nuclear polarisation then the quantitative information obtained could be integrated into the potential energy surface with an expected improvement in the corresponding experimental properties calculated from this potential energy surface. Because of the uncertain reliability of these nuclear polarisation calculations, the associated corrections to the rigid rotor potential energy surface have been neglected.

Calculations to estimate the BSSE by counterpoise correction have not been performed. The anticipated corrections are likely to be too small to justify expensive calculations.

8.4.2 Comparison of the Potential Energy Surfaces of Li^+—CO and Li^+—N_2

The radial functions V_2, V_0, and V_4 at the MP4SDQ/6–311+G(2df) level of theory for the Li^+—CO and at the MP4SDTQ/6–311+G(2df) level of theory for the Li^+—N_2 system are plotted in figure 8.9. There are similarities between the expansions which is not surprising considering the electronic similarities of the two systems. Böttner *et al.* [166] have already noted the similarities of these two potential energy surfaces, and commented that the greater amount of rotational excitation seen in the Li^+—CO system results from the presence of the V_1 term in the Legendre expansion. The agreement between the two systems is best at short-range and is best for the V_0 expansion. The well depths of the isotropic radial function for the two systems, namely 0.254 eV and 0.250 eV for Li^+—N_2 and Li^+—CO, respectively, and the dipole-polarisability for the two systems, namely 10.42 *a.u.* and 11.85 *a.u.* for Li^+—N_2 and Li^+—CO respectively, are also very similar. This suggests that the two potential energy surfaces are in fact very similar and this result is in accord with the results of Gislason *et al.* [131] who found the expansion for the isotropic radial function to be remarkably similar for two ion-molecule systems.

8.5 Conclusion

Ab initio calculations of the potential energy surface of the Li^+—CO system have been reported at the HF and MP4SDQ level of theory with a 6–311+G(2df) basis

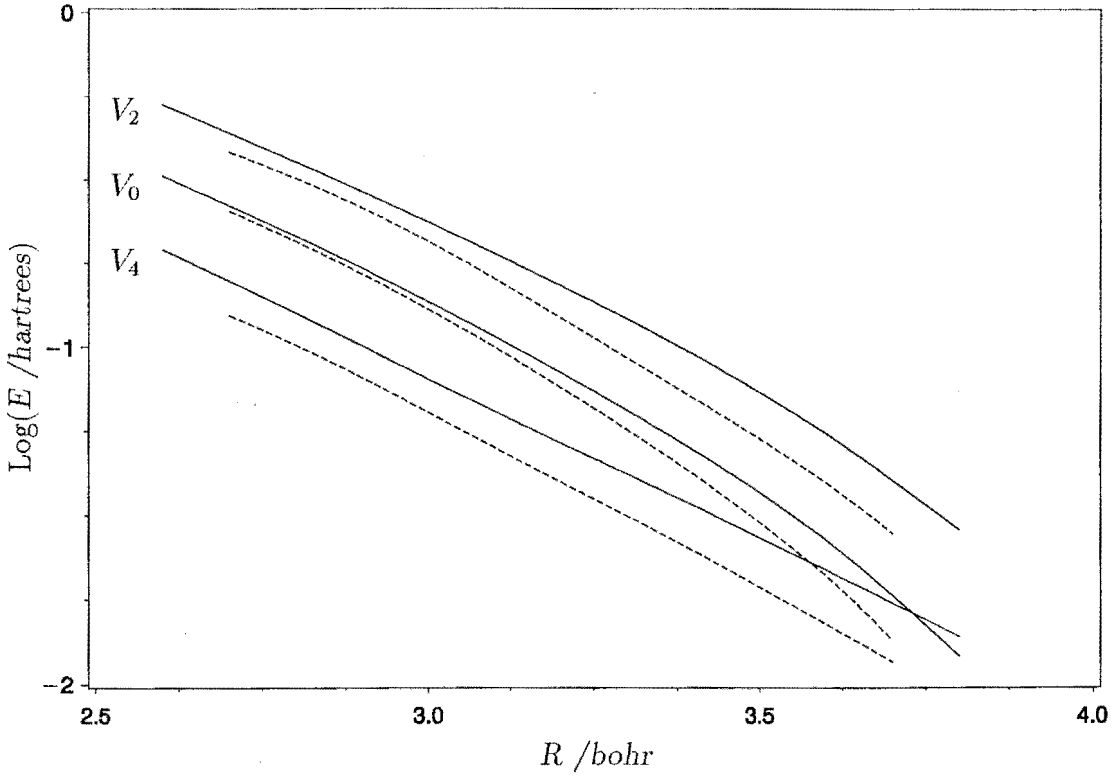

Figure 8.9: Comparison of the short-range Legendre radial functions of the MP4SDQ/6-311+G(2df) potential energy surface of Li^+—CO and Li^+—N_2. The radial functions V_n are labelled in the figure. The Li^+—CO expansions are plotted as solid lines, and the Li^+—N_2 expansions are plotted in the dashed line.

set. This basis set was selected to optimise agreement between the experimental and theoretical electrical properties of the isolated sub-units. The calculated dipole moment, quadrupole moment, and parallel and perpendicular dipole polarisabilities differ from the experimentally reported values by 77.3% (MP4SDQ), 15.6% (MP2), 16.5% (MP4SDQ), and 4.7% (MP4SDQ) respectively. The apparently large difference between the experimental and theoretical results for the dipole moment of CO is due to the small absolute value of the dipole moment and while the ion-dipole interaction is the dominant long-range interaction the absolute error remains small. The isotropic radial function of the Legendre expansion agrees well with the experimental results of Gislason *et al.* [131] which were derived from total scattering cross sections. The isotropic radial function has a well depth of 0.250 eV at 4.934 *bohr* at the MP4SDQ level of theory.

While this study of the potential energy surface of Li^+—CO represents a significant improvement on any potential energy surface currently available, it has some deficiencies because of the inherent difficulties of describing this system. These deficiencies are a result of a complex interplay between the bond length of CO, the treatment of electron correlation of CO, and the dipole moment of CO. It has been shown that electron correlation has increased the bond length of CO and therefore makes the dipole moment more positive. Thus, electron correlation must be taken into account in the calculation of the bond length for an accurate calculation of the long-range potential energy surface. The dependence of the dipole moment of CO on the bond length should also impact on the potential energy surface via nuclear polarisation at short-range. This is experimentally observed as the greater likelihood of vibrational excitation of the Li^+—CO system compared with the Li^+—N_2 system. The greater complexity of the Li^+—CO system compromises the accuracy of any practical calculation method which can be applied.

The potential energy surfaces of Li^+—CO and Li^+—N_2 have been calculated in order to derive the transport properties of Li^+ in the gases CO and N_2. It is anticipated that the Li^+—N_2 potential energy surface is of sufficient accuracy to reproduce the experimentally measured transport coefficients, however the Li^+—CO potential energy surface has been determined less confidently and it cannot be expected to perform to the same degree of accuracy. It is difficult to assess the component uncertainty of the calculated transport coefficients that is due to the known inaccuracies of the potential energy surface. However, a conservative estimate of not greater than 3—5% at low E/N, may result from probing the parts of the potential energy surface with known errors due to the electric multipole moments of CO, reducing to substantially less than this for intermediate and high E/N, where the angular variation of the potential energy surface has been well characterised.

Chapter 9

Cross Sections and Transport Numbers of Li^+—CO

9.1 Introduction

Due to the success of the theoretical calculations of the transport coefficients of Li^+ ions in N_2 gas, further more complicated calculations were required to test the theory and its implementation for atomic ion/diatom systems. The Li^+—CO system was chosen, because of the greater complexity of its potential energy surface due to the electronic structure of CO and its reduced symmetry compared to N_2. The similarity between the potential energy surfaces of the Li^+—N_2 and the Li^+—CO systems has been outlined in chapter 8. Very little accurate information has been published concerning both the potential energy surface and the transport properties of the Li^+—CO system. Thus this calculation is intended to be an *a priori* test of the theory and indication of the accuracy of the potential energy surface.

Toennies *et al.* [163] have reported inelastic scattering studies of both the Li^+—N_2 and Li^+—CO systems. While there were similarities in the time of flight mass spectra of the two systems, the Li^+—CO system exhibited a greater likelihood of vibrational excitation in the energy range which they studied. The differences between the two spectra were rationalised in term of differences in the "potential hypersurface".

Staemmler has performed an *ab initio* SCF study of the Li^+—N_2 [122] and Li^+—CO [164] systems, in order to rationalise the differences in Toennies TOF spectra.

Staemmler concluded that the dependence of the force constant of the diatomic on the vector R was greater for the CO molecule than the N_2. Unfortunately further conclusions are impossible to make without the aid of a mechanistic approach to collisions using trajectory calculations, and it is unlikely that either of Staemmlers' potential energy surfaces are accurate enough to be reliable in this regard.

Other authors [125, 131] calculated the short-range isotropic potential energy surface from integral scattering cross section measurements and have concluded that the Li^+—CO and Li^+—N_2 systems are very similar. We have performed an *ab initio* study of the Li^+—CO surface and compared the angular components of the full rigid rotor potential energy surface with the corresponding expansions for the Li^+—N_2 system, and shown the similarities which support the results of Kita [125] and Gislason *et al.* [131]. Unfortunately the rigid rotor potential energy surface contains little information about the internal vibrational coordinates of the system and as a result no conclusions about the differences in the inelastic differential scattering cross section results of Toennies *et al.* [163] can be made.

The aim of this chapter is to test the accuracy of the interaction potentials described in chapter 8 by comparing the experimental values of the transport coefficients with those derived from the potential energy surface for the Li^+—CO system. This will be achieved with the use of a similar method to that described in chapter 7. Several of the statements presented supporting the calculation of the transport coefficients for the Li^+—N_2 system are equally valid for the Li^+—CO system. This includes the validity of using classical mechanics to calculate the cross sections defined by equations 7.1 and 7.2, and the use of the classical kinetic theory to calculate the transport cross sections.

In section 9.2 the details of the trajectory calculations are outlined followed by the calculations of the transport cross sections. In the following section transport coefficient calculations are described which in turn are followed by a discussion of the results. Particular attention is paid to the uncertainties of the experimental and theoretical transport coefficients. Finally a conclusion is given in section 9.4.

9.2 Classical Trajectory Calculations of the Li^+—CO system

This section outlines the trajectory calculations that were required to calculate the transport cross sections that are defined by equations 7.1 and 7.2. The code of program TRAJECK had to be slightly altered to account for the lower $C_{\infty v}$ symmetry of the CO molecule compared to the N_2 molecule. The greater anisotropy of the potential energy surface due to the lower symmetry is outlined in chapter 8.

The numerical calculation of the cross sections defined by equations 7.1 and 7.2 becomes a trade off between the accuracy required for the calculation of the transport coefficients and the available computer time. It has been shown that the accuracy of the theoretical transport coefficients will be limited by the accuracy of the potential energy surface. The electronic structure of the CO molecule has proven difficult to theoretically model using high level computational methods. For example, Scuseria *et al.* [165] have shown that the theoretical dipole moment of CO does not converge to the experimental value for the Møller-Plesset methods as a function of the order of the theory used. Careful attention was paid to the calculation of the cross sections using trajectory calculations in order that the numerical accuracy did not unnecessarily exceed the estimated accuracy of the Li^+—CO potential energy surface. To calculate the transport cross sections to an accuracy of that calculated for the Li^+—N_2 system would have been expensive, while it would yield no additional information as to the real potential energy surface. Thus the trajectory parameters were systematically varied with the aim of calculating the transport cross sections with an uncertainty of not greater than 1%. This required several calculations of the cross sections defined by equations 7.1 and 7.2, which are detailed in the following sub-sections.

9.2.1 Calculations of Accurate Cross Sections for the Li^+—CO system

Because of the long-range ion-dipole interaction of this system, a slightly different strategy for varying the parameters to obtain accurate cross sections was adopted. The variation of the parameter R_s was primarily investigated for convergence before

other parameters. Convergence of the cross sections was tested in each order of $y = \epsilon/k_bT$. A selection of the studies of the accuracies of the cross sections are given below.

9.2.1.1 Convergence of Cross Sections for $\log(y) = 3.0$

Table 9.1 displays the numerical effect of varying the parameter R_s on the values of some of the cross sections. These cross sections have been calculated with a total energy of 0.95089 *a.u.* and a kinetic energy of 0.95001 *a.u.*, with ACC $= 1\times10^{-8}$, $b_s =$ 8.0 *a.u.*, $c = 1.0$, N1+N2=20+4, and N3=N4=N5=6. From table 9.1 it is apparent that R_s must be at least 120 *bohr* in order to obtain a convergence of the cross sections of less than 1%. Note that the ion-dipole interactions are approximately the same strength at 120 *bohr* as the ion-quadrupole interaction at 40 *bohr*, which is the value used for this energy range in the cross section calculations for the Li^+—N_2 system.

Table 9.1: Effect upon transport cross sections of varying the initial (and final) separations of the trajectories.

$R_s(a.u.)$	80.0	100.0	120.0	140.0
$q^{(1,0)}$ $(a.u.)$	14.9572	14.9828	14.9983	15.0054
$q^{(1,3)}$ $(a.u.)$	15.8836	15.9508	16.0874	16.0996
$q^{(3,1)}$ $(a.u.)$	36.9329	27.0051	27.0934	27.1096
$q^{(12,6)}$ $(a.u.)$	42.9367	43.1056	43.6869	43.6166
$q^{(18,0)}$ $(a.u.)$	48.5980	48.8220	49.1556	49.2021

Table 9.2 summarises the effect of varying the accuracy parameter, ACC, of the integration procedure. All parameters other than ACC were the same as those used to calculate table 9.1. From surveying the 84 cross sections calculated with the program TRAJECK it was concluded that the variable of ACC $= 1 \times 10^{-8}$ was of sufficient accuracy to converge the cross sections to less than 1%.

Tables 9.3 and 9.4 summarise the effect of increasing the number of impact parameters, N1 and N2 sampled, respectively. The ACC parameter was chosen to be 1×10^{-9} while all other parameters were the same as those used to calculate the cross sections for table 9.2. The effect of the partitioning of the impact parameters was investigated on the number of impact parameters required in each region divided

Table 9.2: Effect upon transport cross sections of varying the accuracy parameter.

ACC	1×10^{-7}	1×10^{-8}	1×10^{-9}
$q^{(1,0)}$ (a.u.)	15.2805	14.9983	14.9688
$q^{(1,3)}$ (a.u.)	18.0705	16.0874	15.9539
$q^{(3,1)}$ (a.u.)	31.8269	27.0934	27.2590
$q^{(12,6)}$ (a.u.)	50.4831	43.6869	43.1747
$q^{(18,0)}$ (a.u.)	54.2612	49.1566	48.7736

by b_s. By restricting the high impact parameters to a minimum number of values, the value of b_s was set to the smallest possible value while retaining convergence of the cross sections to better than 1%. From the values of the cross sections it was concluded that with b_s=8 *a.u.* at least 24 low and 4 high impact parameters were required to calculate the cross sections to an accuracy better than 1%.

Table 9.3: Effect upon transport cross sections of varying N1, the number of impact parameters sampled.

Lower values	16	20	24	32
Higher values	4	4	4	4
$q^{(1,0)}$ (a.u.)	14.9732	14.9688	14.9715	14.9729
$q^{(1,3)}$ (a.u.)	15.9510	15.9539	15.9531	15.9560
$q^{(3,1)}$ (a.u.)	27.1945	27.2590	27.2571	27.2639
$q^{(12,6)}$ (a.u.)	43.2911	43.1747	43.3789	43.0882
$q^{(18,0)}$ (a.u.)	48.0541	48.7736	47.6899	47.7866

Table 9.4: Effect upon transport cross sections of varying N2, the number of impact parameters sampled.

Lower values	24	24	24
Higher values	3	4	5
$q^{(1,0)}$ (a.u.)	14.9711	14.9715	14.9700
$q^{(1,3)}$ (a.u.)	15.9499	15.9531	15.9423
$q^{(3,1)}$ (a.u.)	27.2505	27.2571	27.2343
$q^{(12,6)}$ (a.u.)	43.3688	43.3789	43.3431
$q^{(18,0)}$ (a.u.)	47.6831	47.6899	47.6644

Table 9.5 summarises the effect of varying parameter c, with N1=24 and N2=4. All other parameters were the same as those used to calculate the cross section in table 9.4. It was concluded that the choice of c is relatively unimportant when considering the accuracy of the calculated cross sections.

Table 9.5: Effect upon transport cross sections of varying the parameter c.

c	0.3	0.4	0.8	1.0
$q^{(1,0)}$ (a.u.)	14.9719	14.9729	14.9750	14.9715
$q^{(1,3)}$ (a.u.)	15.9017	15.9091	15.9235	15.9531
$q^{(3,1)}$ (a.u.)	27.1822	27.1980	27.2287	27.2571
$q^{(12,6)}$ (a.u.)	43.0516	43.0760	43.1269	43.3789
$q^{(18,0)}$ (a.u.)	48.6792	48.6962	48.7374	48.6899

Table 9.6 summarises the effect of varying the number of angles sampled, with $c = 1.0$, and N1+N2=24+3. All other parameters were the same as those used to calculate the cross sections in table 9.5. It was concluded that adequate accuracy of the cross sections required at least 6 angles of each of the three angular quadratures, χ, ϕ_L, and ϕ_j.

Table 9.6: Effect upon transport cross sections of varying the number of angles sampled for each of the angular quadratures.

Angles	6×6×6	8×6×6	6×8×6	6×6×8	8×8×8
$q^{(1,0)}$ (a.u.)	14.9715	14.9757	14.9728	14.9771	14.9754
$q^{(1,3)}$ (a.u.)	15.9531	15.9261	15.8808	15.9226	15.8783
$q^{(3,1)}$ (a.u.)	27.2571	27.2274	27.3202	27.2259	27.3272
$q^{(12,6)}$ (a.u.)	43.3789	43.1262	42.9439	43.0672	42.9869
$q^{(18,0)}$ (a.u.)	48.6899	48.7678	48.8412	48.7200	48.9666

The cross sections defined by equations 7.1 and 7.2 are evaluated by averaging over the rotational energy by N6-point Gauss-Legendre integration at low w, and N7-point Gauss-Laguerre integration over high w, in an identical manner to that described in section 7.2.1. Table 9.7 summarises the effect of varying the number of rotational energy quadratures on the rotational energy averaged cross sections. It was concluded from table 9.7 that 4 high and 4 low rotational energy quadratures are sufficient to calculate the cross sections to an accuracy of better than 1%.

Table 9.7: Effect upon rotationally-averaged transport cross sections of varying the parameters listed.

w values	3+3	4+4	5+5
$\Sigma^{(0,1)}$ (a.u.)	13.4317	13.4333	13.4337
$\Sigma^{(1,0)}$ (a.u.)	14.9980	14.9988	14.9991
$\Sigma^{(11,0)}$ (a.u.)	721.4245	722.5840	723.4099
$\Sigma^{(11,7)}$ (a.u.)	9.4969	9.3373	9.2565

9.2.1.2 Convergence of Cross Sections for log(y) = 2.0

Table 9.8 summarises the numerical effect of varying the parameter R_s on the values of some of the cross sections. These cross sections have been calculated for a total energy of 0.095089 *a.u.* and a kinetic energy of 0.095001 *a.u.*, with ACC = 1×10^{-8}, b_s = 8.0 *a.u.*, c = 1.0, N1+N2=20+4, and N3=N4=N5=6. From table 9.8 it is apparent that R_s must be at least 160 *bohr* in order to obtain a convergence of the cross sections of much less than 1%, in this energy range.

Table 9.8: Effect upon transport cross sections of varying the initial (and final) separations of the trajectories.

R_s(a.u.)	120.0	140.0	160.0	180.0
$q^{(1,0)}$ (a.u.)	39.4069	39.4010	39.4821	39.4680
$q^{(1,3)}$ (a.u.)	57.5191	57.3978	57.8447	57.7998
$q^{(3,1)}$ (a.u.)	74.7211	74.6242	74.9430	74.9425
$q^{(12,6)}$ (a.u.)	171.6517	171.2896	172.3464	172.4764
$q^{(18,0)}$ (a.u.)	212.1743	212.0950	212.6521	212.8461

Table 9.9 summarises the effect of varying the accuracy parameter ACC of the integration procedure. All parameters other than ACC, were the same as those used to calculate table 9.1, except for R_s which was fixed to 160 *bohr*. From surveying the 84 cross sections calculated with the program TRAJECK it was concluded that the variable of ACC = 1×10^{-9} was of sufficient accuracy to converge the cross sections to less than 1%, in this energy range.

Tables 9.10 and 9.11 summarise the effect of increasing the number of impact parameters, N1 and N2 sampled, respectively. The ACC parameter was chosen to be 1×10^{-9} while all other parameters were the same as those used to calculate the

Table 9.9: Effect upon transport cross sections of varying the accuracy parameter.

ACC	1×10^{-8}	1×10^{-9}	1×10^{-10}
$q^{(1,0)}$ (a.u.)	39.4821	39.4561	39.4534
$q^{(1,3)}$ (a.u.)	57.8447	57.6622	57.6439
$q^{(3,1)}$ (a.u.)	74.9430	74.8124	74.7993
$q^{(12,6)}$ (a.u.)	172.3464	171.7209	171.6580
$q^{(18,0)}$ (a.u.)	212.6521	212.1802	212.1325

cross sections for table 9.9. The effect of the partitioning of the impact parameters was investigated on the number of impact parameters required in each region divided by b_s. By restricting the high impact parameters to a minimum number of values, the value of b_s was set to the smallest possible value while retaining convergence of the cross sections to better than 1%. From the values of the cross sections in this and other studies it was concluded that with b_s= 10 *a.u.*, at least 32 low and 6 high impact parameters were required to calculate the cross sections to an accuracy better than 1%.

Table 9.10: Effect upon transport cross sections of varying N1, the number of impact parameters sampled.

Lower values	20	24	32	48
Higher values	4	4	4	4
$q^{(1,0)}$ (a.u.)	39.4561	39.4575	39.4579	39.4579
$q^{(1,3)}$ (a.u.)	57.6622	57.6664	57.6686	57.6683
$q^{(3,1)}$ (a.u.)	74.8124	74.8174	74.8164	74.8164
$q^{(12,6)}$ (a.u.)	171.7209	171.6559	171.6189	171.6185
$q^{(18,0)}$ (a.u.)	212.1802	212.5238	212.1310	212.0013

Table 9.12 summarises the effect of varying the number of angles sampled. All other parameters were the same as those used to calculate the cross sections in table 9.11. It was concluded that adequate accuracy of the cross sections required at least 6 angles of each of the three angular quadratures, χ, ϕ_L, and ϕ_j, in this energy range.

Table 9.13 summarises the effect of varying the number of rotational energy quadratures on the rotational energy average cross sections. It was concluded from

Table 9.11: Effect upon transport cross sections of varying N2, the number of impact parameters sampled.

Lower values	20	20	20	20
Higher values	4	5	6	8
$q^{(1,0)}$ $(a.u.)$	39.4561	39.4561	39.4525	39.4572
$q^{(1,3)}$ $(a.u.)$	57.6622	57.6580	57.6404	57.6728
$q^{(3,1)}$ $(a.u.)$	74.8124	74.8150	74.7975	74.8209
$q^{(12,6)}$ $(a.u.)$	171.7209	171.8259	171.7256	171.8361
$q^{(18,0)}$ $(a.u.)$	212.1802	212.4110	212.2364	212.3228

Table 9.12: Effect upon transport cross sections of varying the number of angles sampled for each of the angular quadratures.

Angles	6×6×6	8×6×6	6×8×6	6×6×8	8×8×8	10×10×10
$q^{(1,0)}$ $(a.u.)$	39.4565	39.4612	39.4054	39.4348	39.4248	39.4408
$q^{(1,3)}$ $(a.u.)$	57.6554	57.6495	57.3637	57.5538	57.4328	57.4520
$q^{(3,1)}$ $(a.u.)$	74.8109	74.8015	74.5725	74.7514	74.6058	74.6607
$q^{(12,6)}$ $(a.u.)$	171.6618	171.6320	171.2344	171.4355	171.4230	171.4074
$q^{(18,0)}$ $(a.u.)$	212.6762	212.5377	212.4925	212.3534	212.6262	212.4363

table 9.13 that 8 high and 8 low rotational energy quadratures are sufficient to calculate the cross sections to an accuracy of better than 1%.

Table 9.13: Effect upon rotationally-averaged transport cross sections of varying the parameters listed.

w values	6+6	8+7	8+8	10+8	10+10
$\Sigma^{(0,1)}$ $(a.u.)$	39.6032	39.6119	39.6020	39.6035	39.6051
$\Sigma^{(1,0)}$ $(a.u.)$	77.1793	77.2305	77.1519	77.1074	77.1137
$\Sigma^{(11,0)}$ $(a.u.)$	189.6150	191.0825	190.9781	190.8961	190.9070
$\Sigma^{(11,7)}$ $(a.u.)$	210.5998	212.6247	212.4913	212.3984	212.3942

9.2.1.3 Convergence of Cross Sections for log(y) = 1.0

As the kinetic energy of the collisions decreases it becomes more difficult to maintain a given accuracy in calculating the cross sections, due to the stability and convergence properties of solving the trajectory problem resulting from longer lasting and more convoluted interactions between the particles. Thus obtaining converged cross sections in the lowest kinetic energy region under study required a slightly different strategy to the other energy ranges. Firstly, a study of the convergence of the parameter ACC was undertaken, on a small set of trajectories. These cross sections were calculated for a kinetic energy of 0.00950 *a.u.*, and a rotational energy of 0.00009 *a.u.*, with the number of angular quadratures for $\phi_L = \phi_j = \chi$ set to 2, while the parameters were R_s= 300 *bohr*, N1 = 10 and N2 = 4. Table 9.9 summarises the effect of varying the accuracy parameter ACC of the integration procedure for this set of trajectories. From surveying the 84 cross sections calculated with the program TRAJECK it was concluded that the variable of ACC = 1×10^{-10} was of sufficient accuracy to converge the cross sections to less than 1%, in this energy range (see table 9.14).

Table 9.14: Effect upon transport cross sections of varying the accuracy parameter.

ACC	1×10^{-9}	1×10^{-10}	1×10^{-11}	1×10^{-12}
$q^{(1,0)}$ (*a.u.*)	273.5003	272.9493	272.9567	272.9553
$q^{(1,3)}$ (*a.u.*)	274.8416	274.7225	274.7264	274.7285
$q^{(3,1)}$ (*a.u.*)	315.5083	315.4090	315.4051	315.4075
$q^{(12,6)}$ (*a.u.*)	406.3966	406.4036	406.3996	406.4099
$q^{(18,0)}$ (*a.u.*)	502.3708	502.4049	502.4005	502.4075

Table 9.15 displays the numerical effect of varying the parameter R_s on the values of a few of the cross sections, with ACC set to 1×10^{-10}. These cross sections have then been calculated with the parameters set at larger values which were subsequently tested for convergence. The number of angular quadratures for $\phi_L = \phi_j = \chi$ set to 8, while the parameters N1+N2=48+8, and b_s were set to 10 *bohr*, with c=1.0. From table 9.15 it is apparent that R_s must be at least 300 *bohr* in order to obtain a convergence of the cross sections of much less than 1%, in this energy range.

Table 9.15: Effect upon transport cross sections of varying the initial (and final) separations of the trajectories.

$R_s(a.u.)$	220.0	260.0	300.0	600.0
$q^{(1,0)}$ $(a.u.)$	251.5904	251.5098	250.4974	250.6363
$q^{(1,3)}$ $(a.u.)$	259.9861	261.0024	261.4364	260.7316
$q^{(3,1)}$ $(a.u.)$	313.3403	314.6331	314.5448	313.1120
$q^{(12,6)}$ $(a.u.)$	396.3593	400.8319	405.6571	402.2627
$q^{(18,0)}$ $(a.u.)$	538.1659	541.0807	543.6333	541.4952

Table 9.16 summarises the effect of increasing the number of impact parameters, N2 sampled. The ACC parameter was chosen to be 1×10^{-10}, with R_s set to 300 *bohr*, while all other parameters were the same as those used to calculate the cross sections for table 9.15. The effect of partitioning the impact parameters on the number of impact parameters required in each region divided by b_s was investigated. The number of low impact parameters was automatically set to the maximum practical possible. By restricting the high impact parameters to a minimum number of values, the value of b_s was set to the smallest possible value while retaining convergence of the cross sections to better than 1%. From the values of the cross sections in several tests it was concluded that with b_s= 20 *a.u.*, at least 48 low and 6 high impact parameters were required to calculate the cross sections to an accuracy of about 1%.

Table 9.16: Effect upon transport cross sections of varying N2, the number of impact parameters sampled.

Lower values	48	48	48	48
Higher values	3	4	6	8
$q^{(1,0)}$ $(a.u.)$	252.1032	252.1168	252.1191	252.1157
$q^{(1,3)}$ $(a.u.)$	259.0749	259.2069	259.2143	259.1888
$q^{(3,1)}$ $(a.u.)$	308.9591	309.0318	309.0425	309.0256
$q^{(12,6)}$ $(a.u.)$	393.2417	393.6029	393.6631	393.5888
$q^{(18,0)}$ $(a.u.)$	535.1033	534.9566	535.1107	535.0820

Table 9.17 summarises the effect of varying the number of angles sampled, with b_s= 20 *bohr*, and N1+N2 = 48+6. All other parameters were the same as those

used to calculate the cross sections in table 9.16. It was concluded that adequate accuracy of the cross sections required at least 10 angles of each of the three angular quadratures, χ, ϕ_L, and ϕ_j, in this energy range.

Table 9.17: Effect upon transport cross sections of varying the number of angles sampled for each of the angular quadratures.

Angles	6×6×6	8×8×8	10×10×10	12×12×12
$q^{(1,0)}$ (a.u.)	252.1191	248.9838	251.3191	250.2835
$q^{(1,3)}$ (a.u.)	259.2143	259.8823	260.2113	260.0801
$q^{(3,1)}$ (a.u.)	309.0425	312.3888	312.3204	313.0443
$q^{(12,6)}$ (a.u.)	393.6631	402.3863	400.0829	398.8019
$q^{(18,0)}$ (a.u.)	535.1107	540.1872	538.9842	538.2128

These cross section calculations have been combined with several other calculations with the aim of maximising the numerical accuracy with the minimum numerical effort. While the amount of time available to calculate the low kinetic energy cross sections is necessarily limited, this has led to a compromise in the accuracy of the cross sections and hence in the subsequent determination of the transport coefficients. Being mindful of the fact that the estimated accuracy of the cross sections should not exceed that estimated for the potential energy surface in a given energy range, the set of trajectories that are defined by the parameters in table 9.18 represent the minimum number of trajectories possible to describe the transport coefficients to an accuracy of at least 1%. The final cross sections have been plotted in figure 9.1. It can be expected that the theoretical uncertainties should decrease at high E/N, where the convergence properties of the relevant cross sections and the potential energy surface that they probe were most accurate.

Improvements in the accuracy of the calculated cross sections may have to await the application of vector pipeline methods [157] in order to make large trajectory calculations feasible.

9.3 Transport Coefficients of Li^+—CO

The transport coefficients of Li^+ ions in CO gas have recently been measured by Satoh *et al.* [172]. The measured mobilities of the Li^+ ions in CO gas showed

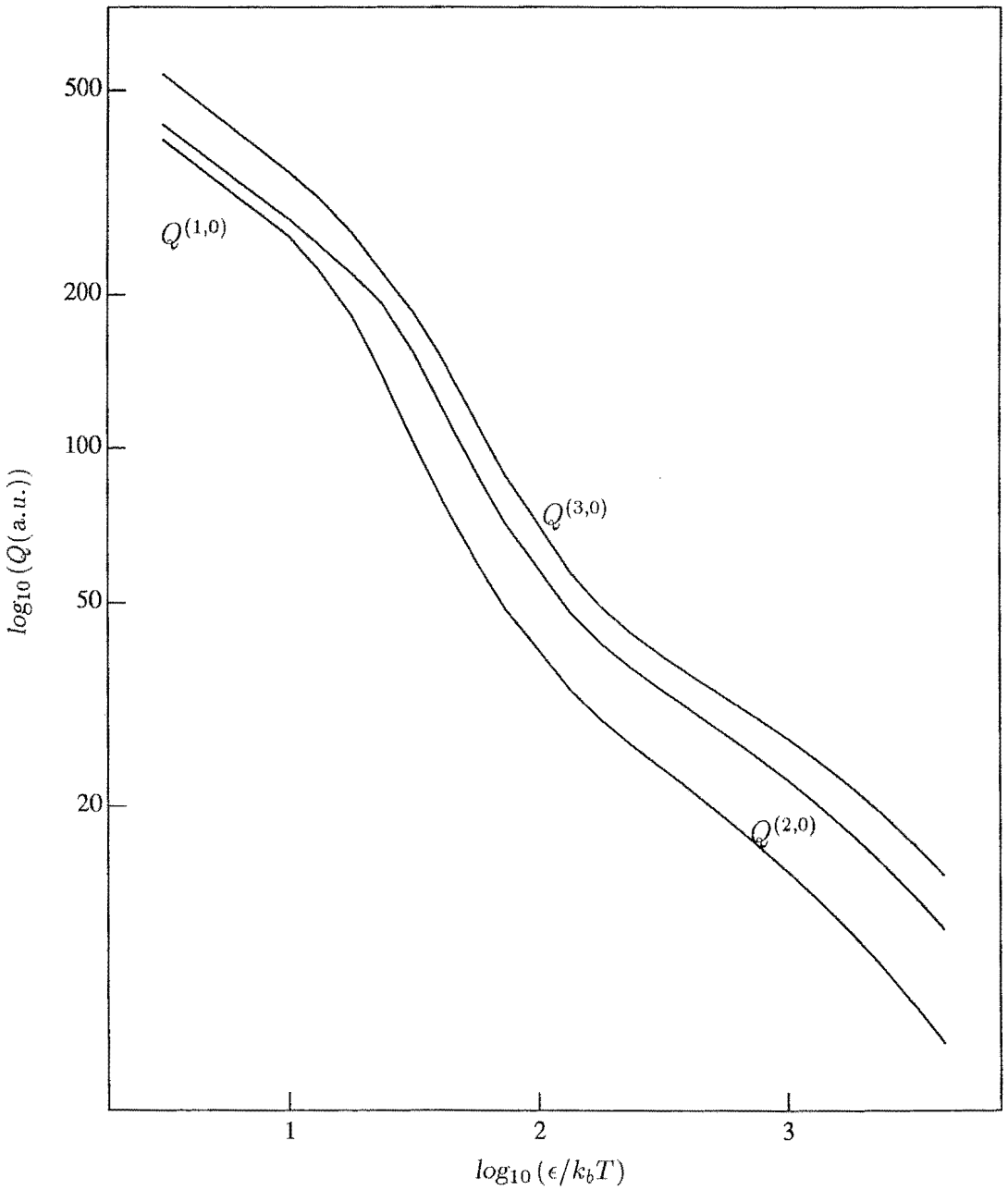

Figure 9.1: The rotationally averaged transport cross sections of Li^+ ions in CO gas, as a function of the dimension-less relative kinetic energy. The transport cross sections are plotted as $\log_{10}$ and in *a.u.* The transport cross section curves for the cross sections $Q^{(1,0)}$, $Q^{(2,0)}$, and $Q^{(3,0)}$ are labelled in the figure. These cross sections have been calculated using the MP4SDQ/6-311+G(2df) method as outlined in section 9.2.1.

Table 9.18: Summary of Li^+—CO trajectory parameters used for the MP4SDQ/6–311+G(2df) potential energy surface.

Range of ϵ (10^{-3})	< 9.5	9.5-95	> 95
Number of ϵ values	2	8	15
Number of ϵ_0 values	20	16	8
ACC	1×10^{-8}	1×10^{-9}	1×10^{-10}
R_s (a.u.)	400	180	120
b_s (a.u.)	20.0	10.0	8.0
c	1.0	1.0	1.0
N1 and N2	48+6	32+6	24+4
N3=N4=N5	10	6	6
Number of trajectories	2160000	1050624	725760

discrepancies with the only other data set in the literature reported by Tyndall [173] at zero field. Tyndall's measurements were also significantly smaller than those for the Li^+—N_2 system, which he then interpreted in terms of the presence of the small dipole moment of the CO molecule. However transport measurements for other alkali-metal ions with N_2 and CO have revealed that the ratio of zero-field mobilities between the two systems were 1.10 for K^+ [174], and 1.11 for Cs^+ [175]. Thus it seems likely that Tyndall's mobility measurements of Li^+ ions in CO gas are in error perhaps due to the presence of fast clustering reactions [161], and that the permanent dipole moment affects the mobility to a small extent at small field strength.

The trajectories that are summarised in table 9.18 were used to calculate the cross sections defined by equations 7.3 and 7.4 using the potential energy surface outlined in chapter 8. The rotationally averaged cross sections were then used as input into the programs `BIMAX` and `MOBDIF` respectively, in order to calculate the transport coefficients of Li^+ ions in CO gas at $T = 300$ K as a function of E/N.

9.3.1 Transport Coefficients Calculated from the Møller-Plesset Potential Energy Surface

The numerical results of the transport coefficients from the program `MOBDIF` at low E/N are displayed in table 9.19. Also displayed is the effective temperature of the ions, T_{ions}, the kinetic energy in the laboratory reference frame, E_{lab}, and the

calculated drift velocity, v_d. Note that the mobility, K_0, and the parallel, $ND_{||}$, and perpendicular diffusion coefficients, $ND_{\perp}$, have converged to an accuracy of $\pm 0.1\%$, $\pm 0.25\%$, and $\pm 0.25\%$ respectively, in this energy range.

Calculations of the transport coefficients at high field strength have been performed and the numerical results from the program `MOBDIF` are displayed in table 9.20. The theoretical accuracy of the calculated transport coefficients can be estimated from a comparison of the 7th- and 8th-order approximation results from the program `MOBDIF`. Note that the mobility K_0, and the parallel $ND_{||}$, and perpendicular diffusion coefficients $ND_{\perp}$ have converged to an accuracy of $\pm 0.1\%$, $\pm 0.25\%$, and $\pm 0.25\%$ respectively, in this range.

To assess the degree of agreement between the theoretically and experimentally derived transport coefficients, an estimate of the uncertainties of the calculations and experiments are required.

The theoretical accuracy of the calculated transport coefficients can be estimated from a comparison of the 7th- and 8th-order approximation results from the program `MOBDIF`. These results show that the mobility has converged to within 0.1% below 100 Td, and 0.1% to 2% in the range 100—130 Td. There is a large region of inconvergence between approximately 130 and 300 Td, followed by between 10% and 2% accuracy for the mobility in the range of 300 to 400 Td, and between 2% and 0.6% in the range of 400—500 Td. The mobility converges to within 0.5% at field strengths beyond 500 Td.

The reduced perpendicular diffusion coefficient, $\tilde{D}_{\perp}$, converged to within 0.25% below 100 Td, within 0.25—4% in the range 100—120 Td, and did not converge in the range 120—400 Td. In the range 400—500 Td the reduced perpendicular diffusion coefficient converged to an accuracy of within 10—4%, and within 4—2% in the 500—600 Td range.

The reduced parallel diffusion coefficient, $\tilde{D}_{||}$, converged to within 0.25% below 90 Td, within 0.25—50% in the range 90—120 Td, and did not converge in the range 120—400 Td. In the range 400—500 Td the reduced parallel diffusion coefficient converged to an accuracy of within 50—20%, and within 20—12% in the 500—600 Td range.

Other sources of uncertainties to the theoretically derived transport coefficients are from the accuracy of the potential energy surface. While the accuracy of the

Table 9.19: Transport properties of Li^+ ions in CO gas at T = 300 K, as calculated from the MP4SDQ/6–311+G(2df) potential energy surface, at low field strength.

E/N	T_{ion}	E_{lab}	v_d	K_0	$ND_{\|\|}$	$ND_\perp$
(Td)	(K)	(eV)	(km/s)	(cm^2/Vs)	$10^{18}/cms$	
10.03871	302.63	.03912	.09758	3.61783	2.233	2.217
11.29265	303.32	.03921	.10961	3.61266	2.247	2.227
12.70692	304.19	.03932	.12312	3.60625	2.265	2.240
13.48089	304.70	.03939	.13048	3.60249	2.276	2.247
15.17777	305.94	.03955	.14655	3.59372	2.301	2.265
17.09649	307.50	.03975	.16458	3.58299	2.333	2.288
18.14882	308.42	.03987	.17441	3.57678	2.351	2.301
19.26898	309.46	.04000	.18482	3.56995	2.372	2.316
20.46183	310.63	.04015	.19585	3.56246	2.396	2.332
23.08702	313.42	.04051	.21991	3.54529	2.451	2.371
26.06898	316.95	.04097	.24690	3.52502	2.521	2.420
29.47076	321.40	.04154	.27723	3.50121	2.608	2.480
31.34746	324.04	.04189	.29377	3.48797	2.659	2.515
33.35366	327.01	.04227	.31130	3.47382	2.718	2.555
35.49587	330.35	.04270	.32986	3.45883	2.783	2.599
37.78850	334.10	.04319	.34956	3.44297	2.857	2.648
40.24098	338.32	.04373	.37055	3.42724	2.931	2.698
42.86514	343.05	.04434	.39270	3.40976	3.024	2.759
45.67315	348.37	.04503	.41619	3.39162	3.128	2.827
48.67766	354.35	.04580	.44110	3.37269	3.242	2.901
51.89171	361.07	.04667	.46756	3.35360	3.376	2.984
55.32855	368.62	.04765	.49566	3.33430	3.529	3.077
59.00146	377.10	.04874	.52550	3.31498	3.703	3.182
62.92368	386.63	.04998	.55721	3.29590	3.903	3.298
67.18899	397.34	.05136	.59093	3.27351	4.136	3.426
71.76586	409.37	.05292	.62682	3.25084	4.406	3.568
76.62350	422.89	.05466	.66533	3.23181	4.777	3.734
81.79297	438.08	.05663	.70617	3.21342	5.182	3.920
87.26748	455.14	.05883	.74978	3.19781	5.675	4.133
93.04814	474.32	.06131	.79532	3.18131	5.978	4.360
99.13171	495.86	.06410	.84409	3.16918	6.342	4.629

Table 9.20: Transport properties of Li^+ ions in CO gas at $T = 300$ K, as calculated from the MP4SDQ/6–311+G(2df) potential energy surface, at high field strength.

E/N	T_{ion}	E_{lab}	v_d	K_0	$ND_{\parallel}$	$ND_{\perp}$
(Td)	(K)	(eV)	(km/s)	(cm^2/Vs)	$10^{18}/cms$	
303.98411	6050.38	.78208	4.29473	5.25845	756.956	90.868
317.21867	6761.13	.87395	4.54622	5.33413	825.920	123.415
332.38213	7559.72	.97718	4.81031	5.38651	797.925	156.617
349.47683	8457.03	1.09316	5.12275	5.45578	729.667	193.059
368.75393	9465.23	1.22348	5.48083	5.53199	669.260	233.811
390.53806	10598.06	1.36991	5.86880	5.59317	635.400	278.305
415.01811	11870.90	1.53444	6.27649	5.62888	628.531	326.129
442.15954	13301.06	1.71931	6.70209	5.64162	641.615	378.127
471.90842	14907.99	1.92702	7.14661	5.63656	672.618	435.309
504.40698	16713.54	2.16040	7.61135	5.61633	714.608	498.483
539.58429	18742.25	2.42264	8.09832	5.58609	772.741	567.990
577.48176	21021.71	2.71728	8.60947	5.54895	845.092	644.736
618.12964	23582.92	3.04835	9.14737	5.50794	932.661	729.775
661.56150	26460.69	3.42033	9.71488	5.46562	1036.123	824.406

MP4SDQ/6–311+G(2df) potential energy surface outlined in chapter 8, is not as accurate as the potential energy surface calculated for the Li^+—N_2 system, a conservative estimate of the error would be a maximum of 5% at large separation and decreasing below 2—3% at smaller separation. The greater uncertainty of the Li^+—CO potential energy surface results from the extra electronic complexity of the CO molecule, particularly with respect to establishing reliable electric multipole moments important in long-range interactions. The other main source of uncertainty in the theoretical calculations results from the choice of trajectory parameters which necessarily limits the number of the trajectory calculations. A conservative estimate of this source of uncertainty is less than 1%. Therefore the combined theoretical uncertainty is greatest ($\leq$ 6%) at small E/N, decreasing to less than 3% at high E/N.

Satoh *et al.* [172] estimates the uncertainties of their measurements as $\simeq$ 3% at low and intermediate E/N, and $\simeq$1.5% at high E/N. The major components of the uncertainties relate to the measurements of temperature and pressure throughout the course of the experiment. The uncertainties of the diffusion coefficients have been extrapolated from the uncertainties for the mobility using equations 7.11. Because

the published graph of the transport coefficients had no associated table of data, the raw data was estimated from a magnified image of the figure. From the resulting variation of adjacent points on the experimental mobility and diffusion coefficient curves they have published, and from previous knowledge of the inherent errors in experimental measurements in drift-tubes, we estimate that the uncertainty of their measurements to be about 5% below 100 Td, and about 2% above 100 Td for the mobility.

The calculated mobilities and diffusion coefficients (which were made dimensionless by equations 7.11 and 7.12) are compared to the results of Satoh *et al.* [161] in figures 9.2 and 9.3 respectively.

Several features are evident in the comparison of the experimentally and theoretically derived mobilities. The two mobility curves are within the mutual uncertainties almost over the entire range of E/N plotted. However, some systematic differences between the actual experimental points and the theoretical curve which were not present in the study of Li^+—N_2 system suggest that the potential energy surface of Li^+—CO is comparatively more inaccurate. These findings are supported by the conclusions of the *ab initio* study outlined in chapter 8. Note also that the agreement to within mutual uncertainties of the experimental and theoretical mobilities results mainly from the greater uncertainties in each data set, due partly to conservative estimates, compared to those for the Li^+—N_2 system.

Considering each region of E/N separately it is apparent that the correspondence between the experimental and theoretical mobilities is reasonable at low E/N up to 100 Td. While there is a consistent displacement between the two data sets, the agreement is within the uncertainties of the experimental error, and the slight differences are not unexpected, bearing in mind the known difficulties of calculating accurate electric multipole moments for CO which are important in determining the long-range potential energy surface. Note that the fitted dipole moment of CO was larger than the experimental value and that this may be responsible for the smaller theoretical mobility at low E/N.

In the region directly after $\simeq$ 100 Td, the problems of inconvergence associated with a rapid rise in mobility were encountered. The mobilities have been spline fitted through the region of inconvergence and plotted as a dotted line. It is clear that theoretical and experimental mobilities started to diverge to the limit of the

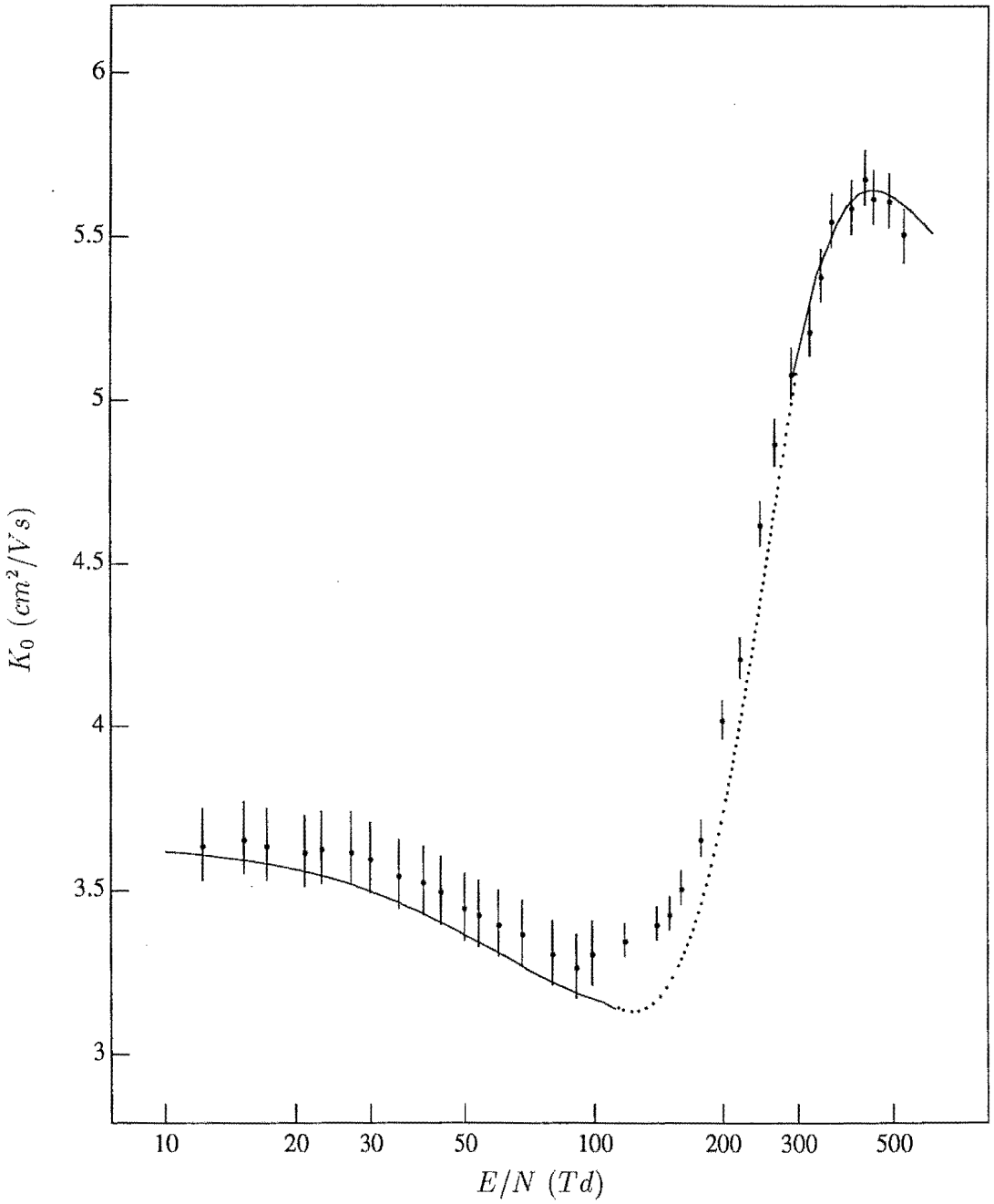

Figure 9.2: The mobility of Li^+ ions in CO gas calculated using MP4SDQ/6-311+G(2df) potential energy surface, at T =300 K, as a function of E/N in units of Td. The points with error bars are the experimental data of Satoh *et al.* [161]. The solid curve was calculated with the program `MOBDIF`, using the cross sections calculated using the parameters as outlined in table 9.18. The mobility has been spline fitted through the region of inconvergence and is plotted using the dotted curve.

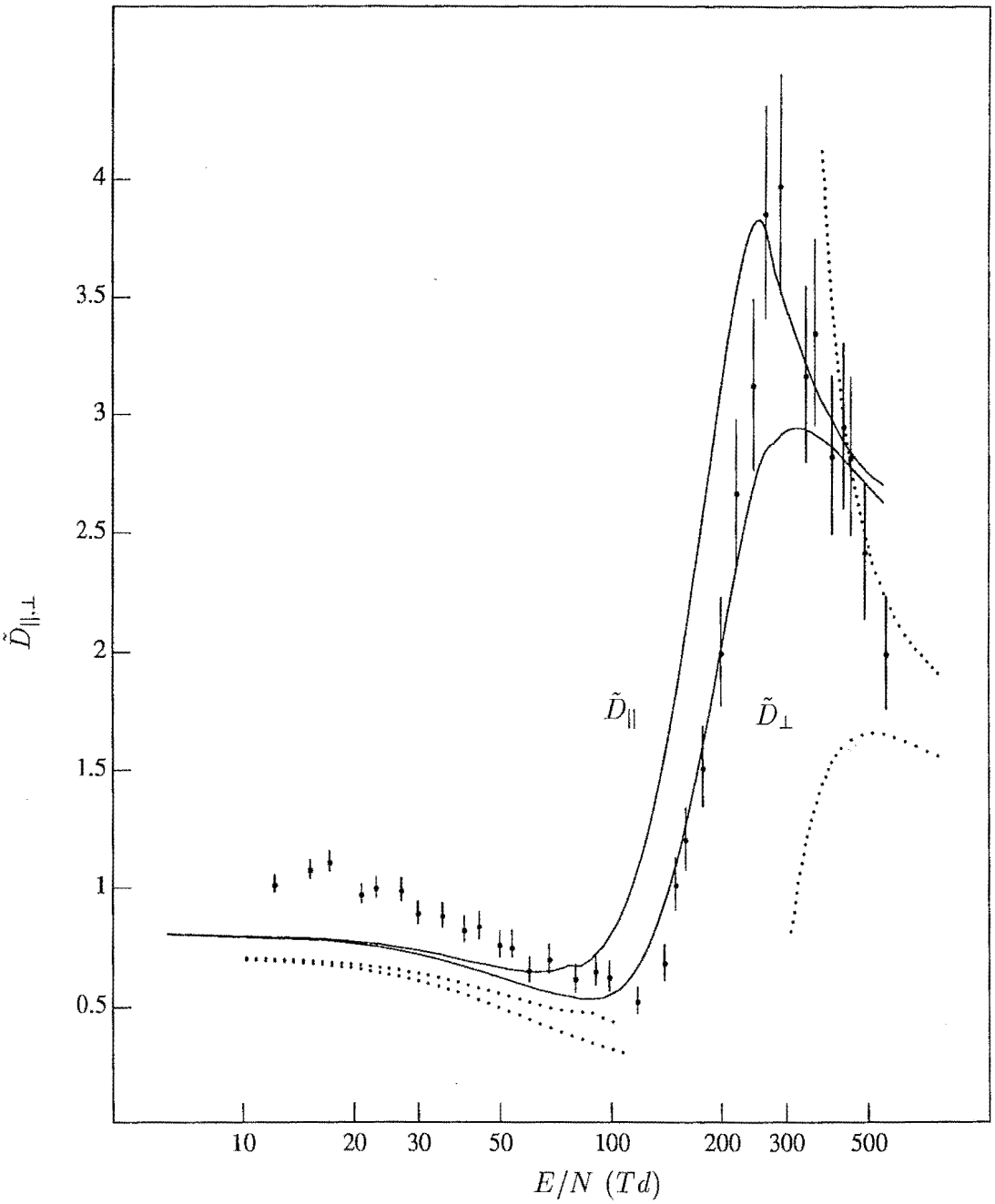

Figure 9.3: The reduced diffusion coefficients of Li^+ ions in CO gas calculated using the MP4SDQ/6–311+G(2df) potential energy surface, at T=300 K, as a function of E/N in units of Td. The points with error bars are the experimental measurements of the parallel diffusion coefficients of Satoh *et al.* [161]. The solid curves, representing the reduced parallel, $\tilde{D}_{\parallel}$, and perpendicular, $\tilde{D}_{\perp}$, diffusion coefficients, were calculated with the program `BIMAX`, using the cross sections calculated using the parameters as outlined in table 9.18. The results were spline fitted through the region of inconvergence. The dotted curves represent the reduced parallel and perpendicular diffusion coefficients calculated using the program `MOBDIF`, which were not plotted in the region of inconvergence. The reduced diffusion coefficients are dimensionless and defined by equation 7.11.

mutual uncertainties that bound the agreement of these data sets. Because the uncertainties of the theoretical calculations are not as small as those corresponding to the Li^+—N_2 system, and because of the inconvergence problems of the kinetic theory, any further conclusions about the potential energy surface are not possible. However it does seem likely that the possible disagreement in this region, which was also observed in the Li^+—N_2 system, is due to the variation of correlation energy obtained from Møller-Plesset calculations as a function of molecular separation [10].

The agreement between the theoretical and experimental data sets at high E/N is excellent. The greater complexity of internal vibrational coordinates of the Li^+—CO potential energy surface at small separation meant that a simple semi-empirical model could not be applied to simply account for the effect of nuclear polarisation. Calculating the effect of nuclear polarisation in this system requires more rigorous treatment of the internuclear coordinate of the CO molecule as a function of the intermolecular vector R. However where such an effect produced a measurable improvement in the case of the Li^+—N_2 systems' transport coefficients, it is doubtful if inclusion of this effect could improve the theoretically calculated mobilities for this system.

Turning to a discussion of the comparison of the experimental and theoretical diffusion coefficients plotted in figure 9.3, it is evident that there is no agreement between the data sets for the parallel diffusion coefficients except above 360 Td, where the correspondence between the reduced parallel diffusion coefficient calculated using the program `BIMAX` and the experimental results of Satoh *et al.* are good. These results complement those found for the mobilities. At low E/N, the consistent differences between the theoretical and experimental reduced diffusion coefficients are exaggerated and beyond the mutual uncertainties. The differences almost certainly result from the inaccuracies of the potential energy surface due to the difficulties of obtaining reliable electric multipole moments from Møller-Plesset methods. The comparison of the theoretical and experimental results for the reduced parallel diffusion coefficients at high E/N suggested that the potential energy surface is accurate. This conclusion is supported by the excellent agreement between the short-range isotropic radial function calculated in chapter 8 and that determined by integral cross sections measurements by Gislason *et al.* [131]. Note that no experimental data for the perpendicular diffusion coefficients has been reported.

9.4 Conclusion

A complete report of the transport calculations of Li^+ ions in CO gas at $T = 300$ K has been given. These results have allowed further conclusions about similar atomic ion-diatom transport systems to be made. The MP4SDQ/6–311+G(2df) potential energy surface presented in chapter 8 was used to calculate the trajectories necessary to obtain kinetic theory cross sections to an accuracy of at least 1%. These cross sections were then used to calculate the transport coefficients of Li^+ ions in CO gas. The comparison of the theoretical and experimental mobilities revealed that the data sets were within the mutual uncertainties although systematic differences were observed at low E/N. The differences between the experimental and theoretical reduced parallel diffusion coefficient were further exaggerated beyond the mutual uncertainties, suggesting inaccuracies in long-range potential energy surface were responsible. The fitted dipole moment of CO was larger than the experimental value and this may well be the cause of the slightly smaller low field theoretical mobilities and diffusion coefficients. Correspondence between the experimental and theoretical mobilities and diffusion coefficients was excellent at high E/N justifying the analysis of the angular anisotropy at short-range for the potential energy surface in chapter 8.

Comparison of the results for the Li^+—CO and the Li^+—N_2 systems has shown some similarities. Inaccuracies in the calculated transport coefficients for these systems about 100 Td suggest that both potential energy surfaces are not accurate in the 6—10 *bohr* separation range. This observation is consistent with the known properties of Møller-Plesset calculations at non-equilibrium geometries [10]. The calculation of the transport properties is further complicated by the known difficulties in achieving convergence when calculating the dipole moment using Møller-Plesset theory. The accuracy of the potential energy surface could be improved with the application of a method with a more stable treatment of electron correlation as a function of separation, such as QCI methods. These methods have also been shown to have improved stability when calculating the electric multipole moments of the CO molecule [165].

Chapter 10

Conclusion

This thesis has succeeded in its main objective. Ion transport properties of systems involving electronic and molecular anisotropy have been calculated. These calculations have generally resulted in good agreement with experiment.

In the process of this work an understanding of the methods and techniques used by theoretical chemists has been gained. The methods and techniques have been applied to several different problems both in the calculation of the thermodynamic and kinetic properties of an organic reaction, and the calculation of ion transport properties of anisotropic systems. Many of the exponents of these methods and techniques have attempted to characterise the status and sophistication of current theory in order to justify its application. However, the role of theory has changed the face of chemistry and now and in the future, chemists can no longer perform experiments without recourse to theory and *vice versa*. The computer is now part of the modern chemistry laboratory.

Finally, it remains to point to the directions that studies in ion transport properties are likely to make. It is clear that experimental laser techniques will play a much larger role in the experimental determination of ion transport properties. Recent measurements of the mobilities of Ba^+ in inert gases [176, 177] by laser-induced fluorescence have allowed experimentalists to directly measure the velocity distribution of the ions drifting in gas. Accurate velocity profiles of these systems will allow comparison with approximations on which the theory is based and this will have implications about the future directions of the theory. Not only have lasers been used to determine the velocity profiles of ions drifting in gases but they have been

used to look at dynamical effects such as rotational alignment of ions [65, 178, 179]. These experimental observation have already led to a series of theoretical studies [180, 181, 182, 183]. The application of laser measurements of the properties of ions in drift tubes will lead to studies that involve both transport theory and dynamics. Viehland [64] has stated his intention of attempting calculations of anisotropic A_2^+—B systems. Such calculations will be relevant to the dynamical effects which are intrinsic to systems with anisotropy, and have been observed in laser-induced fluorescence measurements.

Acknowledgements

I would like to thank my supervisors Dr. R. G. A. R. Maclagan and Dr P. W. Harland for their interest and support during the course of this research programme. I am grateful to Prof. L. A. Viehland for the opportunity to collaborate with him on the work concerning the ion transport properties of atomic ion-diatom systems, to Prof. D. C. Clary, Prof. A. D. Buckingham, and Prof. E. E. Fergusson for their advice and encouragement concerning the ion transport of open shell atomic ions, and to Dr D. Q. MacDonald and Prof. J. M. Coxon for their discussions on Diels-Alder reactions.

I would like to thank my father, Trevor, my sisters Jacinta and Christine, and my brothers Leon and Jonathan, who are all eccentric. My good friend Dr. Pravit Sudkeau and I worked in the same study for most of the time that this research took place. I thank him for his comany and the many fine dinners that we shared, and I hope that we can share many more in the future. Tony Clear deserves praise for his stamina in the course of editing this thesis, and I thank him for his support in this regard, and for his presence in recent and difficult times. My thanks would not be complete without mentioning Andrea, my beautiful companion, and now my wife!

Finally, this thesis has not been a single effort. I would like to thank my mother, Bernadette, for the struggles that she been through to make this possible. Her tremendous strength and courage was my inspiration and I trust that she is rewarded in proportion with her amazing efforts.

Publications

Ab initio Calculation of the Mobility of C^+ (^2P) and C^+ (^4P) in Helium.
with P.W. Harland, R.G.A.R. Maclagan, and R.W. Simpson.
Int. J. of Mass Spect. and Ion Proc.,87,(1989),181-186.

Experimental Measurements and Theoretical Calculations of the mobility of the N^+ ion in helium.
with P.W. Harland, J.A. Harrison, R.G.A.R. Maclagan, and R.W. Simpson.
Int. J. Mass Spect. and Ion Proc.,107,(1991),215-224.

Ab initio C_s Transition State for the Diels-Alder Reaction of Acetylene and Butadiene.
with J.M. Coxon, R.G.A.R. Maclagan, and D.Q. McDonald.
J. Org. Chem., 55,(1990),3804-3807.

Calculation of the Potential Energy Surface of $Li^+ + N_2$.
with P.W. Harland, and R.G.A.R. Maclagan.
Chem. Phys., 165,(1992),73-88.

Transport Coefficients for Lithium Ions in Nitrogen Gas: A test of the $Li^+ - N_2$ Interaction Potential.
with L.A. Viehland, and A.S. Dickinson, and R.G.A.R. Maclagan
Chem. Phys., 165,(1992),11-20.

Calculation of the Potential Energy Surface of Li^+ + CO.
with P.W. Harland, and R.G.A.R. Maclagan.
in preparation.

Transport Coefficients for Lithium Ions in Carbon Monoxide Gas: A test of the $Li^+ - CO$ Interaction Potential.
with L.A. Viehland, and R.G.A.R. Maclagan
in preparation.

Theoretical and Experimental Exploration of Gas Phase Ion Transport and Ion-Neutral Interaction Potentials.
with P. W. Harland.
invited review, *J. Chem. Soc. Faraday Disc.*
in preparation.

Bibliography

[1] H. F. Schaeffer III, The Electronic Structure of Atoms and Molecules, (Addison-Wesley Publishing Company, 1972).

[2] M. W. Schmidt, K. K. Baldridge, J. A. Boatz, J. H. Jensen, S. Koseki, M. S. Gordon, K. A. Nguyen, T. L. Windus, and S. T. Elbert, *Quant. Chem. Prog. Ex. Bull.*, 10(1990)52.

[3] Gaussian82, J. S. Binkley, M.J. Firsch, D.J. DeFrees, K. Raghavachari, R.A. Whiteside, R. A. Schlegel, E. M. Fluder, and J. A. Pople. Carnegie-Mellon University: Pittsburgh, PA., 1982.

[4] Gaussian90, Revision F., M.J. Firsch, M. Head-Gordon, G.W. Trucks, J.B. Foresman, H.B. Schlegel, K. Raghavachari, M. Robb, J.S. Binkley, C. Gonzalez, D.J. DeFrees, D.J. Fox, R.A. Whiteside, R. Seeger, C.F. Melius, J. Baker, R.L. Martin, L.R. Kahn, J.J.P Stewart, S. Topiol, and J.A. Pople. Guassian, Inc., Pittsburgh PA, 1990.

[5] H. Heitler and F. London, *Z. Phys.*, 44(1927)455.

[6] W. J. Hehre, L. Radom, P. V. Schleyer, and J. A. Pople, *Ab Initio* Molecular Orbital Theory, (Wiley Intersceince, New York, 1986).

[7] A. Szabo and N.S. Ostlund, Modern Quantum Chemistry: Introduction to Advanced Electronic Structure Theory, (Macmillan Publishing Co., Inc., 1982).

[8] S. F. Boys, *Proc. Roy. Soc.*, A200(1950)542.

[9] S. Huzinaga, *J. Chem. Phys.*, 42(1965)1297.

[10] J. A. Pople, M. Head-Gordon, and K. Raghavachari, *J. Chem. Phys.*, 87(1987)5968.

[11] O. Diels amd K. Alder, *Justus Liebigs Ann. Chem.*, 460(1928)98.

[12] J. Suaer and R. Sustmann, *Angnew. Chem. Int. Ed. Engl.*, 19(1980)779.

[13] R. B. Woodward and R. Hoffmann, *J. Am. Chem. Soc.*, 87(1965)394.

[14] R. B. Woodward and R. Hoffmann, *J. Am. Chem. Soc.*, 87(1965)2046.

[15] R.E. Townscend, G. Ramunni, W.J. Hehre, and L. Salem, *J. Am. Chem. Soc.*, 98(1976)2190.

[16] F.K. Brown and K.N. Houk, *Tetrahedron Lett.*, 25(1984)4609.

[17] F. Bernardi, A. Bottini, M.J. Field, M.F. Guest, I.H Hillier, M.A. Robb, and A. Venturini, *J. Am. Chem. Soc.*, 110(1988)3050.

[18] R.D. Bach, J.W. McDouall, H.B. Schlegel, and G.J. Wolber, *J. Org. Chem.*, 54(1989)2931.

[19] K.N. Houk, Yi-Tsong Lin, and F.K. Brown, *J. Am. Chem. Soc.*, 108(1986)554.

[20] J.J. Gajewski, K.B. Peterson, and J.R. Kagel, *J. Am. Chem. Soc.*, 109(1987)5565.

[21] M. Ortega, A. liva, J.M. Lluch, and J. Bertran, *J. Chem. Phys. Lett.*, 102(1983)317.

[22] M.J.S. Dewar, S. Olivella, and J.J.P. Stewart, *J. Am. Chem. Soc.*, 108(1986)5771.

[23] K. N. Houk, R. J. Loncharich, J. F. Blake, and W. L. Jorgensen, *J. Am. Chem. Soc.*, 111(1989)9172.

[24] M.J.S. Dewar, E.G. Zoebisch, E.F. Healy, and J.J.P Stewart, *J. Am. Chem. Soc.*, 107(1985)3902.

[25] R.D. Bach, G.J. Wolber, and H.B. Schlegel, *J. Am. Chem. Soc.*, 107(1985)2837.

[26] N.D. Epiotis, Unified Valence Bond Theory of Electronic Structure, (Springer Verlag, Berlin, 1982).

[27] United States Patent Office, 1970. 3,513,208.

[28] J.M. Coxon, S.T. Grice, R.G.A.R. Maclagan, and D.Q. McDonald, *J. Org. Chem.*, 55(1989)3804.

[29] D. Quentin McDonald, PhD thesis, University of Canterbury, 1991.

[30] K.N. Houk, R.W. Gandour, R.W. Stozier, N.G. Rondan, and L.A. Paquette, *J. Am. Chem. Soc.*, 101(1979)6797.

[31] B.A. Hess Jr., L.J. Schaad, and D.N. Reinhoudt, *Int. J. Quantum Chem.*, 29(1986)345.

[32] L. Boltzmann, *Wien Ber.*, 66(1872)275.

[33] K. Kumar, H. R. Skullerud, and R. E. Robson, *Aust. J. Phys.*, 33(1980)469.

[34] K. Kumar, *Aust. J. Phys.*, 33(1980)449.

[35] K. Kumar, *Aust. J. Phys.*, 33(1980)343.

[36] W.A. Wakeham and V. Vesovic, Status and Future Developments in the Study of Transport Properties, (Kluwer Academic Publishers, Dordrecht, The Netherlands, 1992).

[37] H. W. Ellis, R. Y. Pai, E. W. McDaniel, E. A. Mason, and L. A. Viehland, *At. Data Nucl. Data Tables*, 17(1976)177.

[38] H. W. Ellis, E. W. McDaniel, D. L. Albritton, L. A. Viehland, S. L. Lin, and E. A. Mason, *At. Data Nucl. Data Tables*, 22(1978)179.

[39] H. W. Ellis, M. G. Thackston, E. W. McDaniel, and E. A. Mason, *At. Data Nucl. Data Tables*, 31(1984)113.

[40] E.A. Mason and E.W. McDaniel, Transport Properties of Ions in Gases, (A Wiley–Interscience publication, 1988).

[41] L. A. Viehland and E. A. Mason, *Ann. Phys.*, 91(1975)499.

[42] L. A. Viehland and E. A. Mason, *Ann. Phys.*, 110(1978)287.

[43] S. L. Lin, L. A. Viehland, and E. A. Mason, *Chem. Phys.*, 37(1979)411.

[44] L.A. Viehland, *Chem. Phys.*, 101(1986)1.

[45] P. J. Drallos and J. M. Wadehra, *Phys. Rev. A*, 40(1989)1967.

[46] R. E. Robson, K. F. Ness, G. E. Sneddon, and L. A. Viehland, *J. Comp. Phys.*, 91(1991)213.

[47] T. Kihara, *Rev. Mod. Phys.*, 25(1953)844.

[48] J. O. Hirschfelder, C. F. Curtiss, and R. B. Bird, Molecular Theory of Gases and Liquids, (John Wiley and Sons, Inc., 1954).

[49] L. Monchick and S. Green, *J. Chem. Phys.*, 76(1975)2000.

[50] S. Green and L. Monchick, *J. Chem. Phys.*, 63(1975)4198.

[51] L. A. Viehland and D. W. Fahey, *J. Chem. Phys.*, 78(1983)435.

[52] L. A. Viehland, *Chem. Phys. Lett.*, 144(1988)552.

[53] L. A. Viehland, S. L. Lin, and E. A. Mason, *Chem. Phys.*, 54(1981)341.

[54] A. M. Authurs and A. Dalgarno, *Proc. Roy. Soc. A*, 256(1960)540.

[55] C. F. Curtiss, *J. Chem. Phys.*, 67(1977)5770.

[56] C. F. Curtiss, *J. Chem. Phys.*, 75(1981)376.

[57] A. R. Edmonds, Angular Momentum in Quantum Mechanics, (Princeton University Press, 1960).

[58] L.A. Viehland and K. Kumar, *Chem. Phys.*, 131(1989)295.

[59] L. A. Viehland, *Chem. Phys.*, 70(1982)149.

[60] A. S. Dickinson and M. S. Lee, *J. Phys. B: At. Mol. Phys.*, 18(1985)3987.

[61] A. S. Dickinson and M. S. Lee, *J. Phys. B: At. Mol. Phys.*, 18(1985)4177.

[62] L.A. Viehland, in: Status and Future Developments in the Study of Transport Properties, ed. W.A. Wakeham and V. Vesovic, NATO Advanced Research Workshop, (Kluwer Academic Publishers, Dordrecht, The Netherlands, 1992).

[63] N. Smith, *J. Chem. Phys.*, 85(1986)1987.

[64] L. A. Viehland. Private Communication, 1992.

[65] R. A. Dressler, H. Meyer, and S. R. Leone, *J. Chem. Phys.*, 87(1987)6029.

[66] C. C. Kirkpatrick and L. A. Viehland, *Chem. Phys.*, 98(1985)221.

[67] L. A. Viehland and E. A. Mason, *J. Chem. Phys.*, 80(1984)416.

[68] A. D. Koutselos, E. A. Mason, and L. A. Viehland, *J. Chem. Phys.*, 93(1990)7125.

[69] R.W. Simpson, P.W. Harland, and R.G.A.R. Maclagan, *Int. J. Mass Spect. and Ion Proc.*, 90(1989)193.

[70] P. C. Hariharan and V. Staemmler, *Chem. Phys.*, 15(1976)409.

[71] H. Inouyne and S. Kita, *J. Chem. Phys.*, 57(1972)1301.

[72] I. R. Gatland, L. A. Viehland, and E. A. Mason, *J. Chem. Phys.*, 66(1977)537.

[73] I. R. Gatland, W. F. Morrison, H. W. Ellis, M. G. Thackston, E. W. McDaniel, M. H. Alexander, L. A. Viehland, and E. A. Mason, *J. Chem. Phys.*, 66(1977)5121.

[74] R. A. Cassidy and M. T. Elford, *Aust. J. Phys.*, 38(1985)587.

[75] T. H. Løvaas, H. R. Skullerud, O. H. Christensen, and D. Linhjell, *J. Phys. D: Appl. Phys.*, 20(1987)1465.

[76] R. Ahlrichs, H. J. Böhm, S. Brode, K. T. Tang, and J. Peter Teonnies, *J. Chem. Phys.*, 88(1988)6290.

[77] P. H. Larsen, H. R. Skullerud, and T. Stefànsson, *J. Phys. B: At. Mol. Phys.*, 21(1988)2519.

[78] U. E. Senff and P. G. Burton, *Mol. Phys.*, 58(1986)637.

[79] S.T. Grice, P.W. Harland, R.G.A.R. Maclagan, and R.W. Simpson, *Int. J. Mass Spect. and Ion Proc.*, 87(1989)181.

[80] S.T. Grice, P.W. Harland, J. Harrison, R.G.A.R. Maclagan, and R.W. Simpson, *Int. J. Mass Spect. and Ion Proc.*, 107(1991)215.

[81] R.W. Simpson, R.G.A.R. Maclagan, and P.W. Harland, *J. Chem. Phys.*, 87(1987)5419.

[82] D. C. Clary, C. E. Dateo, and D. Smith, *Chem. Phys. Lett.*, 167(1990)1.

[83] R. Thomas, J. Barassin, and A. Barassin, *Int. J. Mass Spect. and Ion Proc.*, 31(1979)227.

[84] I. Dotan, F. C. Fehsenfeld, and D. L. Albritton, *J. Chem. Phys.*, 71(1979)4762.

[85] K. Peska, G. Sejkora, H. Stori, F. Egger, H. Ramier, M. Kriegel, and W. Lindinger, in: 3rd Symp. Atomic and Surface Physics, ed. W. Lindinger, (Innsbruck, 1982).

[86] N. D. Twiddy, A. Mohebati, and M. Tichy, *Int. J. Mass Spect. and Ion Proc.*, 74(1986)251.

[87] S. W. Harrison, G. A. Henderson, L. J. Massa, and P. Solomon, *Astrophys. J*, 189(1974)605.

[88] D. L. Cooper and S. Wilson, *Molec. Phys.*, 44(1981)161.

[89] W. Koch and G. Frenking, *Int. J. Mass Spect. and Ion Proc.*, 74(1986)133.

[90] G. Frenking, W. Koch, F. Reichel, and D. Cremer, *J. Am. Chem. Soc.*, 109(1987)5917.

[91] S. E. Young and M. J. Coggiola, *Int. J. Mass Spect. and Ion Proc.*, 74(1986)137.

[92] C. E. Moore, Ionization Potentials and Ionization Limits Derived from the Analyses of Optical Spectra, (National Standards Reference Data Service, 1971).

[93] A. R. Lee, C. S. Enos, and A. G. Brenton, *Int. J. Mass Spect. and Ion Proc.*, 105(1991)63.

[94] N. Toshima, *J. Phys. Soc. Jpn.*, 38(1975)1464.

[95] D. W. Fahey, F. C. Fehsenfeld, and D. L. Albritton, *J. Chem. Phys.*, 74(1981)2080.

[96] R. Johnson, H. L. Brown, and M. A. Biondi, *J. Chem. Phys.*, 52(1970)5080.

[97] M. McFarland, D. L. Albritton, F. C. Fehsenfeld, E. E. Ferguson, and A. L. Schmeltekopf, *J. Chem. Phys.*, 59(1973)6610.

[98] Y. Kaneko, T. Koizumi, and N. Kobayashi, *Mass Spectosc. (Tokyo)*, 26(1978)35.

[99] H. A. Fhadil, A. T. Numan, T. Shuttleworth, and J. B. Hasted, *Int. J. Mass Spect. and Ion Proc.*, 65(1985)307.

[100] P. W. Harland and B. J. McIntosh, *J. Chem. Soc., Faraday Trans. 2*, 81(1985)169.

[101] P. W. Harland, N. Kim, and S. A. H. Patrie, *Aust. J. Chem.*, 42(1989)9.

[102] F. C. Fehsenfeld, D. L. Albritton, Y. A. Bush, P. G. Fournier, T. R. Grovers, and J. Fournier, *J. Chem. Phys.*, 61(1974)2150.

[103] D. Smith and N. G. Adams. Private Communication, 1988.

[104] J. F. Liebman and L. C. Allen, *J. Am. Chem. Soc.*, 92(1970)3539.

[105] W. Koch, G. Frenking, J. Gauss, D. Cremer, and J. R. Collins, *J. Am. Chem. Soc.*, 109(1987)5917.

[106] R. Johnsen and M. A. Biondi and, *J. Chem. Phys.*, 73(1980)190.

[107] B. R. Rowe, D. W. Fahey, F. C. Fehsenfeld, and D. L. Albritton, *J. Chem. Phys.*, 73(1980)194.

[108] H. A. Fhadil, D. Mathur, and J. B. Hayashi, *J. Phys. B: At. Mol. Phys.*, 15(1982)1443.

[109] E. E. Fergusson, F. C. Fehsenfeld, and D. L. Albritton, *Gas Phase Ion Chem.*, 1(1971)45.

[110] M. Oppenheimer, E. R. Constantinides, K. Kirby-Docken, G. A. Victor, and A. Dalgarno, *J. Geophys. Res.*, 82(1977)5485.

[111] S. D. Augustin, W. H. Miller, P. K. Pearson, and H. F. Schaeffer, *J. Chem. Phys.*, 58(1973)2845.

[112] R.W. Simpson, PhD thesis, University of Canterbury, NZ, (1988).

[113] M. W. Lindinger and D. L. Albritton, *J. Chem. Phys.*, 62(1975)3517.

[114] E. E. Fergusson, D. W. Fahey, F. C. Fehsenfeld, and D. L. Albritton, *Planet. Space Sci.*, 29(1981)307.

[115] J. L. Turner and A. Dalgarno, *Astrophys. J.*, 213(1977)386.

[116] D. W. Fahey, F. C. Fehsenfeld, and E. E. Fergusson, *J. Chem. Phys.*, 75(1981)669.

[117] E. D. Jemmis, M. W. Wong, Hans-Beat Bürgi, and L. Radom, *J. Mol. Struc. (Theo)*, 261(1992)385.

[118] M. W. Wong and L. Radom, *J. Am. Chem. Soc.*, 110(1988)2375.

[119] L. Radom, P. M. W. Gill, M. W. Wong, and R. H. Nobes, *Pure Appl. Chem.*, 60(1988)183.

[120] M. W. Wong and L. Radom, *J. Phys. Chem.*, 93(1989)6303.

[121] C. E. Dateo and D. C. Clary, *J. Chem. Phys.*, 90(1989)7216.

[122] V. Staemmler, *Chem. Phys.*, 7(1975)17.

[123] G.D. Billing and A. Hunding, *Chem. Phys. Lett.*, 44(1976)30.

[124] T.F. Ewing, J. Detrich, and R.W. Conn, *J. Chem. Phys.*, 69(1978)4662.

[125] S. Kita, K. Noda, and H. Inouye, *Chem. Phys.*, 7(1975)156.

[126] L.D. Thomas, *J. Chem. Phys.*, 67(1977)5224.

[127] G.D. Billing, *Chem. Phys.*, 36(1979)127.

[128] D. Poppe and R. Böttner, *Chem. Phys.*, 30(1978)375.

[129] G.A. Pfeffer and D. Secrest, *J. Chem. Phys.*, 78(1983)3052.

[130] U. Gierz, J.P. Toennies, and M. Wilde, *Chem. Phys. Lett.*, 110(1984)115.

[131] E.A. Gislason, P. Polak-Dingels, and M.S. Rajan, *J. Chem. Phys.*, 93(1990)2476.

[132] T.D. Selnæs, T.H. Løvaas, and H.R. Skullerud, *J. Phys. B: At. Mol. Phys.*, 23(1990)2391.

[133] M. Waldman and R.G. Gordon, *J. Chem. Phys.*, 71(1979)1353.

[134] J.E. Del Bene, M.J. Frisch, K. Raghavachari, J.A. Pople, and P.v.R. Schleyer, *J. Phys. Chem.*, 87(1983)73.

[135] S. Ikuta, *Chem. Phys.*, 95(1985)235.

[136] J. Sauer and P. Hobza, *Theoret. Chim. Acta*, 65(1984)291.

[137] V.M. Pinchuk, *J. Struc. Chem.*, 26(1985)350.

[138] J.E. Del Bene, *J. Comp. Chem.*, 7(1986)259.

[139] D.A. Dixon, J.L. Cole, and A. Komornicki, *J. Phys. Chem.*, 92(1988)1378.

[140] P.W. Harland, R.G.A.R. Maclagan, and R.W. Simpson, *J. Chem. Soc., Faraday Trans. 2*, 84(1988)1847.

[141] R.W. Simpson, R.G.A.R. Maclagan, and P.W. Harland, *J. Phys. B: At. Mol. Phys.*, 20(1987)2723.

[142] J. Hout and T.K. Bose, *J. Chem. Phys.*, 94(1991)3849.

[143] D. Sundholm, PhD thesis, University of Helsinki, 1985.

[144] K.P. Huber and G. Herzberg, Molecular Spectra and Molecular Structure. IV. Constants of Diatomic Molecules, (Van Nostrand Rienhold Co., 1979).

[145] P.E. Cade, K.D. Sales, and A.C. Wahl, *J. Chem. Phys.*, 44(1966)1973.

[146] D.J. DeFrees and A.D. McLean, *J. Chem. Phys.*, 82(1985)333.

[147] G.A. Gislason, F.E. Budenholzer, and A.D. Jorgensen, *Chem. Phys. Lett.*, 47(1977)434.

[148] W.H. Press, B.P. Flannery, S.A Teukolsky, and W.T. Vetterling, Numerical recipes, (Cambridge University Press, 1986).

[149] R. Johnsen, M. A. Biondi, and M. Hayashi, *J. Chem. Phys.*, 77(1982)2545.

[150] A. M. Arthurs and A. Dalgarno, *Proc. Roy. Soc. A*, 256(1960)540.

[151] R. T. Pack, *J. Chem. Phys.*, 62(1975)3143.

[152] M. D. Pattengill, in: Atom-Molecule Collision Theory, ed. R. B. Bernstein, (Plenum Press, 1979).

[153] D. L. Bunker, *Methods Comput. Phys.*, 10(1971)287.

[154] R. N. Porter, *Ann. Rev. Phys. Chem.*, 25(1974)317.

[155] W. H. Miller, *J. Chem. Phys.*, 54(1971)5386.

[156] A. S. Dickinson and M. S. Lee, *J. Phys. B: At. Mol. Phys.*, 18(1985)3987.

[157] D. L. Cochrane and D. G. Truhlar, *Parallel Computing*, 6(1988)63.

[158] N. Takata, *Phys. Rev. A*, 10(1974)2336.

[159] I. R. Gatland, L. M. Colonna-Romano, and G. E. Keller, *Phys. Rev. A*, 12(1975)1886.

[160] T. Koizumi, *J. Phys. Soc. Japan Rev. A*, 43(1977)1465.

[161] Y. Satoh, M. Takebe, and K. Iinuma, *J. Chem. Phys.*, 87(1987)6520.

[162] K. F. Ness and L. A. Viehland, *Chem. Phys.*, 148(1990)255.

[163] R. Bottner, U. Ross, and J.P. Toennies, *J. Chem. Soc., Faraday Disc.*, 1(1973)221.

[164] V. Staemmler, *Chem. Phys.*, 17(1976)187.

[165] G.E. Scuseria, M.D. Miller, F. Jesen, and J. Geertsen, *J. Chem. Phys.*, 94(1991)6660.

[166] R. Böttner, U. Ross, and P. Toennies, *Chem. Phys.*, 30(1978)33.

[167] L.D. Thomas, W.P. Kraemer, and G.H.F. Diercksen, *Chem. Phys.*, 30(1978)33.

[168] L.D. Thomas, W.P. Kraemer, and G.H.F. Diercksen, *Chem. Phys.*, 27(1978)237.

[169] L.D. Thomas, W.P. Kraemer, and G.H.F. Diercksen, *Chem. Phys. Lett.*, 74(1980)445.

[170] S. Ikuta, *Chem. Phys. Lett.*, 109(1984)115.

[171] H. H. Landolt and R. Börnstein, *Zahlenwerte und Funktionen*, 1(1951)510.

[172] Y. Satoh, M. Takebe, and K. Iinuma, *J. Chem. Phys.*, 88(1988)3253.

[173] A. D. Tyndall, The Mobility of Positive Ions in Gases, (Cambridge University, Cambridge, 1938).

[174] G. M. Thomson, J. H. Schummer, D. R. James, I. R. Gatland, M. R. Flannery, and E. W. McDaniel, *J. Chem. Phys.*, 58(1973)2402.

[175] M. G. Thackston, F. L. Eisele, H. W. Ellis, and E. W. McDaniel, *J. Chem. Phys.*, 67(1977)1276.

[176] S. M. Penn, J. P. M. Beijers, R. A. Dressler, V. M. Bierbaum, and S. R. Leone, *J. Chem. Phys.*, 93(1990)5118.

[177] R. A. Dressler, J. P. M Beijers, H. Meyer, S. M. Penn, V. M. Bierbaum, and S. R. Leone, *J. Chem. Phys.*, 89(1988)4707.

[178] C. P. Lauenstein, M. J. Bastian, V. M. Bierbaum, S. M. Penn, and S. R. Leone, *J. Chem. Phys.*, 94(1991)7810.

[179] M. A. Duncan, V. M. Bierbaum, G. B. Eliison, and S. R. Leone, *J. Chem. Phys.*, 79(1983)5448.

[180] B. Follmeg, H. Werner, and P. Rosmus, *J. Chem. Phys.*, 95(1991)979.

[181] B. Follmeg, P. Rosmus, and H. Werner, *J. Chem. Phys.*, 93(1990)4687.

[182] H. Meyer and S. R. Leone, *Mol. Phys.*, 63(1988)705.

[183] S. Miller, J. Tennyson, B. Follmeg, P. Rosmus, and H. Werner, *J. Chem. Phys.*, 89(1988)2178.